Title
Revealing the Magnetic Structure of the Solar Corona and Inner Heliosphere in the Era of Parker Solar Probe

Author
Badman, Samuel Timothy

Publication Date
2022

Peer reviewed|Thesis/dissertation

Revealing the Magnetic Structure of the Solar Corona and Inner Heliosphere in the Era of Parker Solar Probe

by

Samuel Timothy Badman

A dissertation submitted in partial satisfaction of the

requirements for the degree of

Doctor of Philosophy

in

Physics

in the

Graduate Division

of the

University of California, Berkeley

Committee in charge:

Professor Stuart D. Bale, Chair
Professor Jonathan Wurtele
Associate Professor Aaron Parsons

Summer 2022

Revealing the Magnetic Structure of the Solar Corona and Inner Heliosphere in the Era of Parker Solar Probe

Abstract

Revealing the Magnetic Structure of the Solar Corona and Inner Heliosphere in the Era of Parker Solar Probe

by

Samuel Timothy Badman

Doctor of Philosophy in Physics

University of California, Berkeley

Professor Stuart D. Bale, Chair

The Sun's atmosphere is a complex and dynamic magnetized plasma and extends all the way from its visible surface out into interplanetary space, carving out a bubble in the interstellar medium which is called the heliosphere. All interactions between the Sun and life on Earth are channelled through this medium. Of particular importance to making Sun-Earth connections are the regions called the corona and the inner heliosphere. These two regimes are strongly coupled together but their mutual boundary may be regarded as the location where the dynamic pressure of the outflowing solar wind overcomes the magnetic pressure of the Sun's intrinsic field. By *inner* heliosphere, we focus on the portion of the Sun's sphere of influence which extends out to 1 au and therefore is most relevant to the Earth and humanity.

Our most complete understanding of the corona and heliosphere comes from large scale physical models which can fill in information about a plasma on a 3D grid. In 2018, Parker Solar Probe (PSP) was launched into an orbit taking it closer to the Sun than any human-made object in history. This has presented an opportunity to directly probe regions of the heliosphere which had hitherto could only be accessed with global modelling. In this body of work we use new data from PSP to improve our knowledge and understanding of this global structure and further derive novel constraints on plasma models of the corona and heliosphere.

Specifically, we first introduce a framework for evaluating models of the coronal magnetic field, which sets how the solar wind emerges and shapes the inner heliosphere. In addition to new PSP data which provides direct boundary conditions on the magnetic skeleton of the corona, we show how it is important to make use of pre-existing observational capabilities to constrain the sizes of coronal holes and the locations of high plasma density indicating the topology of the coronal streamer belt. We illustrate how models must be constrained at multiple boundaries to give an accurate representation and that focusing on individual specific metrics can lead to different conclusions about optimum model parameters.

Next, we use the full data set of the heliospheric magnetic field taken by Parker Solar Probe in its first four years on orbit to directly measure the heliospheric magnetic field down to 0.13 *au* and compare directly to the large scale expectations of the Parker magnetic field. We present evidence that at 0.13 *au* the heliospheric magnetic field remains latitudinally isotropic, indicating the coronal field has already relaxed to this state within this radius. We measure the open magnetic flux and confirm it is conserved between 1 au and PSP's closest approach to date. This conservation implies a deficit in open magnetic flux according to coronal models with typically accepted model parameters. We also compare the mean direction of the heliospheric magnetic field to the expectation of the Parker spiral model, finding very good agreement which is tending to improve with closing distance from the sun as the ratio of average field strength to random fluctuations increases.

Third, we present a study in which we determine Parker Solar Probe's magnetic connectivity back to specific coronal sources for its first solar encounter. This exercise allows determination of specific locations on the Sun which emit solar wind plasma later measured by PSP, and therefore contextualises its measurements. This application of combining coronal modelling and PSP data shows how making these connections is a vital building block for understanding other peculiar plasma physics observed as PSP as it has explored new regions of the inner heliosphere. Further, it allows disambiguation of spatial and temporal phenomena.

Finally, we present recent work using observations by Parker Solar Probe and other 1 au spacecraft to localise type III radio bursts, an impulsive solar ejection of electron beams, from emission at the solar surface out into the inner heliosphere. These events have the potential to act as passive tracers of coronal and heliospheric structure. We comment on the future prospects of using this localisation to constrain magnetic connectivity and density structure.

We close with a summary of these results and the outlook for further improvement of our understanding of the coupled corona and inner heliosphere ans PSP continues to approach the Sun and as other advances in space based instrumentation are made, such as the gradual escape of the Solar Orbiter to higher latitudes.

The individual investigations, which are briefly introduced above, are united in highlighting several specific advances in our understanding of the Sun's atmosphere facilitated by the addition of Parker Solar Probe to humanity's suite of heliospheric instrumentation. Specifically, we exemplify how multi-point, multi-spacecraft and *multi-messenger* observations at different heliographic locations are vital in making progress in constraining our physical models; using just one vantage point or one physical observable can lead to false conclusions about model optimisation. We also observe an underlying thread of the surprising utility of the very simplest model representations of the corona and heliosphere, for example a current-free corona and essentially hydrodynamic heliosphere can accurately predict the magnetic polarity structure, and even the velocity stream structure measured *in situ* by PSP. Lastly,

we verify that as one would expect from sending an instrument to never-before explored regions of interplanetary space, new gaps in our understanding are identified. For example, confirming that coronal models do not open enough magnetic flux to the inner heliosphere, or showing at several points that while we make substantial progress exploring closer to the Sun, a lack of far-side and high latitude remote sensing (most critically of the photospheric magnetic field), remains a big limitation to accurately reproducing the physical structure of the heliosphere.

Contents

List of Figures

List of Tables

Acknowledgments

It may be a cliché, but this really took a village to accomplish. My Ph.D. has been a brilliant experience due to the great network of support I've had around me.

Firstly I thank my advisor Stuart Bale who from day one has passed me exciting topics and nudged me to work on them, given me sage career advice and plugged my work at every chance he got. Thank you also to Jonathan Wurtele, Aaron Parsons, Forrest Mozer and Joelle Miles for helping me through the hoops and hurdles of the Ph.D. program.

I thank the enormous list of co-authors and collaborators who've contributed to the publications reproduced in this work, none of this would be possible without them. I especially thank the teams behind the FIELDS and SWEAP instruments on PSP, and everyone who brought the Parker Solar Probe mission together just in time for the start of my thesis work. I also want to thank the open source heliospheric and solar physics software communities, and especially David Stansby, the author of `pfsspy` and many other python libraries which are the fundamental backbone to this thesis. Lastly, I thank the NASA Earth and Space Science Fellowship which supported the middle years of my Ph.D.

My heartfelt gratitude to Eoin Carley, Peter Gallagher, Eamon Scullion, Lindsay Glesener, Milo Buitrago-Casas, Mitsuo Oka and Claire Raftery without whom I would never have learned about and got involved in the fields of solar and heliophysics. Thanks also to Brian Smith, who supported me in trying to go to graduate school when I really needed it.

Of course, my family who've plenty of time been my escape and source of free therapy (especially my mum, Suzanne!). Love to you all Suzanne, C, Tim, Aurélie, and to Nils & Lucie for whom the last six years are most or all of your whole lives! Love also to David and Claire who I give substantial credit to getting me interested in space in the first place, and to Larry (who I hope isn't tired of me sending links about my research) and Ann who I miss dearly.

Next, my wonderful labmates, friends and colleagues past and present who've made my time at SSL and Berkeley so much fun. Those ahead of me, thanks for all your advice and guidance, those following me - let me know however I can help! To Chris, Milo and Juan who I shared an office with for half a decade - miss you already.

Last but not least, so many friends and roommates from my school days through till now who have helped me and supported me in so many ways. A special shout out to Victoria, without whom my time in Berkeley would not have been the same. And of course, the King Dong club, my MapleLegends friends, Joe and Helen, Lily, Byeonghee, Neha and Best - I credit you all with getting me through the pandemic!

Chapter 1

Introduction

We begin with background material on the key ingredients for the various studies expounded on in this thesis. We discuss the physical objects of interest (the magnetic field of the corona and inner heliosphere) and the motivation for studying them, modelling approaches to understanding them, the Parker Solar Probe mission, and lastly the various other sources of in situ and remote observational data used throughout this body of work.

1.1 The Corona and Inner Heliosphere

The solar atmosphere extends outwards from the visible surface of the Sun (the photosphere) at $1R_\odot$, initially as a magnetically dominated corotating plasma comprising the corona. As altitude increases, the plasma gets heated [e.g. 88], energized and accelerated [e.g. 101] through processes which are still much-debated today [217]. At a certain height, outwards dynamic pressure becomes the dominant, the plasma becomes gravitationally unbound and begins to escape into interplanetary space as a supersonic radial outflow termed the solar wind [154]. This outflow continues for tens to hundreds of astronomical units (au) until it eventually reaches a pressure equilibrium with the interstellar medium. This boundary defines the outer limits of the Sun's sphere of influence which, as a whole, is called the heliosphere [172] and whose large scale shape is also much-debated [87].

In this thesis, we are focused on the portion of the heliosphere which extends out to $\sim$1 au, i.e. the region of the Sun's atmosphere that governs the relationship between the Sun and the Earth, which we term here the "inner heliosphere". The magnetic structure which threads and links this medium and the corona acts as ducts along which solar eruptions of energetic plasma travel, and therefore governs when and where the Sun can cause transient disturbances in interplanetary space [208]. Of most relevance to humanity is of course the near-Earth region and its local space weather, but understanding the medium as a whole is of critical importance for making and improving predictions and our overall knowledge of the influence of the Sun on its local environment.

The primary challenge in understanding this medium's magnetic field is the difficulty in

directly observing and measuring it. Indirect methods of estimating the magnetic field from remote observations provide limited constraints in the corona, usually in the plane of the sky only [e.g. 21, 90]. In the interplanetary medium there are even fewer diagnostic observables besides directly sending out spacecraft with magnetometers on board (one possibility involving solar radio bursts as a passive tracer is the subject of chapter 5 of this dissertation). Historically, most such measurements have been made at 1 *au* in the ecliptic plane, although Helios [163] explored down to 0.3 au and ULYSSES [229] explored further out than Earth at almost 90 degrees to the ecliptic, both made groundbreaking advances in our understanding. This thesis is primarily concerned with developing new constraints and measurements of the medium on larger scales and in new locations as has become available with the launch of Parker Solar Probe (section 1.4) which, as discussed later, is exploring closer to the sun than ever before and will ultimately reach down to the corona-heliosphere boundary.

The above mentioned transition from magnetically dominated to dynamic-pressure dominated plasma marks the transition between the solar corona and inner heliosphere. These two regions are overlapping and intrinsically coupled, a precise definition of where one ends and the other begins is difficult and perhaps not meaningful, but for the purposes of this thesis and for modelling and studying them, some broad distinctions can be made. We therefore now introduce both these elements individually.

The Solar Corona

The solar corona [see e.g. review 40] is the portion of the Sun's atmosphere that extends out to around $2-5R_{\odot}$ and is most recognizable as the tenuous outer reaches of visible light which can be seen whenever a solar eclipse occurs [e.g. 4].

The corona is a magnetically dominated plasma which corotates with the Sun (whose equatorial angular velocity is $\sim$14 degrees per day, [e.g. 77]). Although extremely dynamic at small scales, the large scale structure of the corona is quite distinctive, consisting of closed loops which glow bright with trapped plasma, and open field lines which are dimmer and rooted in regions of reduced extreme ultra-violet (EUV) intensity termed "coronal holes". At higher altitude, these open field lines expand to fill most of the volume around the Sun as solar wind acceleration takes over as the dominant forcing mechanism and the coronal plasma is everywhere starting to flow radially outwards.

The structure of the corona is highly variable with the solar cycle, the 11 year cycle over which the solar dynamo reverses direction [65]. In terms of the magnetic structure, at solar minimum the closed loops are concentrated around equatorial latitudes forming a bright region encircling the sun termed the 'streamer belt'. The majority of open field lines at these times are rooted in two large coronal holes of opposite magnetic polarity near the rotational poles and expand outwards to fill interplanetary space as two hemispheres of opposite polarity field separated near the solar equator by the streamer belt. At solar maximum, the picture is more complicated: While at solar minimum, the solar magnetic field is dominated by a dipolar component, as the coherence of the dynamo weakens at solar maximum, this component weakens and higher order multi-polar moments become

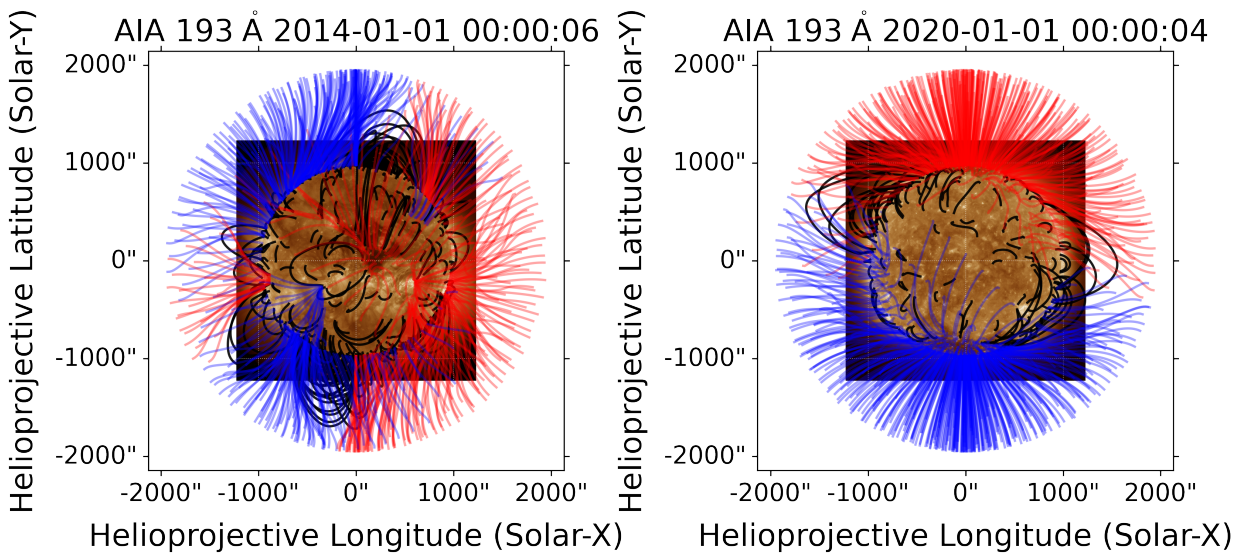

Figure 1.1: Illustration of the difference between coronal magentic configurations between solar maximum (left hand panel) and solar minimum (right hand column). Each panel shows PFSS (see section 1.2) extrapolated field lines plotted on an 193$\mathring{A}$ image of MK plasma in the lower corona. Red, blue and black field lines are respectively open and antisunward, open and sunward and closed (both footpoints rooted at the photosphere). The important features and differences between solar minimum and solar maximum are discussed in the main text.

more important. This results in open field and coronal holes being observed at all different latitudes around the Sun with smaller scale closed loops associated with active regions and sunspots observed ubiquitously in mid-latitudes.

This large scale structure variation is illustrated in figure 1.1 where two columns display coronal magnetic topology (as modeled with a PFSS model, see section 1.2) from 2014 (near solar maximum), and from 2020 (near solar minimum). These panels shows magnetic fields mapped from the photosphere out to $2.0R_{\odot}$ with red and blue indicating open field lines and black indicating closed field lines. We see immediately that at solar maximum, both polarities are distributed over all solar latitudes and open field maps down to all over the sun, while at solar minimum, the field lines are strongly organized into a dipolar pattern, with most field lines mapping down to the solar poles. This figure shows an example of coronal modelling, which is a key tool used throughout this thesis, introduced below in section 1.2.

The Inner Heliosphere

Next, we introduce the inner heliosphere, which we define here as the Sun's atmosphere from the outer edge of the corona where dynamic pressure dominates over magnetic pressure,

and out to ∼1 au. The structure of this medium is strongly coupled to and controlled by the solar corona below [217]. This influence, at least at the largest scales, is one-way for most of the volume of the inner heliosphere since the radially outflowing solar wind in the inner heliosphere is supersonic to all magnetohydrodynamic wave modes from about $10R_\odot$ outwards (a model prediction [36] which is now being tested directly by Parker Solar Probe [82]), and so cannot produce information or disturbances which can reach the corona.

Although intrinsically coupled, the magnetic field of the inner heliosphere is quite distinct in its structure compared to the corona. It is larger scale ($\mathcal{O}(1\text{au} \sim 215R_\odot)$, more simply configured and is latitudinally isotropic as shown by the ULYSSES mission [194, 195]. Broadly speaking, the background field is everywhere topologically open and frozen in to the solar wind flow. The field is divided into regions of sun-ward and anti-sunward magnetic field, with polarity set by the roots of those field lines in the corona. At solar minimum, the polarity is organized into two hemispheres separated by the heliospheric current sheet (HCS) which is a narrow boundary comprising a polarity inversion line and surrounded by a plasma sheath. The HCS generally corresponds very well to the topology of the streamer belt lower in the corona, allowing for solar rotation over time [68].

The general geometry of the field lines is the "Parker Spiral" (discussed further below in section 1.3) which is a result of the field being frozen-in to the radial outflow and rooted in the co-rotating corona [154]. The curvature of the spiral is set by the solar wind velocity such that slower solar wind gives rise to more curved field lines. As a result of varying solar wind velocity from differing locations on the sun, this results in "stream interaction regions" where a more tightly wound spiral line from a fast wind stream runs into a more curved slow wind stream and is compressed and bent. This leads to increased field strength and, further form the Sun, can produce a shock front which can accelerate charged particles [28].

Other perturbations to the Parker spiral background include coronal mass ejections which involve a closed loop of field lines (potentially including a flux rope) and constituent trapped plasma advecting outwards. These are transient events and our typical approach throughout this body of work is to study intervals where such events are not present.

A broadbrush schematic of the magnetic field of the inner heliosphere is shown in chapter 4, figure 4.2 displaying the general scale size relative to the Earth's orbit, the Parker spiral, and the (unphysical) overlap of field lines where stream interactions regions would occur. A useful review of the heliospheric magnetic field is presented by Owens & Forsyth (2013) [152].

1.2 Global Coronal modelling

As discussed above, the primary difficulty in making advances in understanding the coronal and heliospheric magnetic field is the intractability of measuring the whole medium simultaneously. A vital tool for filling in the gaps is global coronal modelling. In this discipline, the large scale structure and physics of the solar corona is represented by numerical codes which solve for plasma properties on a 3D grid. By global, we refer to 4π steradian coverage of the

model. This annular domain typically extends from the coronal base ($\sim 1\ R_\odot$) out to 2-5 $R_\odot$. As expanded on below, differing but commonly used models vary widely in the plasma physics they try to represent, ranging from just capturing the magnetic skeleton, through to capturing all MHD plasma moments, composition and even simulating radiative emission to simulate eclipse photographs. For a more exhaustive review of this topic, see Wiegelmann et al. (2017) [231].

Potential Field Source Surface models (PFSS)

Several studies in this work make substantial use of the Potential Field Source Surface [PFSS; 186, 4] model of the corona which, at over 60 years old, is one of the longest-lived and simplest methods of modelling the magnetic field of the corona. In this framework, the corona is assumed to be a magnetostatic object, i.e. static in time, current free and in vacuo. With these assumptions, the equations describing it are the source-free Maxwell equations with no electric field. :

$$\nabla \cdot \boldsymbol{B} = 0 \tag{1.1}$$
$$\nabla \times \boldsymbol{B} = 0 \tag{1.2}$$

which may be solved with a magnetostatic scalar potential $\nabla \Phi_B = -\boldsymbol{B}$ satisfying the Laplace Equation :

$$\nabla^2 \Phi_B(r, \theta, \phi) = 0 \tag{1.3}$$

In PFSS, this equation is solved in an annular domain $1R_\odot < r < r_{SS}$ where r_{SS} is a free parameter termed the 'source surface radius'. The Laplace equation is uniquely solved subject to boundary conditions specified on the inner and outer boundaries.

The inner boundary is specified by a direct measurement of the radial component of the photospheric magnetic field, which is called a magnetogram. Since only part of the Sun is visible from Earth at any one point in time, the complete 4π steradian boundary condition is derived by merging magnetogram measurements as the sun rotates, which takes approximately 27 days for a complete revolution as seen from Earth. The result of this merging is termed a 'synoptic magnetogram' when the data is merged together directly and a 'synchronic magnetogram' when the far-side parts of the Sun are modeled forward in time. Magnetograms are a fundamental component of nearly all coronal and heliospheric models and worthy of discussion in their own right as we do below in section 1.6.

The outer boundary condition is simpler but vitally important for the success of PFSS in reproducing the magnetic topology of a magnetized plasma without any plasma physics. The outer spherical boundary at r_{SS} is specified to be an equipotential ($\Phi_B(r = r_{SS}, \theta, \phi) =$ const), or equivalently that the field is orientated radially everywhere on that surface. This

requirement effectively simulates the effect of solar wind outflow in dragging field lines out into interplanetary space in the upper reaches of the corona.

Laplace's equation for the magnetic scalar potential is then solved to produce the magnetic field vector throughout the model domain. Numerous solution methods exist: The original implementations [186, 4] leverage the spherical geometry and express the solution as a superposition of spherical harmonic functions and solve for the coefficients of each term. This results in a solution which is manifestly divergence free and highly compressed as the full field solution can be reduced to the list of coefficients for each term in the expansion. The resolution and precision of the model is then set by the highest order multipole moment for which coefficients are solved for. The alternative approach is a brute force numerical solution on a grid. This approach is taken by pfsspy [235, 201], the main PFSS implementation used in this thesis, and also in POT3D [32] where the authors were seeking to maximise the PFSS resolution. For numerical solutions, the resolution is set by the grid cell size. This method is more direct and applicable to different geometries beyond spherical [e.g. 191, 97], although its output takes up much more computing memory since the field values are solved at every grid point. In practise there is very little difference between the approaches when comparing solutions where the highest order harmonic and grid cell have a similar spatial scales (see chapter 2).

PFSS + Current Sheet Models (PFSS+SCS)

An additional layer of complexity that can be added to PFSS models is adding a so-called Schatten Current Sheet layer [SCS; 187] applied to the outer boundary of the PFSS domain. In this approach, the outer layer of the PFSS model (where the field is radial everywhere) is extracted and the magnitude of the field values taken such that it is unipolar. This unipolar map is then used to drive an additional PFSS model, with boundaries set at about $2.5R_\odot$ and $5R_\odot$. Again the outer boundary is defined as an equipotential. This results in a spherical harmonic solution for this outer domain with a significant monopole component (owing to the unipolar input). The final step is to restore the polarity information that was lost by the magnitude step by tracing field lines from every pixel in the SCS inner boundary map that was initially negative, and restoring that polarity along each field line. The resulting model provides a coronal field out to $5R_\odot$ and most notably has the overall effect of flattening the heliospheric current sheet, making the field more latitudinally isotropic (as it is observed to be in the heliosphere [194, 195]), and making the streamer belt cusps more sharpened (which agrees better with eclipse and coronagraph observations [4, 171]).

The most notable contemporary implementation of the PFSS+SCS model is the Wang-Sheeley-Arge model [6, 11, 10]. This implementation is widely used not just scientifically but also operationally in US space weather predictions [158]. WSA in addition to the SCS layer adds in an empirical solar wind velocity field at the model outer boundary utilizing the Wang-Sheeley [227] result that magnetic field line expansion factor in PFSS models inversely correlates with asymptotic solar wind velocity at 1 au. Thus, without any detailed plasma physics modelling, the WSA model specifies a magnetic field and velocity field around $5R_\odot$

and this is widely used as an inner boundary condition for full MHD modelling including space weather prediction frameworks such as the ENLIL model implemented at the Solar Wind Prediction Center [158] and the very recent EUropean Heliospheric FORecasting Information Asset [162].

Magnetohydrodynamic Global Models (MHD)

At the other end of the complexity spectrum from PFSS models are global coronal modelling with magnetohydrodynamic (MHD) physics. MHD simplifies kinetic descriptions of plasmas to a smooth magnetized neutral fluid and closes its system of equation with application-specific heating sources and sinks. For the purposes of numerical modelling, MHD is described by 3 fluid moment equations (conservation of mass, momentum and energy) and the Maxwell equations with no space charge. An example set of equations from the Magnetohydrodynamics Algorithm outside a Sphere [131, 133, 177] (results from which are used later in chapter 2) is given below to illustrate these components and highlight some specific elements in the coronal context :

$$\frac{\partial \rho}{\partial t} = -\nabla \cdot (\rho \boldsymbol{v}) \tag{1.4}$$

$$\rho \frac{\partial \boldsymbol{v}}{\partial t} = -\rho \boldsymbol{v} \cdot \nabla \boldsymbol{v} + \frac{1}{c} \boldsymbol{J} \times \boldsymbol{B} - \nabla (p + p_w) + \rho \boldsymbol{g} + \boldsymbol{F_c} + \nabla \cdot (\rho \nabla \boldsymbol{v}) \tag{1.5}$$

$$\frac{\partial T}{\partial t} = -\nabla \cdot (T \boldsymbol{v}) - (\gamma - 2)(T \nabla \cdot \boldsymbol{v}) + \frac{\gamma - 1}{2 k_B} \frac{m_p}{\rho} \left[-\nabla \cdot (\tilde{\boldsymbol{q_1}} + \boldsymbol{q_2}) - \frac{\rho^2}{m_p^2} \tilde{\boldsymbol{Q}} + \boldsymbol{H} \right] \tag{1.6}$$

$$\frac{\partial \boldsymbol{A}}{\partial t} = \boldsymbol{v} \times \boldsymbol{B} - \frac{c^2}{4\pi} \nabla \times (\nabla \times \boldsymbol{A}) \tag{1.7}$$

Equation 1.4 describes continuity of conservation of mass, equation 1.5 describes momentum conservation of force balance, equation 1.6 describes energy balance and equation 1.7 succinctly describes Maxwell's equations with $\nabla \cdot \boldsymbol{B} = 0$ and no space charge accumulation. The magnetic field and current density are related by $\boldsymbol{J} = \frac{c}{4\pi} \nabla \times \boldsymbol{B}$. We have removed some terms and factors which MAS uses for numerical stability since our purpose here is just to remark on some of the physical content present in coronal MHD models, the full equations and more detailed discussion of the model may be found at the following url : `https://www.predsci.com/corona/model_desc.html` .

The most important quantities here are the fluid moments (plasma density ρ, velocity $\boldsymbol{v}$ and temperature T, the derived quantity, fluid pressure $p = 2 k_B T \rho / m_p$), and the electromagnetic components (magnetic field / vector potential $\boldsymbol{B} = \nabla \times \boldsymbol{A}$ and derived quantity current density $\boldsymbol{J} = \frac{c}{4\pi} \nabla \times \boldsymbol{B}$).

Force balance (equation 1.6) shows some notable features of the coronal system : $\boldsymbol{g}$ is the Sun's gravity. $\boldsymbol{F_c}$ is the sum of the coriolis force and centripetal acceleration arising from the Sun and corona's rigid rotation and the usual practice of solving the system of equations in this co-rotating frame. An additional pressure p_w is used in the MAS model to supply

'alfven wave pressure', an important forcing term from observations of wave modes in the corona.

Variation between MHD coronal modelling typically manifests in the energy equation (equation 1.6) in the assumptions made on the heating mechanism at the coronal base and conduction throughout the medium. In the MAS model, an energy input is cast into a heating term $\boldsymbol{H}$, and several possibilities for this exist even within the MAS model itself (e.g. [180]). Other important physics in the energy equation is the collisional (Spitzer-Harm (1953) [198]) and collisionless heat fluxes ($\tilde{\boldsymbol{q}_1}$ and $\boldsymbol{q_2}$ respectively above) and radiative losses via electromagnetic radiation ($\tilde{\boldsymbol{Q}}$ above).

Thus, MHD models constitute a much more realistic and capable set of physics for describing the solar corona compared to, for example, PFSS models. Specifically, they are able to make predictions of spatially and temporally varying plasma density, fluid flow, temperature, and non-magnetostatic magnetic fields. Correspondingly, solving this set of equations is far more computationally intensive than the potential computation. For this reason, and that at both ends of the complexity spectrum the modeled underlying magnetic skeleton of the corona are very similar [173], having this range of modelling approaches remains useful for studying the solar corona. For example, MHD models are currently too expensive to run operationally (i.e. in real time), therefore most solar wind prediction frameworks currently use potential models to fill in their coronal regions and derive a boundary condition for simpler MHD simulations of the solar wind, although this may be about to change with improving computational resources and numerical codes (e.g. the COCONUT model, [155], which is planned to be integrated with EUFORIA [162]).

Although the MAS model is the only MHD model used in this thesis (chapter 2, some examples of other implemented global coronal codes which have recently been used for applications similar to that presented in this work (namely, modelling and connecting data produced by Parker Solar Probe), include:

- The Multi-Scale Fluid-Kinetic Simulation Suite [MS-FLUKSS; 159], which includes coupled charged fluid and kinetically described neutral particles. MS-FLUKSS also includes a heliospheric extension. [84] used this model to probe in detail the first three solar encounters of Parker Solar Probe and make predictions for the fourth.

- The Alfven Wave Solar Model [AWSoM 212, 213, 214], designed to have a realistic alfven wave heating model (rather than an ad hoc energy injection) and was applied in 2019 to make blind predictions of what Parker Solar Probe would see on its first orbit.

- PLUTO [130], designed as a general astrophysical MHD code and adapted by Reville et al. (2020) [170] to include alfven wave heating and propose explanations of early Parker Solar Probe observations.

Other Coronal Models

The three flavors of global coronal models described above (PFSS, PFSS+SCS, and MHD) constitute the set which we use in detail in this thesis. However for completeness, we close our discussion of coronal modelling with a brief review of other global coronal modelling approaches which exist in the literature.

Magneofrictional modelling (e.g. [171]) extrapolates the coronal magnetic field from magnetograms subject to an imposed (i.e. assumed) velocity field $\boldsymbol{v}$ which is introduced with a frictional component into the plasma momentum equation $\nu\boldsymbol{v} = D\boldsymbol{v}/Dt$. The result is a partial differential equation for $\boldsymbol{B}$ given a function for the velocity field $\boldsymbol{v_{out}}$:

$$\left(\frac{(\nabla \times \boldsymbol{B}) \times \boldsymbol{B}}{\nu} + \boldsymbol{v_{out}}\right) \times \boldsymbol{B} = 0 \tag{1.8}$$

[171] showed that this results in a computationally simple model but (at least qualitatively) shows an improvement in magnetic field topology compared to potential field models, specifically that the streamer belt cusps become sharper and more similar to that seen in eclipse or coronagraph observations.

Linear and Non-linear Force Free Modelling relaxes the potential field "no-current" condition to a state where currents are freely able to conduct parallel to magnetic field lines, which is know as the "force free" condition ($\nabla \times \boldsymbol{B} = \alpha\boldsymbol{B}$). The "linear" case refers to the proportionality constant α being constant, and "non-linear" when it can spatially vary (first solved in [183]. NLFF extrapolations are a very actively researched modelling subdiscipline, but most commonly applied to limited areas of the solar disk e.g. active regions and sunspots. A general review of these models and applications is given by [232]. However, they have also been applied to model the corona globally (see e.g. [235]).

The motivation for these endeavours is to achive numerically simple ways to model the solar corona while allowing free energy to persist in the field. This is vital for allowing models to address eruptions such as flares or coronal mass ejections. where free energy must exist in order to be released. PFSS models represent the lowest energy state consistent with the photospheric magnetic field and cannot model eruptions. NLFF, magnetofriction or other examples e.g. fluxon modelling [42] all have this capability, producing reduced representations of the corona (just magnetic fields and currents) but with free energy.

1.3 Modelling the Inner Heliosphere

We next discuss global modelling approaches for the magnetic field of the inner heliosphere (the interplanetary magnetic field (IMF) or heliospheric magnetic field (HMF), terms which are used interchangeably in the literature).

The Parker Model of the Inner Heliosphere

Motivated by observations of comet tails being directed anti-radially with respect to the Sun [20], Parker (1958) [154] first theorized the existence of an accelerating, supersonic, radially-outflowing solar wind filling interplanetary space using an analytic spherically symmetric hydrodynamic model of a fluid heated at the inner boundary to millions of Kelvin, as had been previously observed remotely with spectroscopy of the corona. This prediction was subsequently confirmed with some of the first plasma measurements of interplanetary space with the Mariner 5 spacecraft [e.g. 142]

This relatively simple hydrodynamic construction applied to a magnetized plasma for which magnetic pressure is sub-dominant readily leads to a model of the interplanetary magnetic field (IMF). With the solar wind radially outflowing from a rotating inner source, the velocity streamlines form archimedean spirals with a curvature set by the solar wind radial velocity and the rotation rate of the Sun. The magnetic field lines which are frozen-in to this flow therefore trace these streamlines and this leads to the "Parker spiral" - a prediction that the magnetic field in interplanetary space, which is expected to be near radial at the outer reaches of corona, should become more inclined to the radial direction with increasing distance from the Sun in the direction perpendicular to the solar rotational axis. Specifically, this leads to the prediction that near 1 au the field should be inclined at nearly 45 degrees, with the specific inclination a function of solar wind velocity. This was again confirmed in the early days of the space age [141]. The equations describing the Parker spiral are simple to write down in spherical coordinates of radius R, heliographic latitude θ and heliographic longitude ϕ with a polar direction aligned with the solar rotation axis :

$$B_R(R,\theta,\phi) = B(R_0,\theta,\phi_0)\left(\frac{R_0}{R}\right)^2 \tag{1.9}$$

$$B_\theta(R,\theta,\phi) = 0 \tag{1.10}$$

$$B_\phi(R,\theta,\phi) = -B(R_0,\theta,\phi_0)\frac{\Omega_\odot R_0}{V_{SW}}\frac{R_0}{R}\sin\theta \tag{1.11}$$

with $\Omega_\odot$ representing the solar rotation rate with respect to the stars, and V_{SW} representing the solar wind velocity. From these equations we see simple predictions of the large scale field include : the radial component of the field decreases with distance form the Sun as $1/R^2$, the tangential component decreases as $1/R$ and is inversely proportional to V_{SW}, and that the field is, on average, aligned on a cone of constant latitude. This field geometry is shown in figure 4.2 in chapter 4 and a 3D version with spirals out of the equatorial plane can be seen in Figure 3 of Owens & Forsyth (2013) [152].

As well as providing predictions for in situ single point measurements throughout the inner heliosphere, this model also allows an estimation of magnetic connectivity between source regions at the edge of the corona and points in interplanetary space. This is done most simply with what is referred to as the "ballistic approximation" [146, 121]. As noted above, the Parker model predicts a solar wind velocity which increases with distance from the

Sun. This leads to a more exact expected trajectory of solar wind streamlines and fieldlines which is not an exact archimedean spiral (fixed curvature) but instead is instantaneously tangential to an archimedean spiral of the curvature for the accelerating solar wind velocity. This ultimately leads to a less tightly wound spiral closer to the Sun relative to if the solar wind was at a constant speed. However , [146] noted that closer to the Sun, an opposing effect emerges as the tidally locked corona relaxes to the unbound solar wind. The tendency of the solar wind to corotate therefore tends to try to straighten streamlines, and this effect opposes the effect of solar wind acceleration. [146] estimated the magnitude of both these effects and concluded that the balance point is well approximated by a constant solar wind archimedean spiral, this is the ballistic approximation. This does not represent a truly accurate interplanetary field line, but does approximate the connectivity between interplanetary space and the solar corona very well. It allows an estimate of the longitudinal offset ($\Delta\phi(r)$) between a point in the solar wind and it's magnetic footpoint close to the Sun with the very simple equation :

$$\Delta\phi(r) = \phi_0 - \frac{\Omega_\odot}{V_{SW}}(r - r_0) \tag{1.12}$$

This will be used extensively in chapters 24.

More sophisticated models of the HMF

Of course, the Parker model is just an approximation and in reality a number of non-ideal and especially non-spherically symmetric qualitative features are known to be manifested in the solar wind. Even neglecting transient disturbances such as coronal mass ejections, long lived non-ideal structures include stream interaction regions, ubiquitous alfvén waves, turbulent fluctuations and many more.

Correspondingly, more sophisticated modelling is required to reproduce some of this structure. Firstly, since the magnetic structure of the inner heliosphere is largely set by the velocity flow, hydrodynamic simulations can be used to generate velocity streamlines to estimate magnetic field lines. Hydrodynamics allows for stream interactions to be modeled since fast moving fluid parcels get slowed down by slower moving parcels ahead of them, and in a more computationally efficient way than full magnetohydrodynamics [e.g. 176, 75, where the authors neglect magnetic fields, gravity and pressure gradients]. Such hydrodynamic solar wind simulations can even be used to inject transient disturbances, and for example estimate the transit time of CMEs [151], all without any magnetic physics.

The WSA coronal model introduced above also includes a semi-empirical velocity stream structure method for propagating solar wind parcels through the inner heliosphere. In their implementation [6], plasma parcels are allowed to propagate radially outwards ballistically in steps of 0.125AU. At each step, adjacent plasma parcels are effectively averaged together with a weighting function that means faster wind parcels running into slower ones ahead of them are impeded and slowed down.

Another semi-empirical method to allow for more complex IMF structure than the Parker model (albeit restricted to the solar equatorial plane) was implemented by Li et al. (2016) [108] where they use *in situ* measurements of the radial and azimuthal components of the magnetic field at 1 au and the solar wind velocity, and backmapped them to the Sun using an earlier model [190] that allows for non-zero azimuthal field at the inner boundary (while the Parker model assumes the field starts from radial). A subsequent extension [207] extended this method to include acceleration of the solar wind (which had previously been kept constant). This modelling introduces additional complexity in the field including closed loops, kinked loops and stream structure due to velocity variation.

Lastly, there is the option of maximizing the physical accuracy and applicability of the model using MHD physics, as is done with most space weather frameworks, for example ENLIL [158], EUFORIA [162] or SWMF [211]. For these models, the inner boundary conditions are set by driving a full coronal model at the interior to get a magnetic and velocity field, most commonly the WSA model, but in the case of EUFORIA, soon to be replaced by a MHD model (COCONUT [155]. This full-fledged modelling allows time dependence, stream interactions, and arbitrary input boundary conditions, but at the price of being computationally expensive.

This concludes our discussion of computational modelling of the corona and inner heliosphere. We now move on to observations and measurements of the corona and inner heliosphere which directly provide physical information and model constraints. We begin with a detailed introduction to Parker Solar Probe, a central data source for this thesis which drives much of the novel investigations detailed in later chapters.

1.4 Parker Solar Probe

Parker Solar Probe [PSP; 52] is a flagship NASA heliophysics mission launched in 2018 to 'touch the Sun', exploring the Sun's atmosphere closer than ever before. Its first perihelion pass in November 2018 broke the previous record of closest approach to the Sun (Helios at 0.29 au in 1976), by almost a factor of 2, reaching $35.7R_\odot$ (0.166 au). At the time of writing this thesis, PSP has completed 12 perihelion passes and is now orbiting with a distance of closest approach of $13.3R_\odot$ (0.062 au); by the end of the prime mission it will reach a closest approach of $9.8R_\odot$ (0.046 au). PSP is therefore exploring a new region of interplanetary space and providing measurements, model constraints and physical insight that was previously unattainable. Much of this thesis is concerned with these new measurements and applying them to understanding the large scale magnetic structure of the solar atmosphere and we therefore present in some detail the specifics of the PSP spacecraft, instrument suite and unique orbit.

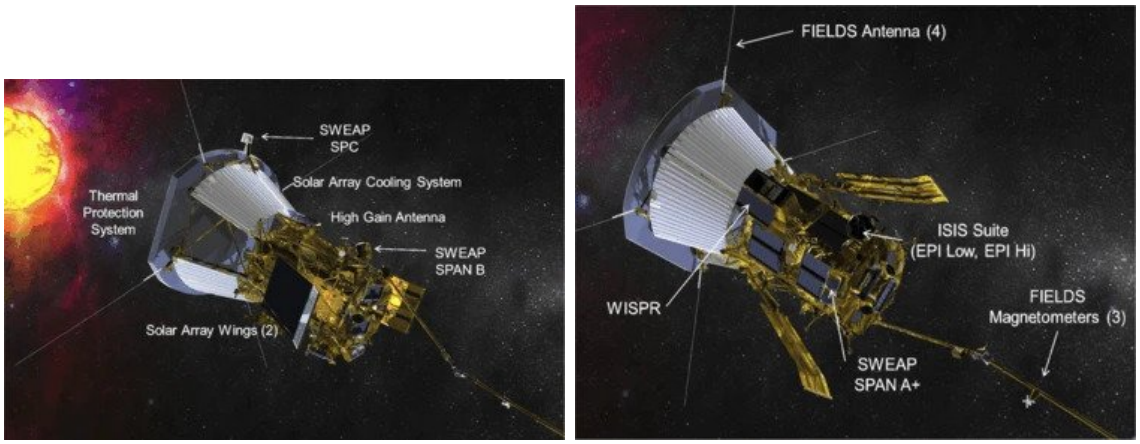

Figure 1.2: Illustration of the Parker Solar Probe spacecraft and instrument suite reproduceed from [52] under the Creative Commons Attribution 4.0 International License (http://creativecommons.org/licenses/by/4.0/). The two panels (figure 15 and figure 16 in the original paper) illustrate the spacecraft from the ram and anti-ram sides (with respect to the spacecraft motion at perihelion). In the left hand panel (anti-ram), we see spacecraft key systems including the heat shield, the solar arrays and the high gain antenna, and the SWEAP components SPC and SPAN B (electron analyzer). In the right hand panel (ram side), more instruments are labeled including the FIELDS antennae and magnetomers, the WISPR cameras, the IS⊙IS enegetic particle instrument and the remaining component of SWEAP that measures thermal ion distributions and electrons on the spacecraft ram side. These elements are described further in the main text.

Spacecraft and Instrument Suite

The PSP spacecraft and instrument suite are illustrates in figure 1.2. The spacecraft bus is dominated by a heat shield and radiator assembly at the front end which is orientated towards the Sun at all times (autonomously) at closest approach, to absorb the radiative load and prevent it damaging the functional systems. The instrument suite and spacecraft control systems are all located in the smaller cuboid sheltered behind the spacecraft. Also visible are the solar panels which are already small compared to the spacecraft size, but additionally fold back so that only the tips are illuminated at perihelion.

Spread across the two panels of the above figure, the full instrument suite is labeled. The WISPR [218] instrument is orientated on the spacecraft ram side, which is the direction in which the spacecraft is moving longitudinally at closest appraoch. WISPR comprises of a white light imaging system with 2 fields of view. It observes scattered light ahead of the spacecraft and sometimes observes ejecta which PSP later passes through.

The Integrated Science Investigations of the Sun or IS⊙IS instrument [127] consists of two individual detectors called EPI-Hi and EPI-Lo. These detectors measure energetic particles,

most commonly solar energetic particles (SEPs) but also of interplanetary and galactic origin, or particles accelerated at shocks or in CMEs. Through having a large number of small apertures on each instrument, IS⊙IS measures directional flux, as well as dynamic energy spectra and mass/charge ratios.

The FIELDS instrument [19] comprises of 4 electric field whip antennas located in the plane of the heat shield, and a set of magnetometers (two fluxgate and one search coil) insulated from system noise by being located out on a boom trailing the spacecraft. The antennae are used to sample single and doubled ended voltages and measure electric fields from DC to AC up to 16 MHz with the radio frequency spectrometer (RFS, [164] and digital frequency board [125]. The magnetometers also cover a range of frequencies from DC to AC and are available as a merged data product [25].

The last instrument, the Solar Wind Electrons, Alphas and Protons instrument (SWEAP [83]), measures the thermal plasma of the solar wind and is distributed across 3 sub instruments : The Solar Probe Cup (SPC [33]), the solar probe analyzer for ions (SPAN-Ai) and the solar probe analyzer for electrons (SPAN-Ae and SPAN-B, [230]. SPC is mounted on the heat shield and looks directly towards the Sun during encounter. It is a Faraday cup instrument and measures particle distributions of protons and alphas, deriving fits and moments of density, flow velocity and temperature. It is most useful at times when the solar wind is coming near radially towards the spacecraft as was the case in the earlier orbits and with the more recent orbits during the inbound and outbound phases. SPAN-i similarly measures protons and alpha distributions and is a top hat analyzer. SPAN-i is mounted on the ram side of the spacecraft, and so takes its best measurements when the spacecraft has significant longitudinal speed with respect to the solar wind. This is generally the case near perihelion on the more recent orbits. Lastly, SPAN-e measures electron distributions and derives fits and moments, although its most widely used data products are the distributions themselves since the pitch angle distribution of electrons are powerful diagnostics of magnetic topology. The raw distribution includes information about the electron strahl or heat flux, which is useful for diagnosing plasma of differing coronal sources.

Orbit

In addition to the physical elements of the spacecraft, the unique orbit of PSP is a key element of the mission, especially for all the investigations detailed in this work.

In figures 1.3 and 1.4 the mission profile is grouped into orbit families of identical orbital parameters (perihelion and aphelion). In the first figure we examine the orbit in inertial coordinates which clearly shows how PSP is in a highly elliptical orbit whose perihelion (and aphelion) is getting progressively closer to the Sun over time.

In the second figure, the same orbits are shown in the Carrington reference frame which corotates with the Sun. This frame is much more useful for seeing the way in which PSP samples the corotating heliospheric and corona structure. Of particular note, a feature of the orbit seen in this frame of reference is the corotation loop around each perihelion: As PSP get's closer to perihelion, its angular velocity with respect to the surface of the Sun

increases. At some particular distance (depending on the orbit family), PSP crosses from rotating slower than the Sun to rotating faster. This means there are intervals in each orbit where PSP hovers over the same location above the Sun moving radially inwards, and then later outwards. Between these two intervals, the spacecraft moves over the Sun in the reverse direction to what it has previously been doing. Further, with the more recent orbital families, the spatial scale of this loop and super-rotational interval is growing enormously. In the most recent orbit family (13.3 $R_{\odot}$, middle-middle panel), the loop now covers 110 degrees longitude between corotation intervals, almost a third of the way around the Sun, and this distance is covered in just 3 days.

Thus, in addition to simply getting closer to the Sun than ever before, PSP is unique in how it samples spatial structure - it samples plasma over a huge range of longitudes in a very short time, providing snapshots of structure - a key feature for a largely in situ-based mission.

1.5 Other In Situ Data Sources

Apart from PSP, several spacecraft *in situ* instrument suites are used extensively in this work.

STEREO

In several chapters (2,3,5), we use data from the Solar Terrestrial Relations Observatory [STEREO; 80] which was originally a 2-spacecraft mission launched in 2006. The two spacecraft, Ahead (A) and Behind (B) were launched respectively into orbits slightly closer and slightly further from the Sun compared to Earth. This had the effect of A moving ahead of the Earth in its orbit, and B lagging behind. Over the course of the prime mission, the two spacecraft gradually separated more and more, before passing each other at superior conjunction. Since then, they have been approaching closer to Earth over time. In 2014, contact was lost with STEREO B, but STEREO A remains functioning to this day.

In the time period since PSP launched (November 2018), STEREO A has been the main source of observations of the Sun off the Earth-Sun line and has been located in a position to observe the parts of the Sun about to rotate in view on Earth (although it does not have a magnetograph so cannot contribute to improving magnetogram realtime coverage). The *in situ* instruments on board are IMPACT, PLASTIC and S/WAVES. Since all of these instruments are used in some capacity over the course of this thesis, we introduce each one briefly. The In Situ Measurements of Particles and CME Transients (IMPACT) suite [119] makes in situ measurements of solar energetic particles, suprathermal electrons and the interplanetary magnetic fields. The Plasma and Suprathermal Ion Composition (PLASTIC) instruments [54] are time of flight mass spectrometers which measure the in situ thermal plasma distributions, estimating plasma moment quantities such as density, velocity and temperature, and also measuring composition as a function of mass-to-charge ratio. Lastly,

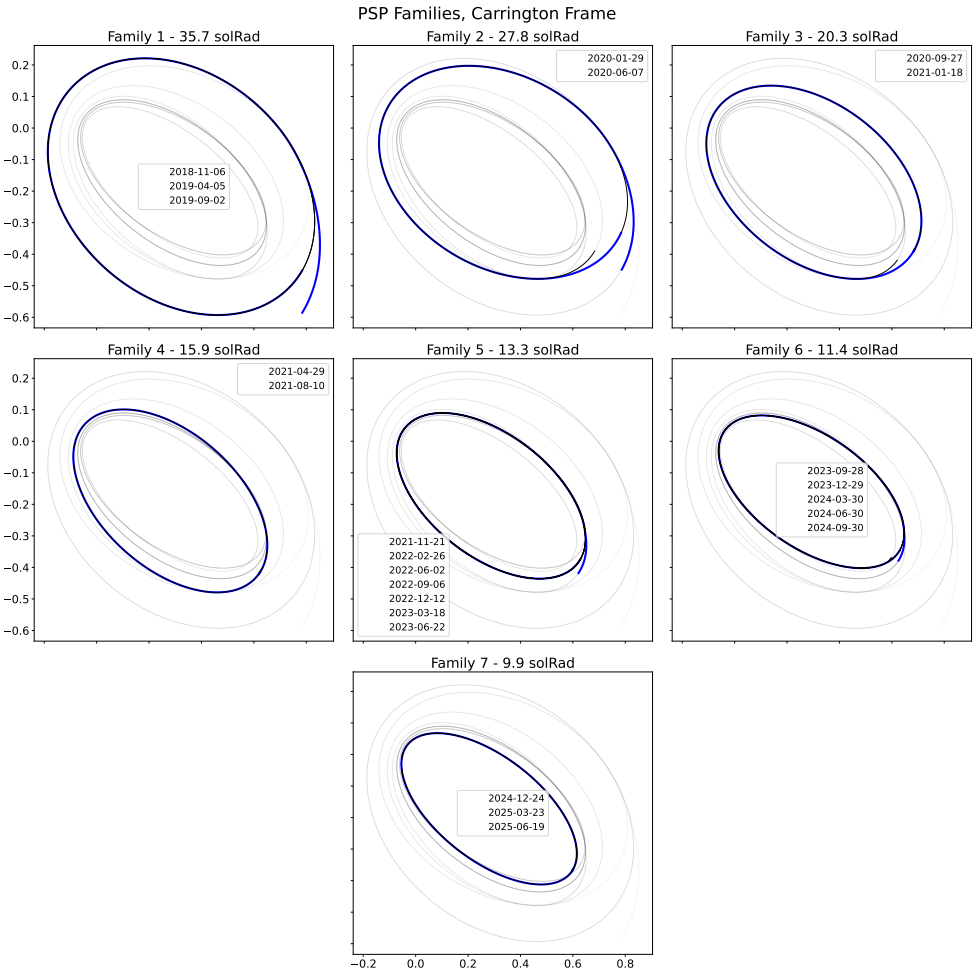

Figure 1.3: The Parker Solar Probe orbit organized by orbit "family" of differing perihelion distances, shown in the inertial frame view. In each panel the date labels of the respective perihelion days are shown. At the time of writing, the mission is in family 5 (middle-middle panel)

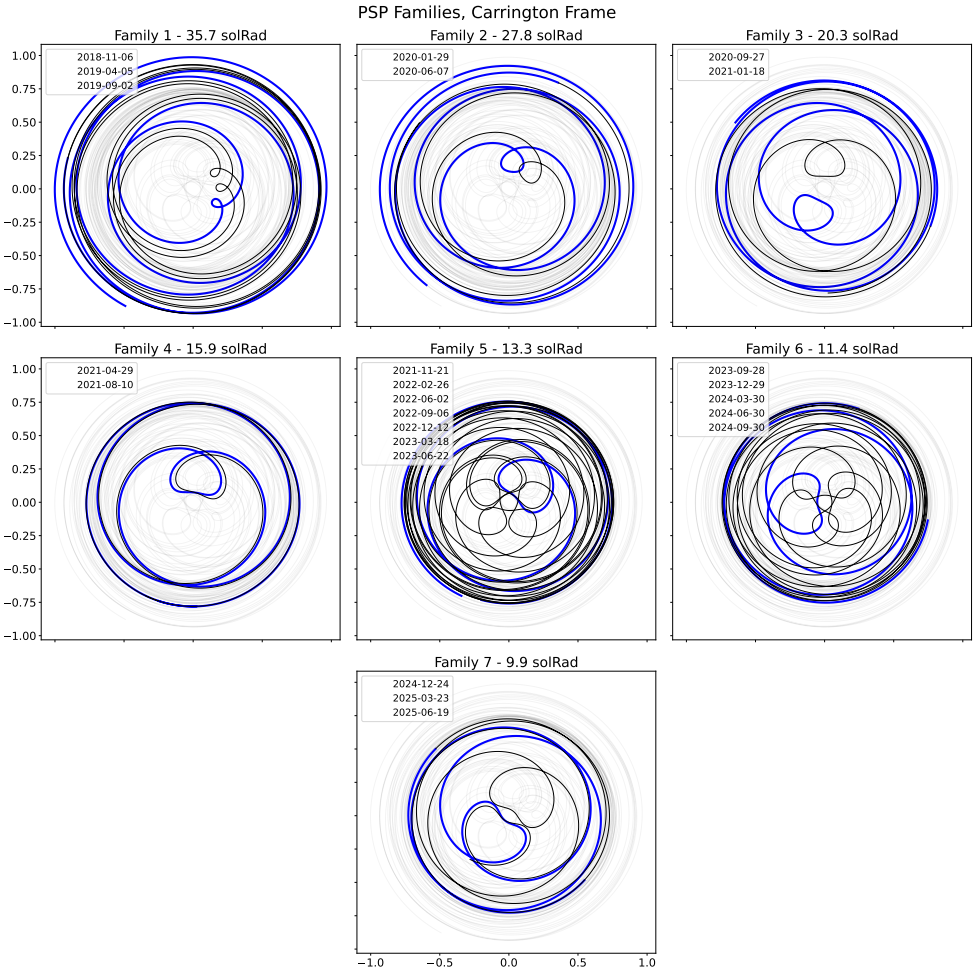

Figure 1.4: Orbit families as arranged in figure 1.3. Here the orbits are shown in the heliographic carrington frame which corotates with the Sun. Alternating periods of super and sub-corotation of PSP with respect to the Sun can be identified by the loops in the trajectory.

the Radio and Plasma Wave Investigation (S/WAVES) [24] measures electric fields from near-DC up to 16MHz, observing typical radio emission in the corona and inner heliosphere.

STEREO also has remote-observing capabilities with The Sun-Earth Connection Coronal and Heliospheric Investigation (SECCHI) suite [74] which contains imaging systems for extremely ultraviolet observations, white light coronagraphs and off limb direct white light imagers (similar to PSP/WISPR), although these data are not used directly in this thesis. These types of remote observations are introduced below in section 1.6.

L1 Monitors: Wind and ACE

Lastly, we introduce two spacecraft located at the Earth-Sun L1 point (at least for the time interval studied in this thesis): Wind [1], launched in 1995, and the Advanced Composition Explorer (ACE) [203], launched in 1997 (both are still functioning). These spacecraft produce in situ measurements of the solar wind on the Earth-Sun line which are a very useful point of comparison to measurements made closer to the Sun. These data are often packaged together to provide a long term coverage dataset through the OMNI data product [85] of plasma moments and in situ magnetic field. Wind also carries a radio spectrometer, WAVES [23], the predecessor to S/WAVES and PSP/RFS.

1.6 Remote observations of the Corona and Inner heliosphere.

Lastly on measurements, we discuss the various *remote observations* used in this thesis, that is data, obtained by imaging the sun and its atmosphere from a distance (usually 1 au).

Magnetograms

A fundamental observed quantity for coronal and heliospheric studies are magnetograms. These are measurements of the photospheric magnetic field on the solar disk via imaging spectroscopy of the Zeeman (or sometimes Hanle) splitting of spectral lines in the photosphere's continuum emission.

This yields the line of sight magnetic field strength or more recently, the full vector [188], across the solar disk at an instant in time. As time passes, the part of the solar disk in view rotates and so subsequent full disk magnetograms can be combined over time to produce what is called a "synoptic magnetogram", which is a map of the Sun's magnetic field covering 4π steradians. These maps are the fundamental boundary condition for all coronal models and subsequently heliospheric models. Examples of synoptic maps are those provided by Global Oscillations Network Group [63] or the data provided by the Solar Dynamics Observatory (SDO) [156], Helioseismic and Magnetic Imager (HMI) [188]

A slight variation on the "synoptic magnetogram" is the "synchronic magnetogram". Again, these are 4π steradian maps of the photospheric magnetic field combining a solar

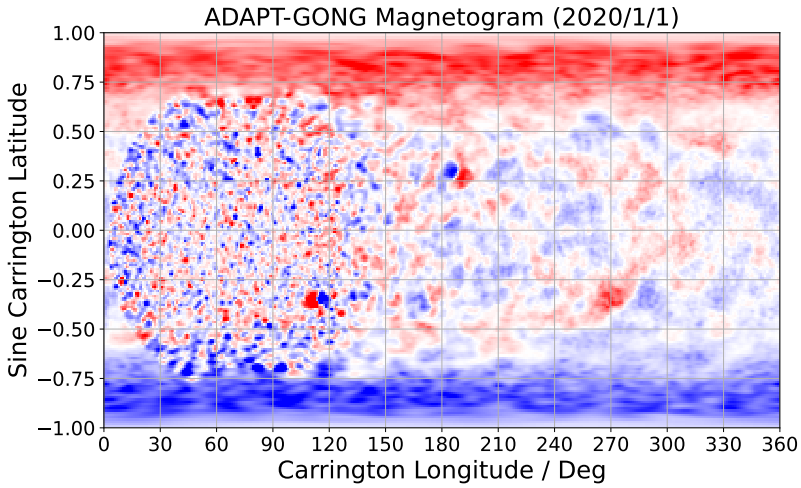

Figure 1.5: An example of a synchronic magnetogram from the ADAPT model [9] for 2020/1/1 (solar minimum, see also right hand panel, figure 1.1) assimilating data from the GONG telescope network. Colorscale is saturated at +/- 1 mT, and blue and red indicates respectively field of negative and positive polarity. The solar minimum configuration of strongly concentrated flux in the polar regions is apparent. The sharper-appearing resolution region centered around 60 degrees longitude marks where recent data is directly assimilated into the model, while the smoother data outside this region shows where flux transport modelling has been applied.

rotations worth of observations, but while synoptic maps directly blend old and new data, in synchronic maps the older observational data is run through a flux transport model to allow it to evolve forward in time after the point it was observed at. Such modelling accounts for differential rotation of the solar poles and equators, and allows for diffusion of strong polarities. An example of a synchronic magnetogram is the Air Force Data Assimilative Photospheric Transport model or ADAPT [9, 7, 8], of which extensive use is made in this thesis.

An example ADAPT magnetogram (average of the 12 ensemble members) from solar minimum is shown in figure 1.5 in which we can see strong unipolar concentrations of magnetic flux in the polar regions and small scale polarity variation across lower latitudes, and additionally can see the most recently assimilated observations as a higher resolution patch in the midst of the more diffused flux-transport forward-modeled older data.

There are several issues with current magnetograms primarily stemming from the fact that historically, all magnetograph observations have been made on the Earth-Sun line. This means that the Sun's polar regions are very poorly observed with large line of sight projection errors. This could be a significant source of error in coronal models which have

to make assumptions or perform additional modelling to fill in these areas in the boundary condition. Specifically, larger than expected flux concentrations in the polar regions are a possible resolution for the apparent lack of magnetic flux escaping the corona in typical models when compared to that measured in the heliosphere ([110] and chapter 3). The other major issue from the lack of multiple magnetograph view points is the aforementioned limitation of necessarily having older magnetogram data included to get full coverage of the boundary condition. Even with flux transport modelling, the older parts of the Sun are always somewhat innacurate, but most significantly when active regions actively emerge on the solar far side. This is not a process that can be reliably predicted in advance and so coronal models can be disturbed significantly when such features rotate into view.

With this inherent uncertainty, significant differences between identical models driven by slightly different magnetogram boundary conditions taken at the same time can be seen (Chapters 2 and 4). A clear avenue for coronal model improvement is therefore identified: observe the Sun with magnetograms from multiple viewpoints. The launch of Solar Orbiter [138] in 2020 has for the first time taken a magnetograph off the Earth-Sun line (the Polarimetric Heliospheric Imager, PHI [197] and new observations with this instrument are eagerly anticipated.

EUV Imaging : SDO/AIA

Key observations and constraints on the solar corona are made through imaging observations in Extreme Ultraviolet (EUV) wavelengths. These wavelengths correspond to spectral line emission from transitions excited by coronal temperatures. In this work, such observations are primarily used from the SDO Atmospheric Imaging Assembly (AIA) [102] which observes coronal altitudes in 171 $\mathring{A}$ (Fe IX, 0.6 MK), 193 $\mathring{A}$ (Fe XII, 1.25 MK, Fe XXIV, 19 MK), 211 $\mathring{A}$ (2 MK), 335 $\mathring{A}$ (2.5 MK). These observations show the locations of concentrations of hot plasma in the corona, but also very importantly, locations where it is absent or lower density. Specifically, dark regions in for example 193 or 211$\mathring{A}$ are very prominent and show the magnetic footpoitns of open field lines along which the solar wind is outflowing. 193 $\mathring{A}$ observations were used for the background image in figure 1.1 above.

White-light Coronagraphs : SOHO/LASCO

Another remote observation used in this work are white light coronagraphs, most notably the Solar and Heliospheric Observatory (SOHO, [43]) Large Angle and Spectrometric Coronagraph Experiement (LASCO) [27]. These instruments take visible=wavelength light images of the tenuous outer corona in the plane of the sky by blocking out the solar disk with an occulter built into the instrument. These instruments need very low light scattering to function and so have to be taken from space above the Earth's atmosphere. These observations show where plasma is concentrated in closed loops at a few solar radii from the surface of the Sun. As well as clearly seeing the morphology of erupting plasma as CMEs, coronagraph

observations show the location of the streamer belt, another key constraint on global corona magnetic topology.

Radio Imaging : LOFAR

In chapter 5 we use observations from the Low frequency array (LOFAR) [216], a ground based array of radio telescopes distributed across Europe, in tandem with the space-based radio spectrometeres Wind/WAVES and STEREO/WAVES mentioned above. LOFAR can measure radio wavelengths from 10-90 MHz and additionally is able to perform tied-array interferometric imaging with its network of 48 distributed stations. This allows it to observe solar radio phenomena which emit at their local plasma frequency in the lower corona, including Type III radio bursts.

As the main subject of chapter 5, we now introduce these phenomena briefly :

Type III Radio Bursts

Type III radio bursts occur when a near-relativistic beam of energetic electrons are injected onto open field lines by processes such as a solar flare or small scale coronal reconnection. This beam travels outwards along these field lines at a sizeable fraction of the speed of light and as they travel they undergo landau damping, producing Langmuir waves in the surrounding plasma. These Langmuir waves further decay via an as yet uncertain process into electromagnetic radiation at the local plasma frequency or a harmonic. This frequency is set by the local plasma density and as the burst propagates outwards its local density decreases, and so the emission is observed as a downward sweep in frequency with time. An example observation of an *interplanetary* type III is shown below in figure 1.6, where the burst escapes the corona and travels out into the inner heliosphere, as observed by its propagation below frequencies of 1 MHz. Further background on type III bursts are given in the introduction of chapter 5. See also [168] for a recent review.

1.7 Thesis Outline

In the following chapters, we present several investigations into the large scale magnetic structure of the solar corona and inner heliosphere using the methods, modelling and observatories which we have prefaced in this section. In chapter 2 we present a new set of metrics to evaluate and constrain global coronal models, allowing cross-comparison between the different types of models discussed earlier in this section. In chapter 3 we compare the magnetic open flux threading the heliosphere as measured by PSP with that predicted by coronal models, investigating if the discrepancy observed by [110] persists 10 times closer to the Sun. In chapter 4 we discuss results from the first solar encounter of PSP where we use field line tracing through heliospheric and coronal modelling, both to estimate solar wind sources to contextualize the in situ measurements, as well as deriving a best fit model and

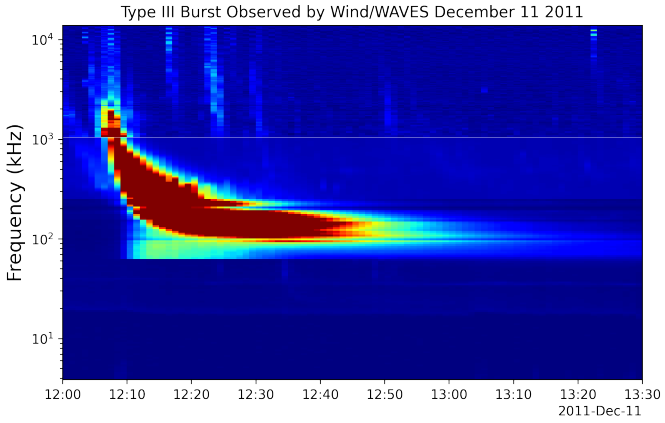

Figure 1.6: An example radio spectrogram observation of an interplanetary type III radio burst by the Wind/WAVES instrument [23] in December 2011 form 14 MHz down ∼200kHz. The color intensity indicates radio flux (as measured in V^2/Hz). The characteristic sweep timescale of several minutes identifies this event as a Type III burst [233]

discussing the meaning of this best fit. In chapter 5 we examine large scale heliospheric and coronal magnetic structure through a slightly different lense by tracking the propagation of a Type III radio burst from its injection low in the corona, through the inner heliosphere and out to 1 au. Although we don't manage to conclude we have directly measured magnetic field lines due to some unquantified uncertainties, we prove the concept of several complementary localization techniques and set the stage for improving these methods with further investigations and extensions using Solar Orbiter. Finally in chapter 6 we summarize the new findings and big picture linking our investigations together.

Chapter 2

Constraining Global Coronal Models with Multiple Independent Observables

In this chapter, we present the peer-reviewed article Badman et al. 2022a [13] published in the Astrophysical Journal in June 2022. With this work we begin our analysis of global coronal models. We design and implement a series of quantitative metrics which can be applied in a model-agnostic way, i.e. facilitating cross-model comparison. As introduced in section 1.2, there are a wide variety of coronal models of differing physics and computational complexity. Further, within an individual model there are a plethora of tunable parameters and choice of input boundary conditions, most critically the magnetogram measurement of the magnetic field at 1 $R_\odot$. For this project, we recognized that (1) there is not a universally agreed on way to quantify coronal model quality, and (2) there is now, more than ever, a wide variety of data that can directly provide independent constraints. We therefore sought to define a framework with three independent and well-defined metric scores that assessed different aspects of coronal models, focusing on the magnetic structure since that is predicted by all models. As part of presenting this, we applied the metrics to a subset of models and input parameters. A full discussion of our findings are in this chapter, but one worth highlighting is that for potential field models (which we make use of in all chapters here) a global optimum is not achieveable : a compromise "best model" can be achieved but the best representation of coronal holes and streamer belts (observable coronal features at opposite boundaries of the model) could not be simultaneously achieved. This tension was also found to be resolvable with the additon of more accurate physics from other models, and this served as a validation of our metric framework showing the more physical models produced more physically justified results.

The full citation for this work as published is Samuel T. Badman et al. "Constraining Global Coronal Models with Multiple Independent Observables". In: *The Astrophysical Journal* 932.2, 135 (June 2022), p. 135. DOI: 10.3847/1538-4357/ac6610. arXiv: 2201.11818 [astro-ph.SR]. The full author list is: Samuel T. Badman, David H. Brooks, Nicolas

Poirier, Harry P. Warren, Gordon Petrie, Alexis P. Rouillard, C. Nick Arge, Stuart D. Bale, Diego de Pablos Agüero, Louise K. Harra, Shaela I. Jones, Athanasios Kouloumvakos, Pete Riley, Olga Panasenco, Marco Velli and Samantha Wallace.

2.1 Abstract

Global coronal models seek to produce an accurate physical representation of the Sun's atmosphere which can be used, for example, to drive space weather models. Assessing their accuracy is a complex task and there are multiple observational pathways to provide constraints and tune model parameters. Here, we combine several such independent constraints, defining a model-agnostic framework for standardized comparison. We require models to predict the distribution of coronal holes at the photosphere, and neutral line topology at the model outer boundary. We compare these predictions to extreme ultraviolet (EUV) observations of coronal hole locations, white-light Carrington maps of the streamer belt and the magnetic sector structure measured *in situ* by Parker Solar Probe and 1AU spacecraft. We study these metrics for Potential Field Source Surface (PFSS) models as a function of source surface height and magnetogram choice, as well as comparing to the more physical Wang-Sheeley-Arge (WSA) and the Magnetohydrodynamics Algorithm outside a Sphere (MAS) models. We find that simultaneous optimization of PFSS models to all three metrics is not currently possible, implying a trade-off between the quality of representation of coronal holes and streamer belt topology. WSA and MAS results show the additional physics they include addresses this by flattening the streamer belt while maintaining coronal hole sizes, with MAS also improving coronal hole representation relative to WSA. We conclude that this framework is highly useful for inter- and intra-model comparisons. Integral to the framework is the standardization of observables required of each model, evaluating different model aspects.

2.2 Introduction

The solar corona is the tenuous outer layer of the Sun's atmosphere extending out to a few solar radii which comprises hot magnetized plasma. This system is of critical importance for understanding how the Sun interacts with its local environment by creating the solar wind, and how it can affect the Earth. While much can be learned about the corona indirectly from remote observations including plasma density and temperature structure [e.g. 228] or magnetic topology [e.g. 21], such investigations are usually limited to the plane of the sky as viewed from Earth or one of the STEREO spacecraft. With direct *in situ* measurements within 1-5$R_\odot$ currently technologically out of reach, a comprehensive synchronic representation of the full 3D structure can only currently be achieved using physics-based modeling.

Accurately reproducing this structure with models is of vital importance for innumerable endeavours in solar and heliophysics. For example, coronal models form the central component of space weather simulation and prediction frameworks [see e.g. review by 49], they enable contextualization and prediction of *in situ* spacecraft data [e.g. 178, 14] and ultimately hold the key to fundamental plasma physics problems that are still unsolved, including coronal heating.

The most commonly used, and one of the earliest implemented coronal models was the Potential Field Source Surface (PFSS) model [4, 186] wherein the corona is assumed to be magnetostatic (i.e. current-free) in an annular domain with an inner boundary of radial magnetic field derived from direct magnetograph observations of the photosphere, and the outer boundary assumed to be an equipotential of radius R_{SS}, called the source surface. (Typically this is set to a value around $2.5R_{\odot}$ [68]). The equipotential surface simulates the outflowing solar wind by forcing field lines intersecting it to be radial and produces "open" field lines along which plasma can escape, without needing detailed plasma modeling.

PFSS models have some obvious drawbacks. While they produce open field typically rooted in observed coronal holes, the highest altitude closed loops are rounded while eclipse observations show that in fact the last closed loops are kinked, and spike outwards in a streamer configuration [4]. Further, the height where field lines are observed to become uniformly radial differs not just from the standard [68] $2.5R_{\odot}$ value, but also varies from location to location on the Sun [173, 21] and in time with the evolution of the solar cycle [169]. PFSS models also only directly predict coronal magnetic structure, and have an indirect connection to solar wind flow speed [223] but otherwise pose no constraints on other plasma properties such as density, temperature or composition. They are also manifestly time-independent. As such, numerous more realistic models have been developed, usually trading improved physical content at the price of computational tractability.

PFSS extrapolations can be extended and improved beyond $2.5\mathrm{R}_{\odot}$ with a Schatten Current Sheet [187], as implemented in the Wang-Sheeley-Arge (WSA) model [6, 11, 10], which produces more kink-shaped streamer topology and a semi-empirical solar wind velocity field which is a function of field line expansion factor and the distance between traced open fieldline footpoints and coronal hole boundaries.

Magnetohydrodynamic (MHD) simulations of the solar corona represent the state of the art of global coronal modeling. To the extent that MHD represents the true physical processes in the Sun's atmosphere, these models constitute a complete, time dependent representation of the associated plasma flows including plasma moments, wave normal modes and instabilities. Variations between MHD models of the corona often stem from how energy is supplied to the corona and hence drives supersonic outflow, and generally come down to the energy equation in the underlying numerical scheme. Numerous model implementations for the Sun's corona exist; examples include the Alfven Wave Solar Model [AWSoM; 196, 213], the Multi-Scale Fluid-Kinetic Simulation Suite [MS-FLUKSS; 160] and the Magnetohydrodynamics Around a Sphere [e.g. 132, 133], the latter of which is used in the present work.

Although the three categories of models mentioned above comprise those examined in

this article, there are numerous other coronal models that are being developed and seek to improve on PFSS models without going as far as full MHD. For example [97] has produced a PFSS extension with an elliptical source surface. [171] proposed a magnetofrictional model which is similar to PFSS models except it produces its coronal field self consistently with an accelerating radially outwards flow which leads to much more compelling streamer belt shapes. Nonlinear Force Free (NLFF) models [see review by 232] are also an improvement on potential fields in that they reduce the severity of the no-current constraint, allowing currents to flow along field lines.

It is clear that there are a plethora of options for coronal modeling, with trade-offs between the physical content of the model, computational time and accessibility of model software. However, there is an implicit assumption here that "more physics" should produce more accurate coronal models. To support this assumption, it is clearly desirable to compare models to each other and assess for improvements in accuracy.

Almost any publication introducing a new or tuned coronal model includes a qualitative or quantitative comparison to empirical measurements of the Sun (either remote or in situ). For example, [100], [5], [14] and [153] all investigated PFSS source surface height with the first comparing the extent of coronal holes, the second trying to match the open magnetic flux in the heliosphere and the latter two trying to match magnetic polarity changes with Parker Solar Probe measurements. Similarly, [96] used ballistically mapped magnetic polarity to study an elliptical outer boundary condition to a potential model. Even the first PFSS papers investigated different observables where [4] focused on comparison to white light (WL) eclipse observations while [186] investigated interplanetary magnetic field strength. While this single metric approach is usually useful to support an author's assertion of improvement, especially when comparing their model to a prior iteration of the same model, there are a couple of issues. Firstly, such comparisons made with one type of metric (for example prediction of current sheet crossing timing, or visual correspondence of model field lines to a coronagraph snapshot) will test and optimize a single aspect of the models' representation of the corona. As we show in this work (section 2.6), it is possible to improve one aspect of a model to the detriment of another. Secondly, this leads to highly non-standardised comparisons across the literature. For illustration, we may know model X produces a more accurate forward model of an eclipse observation than model Y, and that model Y produces a much more accurate timeseries prediction of velocities compared to the *in situ* measurements than model Z. However this does not allow us to compare model X to model Z, without significant further work.

The goal of this work is to define a model-agnostic framework to evaluate quantitatively the representation of the corona for different coronal models and to use multiple independent comparisons to do so. We study PFSS, WSA and MAS MHD model results and for consistency, we study the minimum set of information which is provided directly by all three models, i.e. the coronal magnetic field. For each model, we require a prediction in a standardized format of 1) the location of coronal holes at the coronal base (i.e. the location of open magnetic field in the model), and 2) the location of the coronal neutral line at the outer boundary of each model which corresponds to the coronal streamer belt and shapes the

heliospheric current sheet (HCS). To test these predictions, we identify three independent observations. The first is EUV observations of the locations of coronal holes, the second is the location of the streamer belt at $5R_S$ observed from white light coronagraphs, and last is the timing of crossings of the heliospheric current sheet as measured by heliospheric spacecraft (Parker Solar Probe, "near-earth" spacecraft via the OMNI dataset, and STEREO A). Each of these three types of observation is compared to the relevant model prediction and a quantitative metric is developed to compare them. We study time intervals of ±30 days from the date of the first three perihelia of Parker Solar Probe (PSP) to focus our investigation and take advantage of novel *in situ* measurements of PSP closer to the Sun than ever before. Our metric scores are probed as a function of the choice of model, input parameters, boundary conditions and time over our model dataset. We present results and inferences for these specific studies (Section 3.4) as well as more general conclusions about our model framework (Section 5.5).

Similar issues have recently been discussed and studied in complementary recent work by [219] with the implementation goal of optimizing the EUropean Heliospheric FORecasting Information Asset [EUHFORIA; 162] model, another example of an MHD model. As in the present work, these authors specify individual independent evaluation metrics between models and observations. In this work, where relevant, we explain the relationship or difference of implementation in our metrics as compared to those of [219].

2.3 Coronal Field Models

As mentioned above, several coronal models are used in this work to define and test our evaluation framework. In this section, we introduce the model types and specific implementations used to then discuss the model-independent format of "observables" that each model is required to produce to facilitate quantitative comparisons.

Models were obtained for three specific time intervals, distributed ±30 days either side of the first three perihelia of Parker Solar Probe (PSP). As mentioned in the introduction, this choice was made to focus our investigation and make use of novel new *in situ* measurements from PSP. For each model, at least one run per interval was generated, but where possible provided full daily updates to the magnetogram input boundary conditions spanning these time intervals.

Potential Field Source Surface (PFSS) Models

PFSS models for this work were generated from two sources:

1. *pfsspy*[1], an open source python implementation [201] with Air force Data Assimilative Flux Transport [ADAPT; 9, 7, 8, 66] magnetograms as their input boundary conditions. ADAPT maps enhance typical magnetogram observations by assimilating direct

[1] `https://github.com/dstansby/pfsspy`

measurements of magnetic fields on the solar near side and helioseismological sounding of far side structure into a self-consistent surface flux transport model. ADAPT map data products include 12 individual realizations obtained by running an ensemble of models. For the PFSS model run here, we average these realizations together, subtracting any residual monopole moment induced by the averaging before feeding it into *pfsspy*. ADAPT maps are regularly produced using magnetographs from both Global Oscillation Network Group [GONG 63] and from the Helioseismic and Magnetic Imager [HMI; 188] on board the Solar Dynamics Observatory [SDO; 156]. Both are used and their separate models generated with *pfsspy* in this model dataset. In this work, these two magnetograms will be referred to as "ADAPT-GONG" and "ADAPT-HMI" respectively.

2. The standard PFSS implementation by the Global Oscillation Network Group [GONG; 63] which utilizes the zero-corrected GONG magnetogram data product [67]. This magnetogram will be referred to as "GONGz" in this work.

As well as being tabulated for each day in the studied time intervals, individual model runs were produced for differing values of source surface height (R_{SS}) ranging from 1.5 to $3.0R_{\odot}$, spanning most of the range typically investigated in studies of R_{SS} [e.g. 100, 5].

Wang-Sheeley-Arge (WSA) Model

The Wang-Sheeley-Arge (WSA) model [6, 11, 10] extends the capabilities of PFSS models with a Schatten Current Sheet [SCS 187] model extending above the potential layer, providing magnetic coronal structure out to $5R_{\odot}$. WSA additionally generates an empirical velocity field at the model outer boundary (generated as a function of expansion factor and the distance of magnetic footpoints to coronal holes) although only the magnetic structure is accessed in the present work. As with *pfsspy*, for this project these models are driven by ADAPT magnetograms. Selection of magnetogram realization varied across different time intervals.

WSA model parameters include a source surface height (R_{SS}) marking the boundary between the PFSS and SCS components of the model, and an outer boundary for the SCS (R_{SCS}). Unless otherwise noted, these values were set to $R_{SS} = 2.5R_{\odot}$ and $R_{SCS} = 5R_{\odot}$.

Full daily evolved models were provided for our data set for the perihelia 1 and 3 intervals. For perihelion 2, a single model run was investigated using an ADAPT-GONG map from 2021-04-10. As will be discussed in section 3.4, encounter 2 was challenging for modelers due to far side active region emergence. This single model run was chosen for encounter 2 as it provided the best representation of PSP in situ magnetic polarity.

Magnetohydrodynamics Around a Sphere (MAS) MHD Model

Lastly, we use results from the Magnetohydrodynamics Around a Sphere (MAS) model [131, 133, 177] for the studied time intervals. As touched on in the introduction, MHD models are

significantly more computationally intensive and as such daily evolution of the magnetogram input was not available for this project. Instead a single model run is provided for each perihelion date based on the closest Carrington rotation number (CRN).

The MAS models extend from the corona out to $30R_{\odot}$. The supersonic solar wind outflow in this case is generated via the PSI thermodynamic energy equation [111, 113]. The magnetograms used to drive them from the inner boundary used HMI data [134, 179]. Again, although the MAS model provides a litany of other physical properties, (e.g. density, flow velocity, temperature), only magnetic structure is extracted for this work.

Derived Observables from Coronal Field Models

A very important step in the framework outlined in this paper is defining a standardized set of "observables" to be produced by each model. This allows inter-model comparison and portability of this method to future models by ensuring that the comparison between observations and models is made in a controlled way that does not depend on any internal properties of the model used to produce them.

Specifically, we require models to produce:

- A 2D open field map at the photosphere uniformly binned in sine heliographic latitude and heliographic Carrington longitude. Each pixel takes either the value 1 to indicate that a field line traced from that point on the photosphere reaches the model outer boundary and is magnetically "open", or 0 to indicate a field line traced from the point is "closed" and re-intersects the photosphere. The left hand edge of the 2D map is required to be at 0 degrees Carrington longitude.

- A 2D map of the position of the heliospheric current sheet at the outer boundary of the model binned in the same way as the coronal hole map. Pixels have the value of +1 for locations where the field is directed outwards (positive polarity) and -1 where the field is directed inwards (negative polarity). Presented in this way, the HCS can be extracted from the map using contouring software in IDL or python at the zero contour level, which allows for the possibility that the HCS consists of multiple closed loops. Although such topologies were not encountered in this study due to the deep solar minimum, this allows this framework to be useful at future (or previous) solar maxima, where such a topology may occur.

Thus, we require models to predict coronal structure at both their inner and outer boundaries. Examples of these two observables may be seen in the top panels of figures 2.1 and 2.2 respectively. Note we are only examining magnetic field structure. While coronal plasma of course comprises many other physical quantities (such as density, flow, temperature and composition), here we opt to restrict to magnetism since this is the minimal physical content common to all realistic coronal models and so allows direct comparison between all commonly used models, including those to come in the future.

2.4 Observations and Measurements

In this section, we describe the corresponding observational data used and processed to facilitate comparison to the models. Data is obtained concurrently with the models, i.e. for the time intervals around each of PSP's first three perihelia.

EUV Coronal Hole Synoptic Maps

We use SDO Atmospheric Imaging Assembly [AIA, 102] observations to prepare our EUV Carrington maps from which coronal holes can be detected. We downloaded 180 s worth of data for the 304 Å, 171 Å, 193 Å, and 211 Å filters each day of the Carrington rotations relevant to PSP encounters 1–3. The data were processed using standard AIA analysis software. We performed a deconvolution of the point-spread-function (PSF) on each image using `deconvolve` from aiapy[2] and produced a median filtered composite image in each wavelength for each day. The daily images were converted from helioprojective coordinates to Carrington longitude and sine latitude using `wcs_convert_to_coord`[3], a routine in the Solar Software (SSW) IDL package [53]. Finally, these are combined to produce an EUV Carrington map for the Carrington rotation. The blending overlap is about 12^o in longitude. PSP perihelia 1 and 3 overlapped mostly with Carrington rotations 2210 and 2221 respectively, but encounter 2 occurred near the boundary of Carrington rotations 2215 and 2216. In this case, we prepared maps for both rotations, switching between them at the appropriate time.

Several methods of coronal hole detection have been used by the community dating back to early efforts using hand-drawn maps [64]. Subsequently, a number of independent detection methods have been developed. For example, using local intensity thresholding [92], forming high contrast images from linear combinations of spectral line properties [124], segmenting images by region growing algorithms [31], and applying intensity thresholding across multi-temperature image passbands [55]. Each of these techniques has its advantages and weaknesses. Automatic detection algorithms, for example, are very powerful for processing large volumes of data.

In this work we experimented with several methods: simple EUV intensity thresholding, the CHIMERA [coronal hole identification via multi-thermal emission recognition algorithm, 55] software package, and the Predictive Science Inc. (PSI) EZSEG image segmentation code [31]. Ultimately we chose to use the EZSEG algorithm. For this work, the chosen algorithm needed to be able to accurately produce contours of coronal holes from 2D Carrington maps to allow direct comparison to our chosen observables (see section 2.5). By visual comparison, the EZSEG algorithm was found to be the best for our circumstances, particularly proving useful at contouring the polar coronal holes which form a large fraction of the global coronal hole area at solar minimum.

[2] `https://aiapy.readthedocs.io/en/latest/`

[3] `https://hesperia.gsfc.nasa.gov/ssw/gen/idl/wcs/conversion/wcs_convert_to_coord.pro`

The software is available as part of the EUV2CHM Matlab package from the Predictive Science Inc. website[4]. We converted the EZSEG algorithm from FORTRAN to IDL to plug-in to our software pipeline. This algorithm uses an initial intensity threshold to acquire coronal hole locations in an EUV image, and then uses an area growing technique to define connected regions. This continues until a second intensity threshold is reached, or the condition for connectivity is not met. The dual-thresholds and connectivity conditions (essentially the number of consecutive pixels), are defined on input. We experimented with the optimal input parameters for each of our 193 Å Carrington maps. As an example, for encounters 1 and 3, thresholds of ∼20% and ∼60–70% of the peak EUV intensity worked well, with connectivity defined as 5 consecutive pixels. For encounter two, thresholds of ∼15% and ∼45% worked better. This reflects the presence of several brighter active regions around the solar surface during encounter two. An example of our 193 Å Carrington maps and the EZSEG output is shown in the middle panel of figure 2.1, and shows how the algorithm performs well at contouring coronal hole regions identified by eye as dark regions in the EUV carrington map. This figure as a whole and section 2.5 explain how we make the comparison of our maps with modeled coronal hole areas.

White Light Synoptic Maps

We exploit continuous white-light observations from the *Solar and Heliospheric Observatory* [*SOHO*: 43] LASCO C2 coronagraph [27] to produce white-light synoptic maps.

The light received by such a detector located at 1 AU is the result of multiple contributions along the lines-of-sight. The most significant contribution is the photospheric light scattered by dust particles, the F-corona. The latter is removed by subtracting background images from raw images in order to reveal the faint amount of photospheric light that is scattered by electrons, the K-corona. Hence this process provides not only access to the overall structure of the corona, but also to detail often observed in eclipse images for instance [21, 44]. Monthly minimum averaged images are used as background images to remove the F-corona. They are accessible via the widely used SolarSoft IDL library. The resulting image can now be used to visualize features of interest such as bright coronal rays that are signatures of enhanced density structures. Streamer rays are good proxies to visualize the dense plasma emanating from the tip of helmet streamers, that in turn supplies the Heliospheric Plasma Sheet (HPS). Hence streamer rays are also useful to get an approximate location of the Heliospheric Current Sheet (HCS), which is likely located inside the thick HPS.

The second step is to concatenate and convert continuous observations into a synoptic format, that is heliographic latitude versus longitude at a given height in the corona. Such maps, if defined in the Carrington frame rotating with the Sun are called Carrington maps. They have been significantly used in the past to exploit 1 AU observations [see e.g. 223, 225, 41, 157, 184, 181].

[4] `http://www.predsci.com/chd/`

To generate such a 2D map from LASCO C2 images, the following steps are followed. For 1 AU observations and small heliocentric distances, a widely used and reasonable approximation is to project images onto the helioprojective sphere (that is centered at the observer, also known as the plane-of-the-sky). The projected image is then converted from helioprojective to Carrington coordinates. As the Sun rotates on itself, the LASCO C2 coronagraph images the plane of the sky above both the East and West limbs, performing a full scan in half of the solar synodic period (13 days). A 3D annular volume of white light intensity is therefore progressively filled up, providing a global overview of the structure of the solar corona at multiple altitudes, similarly to tomographic imagery techniques [137]. Finally, we extract a single slice from this 3D volume at a specific heliocentric distance, getting at last a 2D synoptic, or Carrington, white-light map. As long as new images are available, the Carrington synoptic map is continuously added to and updated, allowing the production of a near-real-time map. An example of a white-light synoptic map is shown in the middle panel of figure 2.2, which has been extracted at 5.0Rs and combines SOHO LASCO-C2 images from October 30 to November 13, 2018.

Once the white-light synoptic map is complete, we perform 2-D median filtering in order to reduce "salt and pepper" noise while preserving edges of features of interest. The streamer belt is a thick band of enhanced brightness in each white-light synoptic map, that shows the overall shape of the HPS around the Sun. It is not always easily distinctive and sometimes can be confused with pseudo-streamers. One needs to adjust the height at which the white-light synoptic map is extracted in order to dispel the ambiguity. For instance, the usual larger radial extent of streamers compared to pseudo-streamers can help to discriminate between both [222]. For a start, we selected a height of 5.0 Rs, large enough to remove most of the pseudo-streamer signatures, while also keeping good image quality [further details can be found in 161]. The outermost boundary of the streamer belt is identified with a simple brightness threshold. The threshold has been adjusted manually until a coherent shape was obtained (see the dark contour in the middle panel of figure 2.2). That provides a rough idea of the shape and thickness of the HPS. For this work, the key feature of interest is the HCS which is likely standing inside the streamer belt and can reasonably be expected to be approximately located where the brightness is maximum within the streamer belt. As such, we trace the locus of maximal brightness at each longitude (see the dark dashed line in the middle panel of figure 2.2), hereafter called the Streamer-Maximum-Brightness (SMB) line via the method described in Algorithm box 2.2. A good correlation has been found between the SMB line and the magnetic sector structure observed *in situ* at 1 AU [see 161]. Similarities between the brightest regions of the K-corona and the magnetic sector boundary have also been highlighted in past studies [59, 73].

PSP and 1AU *in situ* Magnetic Polarity Measurements

The final observation we use in our model comparisons are direct *in situ* measurements of the magnetic field polarity in the inner heliosphere over the time intervals of interest combined with knowledge of the corresponding spacecraft's position. We use data from the FIELDS

instrument [19] on the *Parker Solar Probe* spacecraft [52] down to $35.7R_\odot$, as well as the OMNI "near-earth" dataset[5] and measurements from the IMPACT [119] instrument on board *STEREO AHEAD* [80] at 1AU. The magnetic field polarity is determined by the sign of the radial component of the field (B_R). We consistently choose to determine this by computing the most probable value over 1 hour intervals of higher cadence data following [14]. This removes small scale fluctuations and gives a resulting observable which indicates what side of the heliospheric current sheet (HCS) that specific spacecraft was located at a particular time. One further step is required for comparison with the location of the neutral line predicted by our coronal models. Since the coronal models predict the neutral line at a distance of a few solar radii, the spatial information of the spacecraft further out must be corrected to account for the Parker spiral. We utilize ballistic propagation [146, 121] whereby a constant solar wind velocity is assumed for a Parker spiral field line intersecting the spacecraft to set the spiral curvature. This velocity is chosen either from *in situ* measurements of the velocity at the spacecraft or otherwise uses a compromise value of slow wind of 360 km/s (typical of low heliographic latitudes). By combining the polarity time series with the spatial location of the spacecraft, we can build up a picture of where warps in the HCS are located. An example of data from PSP/FIELDS during its first solar encounter (October/November 2018) is shown in figure 2.3 where, in the middle panel, we see PSP's trajectory (ballistically mapped to the edge of the corona) colorized by the polarity measured as it traveled through each position.

The final derived observation is then a list of timestamps, polarity values, and ballistically corrected heliographic latitudes and longitudes of the spacecraft at the outer boundary of the coronal model (typically 2.0-2.5 $R_\odot$ for PFSS models). Our method of comparison to this observation is described below in section 2.5.

2.5 Prediction-Observable Comparisons

We next introduce our three metrics for comparing the data and modeled observables introduced in the previous sections.

Coronal Holes

Our aim here is to provide some measure of how well the coronal magnetic field models are able to predict the true open magnetic field on the Sun during each of the PSP encounters. We compare the model predictions of the locations of open field (black regions, top panel, figure 2.1) with the locations and extent of coronal holes detected in our 193 Å Carrington maps (white contours, middle panel, figure 2.1). Each of the models outputs a Carrington map of open and closed magnetic field. Similarly, EZSEG (section 2.4) produces a pixel map of coronal hole detections. We take the EZSEG map of coronal hole detections to be the ground truth open field dataset and apply a binary classifier algorithm to make the model comparison. This overall procedure is summarized in algorithm box 2.1.

[5] `omniweb.gsfc.nasa.gov/`

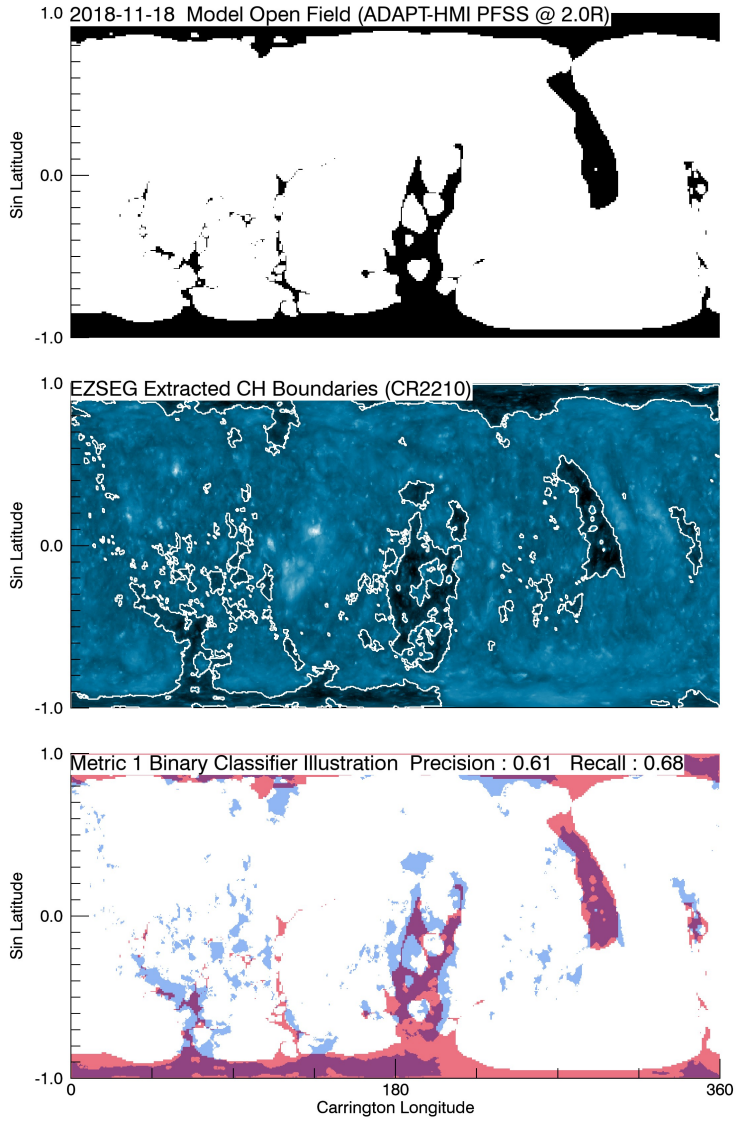

Figure 2.1: Illustration of construction of metric 1 using the example of an ADAPT-HMI PFSS model from 2021/11/18 during PSP Encounter 1 with a source surface height parameter of $2.0R_{\odot}$. Top panel: Mask of coronal hole locations (black shading) predicted by the PFSS mode model, i.e. pixels in the input magnetogram which map to open field lines. Middle panel: Coronal hole locations as determined by applying the EZSEG algorithm to AIA/EUVI maps of 193Å coronal emission, as described in the main text. The background image depicts the EUV Carrington map and the white contours indicate the areas identified by EZSEG. Bottom panel: Shading depicting the comparison of the observed and modeled coronal holes and metric construction. Blue shading indicates pixels that are identified as coronal hole by EZSEG, and red shading indicates locations predicted open by the model. Where they overlap, purple shading indicates the pixels are predicted and measured as coronal hole. The main text (section 2.5) describes how these regions are used to generate the precision, recall and final 'f-score' metrics to quantify the agreement.

Table 2.1: Process to Generate Coronal Hole F-Score

1) Prepare [or download from Zenodo repository: 12] a 193 Å EUV Carrington map for time interval of interest.
2) Prepare coronal hole map from model output (0 = Closed, 1 = Open), Map A.
3) Apply EZSEG [31] to 193 Å EUV Carrington map to obtain a binary map of "measured" open and closed pixels, again 0 = Closed, 1 = Open: Map B.
4) Interpolate model coronal hole map to the same resolution as the binary map
5) Compute true positive rate t_p : Number of pixels open in Map A AND Map B
6) Compute false positive rate f_p : Number pixels which are open in Map A and closed in Map B
7) Compute false negative rate f_n : Number of pixels which are closed in Map A and open in Map B.
8) Follow equations 2.1-2.3 to compute precision, recall and f-score respectively.

The algorithm computes three metrics: the precision (p), recall (r), and f-measure (f). These are familiar concepts in machine learning and statistics and are defined as

$$p = t_p/(t_p + f_p) \tag{2.1}$$
$$r = t_p/(t_p + f_n) \tag{2.2}$$
$$f = 2pr/(p + r) \tag{2.3}$$

where t_p is the number of true positives, f_p is the number of false positives, and f_n is the number of false negatives. Each metric falls in the range of 0–1. Here, a true positive is recorded when a pixel marked as a location of open field in the model is found to be open in the ground truth map (purple or "overlap" pixels in the bottom panel of figure 2.1) A false positive is recorded when a pixel marked as a location of open field in the model is found to be closed in the ground truth map (red pixels in figure 2.1). Similary, a false negative is recorded when a pixel location marked as closed field in the model is found to be open in the ground truth map (blue pixels in figure 2.1). The precision is therefore the fraction of open field predicted by the model that is actually open according to the detection of coronal holes in the 193 Å Carrington synoptic map, that is the number of purple pixels as a fraction of the number of pixels which are red or purple. Conversely, recall is the fraction of actual open field (according to the coronal hole detection map) that is predicted to be open by the model, or number of purple pixels as a fraction of the number of blue or purple pixels. These two metrics are useful for understanding how the models are performing, but, as can be seen in panel-by-panel comparison in appendix A, they are anti-correlated, so we calculate the f-measure (the harmonic mean of the precision and recall) to classify which models are best. The harmonic mean gives high values if both constituents have high values, but gives low values if *either* constituent is low-valued independent of the other.

By now it should be clear that there are some limitations to our comparisons. First, we assume that all the magnetic field within all the detected coronal holes is open. There is, of

course, a transition to closed field close to the boundary. Second, we assume that there is no open field outside of coronal holes. Comparisons of PFSS extrapolations with actual solar features indicate that this is not the case - see, e.g., the full Sun intensity and open-field maps of [26] that suggest a large contribution to the slow solar wind from active region outflows. Although the time intervals studied in this work occur during deep solar minimum, we do have one interval when there was significant solar activity.

As will be shown later, metric scores typically didn't exceed 60%. Figure 2.1 illustrates some of the reasons for this. For the example shown, the model appears to overexpand the polar coronal holes and underexpand the mid-latitude ones. Since the polar coronal holes are the largest open regions by solid angle, they became an important point of comparison for the models and is what led us to prefer EZSEG as the algorithm for detection (recall the discussion in Section 2.4). As we can see in the middle panel of figure 2.1 (white contours), EZSEG does a good job detecting the polar coronal holes while other algorithms were less effective. Conversely, there are quite a few small observed coronal holes that appear dubious. These, however, constitute a small fraction of the total area of detections so are a minor contributor to our results. An example showing the f-measure comparisons for all the models we investigated for encounter 1 is included in the Appendix (Figure A.1) and linked to full encounter movies in the electronic version of the manuscript.

[219] also make comparisons between EUV images and open field models (specifically from the EUHFORIA model). In their work, they use a simple threshold condition after [92] to obtain observed coronal holes, and use a similar set of binary classification metrics [see 219, for details]. This work addresses the difficulty with polar coronal holes by truncating their binary classification to between $\pm 60^o$ latitude, and therefore score the model based on mid and low latitude coronal holes only. In the present work, our choice is to use a more complex coronal hole extraction software (EZSEG) and therefore a slightly more convoluted analysis pipeline with the advantage of having a higher degree of confidence in our extracted polar coronal holes. Indeed, we should note that the polar coronal holes, in general, are poorly observed both in EUV and the magnetograms driving the models. However, their equatorward extent is usually well observed, at least in one hemisphere. Accepting this uncertainty, we make use of sine latitude (or cylindrical-equal-area, CEA) projections in our maps which limit the area occupied by the polar coronal holes, effectively assigning a lower weighting to those pixels by preserving pixel area at higher latitudes. Future work may seek to improve equations (2.1-2.3) with an explicit weighting for different types of coronal holes, and even further afield, direct solar polar observations may negate such considerations altogether. However, in the present work we proceed with this straightforward classification scheme and argue that due to the deep solar minimum conditions that our studied time intervals occur during, it is important to assess the polar coronal holes in our metrics.

Streamer Belt

As discussed in subsection 2.4, we built and exploited white-light synoptic maps to get an approximate shape of the HCS, or magnetic sector structure, via what we called the

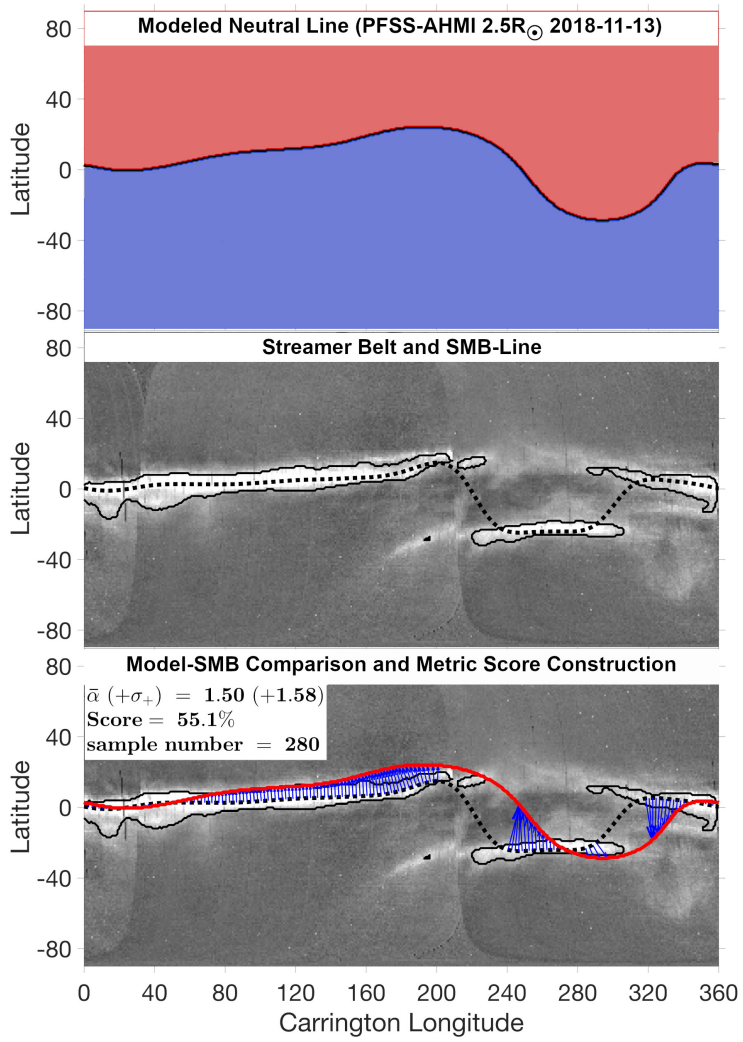

Figure 2.2: Illustration of the construction of Metric 2. Top panel: Model input - contour of polarity inversion line as predicted by coronal models. Middle panel : Observation input - a white light synoptic map of the streamer belt (Carrington map) constructed at a height of 5 $R_\odot$ from SOHO LASCO-C2 images taken between 2018, October 30 and 2018, November 13. The streamer belt contour is plotted in dark. The core of the streamer belt identified by the SMB line is traced as a dark dashed line. Bottom panel - Comparison between the SMB line and the modeled polarity inversion line (solid red line). The angular deviations between the two lines that are used to compute the white light (WL) metric are represented by the blue arrows. Results from the WL metric are given in the legend, of which the WL global score (in %) calculated from the mean $\bar{\alpha}$ and mean deviation σ_+.

Table 2.2: Process to Generate White Light Streamer Belt Score [161]

1) Prepare [or download from Zenodo repository: 12] WL Carrington map for time interval of interest.
1a)(recommended) Clean up the WL map with a 2-D gaussian filtering (e.g. using the `medfilt2()` function in MATLAB).
2) Prepare neutral line from model output (2D map of polarity at model outer boundary, pixel values = ± 1).
3) Extract (or download) the SMB line. If downloaded then jump directly to step 4.
3a) Find longitudes and latitudes of max brightness points in the WL Carrington map.
3b)(optional) Smooth out the SMB line with a 1-D gaussian filtering (e.g. using the `smoothdata()` function in MATLAB).
4) Measure (or download) the streamer belt (half) width (T_i) (provided in the SMB .ascii files in the Zenodo repository). One could also simply assume a constant streamer belt width and jump to step 5. If you choose the download option or want to perform your own measurements, please read carefully the footnote [6]. Follow steps 4a and 4b if you decide to perform your own measurements or else jump to step 5.
4a) Draw streamer envelope with a simple contour threshold.
4b) Measure the angular distances (T_i) between each point of the SMB line and the extracted contour of the streamer envelope.
5) Measure for each grid point along the SMB line, the angular distance (α_i) to the model neutral line extracted at step 2. Make sure to make these measurements along the same directions as in step 4b.
6) Normalize each angular distance (α_i) computed in step 5 by its associated streamer (half) width (T_i) measured in step 4.
7) Apply equation 2.4 to obtain the streamer belt metric score $C(\bar{\alpha}, \sigma_+)$.

streamer-maximum-brightness or SMB line. As a consequence the SMB line can then be easily compared to any global coronal model. The steps we follow are summarized in algorithm box 2.2. However with the SMB being extracted at a specific height, some precautions must be taken prior any comparison being made.

In this work, we performed PFSS modeling with a source surface height up to 3.0Rs. Above this height, the magnetic field is assumed to be purely radial and hence the line of polarity inversion or neutral line (NL) remains the same in a latitude vs longitude format. Assuming that the streamer topology does not change significantly between the PFSS source surface height and $5R_{\odot}$, the SMB can be compared with the PFSS neutral line. The overall shape of the streamer belt is not expected to vary significantly but a slight narrowing of the streamer belt could be observed still. The outer boundary of the WSA runs is located

at $5R_\odot$, so at the exact same height at which the SMB line is extracted allowing a direct comparison. The MAS MHD simulations from PSI extend much further and the NL is extracted at $30R_\odot$. In principle, this means the HCS could be shifted up to 8 degrees due to Parker spiral curvature, but in practise this is a small correction compared to the dispersion of neutral line topology amongst our dataset of model runs.

In order to compare in a statistical manner white-light observations and global coronal models we need to define a metric that is accurate and robust. To compare the SMB with the modeled neutral lines, various techniques can be tested. We decided to measure the angular distances between the two lines. These angular distances α_i are then normalized by the local streamer (half) thickness T_i which is obtained from the streamer belt contour identified beforehand. The reason for choosing this normalization is twofold: the streamer thickness is a physical measure that helps to interpret the final metric; and also the final metric is therefore not affected by the streamer thickness variability over space and time. In particular, this normalization leads to the useful intuition that scores above 50% correspond to model neutral lines lying on average within the bright white light emission of the streamer belt. The final step consists of calculating an averaged score over the full Carrington longitude range. The global score is built so that a model having a good overall match with WL coronagraphic observations would still be penalized in case of local and large deviations from the SMB line. Further details on the derivation of this global score can be found in [161] where the following formula has been retained:

$$\begin{aligned} C(\bar{\alpha}, \sigma_+) &= g(\bar{\alpha}) \times [1 - p(\sigma_+)] \\ g(\bar{\alpha}) &= \frac{1}{1 + (99)^{\bar{\alpha}/2-1}} \\ p(\sigma_+) &= \frac{1}{1 + \left(\frac{1}{99}\right)^{\sigma_+/2-1}} \end{aligned} \tag{2.4}$$

where $\bar{\alpha} = \frac{1}{n}\sum_{i=1}^{n} |\alpha_i|/T_i$ is the mean over longitude of the normalized angular distances to the SMB line, and $\sigma_+ = \sqrt{\frac{1}{n}\sum_{i=1}^{n}(|\alpha_i|/T_i - \bar{\alpha})^2}$ represents the mean deviation. Note that a looser version of the formula has been adopted in this work to better cover the dispersion amongst all model runs.

An example is illustrated in Figure 2.2 where the WL metric has been applied to a PFSS model based on the ADAPT/HMI map of 2018, November 13. For this particular case, the polarity inversion line remains mostly at the edge of the streamer belt that is reflected with a mid-range WL score of 55%. In regions where the HPS is significantly warped, the WL signature is too faint to allow a precise detection of the shape of the streamer. This happens when the line-of-sight of an imager, or coronagraph, gets significantly inclined with respect to the HPS such that the light scattered by electrons is integrated over a much shorter path. Hence, the WL metrics is configured to not evaluate the model in these specific regions, as shown by the absence of blue arrows in Figure 2.2. This constrains the effectiveness of this metrics to simple solar configurations where the HCS shape is not too complex.

Table 2.3: Process to Generate In Situ Polarity Score

1) Prepare [or download from Zenodo repository: 12] measured in situ polarity timeseries. If preparing yourself, recommended to follow processing routine here where for each hour of data, generate histogram of B_R and take polarity of most probable value as the polarity "measurement" for that time. 2) Produce model-predicted polarity timeseries by following these steps : 2a) Use spice kernels to generate spacecraft position in the heliographic frame at an hourly cadence over the time interval of interest. 2b) Ballistically propagate this position inwards to $2.5R_\odot$ using the equation for the Parker spiral [Equation 1, 14] 2c) Sample the modeled 2D map of the neutral line using this projected orbit (via interpolation or nearest neighbor) to generate a timeseries of predicted polarity. 3) Combine modeled and measured timeseries via equation 2.5 to obtain the in situ polarity metric score.

As a consequence, the reliability of this metric is uncertain for highly structured coronal configurations typically observed during periods of high solar activity. Future improvements which may increase the reliability of this metric for more complex configurations are discussed in further detail in [161]. The conversion in an all-in-one metric that evaluates both the pseudo-streamers and regular streamer locations should alleviate the uncertainty in using the SMB line alone for complex coronal configurations. WL synoptic maps produced by merging multi-viewpoint coronagraphic observations [see e.g. 184] should also be more appropriate to catch the dynamic reconfigurations of the solar corona arising with higher solar activity.

[219] also define metrics to compare white light observations to model results, focusing on snapshots of coronagraph observations and projecting their model results into the relevant plane of the sky. Their method requires a user to "point and click" to associate features in model and data and measure, for example, the angular difference between a modeled and observed streamer structure. This method enables very detailed comparisons at different coronal altitudes, albeit at the cost of requiring human intervention, and also only focuses on one plane cut through the model at a given time. Our chosen method after [161] is automated and evaluates agreement at all longitudes, but at the cost of not tracking variation with coronal altitude.

Magnetic Sector Structure

From our *in situ* observations described in Section 2.4 we have a measured timestamp, polarity and a ballistically mapped spacecraft location at the outer boundary of a given coronal model. To compare this observation to the model's prediction of the location of the heliospheric current sheet, we produce a predicted time series of magnetic polarity. For each timestamp, we take the model output closest in time to that timestamp and sample the polarity at the outer boundary of the model at the location of the associated ballistically

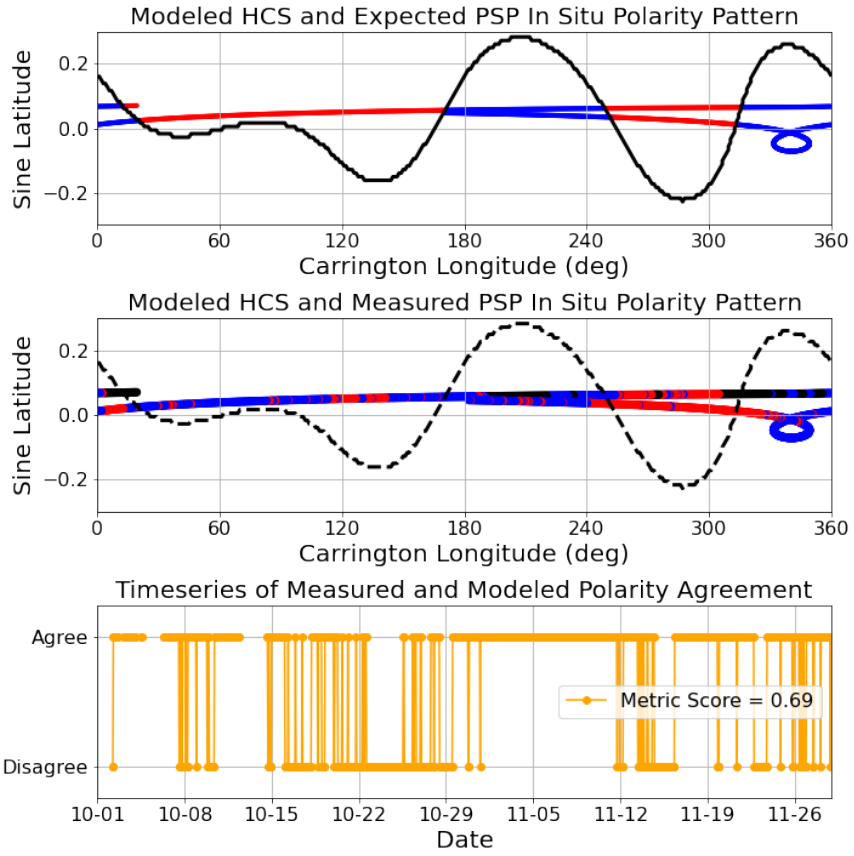

Figure 2.3: Illustration of Construction of Metric 3. Top panel: Model input - contour of polarity inversion line as predicted by coronal models and resulting predicted polarity that PSP's trajectory is expected to trace out according to the model. Middle panel : Observation input - same trajectory of PSP but colored by measured polarity. Dashed curve indicates the same polarity inversion line from the top panel showing the model-data agreement is imperfect. Bottom panel: Product of measured and predicted polarity timeseries. Values are +1 for agreement and -1 for disagreement. Metric is the ratio of agreements to the number of measurements, as described in the main text, Section 2.5

mapped footpoint location. We then have for each timestamp, i, a measured (m) and predicted (p) value of the polarity. While each individual measurement-prediction comparison gives very little information, we can multiply the whole timeseries together, and divide the total number of agreements (value of +1) by the total number of measurements to give a single value representing the fraction of measurements and predictions which agree, giving a single number between 0 and 1 evaluating the model and *in situ* measurement agreement for a given encounter. This operation may be mathematically expressed as with the Heaviside step function $\Theta(x)$ as :

$$\sigma(\text{sign}(B_R)) = \frac{1}{N}\sum_{i=1}^{N}\Theta(B_R^{m,i}B_R^{p,i}) \tag{2.5}$$

We note that a value of this metric of 0.5 would indicate as many agreements as disagreements in the timeseries and thus approximately equivalent to random chance. Thus, values above 0.5 are required for this metric to convey "good" agreement.

The construction of this metric is illustrated in Figure 2.3 in a similar 3 panel format as for the previous two metrics. In the top panel, a modeled HCS is depicted as a solid black curve and the trajectory of PSP projected onto the model outerboundary is superimposed. The color of the trajectory (red or blue) shows the model's prediction of the *in situ* polarity measurement according to which side of the HCS PSP is located. The equivalent data is shown in the middle panel where the same trajectory is colorized by the measurements for the relevant time interval. For reference, the model HCS is again included as a dashed curve to show that the measurement and model do not agree perfectly. Finally, the construction of the metric is illustrated in the bottom panel where a timeseries of predicted and observed *in situ* measurements are combined to produce a timeseries of agreement or disagreement. The score shown in the metric is produced from this data according to equation 2.5. This overall procedure is also summarized in algorithm box 2.3.

2.6 Results

Having introduced our models, derived observables, sources of observation and the construction of each metric in the prior sections, we proceed to compute metric scores and explore the results. We study time intervals for +/- 30 days for each of PSP's first three encounters, and for each encounter study metric scores for PFSS models with different source surface heights ranging from $1.5R_\odot$ to $3.0R_\odot$, and with different magnetogram inputs (ADAPT-GONG, ADAPT-HMI and GONGz), and for WSA and MAS models for the same time intervals. Given the large number of parameters to explore (time interval, magnetogram, source surface height, model physical content), we divide the presentation of the results into a series of specific studies. A more exhaustive exposition of the scores as plots and movies are shown in appendix A and online material.

PFSS Models : Source Surface Height Study

We begin by studying metric scores for the Potential Field Source Surface models. In figure 2.4, metric scores are depicted for each encounter (column by column) as a function of source surface height. Results using different input magnetograms are shown in different colors (blue for ADAPT-GONG, red for ADAPT-HMI and black for GONGz). For metrics 1 and 2 the score shown is the average over that encounter, and the error bar is the standard deviation. For metric 3, there is only one value as the metric is integrated over the encounter and there is therefore no equivalent error bar.

The coronal hole metric is shown in the top row of the figure. All models depict a lower score for the higher source surface heights and have the same qualitative variation for each encounter. The two ADAPT magnetograms (blue and red) follow each other very closely, with the GONGz diverging in qualitative behavior: The ADAPT magnetograms consistently show a maximum coronal hole F-score for a source surface height of 2.0 $R_\odot$ with a small reduction at either lower or higher values. GONGz magnetograms result in a maximum F-score for the lowest source surface height ($1.5R_\odot$) and a monotonic decrease for higher values and gives significantly lower values for 2.5 and $3.0R_\odot$ source surface heights. The actual average scores vary with a maximum of 0.6 and a minimum for GONGz of $\sim$0.3 and for the ADAPT maps around 0.55. Error bars indicate the variation of the metric over time within each encounter is small (<10%), which will be verified later in section 2.6. The bifurcation between the coronal hole representation of the ADAPT maps compared to GONGz, independent of which time interval is examined, suggests the surface flux transport treatment of the ADAPT maps has a stronger impact than variation between GONG or HMI data. Specifically, the ADAPT scores optimize around $2.0R_\odot$ while for GONGz, the lower the source surface height the better. As discussed further in section 5.5, this appears to relate to the extent of the polar coronal holes in the model and therefore may relate to the treatment of polar flux. The worsening scores with increasing source surface height is driven by the smaller extent of coronal holes predicted by PFSS as the outer boundary of the model is raised [e.g. 100]. The maximum F-score derived is around 60% which is far from perfect. As a reminder, the F-score is the harmonic mean of the precision and recall, which have the physical meanings respectively of "fraction of measured open field captured by the model" and "fraction of modeled open field which is actually open".

Results for the streamer belt metric are depicted in the middle row of figure 2.4. Conversely to the coronal hole metric, the PFSS representation of the streamer belt according to our metric *improves* monotonically with source surface height. This is true for each encounter, and independent of the magnetogram driving the model. The scores vary from near zero for the lowest source surface heights ($1.5R_\odot$) to greater than 80% for the highest values. The improvement with source surface height starts to flatten above $2.5R_\odot$. A dashed curve at a metric score of 50% indicates the score at which the majority of the modeled HCS remains within streamer belt latitudes, as defined by the intensity threshold discussed in Section 2.5. All PFSS models exceed this score for $R_{SS} \geq 2.5R_\odot$ and many exceed it by $2.0R_\odot$. There is variation in the ordering of scores according to magnetogram from en-

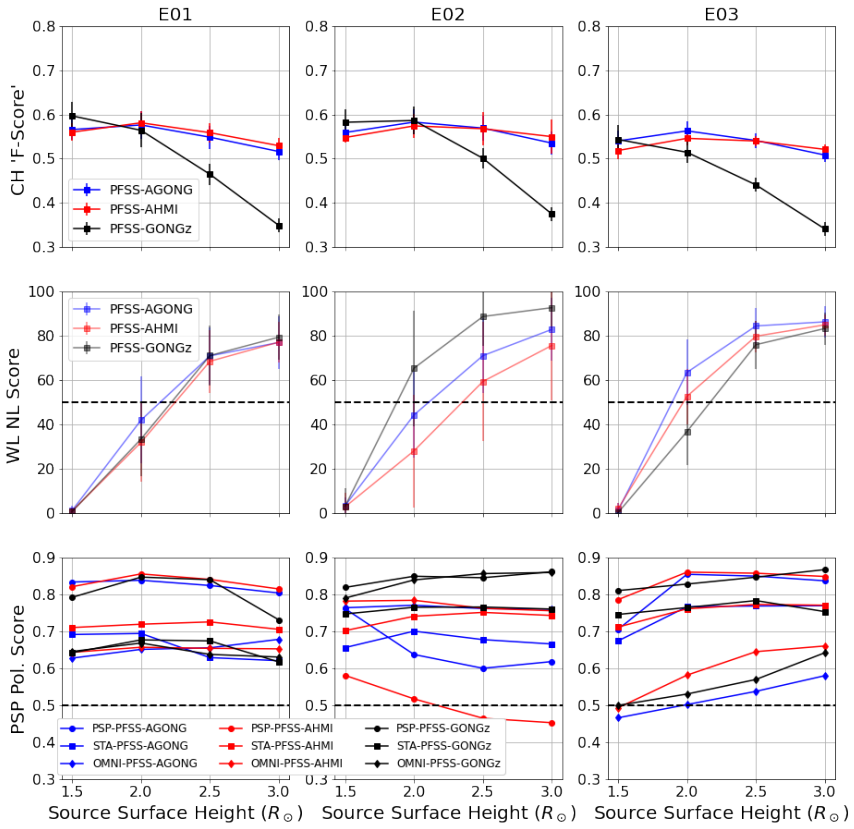

Figure 2.4: Summary of metric scores for PFSS models as a function of source surface height. Left, middle and right column show PSP Encounters 1,2 and 3 respectively. Top, middle and bottom row show metric 1 (coronal holes - Section 2.5), metric 2 (streamer belt topology - Section 2.5) and metric 3 (*in situ* magnetic polarity - - Section 2.5). Each panel shows the respective metric score (averaged over the corresponding PSP encounter for metrics 1 and 2) as a function of source surface height of the PFSS model. Different colors indicate results utilizing different magnetograms (Blue : ADAPT-GONG, Red : ADAPT-HMI, Black: GONGz). The bottom row showing metric 3 has *in situ* polarity scores for PSP/FIELDS, STEREO A/MAG and OMNI data shown by different symbols (circles, squares and diamonds respectively). All metrics are oriented such that a higher metric value indicates a "better" score. The middle row depicting metric 2 has a dashed horizontal line marking the 50% score threshold which indicates that the modeled HCS lies primarily within the observed extent of the streamer belt. The bottom row has a similar horizontal dashed line indicating the 0.5 score threshold corresponding to the result randomly generated measured polarities would achieve. Metric 1 and 2 scores have error bars indicating the standard deviation of the score throughout the encounter.

counter to encounter: For encounter 1 all model scores are nearly on top of each other with ADAPT-GONG being slightly better at $R_{ss} = 2.0R_{\odot}$. For encounter 2, there is significant divergence, with GONGz doing the best followed by ADAPT-GONG and ADAPT-HMI. For encounter 3, GONGz has the lowest score, with ADAPT-HMI slightly better and ADAPT-GONG the best. The monotonic increase in score with source surface height is driven by the extent to which the modeled HCS is warped: At lower values of R_{SS} PFSS derived HCS curves are very warped and span large ranges in latitude, while at higher values the HCS flattens out (tending to a flat line at infinite R_{ss}). Clearly, the observed latitudinal extent of the streamer belt is smaller than the HCS variation produced by PFSS models for lower source source surface heights.

Finally, the bottom row shows the *in situ* polarity scores. In addition to the difference between different models, results are shown for *in situ* data taken by PSP from $\sim$ 37.5-50$R_{\odot}$ (circles), and at 1AU by OMNI (diamonds) and STEREO A (squares). A dashed curve at a score of 0.5 indicates the threshold above which the metric score is better than random chance; the majority of scores do exceed this value. In general, the scores are relatively flat with respect to source surface height. Interestingly, although they are nominally testing the same model output as the streamer belt metric (model HCS), the profiles are more similar to the coronal hole metric. The highest metric scores are typically largest for 2.0 or 2.5$R_{\odot}$ with a small drop off for the low and high source surface height extremes. In terms of comparison between spacecraft, for encounters 1 and 3, PSP gave the highest scores for all source surface heights independent of magnetogram. For encounter 2 PSP gave both the lowest scores (ADAPT-HMI near 0.5) and the best (GONGz near 0.75). Other than for encounter 1, it is not clear that PSP's *in situ* measurements close to the Sun are better modeled than *in situ* measurements at 1AU. For encounter 3, PSP and STA performed identically (with high scores) while OMNI data gave significantly worse scores near the random chance threshold. The variation between spacecraft metric scores and different magnetogram scores for the same spacecraft is not consistent. For encounters 1 and 3, scores for a given spacecraft are tightly clustered together for different magnetograms while for encounter 2 there can be wide variation in a given spacecraft score for different magnetograms.

Taken together, there is a clear tension between our different metrics. The higher the source surface height, the better agreement is produced between the modeled HCS and the observed streamer belt location, while at the same time the coronal hole extent produced by the model decreases and gives worsening coronal hole scoring. The higher source surface height also gives slightly worsening *in situ* scores, implying that while the amplitude of warping of the HCS is more consistent with streamer belt observations, the locations where those warps intersect spacecraft orbits are less well represented. These results demonstrate that there is no global optimum source surface height which gives a best representation of all aspects of the magnetic structure of the corona.

To investigate if this tension can be eased by the physical insight introduced in more complex coronal models, we compare PFSS results to those of other models in the next section.

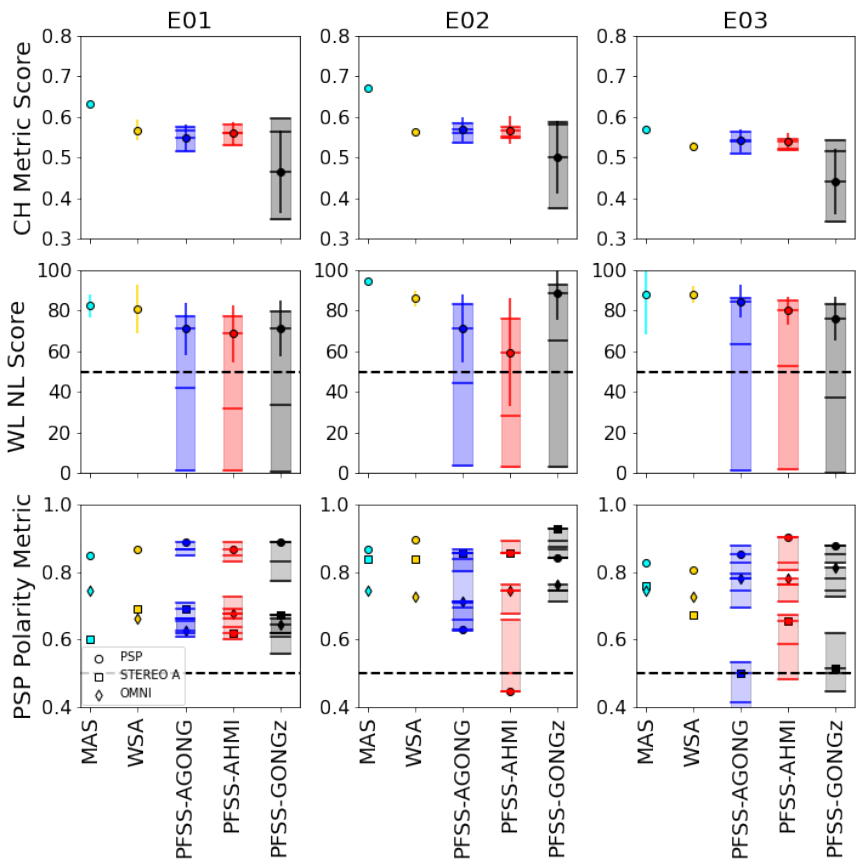

Figure 2.5: Inter-model comparison of metric scores. Columns and rows arranged as in figure 2.4 separating out results for each metric and PSP encounter. In each panel, results are shown for the MAS model (cyan), WSA model (yellow) and PFSS models driven by ADAPT-GONG (blue), ADAPT-HMI (red) and GONGz (black) magnetograms. Mean and standard deviation in metric scores across each encounter are indicated by the plot markers and error bars. For the PFSS models, the plot marker and error bar indicates results for a source surface height of $2.5R_{\odot}$; shading and horizontal bars indicate the range of metric scores with variation in source surface height. For metric 3 (bottom row), circle, square and diamond markers show different results for PSP, STEREO A and OMNI *in situ* measurements respectively. Dashed horizontal lines in rows 2 and 3 are as in figure 2.4.

Inter-model Comparison

Metric scores for the MAS MHD model, WSA model, and the PFSS results discussed in the previous section are compared in figure 2.5. The panels are laid out as in figure 2.4 (columns and rows differentiating encounter number and metric respectively). In each panel, a metric score for each model is shown, with the main new information coming from the scores for

the MAS model in cyan and WSA models in yellow. For the PFSS results, the main marker and error bar shows the results for a source surface height for the standard value of $2.5R_\odot$, but the variation within source surface height is captured by shaded regions indicating the range of variation, and horizontal bars indicating the distribution of scores which generate that range. The blue, red and black colors follow the scheme from figure 2.4 in differentiating ADAPT-GONG, ADAPT-HMI and GONGz magnetograms respectively.

The top row again shows the coronal hole metric scores. For each encounter the MAS model produces higher scores than the best achievable score for PFSS (although only slightly better for encounter 3). There is no error bar shown for the MAS score since there is only 1 coronal hole map generated due to computational tractability. As a reminder, the MAS model is driven by magnetograms from the Carrington rotation of the perihelion in each encounter (CR2210,CR2215 and CR2221). WSA on the other hand does not show significant improvement over the PFSS models in terms of coronal hole representation. For encounter 1, it is slightly better than the $2.5R_\odot$ ADAPT PFSS results but less than the best score generated by lowering the source surface height. For the other encounters it is slightly lower scoring than $2.5R_\odot$ ADAPT PFSS results. Note that the WSA model is driven by ADAPT-GONG magnetograms.

Metric 2 as depicted in the middle row of figure 2.5 shows that typically the MAS and WSA models produce better agreement between the model HCS and the observed extent of the streamer belt than the best achieved by PFSS results (recall these best scores were obtained by the highest source surface height explored, $3.0R_\odot$), with the exception of the encounter 2 PFSS-GONGz results which produced comparable scores to the other models for 2.5-$3.0R_\odot$ source surface height. The PFSS shaded bars in this row demonstrate the stark decline in PFSS scores with lowering source surface height, and we again see heights of $2.0R_\odot$ or below tend to produce scores less than 0.5 (dashed horizontal line), indicating the model HCS is reaching higher latitudes than expected from streamer belt observations. In all cases, the MAS score is the same or higher than the WSA score.

Metric 3 finally is compared between models in the bottom row of figure 2.5. As previously, circles, squares and diamonds indicate scores for PSP, STEREO A and OMNI *in situ* measurements respectively. For encounters 1 and 3, for each model the best score is for PSP and scores worsen for OMNI and STEREO A. The ordering of the spacecraft scores is consistent between metrics (PSP $\approx$ STEREO A $\approx$ OMNI for E01 and PSP $\approx$ OMNI $\gg$ STEREO A for E03). Comparing scores for a single spacecraft between models, for E01 and E03, MAS and WSA models give comparable or slightly worse scores compared to PFSS. The exception is the STEREO A scores for E03 which are significantly better in the WSA and MAS models as compared to the PFSS scores which are close to the 0.5 random chance threshold.

Staying with the *in situ* polarity metric, the result for encounter 2 is significantly different: the ordering of the spacecraft scores is reversed between the MAS and WSA models compared to PFSS models: PSP continues to give the best score for MAS and WSA, but is the worst for the ADAPT PFSS models (middle scoring for GONGz). We also note the variation in the PFSS scores as a function of source surface is often comparable to the difference between

different spacecraft at the same source surface height, indicating that the location in the heliosphere at which the *in situ* data is taken can be as important as the specifics of the model. We note that since the boundary conditions for the WSA model in encounter 2 is a single magnetogram chosen specifically to match PSP polarity measurements, it is not surprising that this specific value of metric 3 is one of the highest observed.

Lastly, bringing the metrics together we make some observations about the differences between the models overall. We see that:

1. Despite only utilizing a single magnetogram compared to the timeseries of magnetograms for the PFSS Models, the MAS model's use of MHD physics leads to improvements of both the coronal hole metric and the streamer belt representation. We note that quiescent solar minimum conditions may be responsible for the applicability of the MHD result from a single magnetogram over a long time interval. It does not significantly improve (or may even worsen) predictions of HCS crossing times (which drives the score of metric 3), except for the second PSP encounter specifically for PSP *in situ* measurements.

2. The WSA model improves the score of metric 2 (streamer belt shape) compared to raw PFSS models, but it does not lead to a noticeable improvement in the coronal hole metric score. It also does not significantly improve scores for the *in situ* polarity metric, except for encounter 2 where this was specifically tuned for. As discussed in Section 5.5, this is an unsurprising result based on the WSA physics which only adds information above the source surface, and therefore forms a good sanity check of our metrics.

Next, we close our exposition of the metric score results by looking at the details of the metric score timeseries for each encounter, from which the averages and error bars in the previous plots were generated.

Metric Score Timeseries

As a reminder, for each encounter for metric 1 and 2, the model output (coronal hole map and neutral line/HCS map) for PFSS and WSA models were evolved daily by using a new magnetogram (excepting E02 for WSA). The observed White Light Carrington map was also updated daily as the longitudes of the streamer belt visible from Earth updated. This means that, for metrics 1 and 2, we have a timeseries of metric scores for the 60 days comprising each encounter for WSA and PFSS models. For metric 3, the score is the output of integrating the full 60 day "measured" and "modeled" polarity timeseries together and therefore is not itself a timeseries.

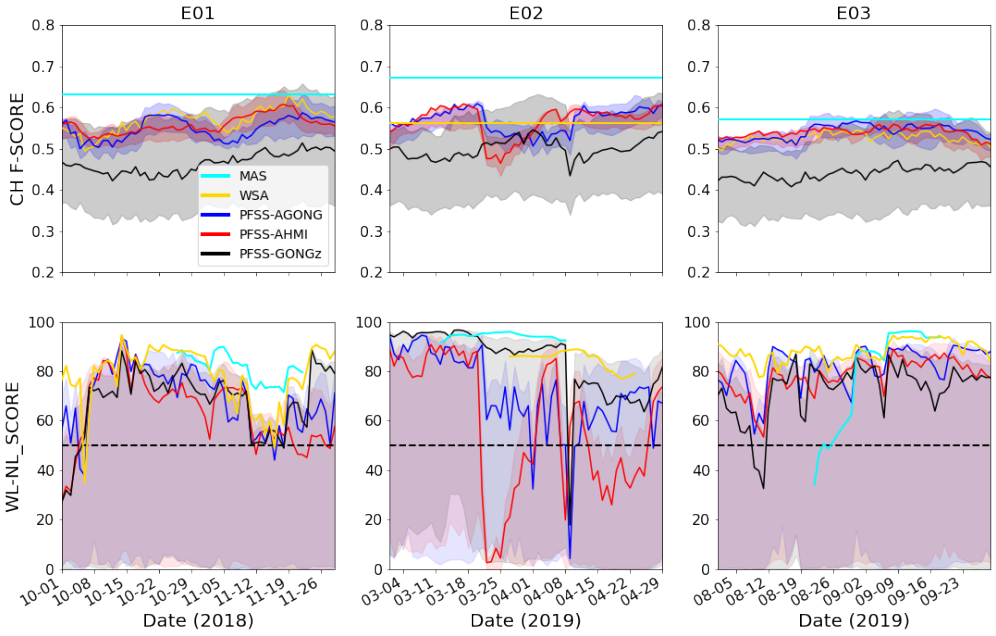

Figure 2.6: Variation of Metric 1 and 2 scores as a function of time within each encounter at a daily cadence. In each panel, colored solid lines indicate different models with the same color scheme as in figure 2.5 where a source surface height of 2.5 $R_\odot$ is chosen for the PFSS models (blue, red, black). Variation according to source surface height for the PFSS models is indicated by the shaded regions bounded by the max and min metric score at each timestamp. The top panel shows the coronal hole score (metric 1), the bottom row shows the streamer belt score (metric 2). Note the timeseries for the MAS model (cyan) is a single value as there is only 1 magnetogram used for each encounter owing to the intractability of running 3D MHD models with time-dependent boundary conditions. For encounter 2, WSA also only uses a single magnetogram and so only has a single value for metric 1 (see main text, Section 2.5).

Coronal hole and streamer belt metric timeseries

In figure 2.6, we depict the timeseries for metrics 1 and 2. The color scheme follows the preceding figures. The top row shows how the agreement between the modeled coronal holes and the EZSEG output of the EUV Carrington map for the relevant rotation evolved each day through each encounter. The bottom row shows the same for the agreement between the modeled neutral line and the observed streamer belt Carrington map. For the PFSS models, semi-transparent shading in the relevant color shows the range of metric values explored by varying the source surface height for each timestamp, while the solid lines show the scores for the canonical source surface height of $2.5R_{\odot}$. The upper bound of these shaded regions therefore shows the timeseries of the optimized source surface height for each mode. Following these timeseries, we can see how the coronal hole representation and streamer belt representation of each model evolved with each encounter.

Examining the coronal hole representation (top row), we see for encounter 1 (top-left panel) of the ADAPT-driven PFSS models and the WSA model (also driven by ADAPT magnetograms) follow each other closely, showing a periodic variation peaking twice, with an amplitude of approximately 0.1 corresponding to about 10% variation in the score. We note that the "observation" EUV Carrington map is static in each time interval, utilising data combined over the course of a Carrington rotation, therefore all evolution shown derives from the evolution of the PFSS model driven by updating its magnetogram boundary condition each day. The PFSS-GONGz score (the only daily-updated model driven by a non-ADAPT magnetogram) is quite different for the same source surface height ($2.5R_{\odot}$), being much lower scoring the entire time, and not following the same periodic pattern. Its variation as a function of source surface height (grey shaded region) does show that at low source surface height, the GONGz maps can still produce good coronal hole scores. Some intervals in fact show the GONGz optimized score to be the best performing of the PFSS models, most notably during the "active region emergence" phase of encounter 2 (see Section 5.5 conclusion C2).

This bifurcation of scores can be seen in the other encounters coronal hole metric scores. For encounter 2, the timeseries are approximately separated into thirds, with the first and last third corresponding to similar scores as encounter 1 for the ADAPT driven models, while in the middle third the scores suddenly drop to similar scores as compared with the GONGz models. Encounter 3 maintains the bifurcation the whole time and all profiles are very flat. GONGz scores are lower the whole time while the other maps scores are indistinguishable. Additionally, the MHD score (which is not time varying due to the single model run and single EUV observation) may be compared to the time varying scores via the horizontal cyan line. For all encounters, the score is never exceeded by the best PFSS $(2.5R)\odot$) or WSA score. For encounter 2 it is better than all other models and input parameters. In encounters 1 and 3 there are time intervals where different (lower) source surface heights yield scores comparable to or exceeding the MHD value, as indicated by the upper extent of the shading in the figure.

Next, examining the white light metric (bottom row), there are some qualitative simi-

larities and differences to the behavior of the coronal hole scores. For encounters 1 and 3, all models (now including GONGz) follow similar variation in time. The encounter 1 time variation does not show the same periodicity as for the coronal hole metric, instead showing a flat, higher score for the first two-thirds of encounter 1, followed by a sharp drop in score (less pronounced for the MAS model). For encounter 3, a similar drop is observed near the start of the time interval followed by a higher and flat score for the remainder. However, these scores should be interpreted carefully during the first third of encounter 3 since significant portions of the streamer belt were missing due to an issue with the background subtraction (see the animated version of figure A.4 for E3 in the online material). Regions with such artifacts are excluded from the metric computation but deteriorates the reliability by decreasing the number of measurements. Encounter 2, is again distinct from 1 and 3. As with the coronal hole metric, there are distinct thirds of the encounter with the first third having all models having high scores indicating agreement with the observations, followed by a precipitous drop in some models, and a further precipitous, but brief (1-2 days only) drop in all models. It is clear there are sharp changes detected by both metrics in encounter 2 on approximately March 23rd 2019 and April 9th 2019. As will be explored in Section 5.5, encounter 2 did contrast to encounters 1 and 3 in terms of the presence of dynamic solar activity through that time interval.

In situ Polarity Timeseries

We conclude our exposition of the metric score results by examining the *in situ* polarity metric in detail. As mentioned above, this metric is formed by integrating measured and modeled polarity timeseries together and therefore only yield one score per encounter. However, we can examine qualitatively how these scores are formed by examining the timeseries of agreement and disagreement for each model and encounter combination.

This information is encapsulated in figure 2.7. Each panel shows model agreement and disagreement for a given encounter, and given heliospheric spacecraft. For times when the model and data agree, the time series has a colored marker (with color indicating differing models) and is blank if they disagree. For times when there is not *in situ* data available, the markers are colored grey. Therefore, times when the measured and modeled polarities disagree (or equivalently, when the positions of predicted HCS crossings are misaligned with the data) may be identified as gaps in the colored lines on the plot. For the PFSS models, lines for different source surface heights are laid out consecutively (from low to high source surface height). The growth or decay of the white gaps on these consecutive lines indicates if a given HCS crossing improves or worsens with changing source surface height.

Overall, it is clear that most spacecraft data and model HCS combinations agree very well for the vast majority of timestamps, which accounts for the high metric scores. Notable exceptions are with PSP in Encounter 2 and OMNI data for Encounter 3 for which there are much larger gaps in agreement indicating severe misalignment between data and model HCS.

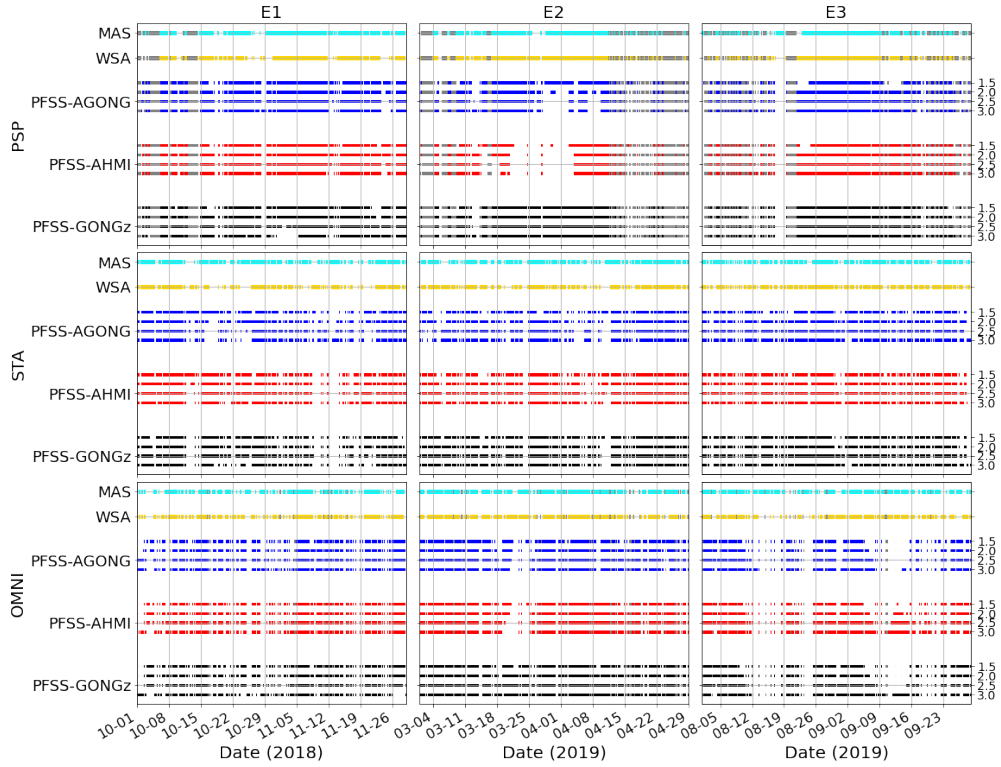

Figure 2.7: *In situ* magnetic polarity and prediction comparison as a function of time for each encounter. Metric 3 produces a single score for each encounter as described in the main text, Section 2.5 so cannot be represented as a timeseries. This figure depicts how the predicted and measured polarity agreed or disagreed as a function of time and therefore produced a high or low metric score. Columns from left to right show encounters 1,2 and 3 respectively, while each row show results from different spacecraft sources: PSP, OMNI and STEREO A respectively. In each panel, results for the different models are shown, following the color scheme from figure 2.5. For the PFSS models, there is a different line of data shown for each source surface height value, ordered from low to high. At an hourly cadence, if the model and measured polarity agree then that point is filled in with the respective color, if the model and measured polarity disagree, that point is left blank, and if *in situ* measurements are missing for a given time, they are colored grey. Therefore, gaps in the lines indicate intervals of disagreement between model and measurement. The larger the fraction of the whole time series which is blank, the lower the resulting metric score reported in figures 2.4 and 2.5.

For the PFSS models, we see that typically the disagreements (blank spaces) occur at the same time *for a given spacecraft in all models* and also usually follow the same qualitative trend as a function of source surface height. This indicates that small misalignments between HCS warps and the empirical data correspond to the same heliographic locations independent of the input magnetogram. The MAS and WSA models sometimes have gaps aligned in time with the PFSS models (for example PSP Encounter 1 10/29, top left panel), but often do not, suggesting the HCS output of these models can be qualitatively different to the PFSS models and sometimes in better agreement with spacecraft data. A very clear example of this is in the top middle panel (E2, PSP) where several large outages in agreement for PFSS models at all source surface heights occur while the MAS and WSA models both correctly predict the polarity of PSP throughout.

The timeseries are usually very different between different spacecraft. The gaps in agreement can occur at different times for a given model. This is not surprising since the spacecraft are at different solar longitudes and crossing the HCS at different times. However, there are also examples where one spacecraft gives much better agreement than another. Encounter 3 is the clearest case of this where results for the OMNI data set show large intervals of disagreement, while PSP and STEREO A have much more continuous agreement (this may be verified by referring to the ordering of the spacecraft scores in the bottom right panel of figure 2.5). Another difference between different spacecraft is that for PSP the agreement overall is much more continuous, while for the 1AU datasets it is more intermittent with agreement switching on and off from one hour to another. This is caused by the relatively larger fluctuation amplitudes and Parker spiral angle in the B_R data at 1AU (OMNI and STEREO A), meaning that the measured timeseries include fluctuations in polarity which do not correspond to current sheet crossings.

This concludes our exposition of the metric scoring results in this work. We next discuss the implications of these results, both on the specific time intervals, models and magnetograms studied here, as well as what they show about this framework for evaluating coronal models.

2.7 Discussion and Conclusions

In this work, we have defined a model-agnostic framework to evaluate and rank coronal models based on their magnetic field topology using three independent sources of observational data. A given coronal model needs only to provide 2D maps of (a) open magnetic field at the photosphere and (b) magnetic polarity at the model outer boundary. Models are given a metric score based on 1) how well they represent coronal holes as observed in EUV data for the relevant Carrington rotation, 2) how well they predict streamer belt topology observed by white light coronagraph observations, 3) how well they predict heliospheric current sheet crossing timing measured *in situ* by various heliospheric spacecraft.

We applied our framework to a dataset of coronal models for the first three encounters of Parker Solar Probe using Potential Field Source Surface (PFSS) models for a range of

source surface heights and input magnetograms, as well as concurrent Wang-Sheeley-Arge (WSA) models and the Magnetohydrodynamic Algorithm outside a Sphere (MAS) models. We carried out three investigations. The first focused on PFSS models only and explored the metric scores as a function of source surface height and choice of magnetogram inner boundary condition. The second compared the PFSS model scores to WSA and MAS scores, evaluating the impact of more physics in the model. The third examined the time evolution of the metric scores in a 60 day interval for each PSP encounter period to look at the stability of the results.

For the PFSS-only investigations, we found :

(A1) *Quality of representation of coronal holes at the photosphere is a function of source surface height:*

Values above 2.5 $R_\odot$ lead to observed coronal holes in EUV not being captured by the model (low precision) regardless of input boundary condition. Values too low can also lead to opening fields in the model which aren't observed in EUV (low recall), although for models driven by the GONGz data product, the best scores occurred for the lowest source surface height. This indicates that for the same source surface height and observation date, ADAPT maps produce more open flux, as was previously observed in [14]. Examining appendix Figure A.1, the optimal score for a given magnetogram occurs when the model and observed boundaries of the polar coronal holes are close together. For ADAPT maps this occurs near $2.0R_\odot$ and below this the polar coronal holes are overexpanded, while for GONGz, the best match is found at $1.5R_\odot$. This suggests the coronal hole metric defined here is sensitive to the polar flux treatment in the input magnetogram. The best F-scores were typically around 60%, requiring both reasonable polar and low latitude coronal hole representation.

(A2) *Representation of streamer belt topology is also strongly dependent on the source surface height of PFSS models, but the dependence is in tension with the coronal hole representation:*

For all magnetogram choices and time intervals, the representation improves monotonically with increasing source surface heights, although with diminishing returns above $2.5R_\odot$. This variation is simply explained by how the warps in the HCS produced by PFSS models are smoothed out with increasing source surface heights. White light Carrington maps of the streamer belt depict a typical low solar activity HCS with warps at most 40 degrees above or below the solar equator.

(A3) *Prediction of HCS crossing times is shown to be only weakly dependent on source surface height.*

This is interesting since we are testing the same model observable as in the streamer belt metric (HCS location), but against a different data source (*in situ* magnetic polarity). While metric (2) is investigating amplitudes of warps in the HCS, this metric is investigating the longitudinal position of these warps along the heliographic equator. Therefore we show that warps in the HCS predicted by PFSS are typically in the correct heliographic

position, regardless of their amplitude, with the correct spacecraft polarity indicated more than 60% of the time and as much as 90% of the time for certain orbits and spacecraft. Is is worth noting that this metric (specifically as applied to 1AU spacecraft) is very similar to the basis for the canonical source surface height of $2.5R_\odot$ established by [69, 68]. We see several examples where this canonical height does give the best polarity score but it is not universally true and the score difference between 2.0 or 2.5 $R_\odot$ is typically very small.

(A4) A "global optimum source surface height" is not in general possible with PFSS models of the solar corona.

Combining our inferences, we see that while it is certainly possible to optimize coronal hole representation, or representation of warps in the HCS, these cannot be achieved simultaneously. This impasse is indicative of the bare-bones physical content of PFSS and provides a simple explanation for why different authors who have focused on different physical coronal signatures [e.g. 69, 100, 5] have arrived at different optimum values for the source surface. Nevertheless, we can also see why PFSS modeling is useful and widely used: with generally accepted source surface height parameters (2.0-2.5 Rs), such models can produce good (if not optimum) metric scores in all 3 metrics. Simultaneous good representation of coronal holes and HCS crossing timing allows for accurate solar wind source mapping and comparison to *in situ* data.

By extending our investigation from PFSS to include other models with additional physics, we found the following :

(B1) *Inclusion of full MHD physics via the MAS model globally improves model scores for metrics (1) and (2), showing MHD predictions of coronal hole locations and general shape of the HCS are more in agreement with observational evidence than PFSS models with any configuration of input parameters.*

This shows, unsurprisingly, that the physics present in MHD does produce a more accurate representation of the magnetic structure of the corona at both the inner and outer boundary. At least for encounter 1, there is a marked asymmetry in the dominant warp in the HCS in the MHD model coming from differential flow velocity [178], providing an example of the physics present in such models that are neglected in potential models.

(B2) *Comparison of WSA results to PFSS shows global improvement in metric 2 (streamer belt representation) but similar results in the other metrics.*

This is not surprising since what WSA adds to PFSS models is a Schatten Current Sheet (SCS) layer, which slightly intersects the PFSS model domain near the source surface. It is thus not expected to drastically change which coronal loops open up to the solar wind, but it does have a strong effect on the HCS beyond the source surface, flattening it. As mentioned earlier, coronagraph observations of the streamer belt show the HCS is flatter or less warped than PFSS models for $R_{ss} \leq 2.0R_S$. Therefore WSA offers a solution to the lack of a global optimum source surface height in PFSS models, while maintaining easy computation: the source surface height could be tuned to optimize coronal hole representation and the WSA

SCS layer would then take care of sufficiently flattening the HCS, allowing both inner and outer model boundary conditions to better match observations.

(B3) *For E1 and E3 metric 3 showed little dependence on the model chosen, and some evidence for MHD improvement for E2 where there was solar activity.*

This indicates that under solar minimum conditions, the location of warps in the HCS in heliographic longitude are fairly accurately reproduced by PFSS models and do not really change with an addition of more physics. The exception to this for our study was encounter 2 where there was significant solar activity and far side evolution in the magnetograms, and therefore less solar-minimum like conditions. Here, the score for specifically Parker Solar Probe was significantly improved in the MHD model, but was also dramatically better in GONGz vs the ADAPT PFSS models. This suggests that this difference may be due to innaccurate modeling of far side evolution in the ADAPT magnetograms as well as a lack of accurate model physics.

Overall, then we conclude that our framework for coronal model evaluation successfully allows comparison between models with very different constituents, and moreover shows expected differences between models with different physical content.

Lastly, the time evolution of the metric scores (where available) showed :

(C1) *Metric scores do evolve in time with a different profile seen for each time interval studied, but profiles are typically very similar between models using the same magnetogram.*

The score ordering between models is therefore preserved as a function of time. This suggests the time evolution is due to new information being introduced into the magnetogram data or remote observations as the Sun rotates which affects the model coronal field in qualitatively the same way between models. This has the implication that far side evolution of the photospheric field, and therefore divergence of the model inner boundary condition from reality, is a fundamental limitation to coronal modeling no matter the physics that is introduced.

(C2) *Far side flux emergence can lead to sudden changes in metric scores.*

The importance of far side evolution is particularly emphasized by PSP encounter 2 (middle column, figure 2.6), where step changes in metric scores are observed (around 2019-03-20 and 2019-04-08). For this specific encounter, there was significant solar activity [165] which evolved and changed the global coronal field while out of view from Earth-based magnetograms, mostly concentrated in two key active regions [AR 12737 and AR12378, 60, 34]. This meant a strong photospheric field concentration rotated on disk twice during this time interval and at this time produced sudden and significant changes in magnetograms. This produced simultaneous sharp changes both in the accuracy of representation of coronal holes, and in representation of the global streamer belt topology (both reductions in accuracy as implied by the metrics defined in this work). This change was also observed as a loss of accuracy in metric 3 (middle column figure 2.7), most dramatically in PSP data but also to some extent in 1AU data, indicating severe distortion to the model HCS topology by this

flux emergence.

(C3) *The agreement between PSP in situ data and the model predictions was typically more continuous than that of STEREO A and OMNI.*

This was illustrated in figure 2.7 and demonstrates a simple advantage of sampling the solar wind closer to the Sun for the application of evaluating coronal models : the amplitude of magnetic vector fluctuations to the base value is reduced and this means a more reliable and continuous measurement of which side of the HCS a given spacecraft is located.

In summary, the focus of this work has been defining a framework for evaluating coronal models using several independent physical observables. A key ingredient was the requirement for models to produce a consistent output (2D maps of the heliospheric current sheet). This means the authors of future coronal models can easily compare to older models and verify if they produce improved results, and if they only improve certain aspects of the coronal field representation of if the improvement is global across different metrics. We demonstrated this with application to a small subset of models centered around the first three Parker Solar Probe perihelia and were able to compare PFSS, WSA and MHD models, investigate the source surface height parameter to PFSS models, and observe the impact of far side evolution and flux emergence on coronal model accuracy.

Having specified this evaluation method, there are many examples of future work that can be tackled. We close with listing a few examples.

This work has entirely focused on 3 time intervals around solar minimum (2018-2019) driven by our use of novel PSP data. As the solar cycle waxes, the behavior of all three metrics on different models will be very interesting to study. For example, it is expected that the accuracy of PFSS models should decay due to the prevalence of non-potential structures in the active Sun, while MHD like models should be more robust.

There is also a wide parameter space of models that should be investigated. The MAS MHD model studied in this work is at the upper end of computational effort and complexity and there are intermediate codes such as PLUTO [130], MS-FLUKSS [160] or AWSoM [213] that could be cross-compared. Even within the MAS framework, several energetics models exist [180] that could be evaluated for impacts on the coronal magnetic structure, thereby allowing these metrics to test different theories of coronal heating and solar wind acceleration. Such investigations could be quite powerful in directly addressing fundamental coronal physics questions.

Further studies of magnetogram-magnetogram comparisons are also clearly motivated by this work. Although we have gone some way towards studying this here through our comparisons of ADAPT-GONG, ADAPT-HMI and GONGz maps applied to the same models, there remain a large number of other magnetogram sources with different polar coronal hole assumptions or different surface flux transport models and different empirical corrections to correct for line of sight or magnetograph saturation effects [e.g. 224]. Additionally, we did not touch here on the question of magnetogram resolution. All maps used here had 1 x 1 degree binning and just by visual inspection of e.g. Figure A.1 we see this is more than

sufficient to pick out detailed structure of both polar and equatorial coronal holes. Nevertheless, both sharper (e.g. HMI) and coarser (e.g. Wilcox Solar Observatory) resolution maps are available. [32] showed how even with potential models, high resolution magnetograms can be used to produce fine-scale coronal structure which is lost at lower resolution. This framework could be used to evaluate the benefit of having increased resolution in terms of matching observational data.

Finally, although not a specific study, a clear further direction for this work is in the creation of an open source tool or web application to perform metric evaluations. This tool could be used by any coronal modeler by submitting the coronal hole and neutral line maps in the format prescribed here and are then presented with the resulting metric scores and supporting plots. While such an integrated software tool is beyond the scope of the current project, we presented in boxes 2.1,2.2 and 2.3 descriptions of the algorithm to produce respective metric score. We also supply the base observational data products to perform the comparisons for the time intervals studied in this work as a Zenodo repository [12] in an effort to allow other modelers to try evaluating this framework on their own models. As well as the specific observational data products, python scripts are included for each metric as examples for loading and plotting the different file types.

Chapter 3

Measurement of the open magnetic flux in the inner heliosphere down to 0.13AU

In the previous chapter, we introduced several metrics and ways of evaluating coronal models specifically analyzing the positions of coronal holes and the shape of the streamer belt. In this chapter, we present the peer reviewed article [15] in which we compare a further specific expectation derived from coronal modeling (the amount of open magnetic flux threading the inner heliosphere) directly with the measurements of the magnetic field strength made by Parker Solar Probe (PSP). Prior results [110] have shown that when the comparison is made with measurement of the field strength in the solar wind close to the earth, the coronal model prediction is significantly lower than what's measured directly. With the launch of PSP to an orbit with a closer perihelion to the sun than ever before, there was an opportunity to test this disconnect and see if it persists closer to the Sun. We find, as presented below, that indeed it does persist and much more conclusively than at 1 au. This shows not only an advantage of getting closer to the sun for testing predictions of the solar magnetic structure (essentially that signal to noise is much reduced as the field strength gets higher) but also highlights a (model-independent) shortcoming in our global coronal modeling methods and highlights a direction for improvement in future development.

The full citation for this work as published is Samuel T. Badman et al. "Measurement of the open magnetic flux in the inner heliosphere down to 0.13 AU". in: *A&A* 650, A18 (June 2021), A18. DOI: 10.1051/0004-6361/202039407. arXiv: 2009.06844 [astro-ph.SR]. The full author list is as follows: Samuel T. Badman, Stuart D. Bale, Alexis P. Rouillard, Trevor A. Bowen, John W. Bonnell, Keith Goetz, Peter R. Harvey, Robert J. MacDowall, David M. Malaspina and Marc Pulupa.

3.1 Abstract

Context: Robustly interpreting sets of in situ spacecraft data of the heliospheric magnetic field (HMF) for the purpose of probing the total unsigned magnetic flux in the heliosphere is critical for constraining global coronal models as well as understanding the large scale structure of the heliosphere itself. The heliospheric flux (Φ_H) is expected to be a spatially conserved quantity with a possible secular dependence on the solar cycle and equal to the measured radial component of the HMF weighted by the square of the measurement's heliographic distance ($B_R R^2$). It is also expected to constitute a direct measurement of the total unsigned magnetic flux escaping the corona (Φ_{open}). Previous work indicates that measurements of Φ_H exceed the value predicted by standard coronal models (the 'open flux problem'). However, the value of the open flux derived from in situ measurements remains uncertain because it depends on the method employed to derive it. Past derivations also pointed towards an increase in Φ_H with heliocentric distance, although this may also be related to its method of computation.

Aims: In this work, we attempt to determine a more robust estimate of the heliospheric magnetic flux (Φ_H) using data from the FIELDS instrument on board Parker Solar Probe (PSP) , to analyse how susceptible it is to overestimation and a dependence on time and space, as well as considering how it compares to simple estimates of Φ_{open} from potential field source surface (PFSS) models.

Methods: We compared computations of the heliospheric magnetic flux using different methods of data processing on magnetic field data from PSP, STEREO A, and Wind. Measured radial trends in fluctuations and background magnetic structure were used to generate synthetic data to analyse their effect on the estimate of $B_R R^2$. The resulting best estimates were computed as a function of time and space and then compared to estimates from PFSS models. *Results:* Radially varying fluctuations of the HMF vector as well as large-scale variations in the inclination of the Parker spiral angle are shown to have a non-trivial effect on the 1D distributions of $B_R R^2$. This causes the standard statistical metrics of the mean and mode (the most probable values) to evolve with radius, independently of the central value about which the vector fluctuates. In particular, the mean systematically underestimates Φ_H for R ¡ 0.8AU and increases close to 1AU. We attempt to mitigate for this by using the 'Parker spiral method' of projecting the vector onto the background Parker spiral direction (which requires vector fluctuations to be evenly distributed about a central value). Even with this method, we find evidence of a small enhancement in flux close to 1AU. The fraction of field which is locally inverted in a given time interval grows with radial distance from the Sun which remains a possible physical reason for this excess but is essentially negligible at PSP's perihelia distances where the impact of fluctuations in general is also much reduced. The Parker spiral method (PSM) and most probable values converge close to the Sun. Our derived best estimate for the time interval studied is $\sim 2.5^{+0.3}_{-0.6}$ nT AU^2. To the extent probed by PSP, no strong dependence on latitude or longitude is apparent, although at 1AU, the spread of measured values appears to grow at the highest latitudes. The best estimate of the heliospheric flux is significantly larger than estimates from PFSS models studied here,

which predict values from 1.2-1.8 nT AU^2, depending on the choice of magnetogram or source surface height.

Conclusion: Of the methods for computing the heliospheric flux over a wide range of heliocentric distances using only magnetic field data considered in this work, the most robust choice is to use the PSM. The decay of fluctuations and weakening importance of local flux inversions at smaller heliocentric distances indicate that the measurement is most accurate close to the sun and that it is justified for us to consider that $\Phi_H \sim \Phi_{open}$ for these measurements. The determined value is too high to be explained via PFSS models. Contemporary magnetohydrodynamic (MHD) models with the same photospheric input are unlikely to close this gap. Therefore, the most likely solutions remain in improvements of coronal models, for example, through improved boundary conditions via the direct measurement of the photospheric field in the solar polar regions or through the inclusion of missing physical processes such as time-dependent or non-potential effects, which can produce a contribution to the open flux that is not rooted in obvious coronal holes.

3.2 Introduction

The coronal magnetic field may be topologically separated into closed field lines, which form loops on coronal length scales that confine coronal plasma, and open field lines, where the dynamic pressure of the out-flowing solar wind dominates over magnetic stresses, thus causing the magnetic field lines to be advected outwards into the heliosphere. Over interplanetary length scales, the solar rotation and radially out-flowing solar wind combine to form the well-established Parker spiral magnetic field [154]. The total unsigned open magnetic flux is the total flux ($|\boldsymbol{B} \cdot d\boldsymbol{S}|$) carried by each open coronal field line, summed over any closed surface encompassing the Sun, but usually integrated over a spherical heliocentric surface. Here, $\boldsymbol{B}$ denotes the coronal or heliospheric magnetic field (HMF) vector, and $d\boldsymbol{S}$ is the differential surface element that the field line intersects. We note the magnitude is taken since the signed open flux cancels out over a closed surface integral, according to Gauss' Law ($\nabla \cdot \boldsymbol{B} = 0$). In this paper, we refer to this integrated quantity as the 'open flux', that is, Φ_{open}.

The open flux is a quantity of significant interest in coronal and heliospheric physics. It determines the HMF field strength, which, in turn, affects the coupling of the solar wind with planetary magnetospheres. It determines the transport properties of cosmic rays through the heliosphere [38]. It has been shown to vary with solar cycle [e.g. 221] and, therefore, it may carry information about the sun's internal dynamo. Finally, given the expected conservation of the quantity, direct measurements of the open flux in interplanetary space, which is the main subject of this paper, can be used to constrain global coronal models for which the open flux is an observable. Typically, interplanetary measurements of Φ_{open} exceed the estimates coming from most global coronal models [the 'open flux problem', 110], with the agreement worsening at solar maximum [220].

As hinted above, there are two typical contexts in which the open flux is computed. The

first is via global coronal models. Such models take maps of the photospheric magnetic field obtained by remote measurements of Zeeman splitting of a photospheric emission line and utilise these boundary conditions to extrapolate a 3D coronal field. The two most common types of global models are the potential field source surface extrapolation [PFSS 4, 186, 223] and magnetohydrodynamics [MHD, e.g. 112].

In PFSS models, the outer boundary of the model (called the source surface) is a sphere at a fixed radius (R_{SS}) at which all intersecting field lines are defined to be radial and open to the solar wind. In MHD models, there is no explicit outer boundary and instead, field lines may be traced and a 'source surface' determined numerically by mapping the region where field lines become radial. The open flux is then computed by integrating the modelled magnetic field $\boldsymbol{B}(R, \theta, \phi)$ over this outer boundary (we note that θ and ϕ here refer to heliographic latitude and longitude, respectively):

$$\Phi_{open} = \int_0^{2\pi} \int_{-\frac{\pi}{2}}^{\frac{\pi}{2}} |B_R(\theta, \phi, R = R_{SS})| R_{SS}^2 \sin\theta d\theta d\phi. \tag{3.1}$$

Both PFSS and MHD models produce similar [173] coronal fields which conform to the standard paradigm that open field lines are rooted in coronal holes, which are dark regions observed on the solar disk at extreme ultraviolet (EUV) wavelengths. This correspondence supplies an observational constraint on such models, namely, the assumption that the footpoints of open field lines must correspond to the observed EUV coronal holes. A good agreement, at least for PFSS models, usually requires the source surface height to be in the range of $1.8 - 2.5 R_\odot$ [e.g. 100, 14, 170]. A complementary method motivated by this required correspondence is to empirically measure coronal hole boundaries in EUV imagery and simply sum the photospheric flux within these contours; [220] showed such estimates are in good agreement with the modelled values of Φ_{open}.

The second context in which open flux is estimated is with the use of collections of single point in situ measurements of the HMF. While a set of single-point measurements confined along a spacecraft trajectory may at first appear to constitute a very weak statement on the state of the whole heliosphere, it is, in fact, extremely powerful due to two key symmetries: the first is that in the [154] model of the HMF, the radial component of the magnetic field along a streamline (θ, ϕ) varies as $B_R(R, \theta, \phi) = B_0(\theta, \phi)(R_0/R)^2$, and, thus, the quantity $B_R R^2$ is independent of radius. The second is one of the seminal results [194, 195] of the Ulysses mission [126], namely, that $B_R R^2$ is independent of latitude (ϕ). Thus, the total unsigned magnetic flux threading a sphere at an arbitrary radius, R_S, in the heliosphere, Φ_H, may be computed as

$$\Phi_H(R_S) = 2R^2 \int_0^{2\pi} |B_R(\phi, R = R_S)| d\phi, \tag{3.2}$$

where the modulus sign is not strictly a correct operation due to the curvature of the Parker spiral. The modulus here really represents assigning the opposite sign to the flux

contribution of field-lines in sunward (S) versus anti-sunward (AS) sectors. The longitudinal variation and this modulus operation are typically approximated with an (as yet ill-defined) 'averaging' procedure, ultimately giving:

$$\Phi_H = 4\pi R^2 < B_R(R = R_S) >, \tag{3.3}$$

which illustrates that single-point measurements of the HMF (in particular the radial field) are actually extremely powerful and in principle allow an estimate of the magnetic flux in the heliosphere. We note that we have purposefully introduced a new symbol to refer to the flux in the heliosphere (Φ_H) in order to allow for the possibility that deviations from the Parker spiral model may result in $\Phi_{open} \neq \Phi_H$. We will also, throughout this paper, normalise these Φ quantities (with nominal units of Webers) by 4π (1AU)^2, which transforms them to units of nT AU^2 and gives them the intuitive meaning of 'magnetic flux density at 1AU'; the magnitude of which is almost exclusively confined to the range $0 - 10$ nT AU^2.

The possibility that $\Phi_{open} \neq \Phi_H$ is motivated by observations by [149] of a possible enhancement of Φ_H with radius, related in past studies to the effect of velocity shears causing warps in the magnetic field [115, 116, 117], and more general local field inversions identified by intervals of sunward electron heat flux [150], which have been shown to become more prevalent with the distance from the sun [120]. Such an overestimation is a compelling possibility due to the open flux problem, which could, in principle, be explained if the overestimation is large enough.

On the other hand, a similar enhancement with radius has been shown to occur artificially due to issues with the definition of the 'averaging' procedure [193]. Typically, averaging for the purposes of computing Φ_H has two critical components. The first is a 'pre-averaging' timescale which is performed on the raw, signed B_R data to produce a base data product. The longer this timescale, the more magnetic sectors cancel out and the distribution of B_R gets closer to zero. To some extent this is a physical operation to get rid of very rapid fluctuations but at some ill-defined timescale will result in artificially low values of B_R - it is clearly desirable for any open flux estimation method to be independent of averaging timescale. The second step [e.g. 149] is to arrest further cancellation by, for example, taking the modulus and averaging this over Carrington rotations to obtain a longitudinal average. This modulus operation, in particular, due to the rectification of inverted field when taking the modulus of B_R was shown by [193] to result in an increase in apparent values of $B_R R^2$ with increasing radius, even in the fast polar coronal hole wind measured by Ulysses at solar minimum, under which conditions kinematic effects and local field inversions are less prevalent.

[47] and [46] proposed avoiding the rectification issue by utilising 2D vector distributions of the field and identifying that these populations are bi-modal and corresponding to anti-sunward and sunward sectors aligned along the Parker spiral. By measuring the field strength along this Parker spiral direction before projecting into the radial direction, these authors showed that the excess flux measured at Ulysses as compared to 1AU data over two solar

cycles was much reduced and the corrected values followed the same large-scale variation with solar cycle as measured at 1AU. Throughout this paper, we refer to this technique as the 'Parker spiral method' (PSM). It is important to note, however, these authors still made the choice to use a 'pre-averaging' timescale of six hours for their time series of B_R (and orthogonal Cartesian component B_T) prior to making this Parker spiral projection.

[150] investigated the impact of pre-averaging on this method and standard averaging of $|B_R|$, in addition to comparing them both to the kinematic and local inversion methods on 1AU data. They showed that this 'pre-averaging' timescale affected the PSM-derived values of Φ_H as well as for standard averaging. [150] also showed, with the caveat that all their data was from 1AU, that: (1) the local inversion method was equivalent to the $|B_R|$ and PSM methods performed on pre-averaged data at a 1 day timescale; (2) with smaller pre-averaging timescales, the PSM method produced lower estimates for Φ_H than the $|B_R|$ method, while for higher pre-averaging timescales, the two methods produced similar estimates. The reason for the dependence of the PSM value on the pre-averaging timescale is due to a very important subtlety with regard to all the implementation of the PSM and pre-averaging on the part of the authors above. Namely, the pre-averaging they employ is applied to the 3D HMF vector in Cartesian coordinates and the resulting averaged-down Cartesian time series are what is used to perform the projection onto the Parker spiral. However, as explored in Appendix B.3, averaging in the Cartesian basis strongly distorts the 2D distribution of vector field measurements due to fact that the Cartesian components are correlated by fluctuations, which are predominantly spherical in nature. This issue can be better addressed by parameterising the vector field in polar coordinates before any pre-averaging is done. We return to this point when we introduce our implementation of the PSM in Section 3.3.

Whether artificial or physical, establishing whether the measurements of Φ_H is an over-estimation is of key importance for the open-flux problem in order to detect whether $\Phi_H = \Phi_{open}$ and, thus, whether this can serve as a real constraint on coronal models. In this paper, we aim to utilise new Parker Solar Probe (PSP) observations at an unprecedented range of heliocentric distances, together with corresponding observations at 1AU, to study the variation of Φ_H throughout the inner heliosphere, assess the dependence on the processing technique, and determine how these measurements contribute to the discussion of the open flux problem. In Section 5.3, we introduce the data set and the different methods that are used to estimate Φ_H. We utilise synthetic data to examine how these different methods are affected by radial trends in the background field and fluctuations. In Section 3.4 we show the results of measurements of Φ_H throughout the inner heliosphere, assess the possible contribution of inverted flux to these measurements and compare them with estimates of the open flux derived with PFSS models. In Section 3.5, we discuss the implications of these results. Finally, in Section 3.6 we summarise our main conclusions.

3.3 Observations and methods

Spacecraft data summary

The Parker Solar Probe [PSP; 52] was launched on August 2018 into a highly elliptical heliocentric orbit with an inclination of $\sim 4^o$ to the solar equatorial plane. With a sequence of Venus gravity assists, PSP's perihelion distance decreases over the course of the mission. As of November 2020, PSP has completed six orbits with its first three perihelia at $35.7R_\odot$ (0.166 AU), and its fourth and fifth both at $27.8R_\odot$ (0.129 AU). The most recent perihelion was even closer at 20.4 $R_\odot$ (0.09 AU). Thus PSP provides measurements of the heliospheric magnetic field more than twice as close to the Sun as the previous record holder, Helios, at $65R_\odot$ (0.3AU). In addition to this unprecedented radial evolution, PSP also samples longitudinal structure in a unique way: as the PSP approaches perihelion, its orbital velocity increases faster than the co-rotation velocity of the Sun and, as a result, it crosses a threshold, where it first co-rotates and then super-rotates with respect to the solar photosphere. The upshot of this is that PSP samples longitudinal variation very slowly, with two intervals of co-rotation (inbound and outbound) where it measures the same solar wind for an extended period. The downside to this is that each PSP perihelion probes only a small range of solar longitude, although data from its cruise phase at larger heliocentric distances provides measurements all around the Sun.

In this work, we utilise DC magnetic field data from the FIELDS instrument [19] [1] from orbits 1-5 of PSP, spanning from August 2018 to July 2020 (data from orbit 6 will soon be available and allow for a further extension of the present study). We utilise the full time-series of the one minute (1 min) averaged data product (B_RTN_1min), in addition to producing histograms of the four-samples-per-cycle (∼4.6 Hz) data product (B_RTN_4_per_cyc) over hour-long and day-long timescales. These data utilise the inertial Radial-Tangential-Normal (RTN) coordinate system, with the R component indicating the radial direction at the spacecraft position, the T component defined as the cross product of the radial direction with the solar rotation axis, and the N component completing the orthogonal triad. In terms of heliographic coordinates, T points along a line of constant solar latitude (ϕ) and N points along lines of constant solar longitude (θ). While B_R is the main vector component of interest in this paper, as discussed at length in Sections 3.3-3.3, knowledge of the full 3D vector is key to understanding the evolution of individual components. Here, we also introduce the angular quantity α, which we refer to as the 'clock angle', which is the angle the HMF vector makes with the radial direction when projected into the R-T plane.

The data from PSP and the near-1AU spacecraft considered in this study are summarised in Figure 3.1. Here, each panel is a 2D histogram of data value on the y-axis and time on the x-axis. The time axis is binned into one day intervals and each column of histogram data shows the distribution of the full resolution data set for each of these intervals. A solid black line threads the modal value of the data and indicates which side of the heliospheric current sheet (HCS) PSP was located on each day. Dashed magenta lines indicate the times

[1] Data publicly available at `https://fields.ssl.berkeley.edu/data/`

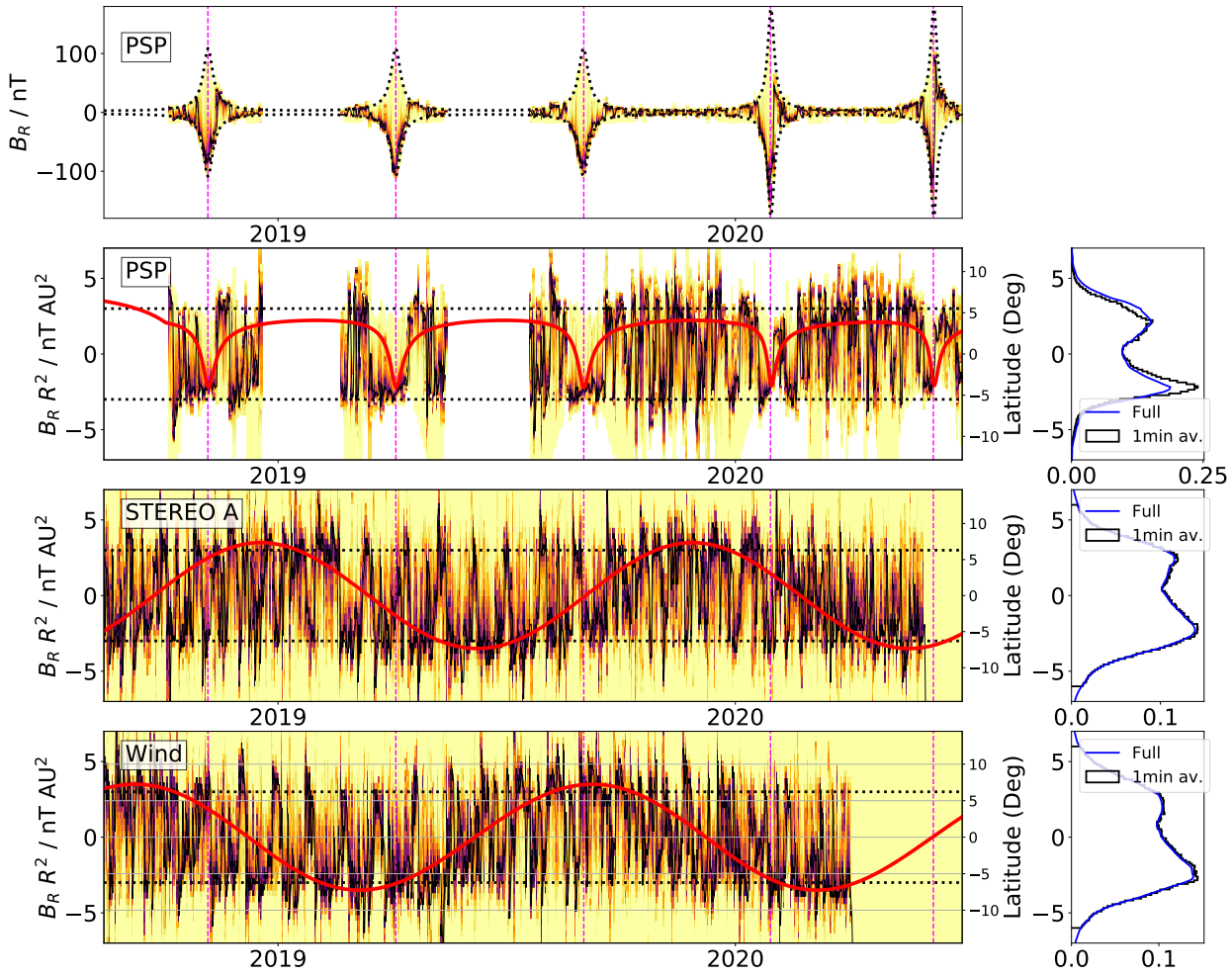

Figure 3.1: Summary of the in situ magnetic field data analysed in this paper. In each panel, the shading is a 2D histogram with the x-axis in 1 day bins. A black solid line threads the histograms and shows the mode of each day. The top panel shows the raw radial magnetic field measured by PSP. Magenta dashed vertical lines indicate successive perihelia of PSP. A faint dotted black line indicates an envelope (3nT (1AU/R^2)) which communicates PSP's changing heliocentric distance. The remaining three rows show the quantity $B_R R^2$ as measured by PSP, STEREO A and Wind respectively. The dotted horizontal line is the same envelope from the top panel scaled by R^2. In each panel, a solid red curve shows the spacecraft latitude. The polarity sampled is controlled primarily by the latitude. Panels on the right are 1D histograms which show in black (blue) the distributions of the 1 min average (full cadence) data of $B_R R^2$ summed over time.

of perihelia and allow reference to the other panels. The colour scale of the histograms

(light to dark) shows the density of measurement (low to high). The top panel shows PSP's measurements of the radial component (B_R) of the Heliospheric Magnetic Field (HMF). A dotted envelope showing $B_R = \pm 3nT(1AU/R^2)$ bounds the data and reveals that, as expected, the predominant variation in this component is proportional to $1/R^2$. It also highlights the lower perihelia distances of orbits 4 and 5, where the envelope and data range gets larger than during orbits 1 through 3. We can also clearly see that no matter which side of the HCS the PSP is located on any given day, there is a non-negligible population of field measurements of the opposite polarity. Particularly at the closest approach, this corresponds to the prominent switchbacks, which were a key early discovery of the PSP [e.g. 18, 81, 45, 72]. The remaining rows show the quantity of principal interest in this paper, $B_R R^2$, displayed in the same histogram format over the investigated time interval as measured by PSP/FIELDS, the IMPACT/MAG [118] instrument on STEREO AHEAD [78] and the MFI investigation [103] on the *Wind* [62] spacecraft. In these latter three panels, a solid red line shows the variation of each spacecraft's heliographic latitude with time. We note PSP's minimum latitude and minimum heliocentric distance are closely related.

Finally, to demonstrate the relation between the full cadence and one minute (1 min) average data products used in this work, 1D histograms of both data products are shown overlaid in a series of inset panels on the right. For 1AU, the distributions are virtually identical. For PSP, the one minute average distribution is slightly distorted compared to the four-samples-per-cycle data. In particular, the positive tail of values is foreshortened by the 1 min averaging data but the peak values are unchanged. Thus, we look to use the more pristine faster cadence data product where possible, however, we argue the distributions are similar, especially with regard to the data set of negative polarity, such that using the 1 min average data where necessary will not present an issue. For computational tractability, the 1 min averaged data will be used when considering the whole set of five orbits, while the higher cadence data will be used when considering one-hour or one-day intervals of data.

From the top panel, the data coverage is immediately apparent, demonstrating that there is no PSP/FIELDS data outside of the 'encounter' phases of encounters one, two, and three, while for orbits 3 to 5, there is continuous data coverage. At all three spacecraft, there is a striking correlation between latitude variation and dominant measured polarity: When the spacecraft are at their minimum (maximum) latitudes, they are more likely to be southwards (northwards) of the HCS and, therefore, more often measuring negative (positive) polarities for B_R. For STEREO A and Wind, whose orbits have a constant angular velocity with respect to the solar co-rotating frame, the variation from two timescales is immediately apparent: slow annual latitude variation and regular HCS crossings due to the $\sim$ 27 day Carrington rotation period. For PSP, at its closest approach, it can be seen that a single dominant polarity is measured for extended periods of time while PSP is close to co-rotation with the Sun, whereas for the aphelion periods between the latter orbits, the familiar Carrington rotation pattern reappears.

A dotted line at $\pm$ 3nT AU^2 in the latter three panels shows the same envelope as in the top panel with the radial variation scaled out. Zooming in this way, we see the 1AU spacecraft regularly measuring values of $B_R R^2$ exceeding this value, while PSP's measure-

ments are generally below this value, especially during the perihelia. While it is clear $B_R R^2$ is approximately of constant magnitude and similar in value at all three spacecraft, there is significant scatter and temporal variation. The remainder of this paper is concerned with analysing these distributions of $B_R R^2$ and the full HMF vector to justify a statistical 'background' value and obtain a best estimate of Φ_H. We assess the extent to which it is conserved throughout the inner heliosphere and, finally, how it compares to estimates from PFSS models.

Radial evolution

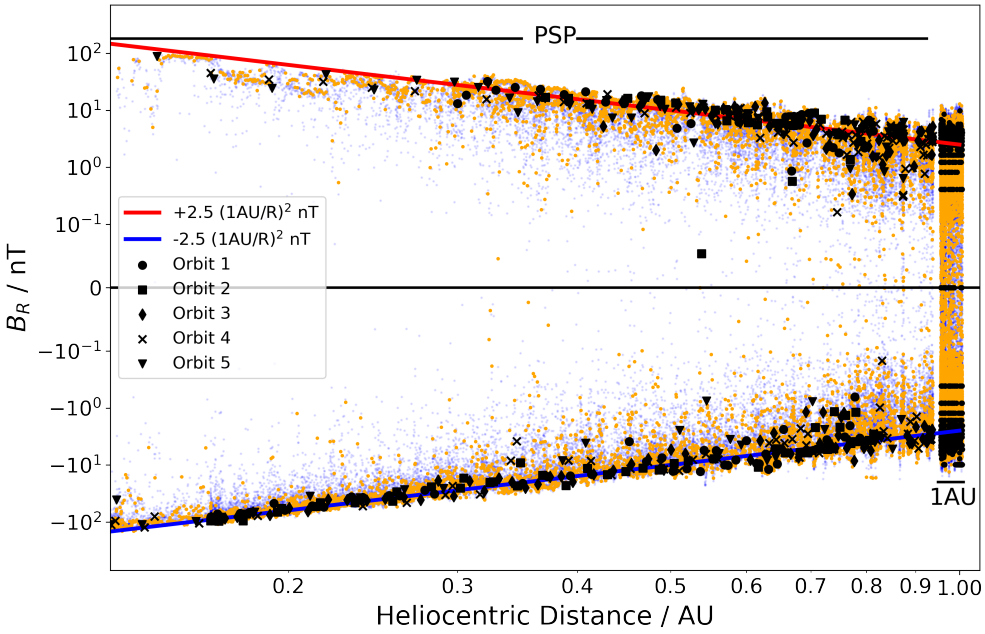

Figure 3.2: Radial scaling of B_R. All the data from Figure 3.1 is re-plotted against radius on a symmetric log - log scale. Data with $|B_R| < 0.1nT$ is plotted on a linear scale, which accounts for the block of data passing through zero near 1AU. One-minute averages are plotted in faint magenta. One-hour modes are shown in orange. One-day modes are shown in black with different symbols differentiating the subsequent orbits. We note that orbits 4 and 5 (crosses and triangles) extend to lower radii than orbits 1 to 3. A 2.5nT $(1AU/R)^2$ trend line is plotted for positive (red) and negative (blue) polarities. A small data gap shows the narrow gap in radial coverage between PSP's aphelia and STEREO A's perihelia.

We first consider the radial variation of B_R directly to confirm the $1/R^2$ transformation

is appropriate for the full data set. The measurements as a function of radius are plotted in Figure 3.2 on a log-log scale. Faint blue dots show the spread of the 1 min averages of B_R from PSP's first five orbits (the lower cadence 'raw' data), while orange dots show the most probable value of B_R for each hour, demonstrating the most probable values of the raw data cluster on a $1/\mathrm{R}^2$ trend line. The black markers indicate the most probable values for each day and the different shaped markers represent the different orbits and are shown to include a data product which is sparse enough for the reader to see the difference between the different PSP encounters. Solid red and blue lines show $\pm 2.5nT(1AU/R)^2$ trend lines. While these trend lines are not fitted and serve here only as a visual aid, as we show in Section 3.4, $\Phi_H = B_R R^2 = 2.5\mathrm{nT\ AU}^2$ actually turns out to be the best estimate for this data set. It is worth noting that while the 1AU data appears to be significantly more spread than the PSP data, this is mostly a distortion due to the combined effects of the higher data density resulting from the limited radial variation of these spacecraft, the symmetric log scale, and the population of vectors where the full field vector fluctuates into the radial direction, such that $B_R = |B|$ instantaneously; at 1AU, $|B|$ is significantly larger than the background B_R value.

This effect aside, we observe: (1) the radial component of the field indeed varies as $1/R^2$ for all radii probed by PSP to date. (2) the scatter around the trend line is proportionally smallest at the closest in heliocentric distances. It is also systematically skewed towards zero but this is not trivial to observe on the log scale. (3) Orbits four and five show a significant departure from the trend line towards weaker field strengths, particularly on the positive field branch around 0.2AU. This is likely due to PSP running very close to a very flat heliospheric current sheet during these latter orbits (Chen et al., submitted to this issue), and thus sampling more weakly magnetised streamer belt plasma. We conclude using (1), that the quantity $B_R R^2$ is a useful quantity which is, at least approximately, conserved throughout PSP's mission so far. There is no suggestion of a break down of the Parker expectation or the Ulysses result of latitudinally isotropised radial magnetic field and suggests the dipole-dominated coronal field has fully relaxed into this isotropic state, which is well within PSP's closest heliocentric distance of $28R_\odot$.

Radial evolution of the distribution of magnetic flux

With the investigation of the quantity $B_R R^2$ remaining well-motivated, we turn our attention to measuring it directly. A key assumption made in displaying the data above, as we have done so far, is to show the most probable value of the field. That is, we take all the data from some time interval or other binning procedure, produce a distribution of that binned data, and assume the peak of that distribution (the bin with highest number of counts) represents the value we are trying to measure.

In Figure 3.3, we demonstrate how the field is distributed in the R-T plane at different heliocentric distances. We very coarsely bin all the data shown in Figure 3.1 into four categories: PSP data for $\mathrm{R} < 0.3$ AU (specifically, PSP data interior to the closest perihelia of Helios), PSP data for $0.3\mathrm{AU} < \mathrm{R} < 0.6\mathrm{AU}$, $0.6 < \mathrm{R} < 0.95$ AU, and finally, all the STEREO A

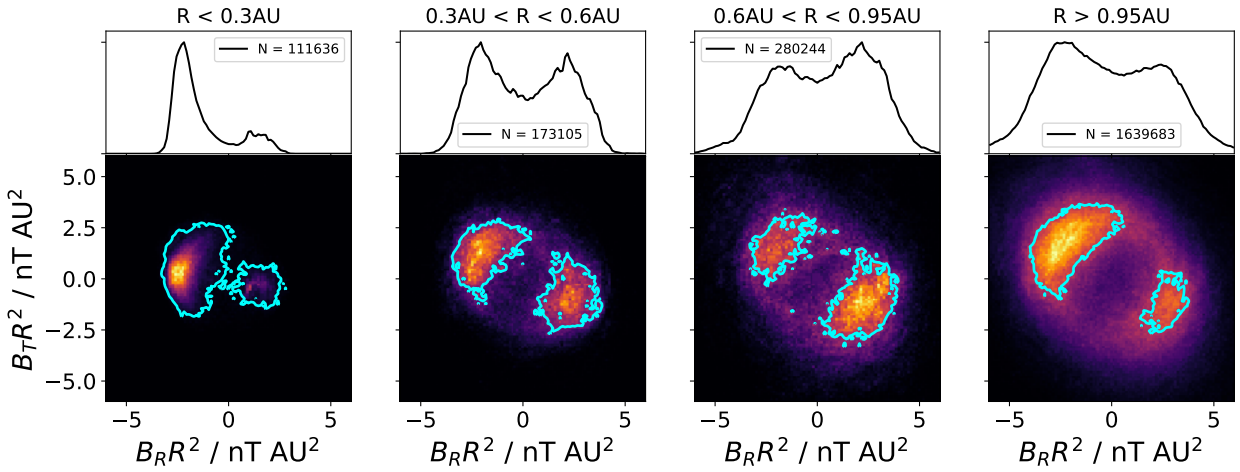

Figure 3.3: Radially evolving distribution of $B_R R^2$. Each panel in the bottom row contains 2D histograms of $B_T R^2$ versus $B_R R^2$, which show the distribution of the field in the RT plane in a given radial bin, indicated for each column. The cyan contour depicts the 90th percentiles of the data. The top row show the resulting 1D distribution of $B_R R^2$. The legend gives the number of data points (1 min averages) in each radial bin. We note the left three columns are from PSP data, while the right hand panel is the summation of two years of Wind and STEREO A data

and Wind data (for which R ¿ 0.95 AU). The data shown here reflect the 1 min averages due to the aforementioned computational tractability issues when working with the whole data set. The top panel for each radial bin shows the 1D distribution of $B_R R^2$, the bottom panel shows 2D distributions of $B_T R^2$,$B_R R^2$. We note that we have made a replacement here, namely, $B_R = |B| \cos\alpha$ and $B_T = |B| \sin\alpha$. Here, $|B| = \sqrt{B_R^2 + B_T^2 + B_N^2}$ is the field magnitude and $\alpha = \arctan 2(B_T, B_R)$ is the field vector angle of rotation in the R-T plane relative to the radial direction, and will be referred to as the 'clock angle'. This transformation is discussed in Appendix B.1. It is done to avoid the effect of projecting fluctuations in the normal direction onto the R-T plane, which can lead to an underestimation in field magnitude. In particular, here we are assuming the normal, tangential, and compressive fluctuations are uncorrelated, and so making this correction to the R-T components does not affect the $|B|$ and α distributions.

We also note that in Figure 3.3, the two peaks values are asymmetric. This is simply a sampling effect based on the spacecraft orbit (especially the heliographic latitude). For example, PSP's orbit is tilted with respect to the solar equatorial plane such that at closest approach, it is also approximately at its minimum (and most negative) latitude. For this reason, PSP for R ¡ 0.3 AU is primarily southwards of the HCS and, therefore, it samples a negative-polarity magnetic field. We can confirm this via an inspection of the second panel of Figure 3.1 in which the dips where PSP goes into negative latitudes correspond to protracted

measurements of negative polarity.

Figure 3.3 shows that the 1D distributions of $B_R R^2$ are the projection of a 2D bi-modal distribution which evolves with radius. This 2D distribution is aligned with a mean Parker spiral direction which becomes closer to radial with decreasing heliocentric distance. The distributions comprise of a sunward (upper left quadrant) and anti-sunward (lower right quadrant) population, and exhibiting some spread in field magnitude ($|B|$) and angle (α) about this mean state. Empirically, these spreads decrease with heliocentric distance and this trend will be quantified in Section 3.3. Further from the Sun, an overlap of the two populations sum together to distort the 1D distribution of $B_R R^2$ by producing a large population of values with $B_R R^2$ close to zero. This effect is much weaker close to the Sun, with the two peaks in the 1D distribution much sharper and better isolated.

In this work, we use distributions of raw (meaning minimally pre-averaged) $B_R R^2$ and $B_T R^2$ measurements, such as those illustrated in Figure 3.3, to produce estimates of the heliospheric flux. We consider three particular methods: the mean, the mode, and the Parker spiral method. The mean and mode are performed directly on the 1D $B_R R^2$ distributions. The mode simply identifies the bin with the most counts for either $B_R > 0$ or $B_R < 0$. For the mean, we take the bi-modal 1D distributions and bifurcate it into two truncated distributions, $B_R > 0$ and $B_R < 0$, and the mean of each is taken. At certain points in this work, we consider one-hour or one-day intervals of data. For these cases, the distributions are usually single-peaked (only one magnetic sector explored) and, therefore, the procedure we follow is to identify the single most probable value for that hour or day and then we use the sign of this value to decide which side of the distribution to truncate. The Parker spiral method utilises the full 2D distribution, which we introduce and describe below.

Considering the 1D distributions we see at all radii, the shape of each half of the distribution is asymmetric (or 'skewed'), meaning that the production of a best estimate of the quantity is not obvious given the mean and mode are non-trivially related (and the dependence of their relationship on radius). The mean in particular is sensitive to the 'overlap' of the two sectors. In the simplest approach [e.g. 149, 110, 220], the modulus of the distribution is taken before computing the mean, which is similar to the truncation procedure we described above. In this method, the larger the 'overlap' population relative to the peak, the higher the mean. Given that this overlap population grows with heliocentric distance (see Figure 3.3 above and also [47]), this may cause the apparent heliospheric flux to grow with radius when this method is used [193].

In a more careful treatment of the bi-modal population, we would need to subtract the population of the opposing sector, for example, by fitting a curve to the distribution, or to make another approximation, such as bisecting the data in the 2D distribution with an approximate Parker spiral, and to assume that no data fluctuates past 90 degrees from the mean Parker spiral direction [46]. An even more sophisticated approach would be to use the electron heat flux to delineate these two populations such that intervals where the electron heat flux is parallel (anti-parallel) to the magnetic field correspond to anti-sunward (sunward) sectors (see Section 3.2 of [120]). As mentioned at several points in this work, this application of the electron strahl remains an important avenue for exploring additions

to the analysis we describe here. We omit the usage of electron strahl measurements due to the more intermittent temporal coverage of solar wind plasma measurements by the PSP Solar Wind Electrons Alpha and Protons (SWEAP) instrument [83] as compared to the full FIELDS data set analysed here.

The mode is more robust in that it is less affected by the two sectors overlapping and has the advantage that it can easily be defined for both sunward and anti-sunward sectors. It is still possible the overlapping populations could change the peak value somewhat. The mode also requires a large sample size in order to be well-defined and can have a large error when computed from a distribution with a flattened peak. In all these regards, we see the mode is better defined for the distribution of $B_R R^2$ closer to the Sun, where the peaks are narrower and the impact of overlap from the positive sector is very weak.

In light of these subtleties, [47] proposed utilising the apparent symmetry in the 2D distributions directly by projecting the data along the nominal Parker spiral direction, computing the mean of data along this direction and projecting this into the radial direction to obtain a best estimate of Φ_H. As shown by the shape of the 2D distributions in Fig 3., this approach is supported by PSP data and even more so close to the sun where the peak in the 2D distributions become very sharply defined (even though, for this data set, they are predominantly in the sunward sector). Moving forward, we refer to this technique as the 'Parker spiral method', or 'PSM'. In this work, we use an empirically measured Parker spiral angle rather than the ideal angle generated with a solar wind velocity as done by [47]. This choice is made because, as mentioned above, the solar wind velocity data set is a subset of the magnetic field data set from PSP that is due to differing instrument operation schedules and constraints. Thus, it is desirable to use a method which can be performed purely with magnetic field observations. Furthermore, the Parker spiral is an idealised model and, in fact, driving a model with a varying solar wind velocity leads to some unphysical inferences, such as slower wind streams overlapping with faster ones (which form stream interaction regions in more realistic simulations). Additionally, recent observations by PSP [81] call into question the Parker spiral assumption that the solar wind velocity flow is purely radial at distances probed by PSP so far. By empirically estimating the background vector field, we avoid the need to assume an exact Parker model or to use more sophisticated models. Finally, an empirical Parker spiral angle allows us to work directly with the vector in a spherical representation when implementing the PSM, which is preferable to the Cartesian representation, as described below.

To implement the PSM, we form 1D distributions of —B— and the clock angle (α) which underlie the 2D distributions in the R-T plane shown in Figure 3.3 and measure the most probable value of these quantities, B_0, α_0. When the distributions are bi-modal, a most probable sunward and anti-sunward value of α_0 is found. The most probable values are computed by identifying the bins of these 1D distributions of $|B|$ and α with the most counts. Then the estimate of Φ_H for the PSM is derived as $\Phi_H = B_0 \cos\alpha_0 R^2$ where R is the spacecraft heliocentric distance relevant to that distribution. The separation of these 2D distributions into 1D magnitude and angle distributions are illustrated in Figures B.2 and B.3 in Appendix B.

Is is important to discuss the effect of pre-averaging on our different estimation methods. When the HMF vector field is pre-averaged in Cartesian coordinates, the whole 3D distribution is deformed by more and more aggressive time-averaging and this procedure affects all the methods, including the PSM and the mode. In particular, the effect on bi-modal distributions is to shift the peaks towards zero, causing estimates of the heliospheric flux to decrease, as observed for all methods by [150]. In terms of the 2D distributions depicted in Figure 3.3, the effect of longer pre-averaging on the raw data would be to shrink the whole annulus of data towards the centre (see Appendix B.3). In terms of quantifying this, [150] showed one hour and one day averages produced significantly lower values of Φ_H (a reduction of $\sim 20\%$, although this only applies to 1AU data) and we should note that [47] used a six-hour average for their PSM implementation. In this work, we attempt to avoid pre-averaging issues primarily by applying our estimation methods to distributions of 1 min averaged or higher cadence data such that our vector distributions are minimally distorted. However, we also note one very important characteristic of our PSM implementation is that we parameterise our vector field in spherical coordinates at very high time resolution. The resulting parameterised distributions are evenly distributed about a central value for most radii. This means that as long as the field stays in one sector (sunward or anti-sunward) for most of each averaging window, these time series of $|B|$ and α should be able to be arbitrarily "pre-averaged" without affecting the results. This is demonstrated with STEREO A data in Appendix B.3. As mentioned above, use of the electron strahl would be a robust way to delineate the sectors a given HMF measurement belongs to.

We reiterate here that in certain parts of this work, our flux estimation methods are applied: (1) to data over one-hour intervals; (2) data over one-day intervals; (3) data from the full mission binned by heliographic location. For case (3), there are sufficient data points using 1 min averages to establish robust histograms to study. For cases (1) and (2), we utilise the four-samples-per-cycle PSP/FIELDS data product, providing N = 16500 data points for each hour and over 400,000 for each day, ensuring well-formed histograms for these cases too. We next move on to compare and contrast our different estimation methods introduced above, starting by applying them to an idealised synthetic data set.

The impact of vector fluctuations on the flux distribution

To investigate how the underlying 2D distribution of magnetic field data affects the statistics of the 1D distributions of $B_R R^2$ and how this affects our different ways of measuring Φ_H introduced in the previous section, we begin by producing a synthetic data set. Motivated by [47], we suggest that the 2D field be modelled in a polar representation as a set of normally distributed fluctuations in vector magnitude ($|B|$) and R-T clock angle (α) with standard deviations $\sigma_{|B|}$ and σ_α, respectively, which may be thought of as encoding the relative balance of compressive and rotational (or Alfvénic) fluctuations respectively. It is important to state we are making a strong assumption that fluctuations are evenly distributed about an average value which also corresponds to the mode and the 'central value'. This assumption allows us to establish a set of quantities ($|B_0|$, α_0, and $B_{R0} = |B_0| \cos \alpha_0$), which can be defined as

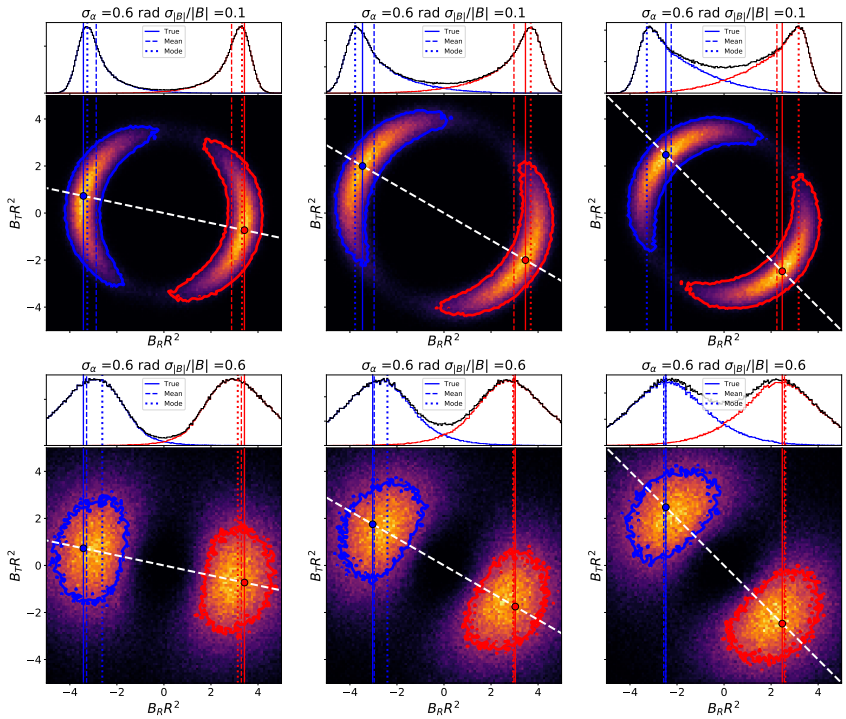

Figure 3.4: Synthetically constructed 2D and 1D distributions of HMF vector measurements and resulting statistics. Similarly to Figure 3, each panel shows a 2D synthetic distribution of $B_T R^2$ - $B_R R^2$ drawn (see main text) from a mean value and standard deviation in clock angle (α) and field magnitude ($|B|$). A separate distribution for sunward (S) and Anti-sunward (AS) sectors are drawn. The colour-map shows the full distribution, and blue and red contours show the 90th percentile of the S and AS sectors. A white dashed line depicts the mean clock angle. The text above each panel describes the standard deviation in angle in radians and field magnitude normalised by mean field (we note that both are dimensionless such that their relative balance is apparent). Red and blue circles indicate the AS and S central ('true') values, respectively. Above each panel is the resulting 1D distribution, with blue and red curves showing the individual distributions and black showing the joint distribution. Solid, dotted, and dashed lines show the results of the PSM, the distribution mode, and the distribution mean as measured from that distribution, respectively. The top row shows the case for fluctuations in the clock angle dominating over fluctuations in magnitude, while the bottom row shows balanced fluctuations. From left to right, the mean clock angle increases from 12^o to 45^o, which is approximately the range of angles probed by PSP as its heliocentric distance varies.

a 'ground truth', and which the PSM measures directly by our method of constructing this synthetic data.

In Figure 3.4, we generate ensembles of synthetic measurements by drawing from normal distributions using the `random` module in the `numpy` library [61] in python over a range of background clock angles and fluctuations, and project them into synthetic 1D $B_R R^2$ distributions as in Figure 3.3. Because we generate the sunward and anti-sunward sectors separately, we can keep track of the individual distributions (red and blue curves) and see how they add up to give the overall distribution. It is immediately apparent that the overlap grows with radius simply because of the increase in the Parker spiral angle [c.f. 47, 46].

We note that for a central value of $|B_0|$, the dimensionless quantity $\sigma_{|B|}/|B_0|$ is a useful figure of merit which may be compared to σ_α, as expressed in radians to describe the balance of fluctuations. In the top row of Figure 3.4, distributions dominated by rotational fluctuations at various background clock angles (α_0, as indicated by the white dashed line) are shown, while in the bottom row, compressive and rotational fluctuations are balanced. By comparing Figures 3.3 and 3.4, we can see that the 'boomerang' shapes of fluctuations dominated by rotations are heuristically more similar to the real PSP data. This will be established quantitatively in the next section.

As expected, the Parker spiral method exactly reproduces the 'ground truth' as indicated by the blue and red circles aligned with the spiral direction in the 2D distributions. The solid (red or blue) vertical lines indicate the value of Φ_H that would be measured by the Parker spiral method, and that link the 2D and 1D distributions. Dotted and dashed vertical lines respectively respectively show the measured mode and mean based on the 1D summed distribution (black curve). The mean for both positive and negative sectors is computed by truncating the distributions at $B_R R^2 = 0$, as discussed in Section 3.3. To be clear, these operations are applied directly to the distributions depicted here which represent the 'pre-averaged' or base data product. At all points in dealing with real data, the maximally pre-averaged data we use are the 1 min averages.

By comparing the vertical lines in Figure 3.4, we see that our three methods give slightly different results and the specific differences depend on both the nature of the fluctuations and the mean spiral angle. In particular, when rotational fluctuations dominate, the mean value is an underestimation, especially when the Parker spiral is close to radial (left-most column). At these spiral angles, the mode is also a slight underestimation; however, at a higher Parker spiral angle (right-most column), the mode appears to overestimate the true value. The skewed 1D distribution is being primarily shaped by the geometry of projecting angular fluctuations and so, the distribution peak does not in general correspond to the 2D background value about which the field vector is fluctuating. Thus, the assumption that the mode is 'more representative' than the mean is not yet justified.

When the compressive and rotational fluctuations are balanced, all three values are closer together (the mean is a better approximation), especially at a higher Parker spiral angle. In this case, for low Parker spiral angles, the mean is, in fact, higher than the mode.

Overall, in this section, we show that the nature of the 2D fluctuations of the vector and the inclination of the Parker spiral angle can affect our measured value of the heliospheric flux. Therefore, if the vector fluctuations can indeed be modelled as normally distributed about a mean magnitude and angle – especially if rotations dominate over vector magnitude

fluctuations and then the Parker spiral method is clearly the most robust and physically motivated method considered here. The fluctuation balance would also determine the appropriateness of each method. Next, we seek to measure the background vector and fluctuation statistics as a function of radius from the real spacecraft data and we also check the extent to which fluctuations are evenly distributed.

Measured fluctuations

In Section 3.3, we found that for idealised synthetic data with symmetrically distributed 2D vector fluctuations, the nature of these fluctuations and the large-scale inclination of the Parker spiral could affect our estimates of the heliospheric flux. In particular, how the fluctuations were partitioned into angular and compressive (—B—) fluctuations had an impact. In this section, we seek to measure the inclination of the Parker spiral and the distribution of 2D fluctuations to assess how these effects manifest in estimates of the heliospheric flux with real data.

In Figure 3.5, we compute the statistics of the field magnitude (scaled by R^2) and clock angle and then we plot the results as a function of radius. We do this by binning all the data by radius (large squares) as well as by binning in time at a daily and hourly cadence (faint and fainter circles). The top row shows the most probable value, the second row shows the standard deviation (for the field magnitude, scaled by the mode to make it dimensionless), and the bottom row shows the skew, defined as the (mean - mode)/standard deviation.

In the top row, we also plot the expectation of these quantities for a Parker spiral model as a function of radius. The analytical expressions [154] are :

$$|B|R^2 = |B_0|\sqrt{1+\left(\frac{R\Omega_\odot}{v_{SW}}\right)^2}, \quad \alpha_\pm = atan2\left(\mp\frac{R\Omega_\odot}{v_{SW}}, \pm 1\right).$$

Here, v_{SW} is the solar wind velocity, $\Omega_\odot$ is the solar equatorial rotation rate (14.17 deg/day), and $+(-)$ indicates the anti-sunward (sunward) sectors. The models shown use $B_0 = 2.2nT$ and $v_{SW} = 300km/s$. As can be seen, in all binning schemes, the most probable value of the data is in good agreement with the model across different radii, with larger scatter for the shorter binning intervals.

For the standard deviations (middle row, Figure 3.5), which describe the relative strength of fluctuations, we see both compressive and rotational fluctuations grow in amplitude with radius, but we also see that at all radii, the amplitude of rotational fluctuations is larger than compressive fluctuations. Binned by radii (such that the distribution is formed over many streams), rotational fluctuations are about three times as large as the compressive fluctuations at closest approach and slightly less than two times as large at 1AU.

The pattern in the skew is less clear. At a one-hour or one-day cadence, there is no trend: at all radii, there are as many distributions skewed positive as negative. For vector magnitude, averaged over many streams, there is a hint of negative skew at perihelion and a

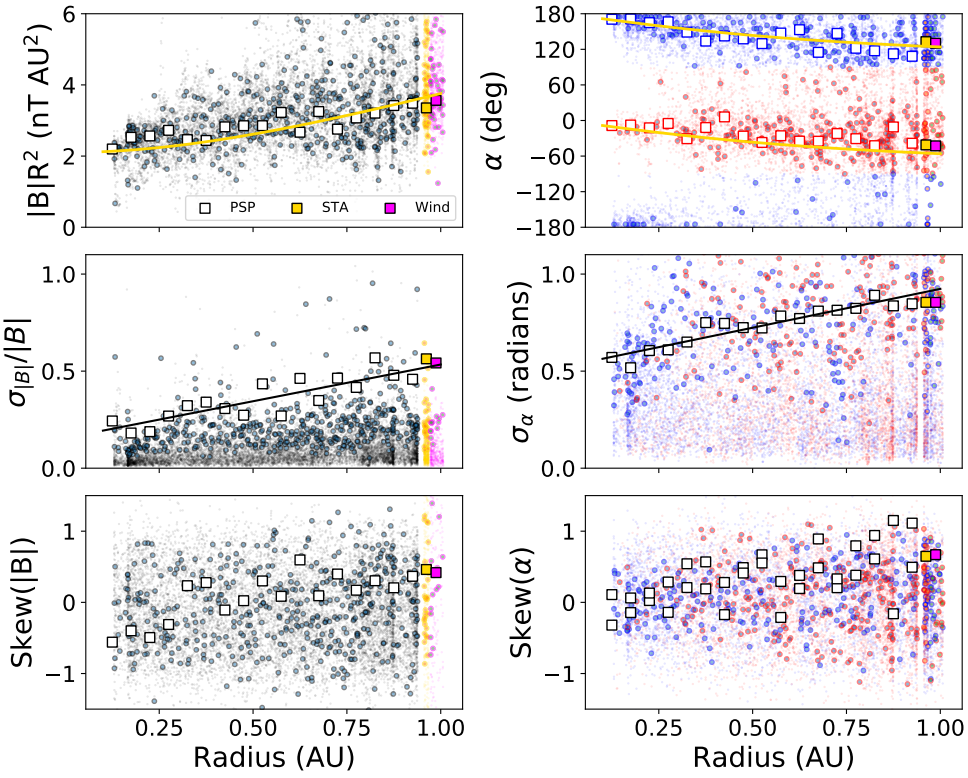

Figure 3.5: Field magnitude and clock angle statistics as a function of radius. In each panel, the faint background shows statistics of one hour intervals, the larger, darker scatter points show statistics of one-day intervals, and the squares depict the statistics within radial bins of width 0.05AU. The gold and the magenta square depict the STA and Wind results, respectively. The left-hand column pertains to $|B|R^2$ (the field magnitude) and the right-hand column to α (clock angle). The top row depicts the measured large-scale structure and shows the most probable values. In yellow, we have the expectation of a Parker spiral model. The middle row shows the dimensionless standard deviations and a black line shows a least squares fitted linear trend, which describes the radial evolution of vector fluctuations. The bottom row shows the skew of the ratio of the (mean-mode)/standard deviation, which describes the extent to which individual distributions are evenly distributed. For the angular quantities, the red and blue colours describe anti-sunward and sunward sectors, respectively.

small positive skew at 1AU. The negative skew at low heliocentric distances arises from the near-HCS weaker field mentioned in Figure 3.2; many single-day intervals at these radii have very low skew. For the clock angle, the skew at perihelion is negligible, but trends positive at 1AU, which means the fluctuations are biased in favour of rotation towards the radial direction.

The relationship of the different timescales considered here and the underlying data products warrants some discussion in passing. Firstly, we note explicitly that the one-hour and one-day cadence data points are computed from the higher cadence four-samples-per-cycle data product, while the data binned by radius (white squares) are based on the 1 min averaged data. The fact that the white squares lie in the middle of the distribution of one-hour and one-day measurements fuels our confidence that the two data products are largely interchangeable. This also shows that at a given radius, non-consecutive hour or day intervals from different orbits with no temporal correlation fill out a well-defined distribution around the relevant white square. This is useful evidence that the central value is not tied to a specific time interval and it is, therefore, real spatial information about the HMF, meaning it is justified to use different timescales for estimating the heliospheric flux at various points in this paper.

To summarise, in this section, we successfully measured the 2D vector fluctuations and underlying large-scale radial trends in the HMF that, as we showed in Section 3.3, could impact our measurements of the heliospheric flux. In addition, we characterised the skew of the distributions, broadly assessing the requirement for the vector fluctuations to be evenly distributed about a central value to justify the use of the Parker spiral method. Additionally, based on this, we infer that: (1) the Parker spiral is a good model for the underlying large-scale structure; (2) at all radii from 0.1-1AU, the amplitude of rotational fluctuations are stronger than compressive ones ($\sigma_{|B|}/|B| < \sigma_\alpha$), but this predominance decreases with heliocentric distance; (3) the Parker spiral method for computing Φ_H (which relies on having an unskewed distribution in magnitude and clock angle) may be less applicable at 1AU, where the distributions averaged over streams appear to have a positively biased skew in both polar components (and the central assumption of evenly distributed fluctuations breaks down). The field magnitude over multiple orbits also showed some signature of skew close to the sun, but this can be attributed to distortion by the weaker field near the HCS during encounters four and five. This is accounted for by taking the most probable value of the magnitude rather than the mean. For reference, the radially binned distributions which give rise to the statistics shown in this section are shown in Appendix B.2. Based on Figure 3.4 and the above observation that the rotational fluctuations are dominant, we expect the mean to be a systematic underestimation of the background value of $B_R R^2$, especially close to the sun.

Synthetic and measured radial trends of flux

Having measured the large scale variation of the HMF and the characteristics of the vector fluctuations, we next seek to quantify the expected and measured variation in the statistical methods of estimating $B_R R^2$ as a function of radius. In Figure 3.6, we compare measurements of the mean (diamonds), modes (squares), and the Parker spiral method (circles) from purely synthetic distributions (top panel) and directly from measurements (bottom panel).

For the synthetic measurements, we take the Parker spiral model values for the background values of $|B_0|(R)$ and $\alpha_0(R)$ from Figure 3.5 (yellow curves, top panels) and for the

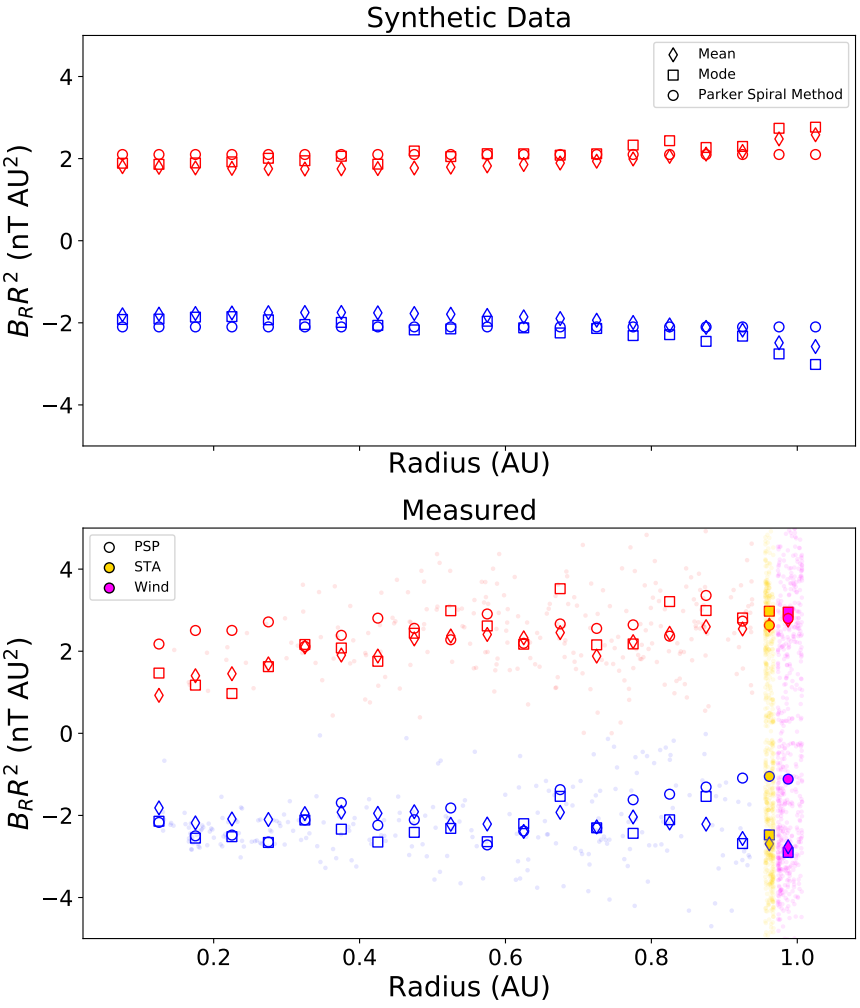

Figure 3.6: Resulting expectations and measurements of the difference between the different measures of $B_R R^2$. In both panels, circles indicate results from the Parker spiral method, squares represent modes, and diamonds represent means, as a function of radius. The top panel shows results for a purely synthetic data set using a Parker model for the "true" field and Gaussian* fluctuations in magnitude and clock angle as modelled by the linear trends shown in fig 3.5. The bottom panel shows the same measurements from the actual PSP data, binned into 0.05AU radial bins. Faint data points in the background show the computed values at one day intervals to show the general scatter (which clearly increases with radius – except where Gaussian fluctuations would cause negative values of B; for details, see main text).

fluctuation amplitudes, we take the linear fits to the standard deviations from the middle panels of Figure 3.5. As earlier, even though we compute the two sectors separately for the synthetic data, we use the joint distribution projected into 1D and split at $B_R R^2 = 0$ to compute the mean and mode. This method simulates the process of obtaining these measurements from the real data where the components of the two magnetic sectors cannot be distinguished in the 1D distribution. We do actually allow the synthetic distribution in magnitudes to have a non-zero skew further from the sun (see Appendix B.2 since fitting a standard deviation from these skewed distributions would produce an nonphysical Gaussian distribution, where a significant population of magnitude values would go through zero. In these cases, we are modelling our 'ground truth' as the peak of the skewed distribution of magnitude.

As expected, for the purely synthetic data, the Parker spiral method produces the same value of magnetic flux for all radii. While this background value remains constant, the estimated mean and modes evolve with radius due to the changing impact of the fluctuations and background Parker spiral angle. For low radii, the mean produces a constant value but significantly underestimates the magnetic flux. Around 1AU, the mean systematically increases relative to the background value, and in this model becomes an overestimation. Closer than about 0.8 AU, the mode is a slightly better estimate of the background value but it fluctuates, at some points, resulting in either an overestimation – or sometimes an underestimation. At 1AU, the mode also systematically increases and overestimates the 'true' value.

For the real data, the PSM is performed directly with the most probable values of —B— and α taken from the white squares in Figure 3.5 to show representative values integrated across multiple orbits. These are derived with the 1 min averaged data products. We note that the yellow and magenta filled data points are from STEREO A and Wind respectively, while the remainder of the data is from PSP. For completeness, we show both the positive and negative sectors measured by PSP, although the trends discussed below are primarily observed in the negative polarity (blue data points). This is due to the limited time intervals where PSP has been above the HCS, particularly at the closest approach. Furthermore, the dominant data contribution above the HCS for radii closer than 0.3AU comes from encounters four and five, which were distorted for extended periods by PSP skirting very close to the HCS (Chen et al., submitted to this issue).

As faint data points in the background, PSM estimates of $B_R R^2$ for one day time intervals are shown from the four-samples-per-cycle data, demonstrating the variability of the estimate from one day to another and that the values of the estimate integrated over multiple orbits lie in the centre of this distribution. This distribution is more spread than the difference in the central value from one radial bin to the next.

Although the trends with real data are unavoidably noisier, when focusing on the negative sector, the mean can be clearly seen to exhibit the same behaviour as in the synthetic data, producing a systematic underestimation close to the Sun, but growing and exceeding the Parker spiral method at 1AU. In the positive sector, the same behaviour is seen, but less clearly for R ¿ 0.3AU, with a flat mean eventually trending upwards for R ¿ 0.8AU.

Importantly, the trends implied by the PSP data converge nicely with the 1AU data. For the negative polarity data trends the mode is also in good agreement with the synthetic observations, providing better agreement with the Parker spiral method close to the Sun, but also systematically increasing near 1AU and at intermediate radii overestimating the PSM. The PSM, while not perfectly flat, is generally quite consistent with the radius, but not dramatically more so than the other methods. For $B_R R^2 < 0$ near 1AU, there is a significant drop-off in the estimate of B_R using the Parker spiral method. This may be related to the growing skew exhibited in the bottom panel of Figure 3.5 and suggests the method may be less robust near 1AU. As mentioned previously, our implementation of the PSM relies on the fluctuations (particularly in the angle) being evenly distributed about a mean. The bottom panels depicting the skew in Figure 3.5 suggests this assumption starts to breaks down close to 1AU.

Overall, we conclude that this model of fluctuations in magnitude and angle is a good approximation for understanding the dependence on heliocentric distance of the different methods of computing Φ_H considered here, at least for R ¡ 0.8 AU. In particular, Figure 3.6 suggests that fluctuations cause the mean of PSP data close to the Sun to constitute an underestimation – and to be an overestimation beyond 0.8AU. Below 0.8AU, at least for the negative polarity measurements, the PSM and mode estimates are comparably variable with radius but show the ordering expected from our model of fluctuations – with a higher value of mode as compared to PSM and a convergence of the values close to the sun. Comparisons of the synthetic and measured 2D distributions and distributions of $|B|$ and α in 0.1AU bins may be found for reference in Appendix B.2.

As a result of the findings in this section, we conclude that it is necessary and important to utilise the 2D distribution of the magnetic flux in order to compute the background value of $B_R R^2$; without this step, the radius-dependent fluctuations can lead to systematic biases in the mean or modal statistics value. Thus, of the methods considered here, the Parker spiral method presents the most robust estimate, although its estimate appears interchangeable with the mode close to the sun and may be less reliable near 1AU. In the next section, we present our results, using the Parker spiral method (and the other statistical methods where justified) to measure $B_R R^2$ throughout the inner heliosphere and, finally, we compare it to expectations from coronal models.

3.4 Results

Bulk measurements

In Figure 3.6, near 1AU, at least for the positive polarity data, all three metrics appear to climb to near 3nT AU^2, possibly indicating a physical enhancement in the heliospheric flux at 1AU. To probe this observation further, as well as to develop a 'best estimate' of the heliospheric flux closer to the sun, we sum together all the $B_R R^2$ distributions over radius and show their bulk statistics. For every hour of data, we compute the mean, mode, and

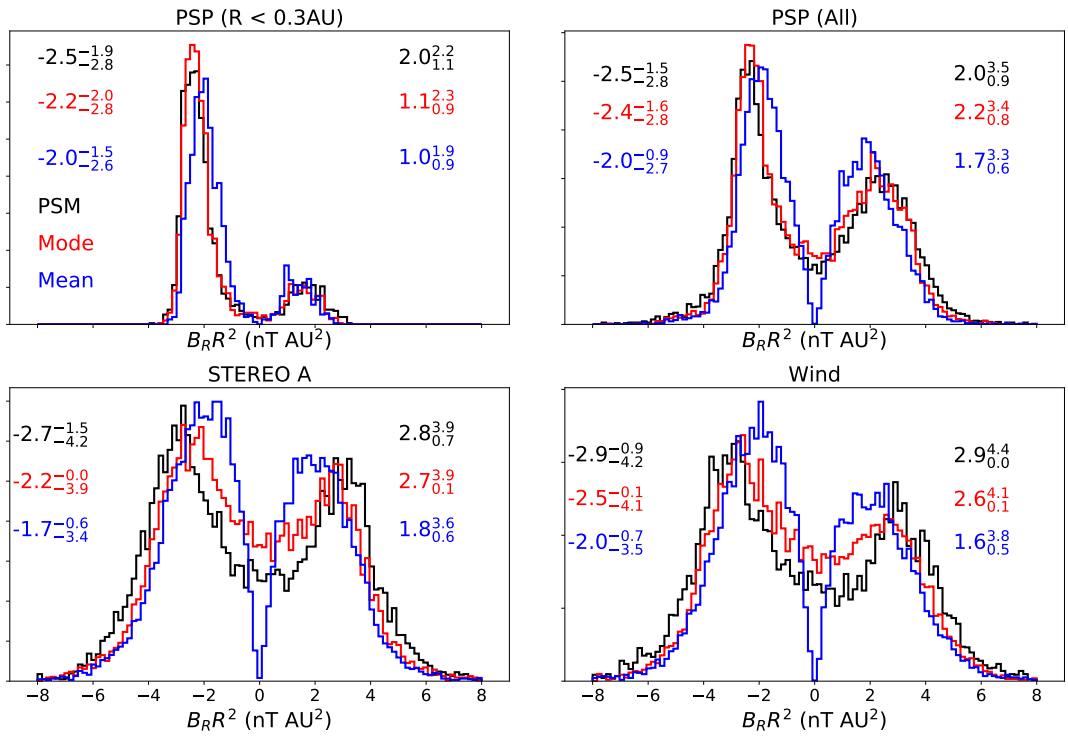

Figure 3.7: Bulk statistics. Each panel shows 1D histograms of all values of $B_R R^2$ computed with the Parker spiral method (black), mode (red), and mean (blue) at one-hour timescales, integrated over all the data shown in Figure 3.1. Reading from left to right, the four individual panels show PSP (for radii less than 0.3 AU), PSP (all data), STA and Wind data respectively. Text in the corresponding colour gives the bi-modal peak values and their upper and lower values defining their full width at half maximum (FWHM) in superscript and subscript.

Parker spiral method estimates as described in Section 3.3 and show how these estimates are distributed over the studied time interval. A one-hour timescale is chosen here to produce a sufficient number of individual ‘measurements (on the order of 15000) with each method across the whole data set expected to produce a robust histogram and define a peak value. A longer integration timescale would sharpen these distributions, but limit the statistics. This means our computations of error are likely conservative.

The results are shown in Figure 3.7. We show the three spacecraft separately – for PSP we include a panel showing only data from close to the sun (R ¡ 0.3 AU) – and overlay the histograms of hourly measurements with the three different methods. The information contained in these histograms is compressed into a most probable value and upper and lower values defining the full width half maximum (FWHM) for both peaks. These data are shown as text in the corresponding colour in the same plot.

We first observe that in all cases, the distributions of measurements using the mode and Parker spiral methods are quite similar to each other, whereas the distribution of mean measurements is strongly distorted: while the truncation procedure (similar to taking the modulus, see Section 3.3) successfully keeps the sunward and anti-sunward peaks distinguishable, the overall distribution is broadened and shifted towards $B_R R^2 = 0$, producing a systematic underestimation compared to the other methods and with a larger uncertainty as encoded by the FWHM. We see by restricting the data to PSP measurements close to the Sun (top left panel in Figure 3.7), the distributions for all methods are the sharpest, although the systematic underestimation between the mean and the other methods persist, as expected from our synthetic data model. The broadening of all distributions with distance from the sun shows the increasingly prominent role of fluctuations and other distorting effects with increasing heliocentric distance.

Distinguishing the mode and PSM is slightly more subtle. With regard to the near-1AU distributions, the Parker spiral method is seen to produce distributions that are more similar to the close approach distributions further from the Sun, doing a better job of removing the population of measurements close to zero and separating the two peaks, as compared to the mode. While this is most clearly seen at 1AU where there is a larger population of $B_R R^2$ measurements close to zero in the red curve (mode) compared to the black curve (PSM), integrating the PSP data over all radii, (top right panel in Figure 3.7), the difference is slight but still observable. Once we restrict the data below 0.3 AU (top left panel in Figure 3.7) both the mode and PSM distributions are close to indistinguishable. This supports our inference, presented in Section 3.3, that the mode is distorted more than the PSM by fluctuations as distance from the sun grows, although for practical purposes, for most of the PSP data, the noise in these distributions means the mode and PSM measurements derived are consistent within the error; the growth of the difference between these methods is most pronounced between the outer ranges of PSP's orbit and 1AU.

We note for the PSP data, the negative peaks are much better resolved than the positive peak due to the same latitudinal sampling effects and near-HCS intervals which caused the trends to be more apparent with the negative polarity data in Figure 3.6. Integrated over all radii, the negative polarity PSM peak gives a bulk value of $\Phi_H = 2.5^{+0.3}_{-1.0}$nT AU^2 where, as mentioned above, we have computed the error based on the FWHM of this profile. Confined to just R ¡ 0.3 AU, the measurement tightens to $\Phi_H = 2.5^{+0.3}_{-0.6}$nT AU^2.

We also see the most probable PSM-derived estimate of $B_R R^2$ at 1AU is significantly larger ($\sim$2.8 nT AU^2) than the value derived above from the negative peak of the PSP data, although just within the error. The enhancement is apparent in both Wind and STEREO A data. The trend is also seen in the most probable value of modal values, but not here for the mean. For the mean, this seems to be an issue with defining the mode for a broad peak, looking at the upper FWHM value, this can be seen to clearly increase for all methods in comparing the top two panels to the bottom two. While we expected from the analysis of fluctuations that the mean and mode of $B_R R^2$ will grow with radius, this cannot explain why the value would be significantly higher than computed with the Parker spiral method. Although we expect the PSM results to be less robust in this vicinity due to apparent skew

of the distributions and associated breakdown of the even distribution assumption (Section 3.3), it is not immediately apparent why this should result in a systematic increase of $B_R R^2$ as opposed to a decrease. Therefore, it appears possible that this flux enhancement could indeed be physical. We investigate a possible explanation for such an enhancement in the next section.

Excess flux

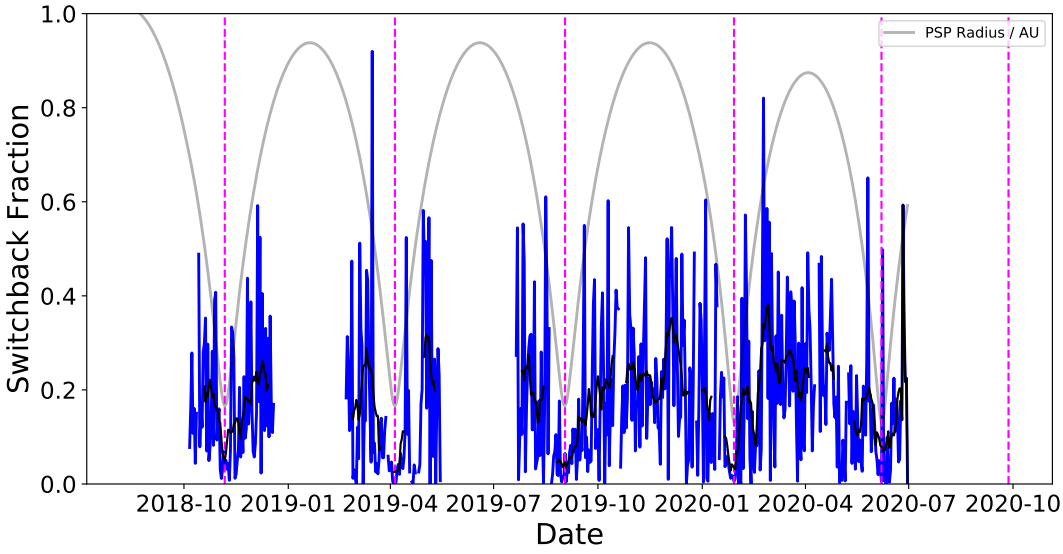

Figure 3.8: Daily switchback fraction. The blue curve shows, for each day of PSP data, the fraction of measured B_R values which are of the opposite sign to the most probable field that day. The light grey curve show's PSP radius in units of AU. The black curve better illustrates the underlying trend, showing the daily fractions smoothed with a window size of five days. The dashed magenta lines indicate the date of each perihelion.

In the heliosphere, numerous physical processes such as waves, turbulence and stream interactions perturb the quiescent picture implied by the Parker model. One particular consequence of such effects is that local field inversions develop wherein the field lines connecting back to the corona warp into an S shape. As argued by [150], such inversions entail the same field line threading a spherical surface at a fixed radius multiple times (see also Appendix B.5 for an illustration) such that a given field line would contribute triple the flux at this radius as compared to its contribution leaving the corona. Therefore, they could contribute to a physical excess flux. The cited authors identify such inversions using the electron heat flux (aka strahl) which follows the HMF topology and carries energy away from that field

line's point of origin in the corona. Therefore, when the strahl is observed to be sunward, it is inferred that the electrons must be travelling along a kinked field line such that they escaped and moved outwards from the sun but have then been guided sunward by a field inversion. This approach was recently applied [81] to probe the topology of the switchbacks observed by PSP. [150] used this method with ACE data over a solar cycle to derive a correction factor to the heliospheric flux. They found this estimate to be consistent with the values obtained by pre-averaging signed $B_R R^2$ data over one day intervals before taking the modulus, and slightly weaker than the kinematic correction factor proposed by [115, 116, 117]. Furthermore, [120] showed with Helios data that the frequency of such local inversions increased with radius from 0.3 to 1.0 AU, suggesting that this correction factor would grow with radius.

In Figure 3.8, we investigate this same radial trend with PSP B_R data from 0.13 to 0.9 AU. For each day of PSP data, we compute the fraction of the distribution which is of the opposing sign to the most probable value, making the assumption that over each 24-hour period, PSP remains on one side of the HCS and that all zero crossings in this interval are due to fluctuations. This is slightly less robust than the [150] strahl method which can distinguish HCS crossings unambiguously and account for transient structures such as coronal mass ejections (CMEs) but still carries useful information about the trend. A one-day interval is chosen as the trend is readily apparent with no further processing; computing it with a shorter time interval, such as one hour, is much noisier. In Figure 3.8, we plot this fraction of inverted flux as a function of time and also show the times of PSP's perihelia and its radial variation. While the metric is noisy, as might be expected given the above assumptions, there is a clear correlation with radius, in which the fraction of inverted flux grows with distance from the Sun, which is consistent with [120]. The fraction has a well-defined floor which varies from $< 3\%$ at perihelion to as much as 20% at 1AU. It is therefore plausible that if such fluctuations can contribute to excess flux, their impact will grow with radius in the inner heliosphere. However, conversely, we see that at perihelion the contribution is extremely small ($< 3\%$). This is interesting given the prominence of the switchbacks observed by PSP. This implies that while these switchbacks are very striking given the large amplitude and sharpness of the rotations [e.g. 72], the population of measurements in which the field actually reverses is a very small fraction of the total. They are transient impacts perturbing a quiescent background state.

To numerically estimate the possible impact of the flux, we make a very simple construction, which is as follows: if there are N open field lines emerging from the corona and a fraction f of them are locally inverted at a given radius, then the true open flux per unit area is $d\Phi_{open}/dA = N$; but the actual measured flux at that radius will be $d\Phi_H/dA_m = (1-f)N + 3fN$. This can be rearranged to relate the true and measured flux : $\Phi_{open} = 1/(1+2f)\Phi_H$. For $f = 3\%$, this simple heuristic implies $< \%5$ open flux estimate error at perihelion and up to a 30% correction at aphelion, which is similar (slightly larger) than the factor derived by [150], as judged from their Figure 5, and significantly larger than the fraction implied by Figure 3.7 in the present work, which suggests a $\sim 20\%$ reduction in flux between PSP and 1AU. This metric is likely an overestimation since it

assumes the switchback fraction measured near the ecliptic plane, where the solar wind is predominantly slow, can be applied uniformly in latitude but, as shown with Ulysses data [47], fast polar coronal hole wind for most latitudes has much lower fluctuation levels than the slow wind.

Regardless, in terms of contribution to the excess flux, near PSP's perihelia flux inversions are largely negligible. Combined with the much reduced relative amplitude of fluctuations at closest approach, we expect that the value of heliospheric flux, Φ_H, at least at PSP's closest approach, should robustly correspond to the true open flux escaping the corona, Φ_{open}, with 5% as an upper bound to the possible deviation.

Heliospheric flux as a function of heliographic position

We show here how the Parker spiral method determination of heliospheric flux varies with heliographic position, while examining all three dimensions of radius as well as heliographic latitude and longitude. The results are summarised in Figure 3.9. In the background, we show 2D histograms of the full data set of 1 min averages (again due to tractability issues of working with the full four-samples-per-cycle data set). In the foreground, we plot the Parker spiral method results computed from each day of data and colour them by the polarity. One-day intervals are used to reduce the scatter and not overcrowd the plot as opposed to one-hour intervals, while spatial binning is avoided so that each data point may simply be assigned a 3D spatial coordinate so that it may easily be plotted against each coordinate (radius, latitude, and longitude). The top row shows results against radius, the middle against latitude, and the bottom row against longitude. Columns from left to right shows PSP, STEREO A and Wind results.

First we see that in all cases, the one-hour estimates trace the regions of highest data density (dark colours in the histograms) well, indicating the close relationship between the Parker spiral method and the mode. Second, plotted against all the coordinates, the PSP data shows the tightest confinement and least scatter due to the much reduced fluctuation levels (see Figure 3.5, middle row). We confirm the heliospheric flux over these two year intervals is largely independent of radius and longitude, but most clearly shown by the PSP data for $R < 0.5$AU and for negative latitudes. To emphasise the radial trend, we make linear fits to the data shown (with negative and positive data points fitted separately). These fits are shown as solid black lines in the top left panel of figure 3.9 and their fitted equations are printed within the same panel. The fit to positive polarity shows a substantial slope due to the positive polarity of the weakly magnetised plasma PSP sampled at it running close to the HCS at closest approach during encounters 4 and 5 (see Figure 3.2 and Chen et al., submitted to this issue). The negative polarity data is much less perturbed by these effects and benefits from a larger sample size (three whole encounters predominantly below the HCS). For this case, the trend is well fit by a constant value indicating constant heliospheric flux as a function of radius and limiting the variation in the flux with radius to 0.1 nT AU^2 per AU. In fact, this fit suggests a weak decrease in flux with radius. We note that as

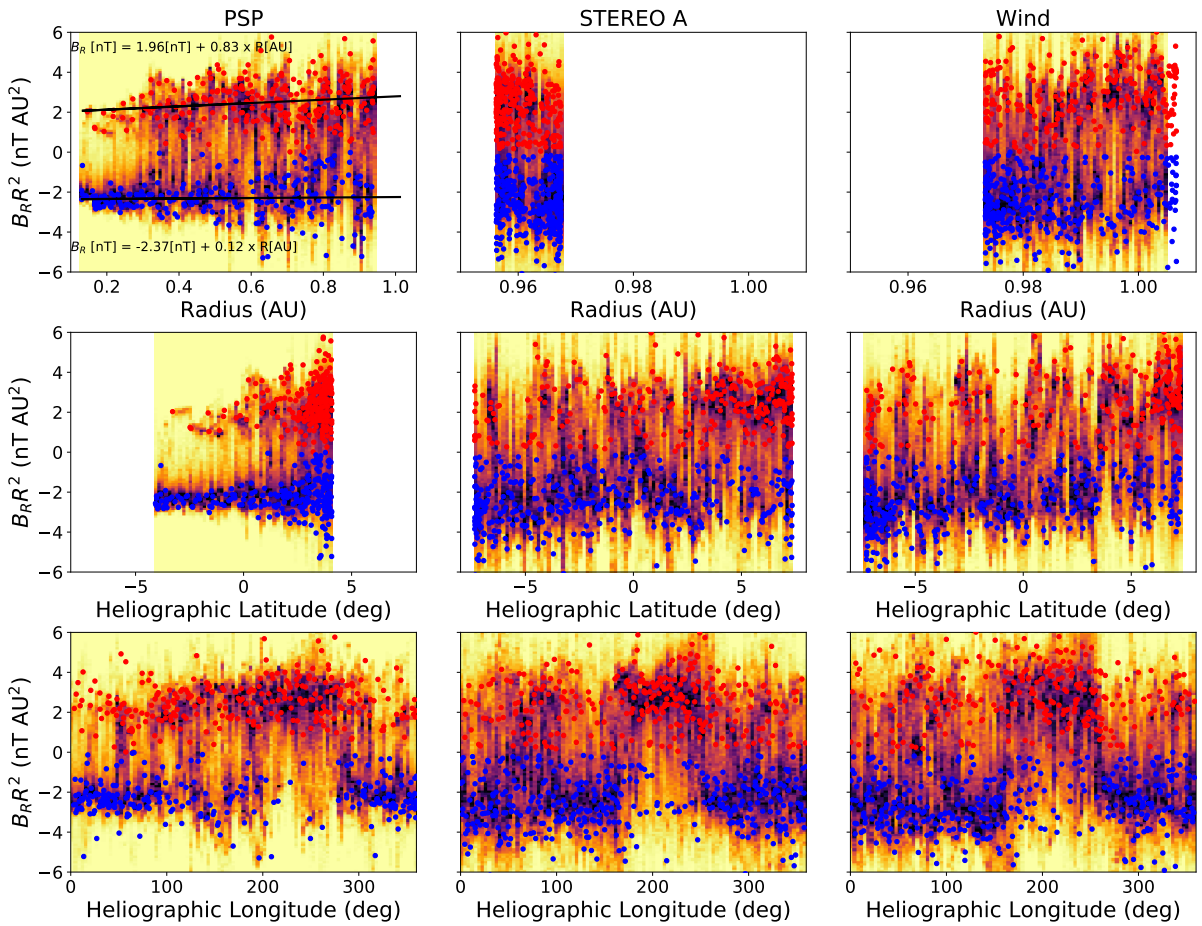

Figure 3.9: Measured flux as a function of heliographic location. Each panel shows a 2D histogram in the background as in figure 1. In the foreground, blue and red dots show the values computed at one day intervals with the Parker spiral method. The top row shows trends versus radius, the middle offers a comparison against heliographic latitude, and the bottom against heliographic longitude. The middle and bottom rows have a common x-axis. The three columns depict data from PSP, STEREO A and Wind respectively. For the PSP heliospheric flux as a function of radius (top-left panel), solid black lines indicate fitted linear trends to the scatter points shown with negative and positive (blue and red) values fitted separately

.

suggested by Figure 3.6, the onset of increasing flux with distance may be non-linear and may inflect close to 1AU.

Over the limited range of latitudes probed by PSP and the 1AU spacecraft, the heliospheric flux is also seen to be constant. It is no coincidence that the latitude and radius

panels show very similar trends since these coordinates are strongly correlated due to the tilt of the spacecraft orbits relative to the solar equatorial plane. The high data scatter at high PSP latitudes is simply a result of PSP being at aphelion during the sampling at these high latitudes, where the fluctuation environment is much noisier.

Comparing the longitude plots, we see a similar sector structure pattern measured by all three spacecraft over the full two-year data set, indicating the dominant warps in the HCS were consistent throughout. The predominantly positive sector in the PSP panel (top right) is shifted to a slightly higher longitude than on the 1AU panels, which is consistent with the Parker spiral shift from PSP's closer heliocentric distance out to 1AU.

The STA and Wind data show a slight asymmetry in field scatter by latitude. At highest latitude, they measure slightly higher positive flux, and at lowest latitude they measure slightly stronger negative flux. The reason is not perfectly clear. From Figure 3.1, it is clear that the latitude and field values are correlated. Extremes in latitude means the spacecraft is spending less time close to the HCS in general. This might mean faster solar wind with lower fluctuation levels and therefore a measured value which is closer to the 'true' open flux and would suggest the excess flux is physical.

Heliospheric flux as a function of time and comparison to PFSS expectations

Lastly, we compare the Parker spiral method measurement results to estimates of the open flux from Potential Field Source Surface models [PFSS 4, 186, 223]. The specific model implementation is the same as described in [14] and makes use of *pfsspy* [235, 199, 201], a python implementation of the PFSS model. The inputs of the model are 2D magnetogram maps of B_R at the solar photosphere, and some choice of source surface height (R_{SS}). The output of the model is the vector magnetic field, $\boldsymbol{B(r)}$, for the annular region between the photosphere and the source surface ($1R_\odot < R < R_{SS}$). The open flux is estimated from this model by integrating the field vector over the source surface, where all field lines are radial by construction and interpreted to be open to the solar wind. This integral is given by Equation 3.1, which is repeated here for convenience: :

$$\Phi_{open} = \int_0^{2\pi} \int_{-\frac{\pi}{2}}^{\frac{\pi}{2}} |B_R(\theta, \phi, R = R_{SS})| R_{SS}^2 \sin\theta d\theta d\phi.$$

As a reminder, to make this quantity comparable to the quantity $B_R R^2$ measured in situ, we normalise it by 4π (1AU)^2, such that is is expressed as a field strength in nT at 1AU.

We used the Air Force Data Assimilative Photospheric Flux Transport [ADAPT, 9] magnetograms [2], which assimilate the most recent available photospheric data (from the visible part of the Sun) into a surface flux transport model which forward-models the magnetogram

[2]ADAPT maps are accessed from `https://gong.nso.edu/adapt/maps/`.

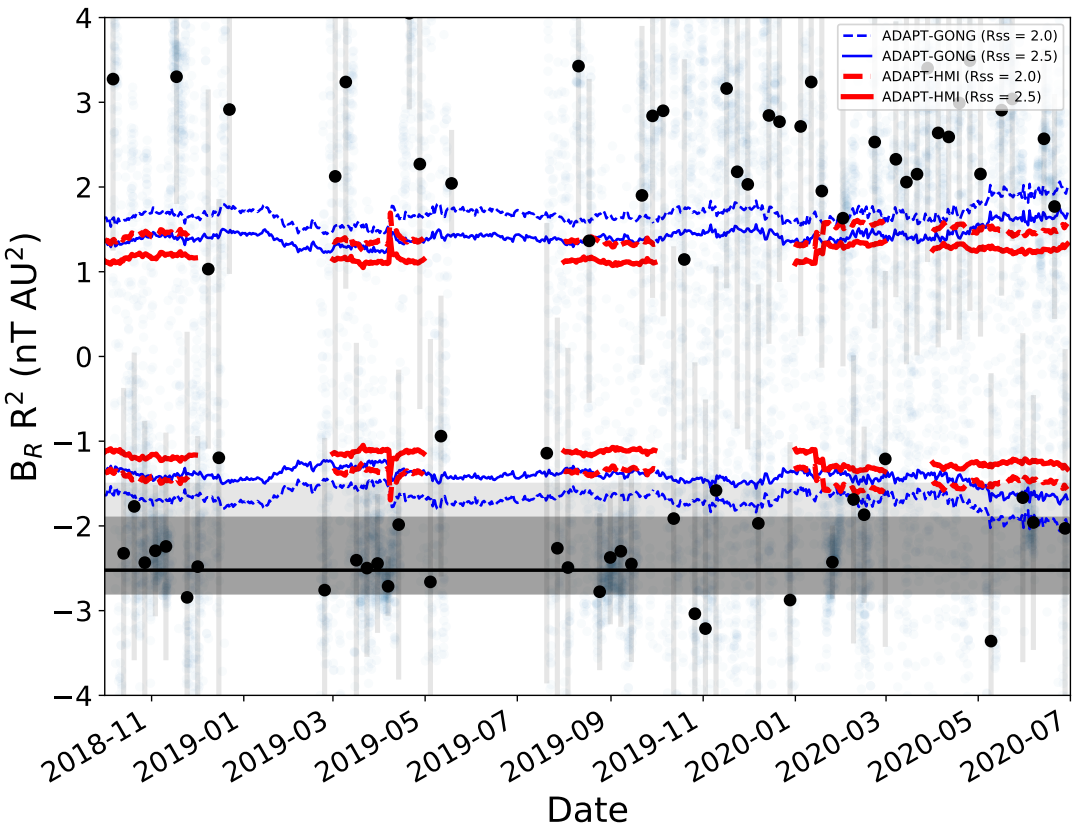

Figure 3.10: $B_R R^2$ versus time and Potential Field Source Surface Flux estimates. As a function of time, black markers represent the most probable Parker spiral method value (at a one hour cadence) of the *in situ* heliospheric flux for each week of data, the grey error bars represent the standard deviation with this week. The light gray and darker grey regions represent the full width half maxima of all PSM method measurements and all measurements within 0.3AU respectively. A horizontal black line shows the most probable value (0.25 nT AU^2) which is common to both the full and radius-restricted data sets (see figure 7). Blue (ADAPT-GONG) and red (ADAPT-HMI) curves show the open flux value predicted (see Equation 3.1) by potential source surface (PFSS) models using daily updating magnetograms over the mission. The solid (dashed) curves show results for 2.5 $R_\odot$ (2.0$R_\odot$) source surface height, and the different colours differentiate the magnetogram source used.

from the previous time-step, taking into account differential rotation and meridional flux transport. In this way, it seeks to model the magnetic field of the entire solar photosphere 'synchronically' (meaning all longitudes are modelled at the same time), as opposed to synoptic magnetograms, which simply merge together old and new data. These maps are produced multiple times per day (much more frequently than a Carrington rotation). In this work, we access one magnetogram per day. We utilise ADAPT magnetograms, which assimilate photospheric data from the ground-based Global Oscillation Network Group [GONG; 63] and space-based Heliospheric Magnetic Imager [HMI; 188] which are both available at the above URL for the PSP mission duration. The HMI data product is only available for about ± 1 month about each perihelion, while the GONG data product is available for the full duration studied.

In Figure 3.10, we compare the open flux estimated from the PFSS models to that measured in situ by PSP as a function of time. Results for two different values of source surface heights ($2.0R_\odot, 2.5R_\odot$) are shown for ADAPT-GONG and ADAPT-HMI maps. The lower value is chosen based on better agreement with the current sheet crossings measuring during PSP's first perihelion [14, 170, 206], while the higher value is the widely accepted canonical value of R_{SS} [68], and which appears a better fit for PSP's second orbit [153].

To compare to the in situ measurements, we here present seven day averages of the hourly Parker spiral method results from Figure 3.9. This is chosen to avoid overcrowding the plot and emphasise where the data is most self-consistent and why the most probable trend line is located where it is. Error bars show the standard deviation of the hourly measurements within these seven days. In addition, the most probable value and error generated from the bulk distribution of the PSM results (histogram peak and upper and lower FWHM, top right panel in Figure 3.7) is shown as a solid black horizontal line and light grey region. In addition, the darker grey region shows the smaller error region of the distribution for R ¡ 0.3 AU, which has the same central value (top-left panel, Figure 3.7). This error region captures all the data points for the first three perihelia well. As noted in Section 3.4, these errors were generated using the distribution of one hour PSM measurements. This short time interval was necessary to produce enough statistics to produce a robust distribution, but as we see in the discussion in Section 3.3, longer time intervals reduce the scatter further and, thus, the error bounds here are likely to be quite conservative. We see that the most reliable measurement of the open flux occurs southwards of the HCS, around perihelion of the first three orbits (November 2018, April 2019 and September 2019). This 'best estimate' is shown only for negative polarity since PSP has been predominantly south of the HCS during each perihelion pass when it measures these low error values and may be summarised as $\Phi_H = \Phi_{open} = 2.5^{+0.3}_{-0.6}$ nT AU^2. We note the 5% error implied by the excess flux discussed in Section 3.4 is 0.125 nT AU^2 and is sub-dominant to the statistical uncertainty.

Comparing the PFSS and in situ results, we see regardless of time evolution, distribution time interval, source surface height, or choice of magnetogram, the best estimate of open flux measured by PSP exceeds that expected by PFSS estimates. As is to be expected, lowering the source surface height increases the estimated flux. Continuing below 2.0 $R_\odot$ would eventually enhance the flux sufficiently to match the in situ data, but this is at the

expense of realistic coronal hole structure [110]. The PFSS estimates shown here do exhibit some limited time evolution over these two years of data but the fluctuations are in general much less than the difference (1) between different PFSS models (source surface height and magnetogram source) and (2) the difference between the model values and the in situ values. Overall, we observe that the open flux measured by PSP for the time interval from 2018-2020 (deep solar minimum) remains too high to be explained by standard PFSS estimates.

3.5 Discussion

We examined the first five orbits of magnetic field data measured by Parker Solar Probe to measure the heliospheric magnetic flux (Φ_H) down to 0.13AU and compared it to simultaneous measurements at 1AU, and estimates of the open magnetic flux escaping the corona as predicted by potential field source surface models.

In this work, we use either 1 min averages or higher cadence data for which the distributions of data are not affected by the cancellation effect that appears with longer pre-averaging timescales. [150] showed that for 1AU data, an appropriate choice of a pre-averaging timescale (enacted on Cartesian components of the measured HMF vector field) has the same effect on the heliospheric flux measurement as using a more physically motivated method, such as accounting for local flux inversions. As shown in Appendix B.3, pre-averaging even over one hour intervals of data strongly distorts the Cartesian components of the HMF vector and so, using any estimation method from such distributions is no longer a physical measurement of the actual magnetic field; and thus the 'correct choice' of the pre-averaging timescale, while potentially useful [e.g. 220], is more of a calibration technique which cannot be determined a priori. Moreover, it cannot be uniformly applied to data at different heliocentric distances as the character of the fluctuations changes. In this work, we utilise distributions of minimally pre-averaged data upon which our estimation methods (mean,mode, and Parker spiral method) are performed. Furthermore, our implementation of the Parker spiral method (PSM) uses a high time-resolution polar representation of the HMF vector, which is much more weakly dependent on a particular pre-averaging timescale (appendix B.3).

We show that the inclination of the Parker spiral and nature of vector fluctuations strongly affects the 1D distribution of measurements of $B_R R^2$ and, thus, can affect estimation methods that operate directly on the 1D distributions (the mean and mode). We also show (see Section 3.3) that the Parker spiral angle and fluctuation characteristics vary significantly with radius in the inner heliosphere and thus the specific distortion to the mean and mode also varies with radius. Under the assumption that the vector fluctuations are evenly distributed about a central value, these effects are mitigated with the PSM by computing the most probable 2D field vector in the R-T plane, and then projecting this into the radial direction, as was first suggested by [47]. The applicability of the assumption of evenly distributed fluctuations was assessed in our computations of distribution skew in Figure 3.5, where we saw an increasing tendency towards skewed angular distributions close to 1AU (R

Table 3.1: Open Flux and Heliospheric Flux measurements estimated from the literature. We note for results quoted in SI units of Wb we make the conversion to 'field strength at 1AU' using 1nT AU$^2 = 4\pi(1.4955978707 \times 10^{11})^2 10^{-9}$Wb $\approx 2.81 \times 10^{14}$Wb

Ref.	**Epoch**	Φ_{open} **(nT AU^2)**	Φ_H **(nT AU^2)**	**Comments**
Present Study	2018-2020	1.2 - 1.8	$2.5^{+0.3}_{-0.6}$	Parker Solar Probe, Figure 3.7
[193]	2006-2007		2-2.5	Ulysses, estimated from Fig. 4
[47]	Various		∼3 (solar min)	Ulysses (1990-2008), ACE (1998-2009), Helios (1975-1980), Conclusion 1 - 1997/1998 solar min
[46]	1990- 2010		3.5-6.5 (1991-1992), 1.8-2.2 (1997-1998) 3-5 (2003-2004) 0.8-1.5 (2009-2010)	Ulysses, OMNI, estimated from Fig 9.
[110]	2010	0.73 ± 0.1 (PFSS 2.5 $R_\odot$) 0.9 ± 0.1 (PFSS 2.0 $R_\odot$) 1.3 ± 0.1 (MHD)	1.7-2.2	Various Magnetograms, OMNI, Mean and SD computed from Table 1
[150] (Strahl method)	1999- 2011		3.1-3,3 (2003-2004) 1.4-1.6 (2009-2010)	ACE, estimated from Fig 5 (red curve)
[150] (Kin. Method)	1999- 2011		2.8 (2003-2004) 1.0-1.2 (2009-2010)	ACE, estimated from Fig 5 (blue curve)
[220]	1990- 2014	2.5-4.6 (1991-1992) 1.8-2.1 (1997-1998) 1.8-2.5 (2003-2004) 0.7-1.1 (2009-2010)	3.9-5.0 (1991-1992) 1.4-2.1 (1997-1998) 3.2-3.9 (2003-2004) 1.1-1.2 (2009-2010)	NSO,ADAPT,OMNI, estimated from Fig. 6

¿ 0.8 AU). Thus, the PSM is likely less robust in this region as compared to closer distances to the sun. In addition, non-fluctuation departures from the Parker spiral direction, for ex-

ample magnetic clouds or field-line distortions near co-rotating interacting regions, may play a role and be a stronger influence further from the sun due to the increasingly inclined mean field and the slower orbital velocity of PSP meaning more such events are measured at these radii. Such distinct topological features would likely require a more detailed analysis such as through examining characteristics of the strahl [150, 120] to remove these measurements from the population of measurements.

As observed by [193] based on Ulysses data, we find that relative to the PSM, the effect of evenly distributed fluctuations which lie on a sphere is to systematically increase the value of the mean and mode with respect to a constant mean 2D vector as the Parker spiral grows more inclined, suggesting typical averaging methods which produce a growing estimate of Φ_H with radius are at least partially due to data processing artefacts.

Such an enhancement in Φ_H with increasing heliocentric distance is indeed observed in the PSP and 1AU data. However, this enhancement is actually observed using the Parker spiral method, as well as the mean and the mode. This suggests either the Parker spiral method is also biased at 1AU, or the enhancement is at least partially physical. As noted above, however, the PSM may be less applicable near 1AU due to the less idealised nature of the angular fluctuations about a central value, which may explain why different behaviours were seen near 1AU for the positive polarity and negative polarity data in Figure 3.6. Locally inverted flux [150] provides a plausible physical basis for such an enhancement and PSP data shows that the fraction of inverted flux grows with radius in agreement with Helios results, [120], although a simple estimate of the effect overestimates the observed discrepancy. In either case, the robustness of the PSP measurements is improved closer to the Sun.

The inverted flux method described by [150] remains an avenue to improve the estimates discussed in the paper especially with regard to quantifying more accurately the possible overestimation of the open flux further from the Sun. As remarked in Section 3.3, data coverage of the electron heat flux from the PSP Solar Wind Electrons Alphas and Protons [SWEAP; 83] instrument are less continuous than that of the magnetic field with FIELDS [19] and, thus, such an estimate will only be possible for a subset of the time intervals investigated here (as an example, the outbound phase of encounter 3 will be missing). Nonetheless, given that near 1AU, all three methods considered in this work have issues, such a cross-check will be an important part of future work. We do expect, in any case, that such an investigation should conclude that the impact of inverted flux during PSP's closest approach to the Sun should remain minimal.

In Section 3.4, we computed measurements of Φ_H across three dimensions in the heliosphere to the extent permitted by the PSP and 1AU orbits. Compared against latitude, longitude, and radius (aside from the above inflection near 1AU), PSP data shows the heliospheric flux is well approximated as a conserved quantity throughout the inner heliosphere down to 0.13AU within at least +/- four degrees of the solar equatorial plane. Making a linear fit to the better resolved negative polarity PSM measurements (blue data points, top-left panel, Figure 3.9) suggests the open flux measured by PSP in the inner heliosphere varies by at most 0.1 nT AU^2 per AU. A corollary to this observation is that the PSP data remains consistent with the Ulysses result [194, 195] that the open flux is uniformly distributed in

latitude. The continuous applicability of the $1/R^2$ scaling implies the latitudinal reorganisation process which the coronal field undergoes as it expands into the heliosphere must be fully completed well within PSP's closest approach of 28 $R_\odot$. This observation is important to establish so that Equation 3.2 can be used for all these PSP measurements and argue that measurements of $B_R R^2$ indeed constitute a direct measurement of the heliospheric flux, Φ_H. We also note the important caveat that given our observation that fraction of inverted flux increases with radius (Figure 3.8), this possible contribution to the flux should be quantified through methods such as described in [150] before a definitive confirmation can be made that the the flat behaviour out to 1AU is continuous. In particular, this is necessary for determining at what radius inverted flux becomes a negligible contribution (which we infer from Figure 3.6 to be approximately 0.8 AU).

Finally, in Section 3.4, we compared the best estimate of Φ_H as a function of time to estimates from PFSS models. Both from the point of view of decaying relative amplitude of fluctuations, the fraction of field which is locally inverted, and the empirical observation that the same value was returned to on three consecutive perihelia at different longitudes, we conclude that the PSP measurements of the heliospheric flux at perihelion represent the most direct measurements to date of the total magnetic flux escaping the corona and, as such, impose a strong global constraint on coronal models.

This constraining value obtained with the PSM ($2.5^{+0.3}_{-0.6}$ nT AU^2) remains significantly higher that that predicted by standard PFSS models for this time interval (1.2-1.8 nT AU^2). As argued above, since PSP measurements are likely to be pristine measurements with little 'excess flux' effects as compared to 1AU, this provides a strong constraint and confirmation of a fundamental mismatch between current coronal models and the known flux in the inner heliosphere [the 'open flux problem' 110].

In addition, we note the large discrepancy between the different magnetograms (e.g. the $2.0R_\odot$ HMI model almost exactly matches the open flux estimate of the $2.5R_\odot$ ADAPT-GONG model). This magnetogram-magnetogram disagreement is a well known issue with measurements of the photospheric field [174, 220], and in the absence of an independent way to calibrate these maps, correction factors have been proposed and evaluated by comparing to in situ measurements [e.g. 175]. However, [220] establish, at minimum, the correction factors must be time-dependent (and, in particular, solar cycle-dependent) and conclude it is most likely that there are a number of reasons why the coronal model and in situ measurements disagree. One possible explanation is the lack of time dependence in PFSS and most MHD models which excludes contributions to Φ_H from transient disturbances, such as coronal mass ejections (CMEs), which can carry previously closed flux into the heliosphere [e.g. 148].

We close our discussion by placing our results in context with a comparison to the actual values of open and heliospheric flux which have previously been reported in the literature. An important caveat here is that it has been well established [e.g. 221, 46, 150, 220] that the open flux varies with solar activity, solar cycle phase, and from one cycle to another. Thus, given the literature considered here is from different epochs, an exact agreement in measurement values is not to be expected. In Table 3.1, we summarise estimates based on previous work. We note the values quoted are mostly estimated from graphical representations of data and

so, they are not extremely precise. We estimate a representative range of values and focus on the years 1991-1992 and 2003-2004 for solar maxima, and 1997-1998 and 2009-2010 for solar minima. While these dates do not precisely match the true inflections of the solar cycle, among the literature studied, they are consistent with the times when heliospheric flux is observed to maximised or minimised. The table lists the relevant reference, the epoch, the value of Φ_{open} if the paper uses coronal models, and Φ_H if the paper uses in situ determinations of the magnetic flux. For each reference, a note is made on the source of the data and the location in the relevant paper where we draw the estimate.

The literature used in our summary [193, 47, 46, 110, 150, 220] spans epochs from 1990 through to 2014, encompassing solar minima in 1997 and 2008 and solar maxima in 1992, 2003, and 2014. The present study occurs in the next solar minimum (2018-2020). In general, the values determined (both for Φ_H and Φ_{open}) are higher in this study compared to values during the 2008 solar minimum and values determined by [110] for data from 2010 (rising phase) and more similar to the 1997 solar minimum, but are less than all values determined for both solar maxima (1992,2003). The ratio of Φ_H/Φ_{open} is similar to that of [110] with values determined from a 2.5 $R_\odot$ PFSS model approximately half the value determined in situ. [220] found the vales to be closer around solar minimum 2008-2009 and their ratio ($\sim$0.7) is similar to the ratio of our 2.0 $R_\odot$ PFSS model to the lower bound of the in situ measurement. However, [220] also see almost identical PFSS and in situ measurements of the flux around solar minimum in 1997.

Overall, the present work shows a consistent relationship between in situ and modelled open flux with prior works but also suggests the solar minimum studied in this work (2018-2019) had an overall higher flux baseline than the previous solar minimum (2009-2010) and, possibly, a worsening degree of the open flux problem as a result.

3.6 Conclusions

In this work we investigate the heliospheric flux content of the inner heliosphere with measurements that were taken closer to the corona than ever before, paying particular attention to the method used to estimate this quantity. We investigate the degree to which this quantity is conserved spatially, and compare it to the expected value of PFSS models. The main conclusions of our investigation are as follows:

(1) In computing the heliospheric magnetic flux, it is very important to recognise that 1D distributions of B_R are, in fact, projections of a fluctuating vector. The balance of vector fluctuations, which show a measurable dependence on distance from the Sun, changes the B_R distribution and, therefore, affects the interpretation of the 'background' value using typical statistical measures such as the mean or mode. Our implementation of the Parker spiral method [PSM, 47, 46] is more robust than the mean or mode under the qualifying assumption of evenly distributed fluctuations of the vector about a central background value. Our implementation of the PSM is also improved on previous iterations by utilising an empirical Parker spiral angle and a high time-resolution (cadence $\leq$ 1 min) parameterisation

of the heliospheric magnetic field (HMF) vector in polar coordinates, which is the most natural basis for analysing the vector fluctuations.

(2) As measured with the PSM, $B_R R^2$ is constant with longitude, latitude, and radius, at least for $0.13 < R < 0.8AU$ and for latitudes within four degrees of the solar equatorial plane. Thus, the PSP measurements are consistent with the [194] and [195] result that asserts that $B_R R^2$ is independent of latitude. In particular, the conservation with radius is evidence that the field is latitudinally isotropic at least down to 28 $R_\odot$ and so, it is well-motivated to assume Equation 3.3 holds and these single point measurements constitute a measurement of the heliospheric flux Φ_H for all probed radii.

(3) Except for intervals where PSP was very close to the HCS, the necessary assumptions of the PSM are well met during PSP's closest approaches to the Sun and, therefore, PSM measurements of Φ_H by PSP during these intervals constitute the most robust in situ estimate of the heliospheric flux in the inner heliosphere to date. Further to this, the much-reduced fluctuation amplitudes and the fraction of flux which is locally inverted suggests these measurements are insulated from physical excess flux; by following the Parker spiral method, they are robust to systematic data processing distortions. Thus, we argue that for these measurements, we can establish $\Phi_H \sim \Phi_{open}$ and this measurement constitutes a real constraint for the open flux that must be produced by coronal models.

(4) The value measured for this period of time (October 2018 - July 2020 at solar minimum) is $\Phi_H = \Phi_{open} = 2.5^{+0.3}_{-0.6} nTAU^2$, where the errors are the FWHM of the distributions of measurements close to the Sun (R ¡ 0.3AU), as depicted in Figure 3.7. This value appears higher than estimates for the previous solar minimum from around 2009-2010, but similar to prior estimates for the solar minimum from the late 1990s.

(5) This value is significantly larger than that implied by PFSS models driven by ADAPT maps over a reasonable range of source surface heights which produce estimates in the range 1.2 - 1.8 nT AU^2. From the results in [110] reported in Table 1 above, as well as in Riley et al. (submitted to this issue), we see most MHD models do not close this gap. Therefore, we infer the resolution to the open flux problem is most likely to be found in new developments in heliospheric modelling or our knowledge of the photospheric field. Such improvements may come from Solar Orbiter [SO; 138] remote observations of the polar magnetic fields [197] or from the development of full time dependent coronal models which allow for processes such as interchange re-connection on a global scale [51, 50], producing open field originating in non-coronal hole regions and which may be a more physical picture, as hinted in [21]. Another idea suggested by [170] was to include Alfvénic turbulence in an MHD simulation and this was seen to produce an envelope of fluctuations of the radial magnetic field which encompassed the amplitude of the PSP B_R measurements from encounter 1.

Moving forwards, PSP will continue to dive deeper into the solar atmosphere in the coming years, eventually reaching a perihelion distance $< 10R_\odot$. Given the current trends, the fluctuations in its magnetic field measurements are expected to continue to decay and the measurements discussed in this paper will likely become more and more accurate. There is some suggestion that the magnetic field could still be reorganising latitudinally as far out as $10R_\odot$ [169] and so we might expect that in its final orbit, PSP may start to detect a divergence

from the $1/R^2$ trend observed in the radial field component so far, indicating a breakdown of the latitudinal isotropy which allows this powerful single point inference of the open magnetic flux. At the same time, such a measurement would be hugely exciting as it would constitute for the first time a direct measurement of the Sun's underlying dipole moment which, aside from being a fundamental quantity of interest, may also be able to address the calibration uncertainty in photospheric maps. We note that PSP's direct latitudinal sampling will remain confined to within four degrees of the solar equatorial plane as it continues to get closer. However, since the Solar Orbiter has now joined the PSP in the inner heliosphere, it will allow multi-point and out of the ecliptic in situ measurements [71] to extend these results and provide even better and more direct constraints on the homogeneity of the heliospheric flux in the inner heliosphere. This includes directly sampling the solar wind eventually as far as 30 degrees from the solar equatorial plane, which will be important in robustly confirming conclusion (2) above.

Chapter 4

Magnetic connectivity of the ecliptic plane within 0.5 AU : PFSS modeling of the first PSP encounter

In this chapter we present the peer-reviewed article [14] which analyzes data from the first orbit of Parker Solar Probe in November 2018 with potential field source surface models and ballistic interplanetary field lines, establishing source region mapping for PSP's first close approach to the sun. Additionally, by reproducing the measured radial magnetic field at PSP as closely as possible, we were able to investigate a number of sources of variability within the modeling and look for optimums. For example, we found an overall best source surface height parameter for the PFSS Model, but also a suggestion that the best applicable height varied in time, a finding supported by complementary work [153]. The timeseries was also better reproduced by the modeling using time-varying magnetogram measurements, i.e. accounting for evolution of the photospheric field. Lastly, slightly better agreement was found using data-driven ballistic mapping compared to assuming a constant solar wind speed for the whole encounter, suggesting stream interactions are important.

This study also showed that a very simple representation of the coronal and interplanetary magnetic field was sufficient to reproduce most of the large scale features measured by PSP/FIELDS in this encounter. This means that the original PFSS and Parker models, both over 60 years old, remain relevant and useful in the era of Parker Solar Probe. Owing to this successful application, this methodology has gone on to be widely used in application to PSP, for example supporting connectivity estimates for the first crossing the Alfven critical surface [82], supporting inferences of solar supergranules leaving imprints in the solar wind [17], and leading to footpoint predictions for planning coordinated observations between ground based observers and PSP `https://whpi.hao.ucar.edu/whpi_campaigns.php`.

The full citation for this work as published is Samuel T. Badman et al. "Magnetic Connectivity of the Ecliptic Plane within 0.5 au: Potential Field Source Surface Modeling of the First Parker Solar Probe Encounter". In: *Astrophysical Journal Supplement* 246.2, 23 (Feb. 2020), p. 23. DOI: `10.3847/1538-4365/ab4da7`. arXiv: `1912.02244 [astro-ph.SR]`.

The full author list is as follows: Samuel T. Badman, Stuart D. Bale, Juan Carlos Martìnez Oliveros, Olga Panasenco, Marco Velli, David Stansby, Juan Camilo Buitrago-Casas, Victor Réville, John W. Bonnell, Anthony W. Case, Thierry Dudok de Wit, Keith Goetz, Peter R. Harvey, Justin C. Kasper, Kelly E. Korreck, Davin E. Larson, Roberto Livi, Robert J. MacDowall, David M. Malaspina, Marc Pulupa, Michael L. Stevens and Phyllis L. Whittlesey.

4.1 Abstract

We compare magnetic field measurements taken by the FIELDS instrument on Parker Solar Probe (PSP) during it's first solar encounter to predictions obtained by Potential Field Source Surface (PFSS) modeling. Ballistic propagation is used to connect the spacecraft to the source surface. Despite the simplicity of the model, our results show striking agreement with PSP's first observations of the heliospheric magnetic field from ∼0.5 AU (107.5 $R_\odot$) down to 0.16 AU (35.7 $R_\odot$). Further, we show the robustness of the agreement is improved both by allowing the photospheric input to the model to vary in time, and by advecting the field from PSP down to the PFSS model domain using in situ PSP/SWEAP measurements of the solar wind speed instead of assuming it to be constant with longitude and latitude. We also explore the source surface height parameter (R_{SS}) to the PFSS model finding that an extraordinarily low source surface height ($1.3-1.5R_\odot$) predicts observed small scale polarity inversions which are otherwise washed out with regular modeling parameters. Finally, we extract field line traces from these models. By overlaying these on EUV images we observe magnetic connectivity to various equatorial and mid-latitude coronal holes indicating plausible magnetic footpoints and offering context for future discussions of sources of the solar wind measured by PSP.

4.2 Introduction

Parker Solar Probe [PSP; 52] is a NASA mission intended to revolutionize our understanding of the solar corona by becoming the first spacecraft to measure it's outer layers in situ. The fundamental science objectives are to (1) Trace the flow of energy that heats and accelerates the solar corona and solar wind; (2) Determine the structure and dynamics of the plasma and magnetic fields at the sources of the solar wind; and (3) Explore mechanisms that accelerate and transport energetic particles [52].

Central to it's science goals is PSP's record-breaking orbit. PSP launched on August 12 2018 and, after it's first Venus gravity assist, entered into the closest-grazing heliocentric orbit ever reached by an artificial satellite. On November 6 2018 PSP completed it's first perihelion pass at $35.7R_\odot$ from the Sun traveling at almost 100 km s^{-1}. Future Venus gravity assists will eventually asymptote these numbers to 9.86 $R_\odot$ closest approach at over 200 km s^{-1} in December 2024. A unique outcome of achieving this rapid orbital velocity is that PSP briefly reached a greater angular velocity than the Sun's equator. This means it moves

very slowly relative to the local corotating magnetic structure and samples the same solar meridians multiple times in the same orbit (Figure 4.1C).

PSP carries a suite of four scientific instruments. The electromagnetic fields investigation [FIELDS; 19] probes in situ electric and magnetic fields and plasma waves, the spacecraft potential, quasithermal noise and low frequency radio waves. The Solar Wind Electrons Alphas and Protons investigation [SWEAP; 83] provides distribution functions and density, velocity and temperature moments of the most abundant species in the solar wind. The Integrated Science Investigation of the Sun [IS⊙IS; 127] observes energetic electrons, protons and heavy ions from 10s of keV to 100 MeV. The Wide-Field Imager for Solar Probe Plus [WISPR; 218] is a white light imager which observes structures in the solar wind, such as shocks, approaching and passing the spacecraft. In this work we utilize FIELDS DC magnetic field data and SWEAP proton velocity moments.

A major source of contextual information for spacecraft in situ measurements of the solar wind comes from global coronal and heliospheric modeling. Modeling techniques of varying complexity [see e.g. review by 231] have been developed using historical measurements (both remote and in situ) as boundary conditions. PSP provides unique constraints on such models given it is sampling entirely new regions of the heliosphere. It is therefore of great interest to compare PSP observations to these models both to contextualize the measurements and to improve the models themselves.

In this work we compare PSP magnetic field observations with predictions made using the widely used Potential Field Source Surface (PFSS) model [4, 186, 68, 223]. PFSS employs two key assumptions: (1) A current-free corona, which is a special case of force free models which require an assumption of very low plasma beta (meaning magnetic pressure dominates over thermal pressure). (2) A spherical source surface of heliocentric radius R_{SS} at which field lines are enforced to be radial, simulating the role of the solar wind in opening these field lines out to interplanetary space. Despite these assumptions PFSS compares well to more modern magnetohydrodynamic (MHD) models [e.g. 173] and is widely used due to it's computational simplicity and associated high resolution.

With zero currents the magnetic field, $\mathbf{B}$, in PFSS may be expressed as a scalar potential, Φ_B, such that $\mathbf{B} = -\nabla\Phi_B$. By the "no-monopole" Maxwell equation, this potential must obey the Laplace equation, $\nabla^2\Phi_B = 0$, for which solutions are very well understood. PFSS solves for the field in an annular volume of radial extent $1R_\odot \leq r \leq R_{SS}$. Boundary conditions are the measured radial magnetic field at the photosphere ($1R_\odot$) and the requirement that the tangential components of $\mathbf{B}$ vanish at R_{SS}. This allows the problem to be uniquely solved as a spherical harmonic decomposition, resulting in a full 3D magnetic field model between the photosphere and source surface. The solution is steady state and represents a low energy bound on more general force free models, [166].

PFSS models have historically been used to predict magnetic polarity at 1AU [e.g 68], coronal structure observed during solar eclipses [e.g. 4], and identifying open field line regions associated with coronal holes [e.g. 226]. In addition, even though PFSS only models the magnetic field directly, [227] showed an inverse correlation between the divergence rate of PFSS field lines with observed solar wind speed at 1AU, indicating that coronal magnetic

field topology plays an important role in the acceleration of the solar wind. This observation has since been refined by [6, 11, 10] into the modern WSA model which assimilates PFSS and a Schatten current sheet model [187], and is currently used operationally in space weather predictions and hosted by NASA's Coordinated Community Modeling Center (CCMC, `http://ccmc.gsfc.nasa.gov`).

Here, we report our results obtained from the use of a simple PFSS model and a ballistic propagation model [146] to connect the spacecraft to the PFSS model domain, and use this to explain features of large scale magnetic structure observed in PSP's first solar encounter. In Section 4.3 we introduce the data taken by PSP used in this work as well as using it to extrapolate magnetic polarity structure out to 1AU and compare to measurements by the Magnetic Field Investigation [MFI; 103] on board the Wind spacecraft [62]. In section 4.4 the implementation of PFSS modeling and the procedure to connect those results to the in situ measurements of PSP are described. Section 4.5 lists the major results from this work: 1) General successful prediction of in situ timeseries measurements. 2) Improvements to modeling through time evolving magnetospheric inputs and use of PSP/SWEAP solar wind velocity measurements. 3) Recovery of smaller scale structure consistent with measurements when the source surface height parameter (R_{SS}) of the PFSS model is dramatically lowered. 4) Identification of mid-latitude and equatorial coronal holes as potential sources of the solar wind PSP measured in it's first encounter. We conclude in section 4.6 with a discussion of the results and interpretation with particular attention to address the limitations of this modeling method in light of it's simplifications, and reference concurrent and future modeling work.

4.3 PSP Data

Timeseries and spatial distribution.

We begin by presenting the data used in this work from the FIELDS and SWEAP instruments on board PSP measuring during the first solar encounter (E1) from 2018-10-15 to 2018-11-30. From FIELDS we use measurements of the radial component of the magnetic field (B_r) and from SWEAP we use the radial component of the proton velocity moment (V_{SW}). Since the focus of this work is the large scale solar wind structure, we first pre-process this data to remove transients and rapid fluctuations such as the newly observed $\delta B/B \sim 1$ magnetic "switchbacks" and velocity spikes (see e.g. [18, 81, 45, 72]. To do this we bin the full cadence data into hourly segments, generate a histogram of the data in each bin and take the modal value (the value corresponding to the peak of the histogram).

The resulting time series are shown in figure 4.1. B_r is shown in panel (A), in which we identify a $1/r^2$ overall trend (dotted line) and colorize by polarity with the convention of red for radially outwards ($B_r > 0$) and blue for radially inwards ($B_r < 0$). This convention will be followed in all plots in this paper. The time of perihelion at $35.7R_\odot$ is easily identified by the occurence of maximum field strength on 2018-11-6. The time series shows generally

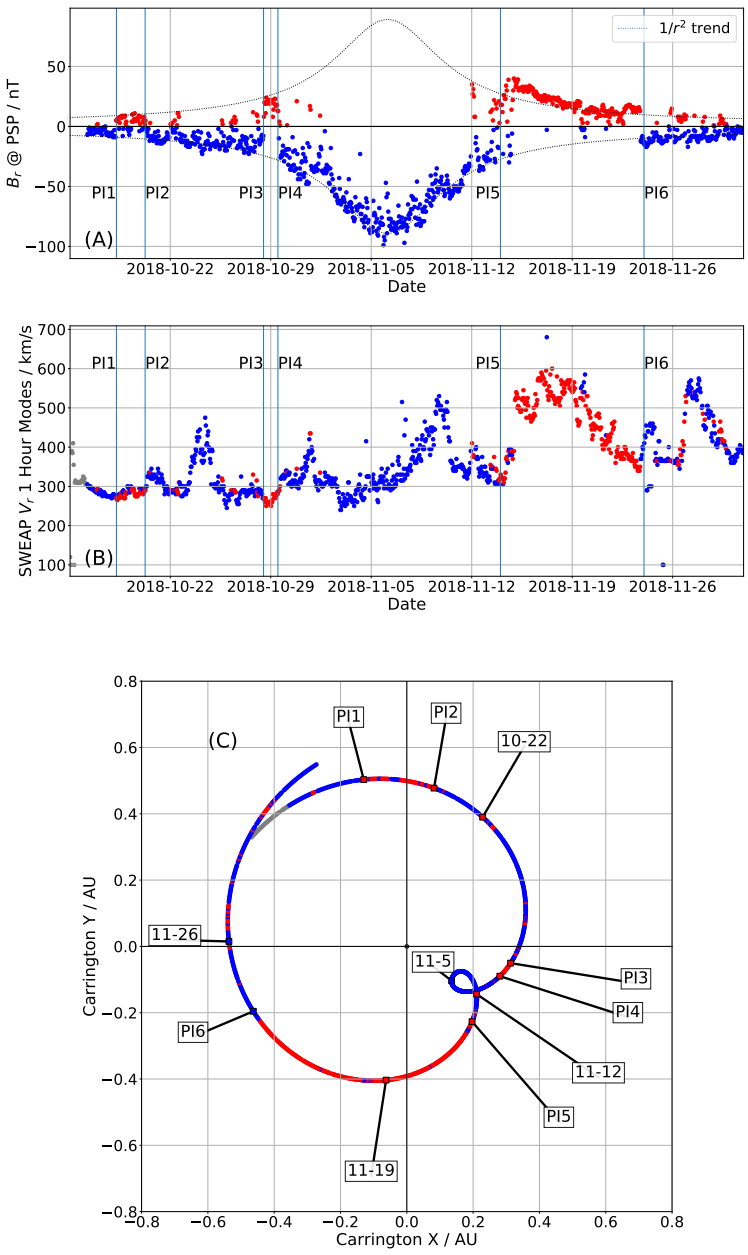

Figure 4.1: **Exposition of 1 hour modes (see main text) of PSP data taken during Encounter 1 (E1) from 2018-10-15 to 2018-11-30.** Perihelion occurred on 2018-11-6. Panel (A): PSP/FIELDS radial magnetic field (B_r) vs. time colored by magnetic polarity: Positive (red) means radially outwards, while negative (blue) means radially inwards. A $1/r^2$ dotted trend line shows the zeroth order behavior. Panel (B): PSP/SWEAP radial proton bulk velocity (V_{SW}) vs. time colored by measured magnetic polarity. Panel (C): The E1 orbital trajectory of PSP plotted in Carrington (solar-corotating) coordinates. The trajectory is colored by the measured magnetic polarity, demonstrating the apparent spatial structure of the magnetic sectors sampled.

negative polarity indicating the orbital trajectory was mostly on the southward side of the heliospheric current sheet (HCS), and a number of clear multi-hour excursions into positive polarity on 2018-10-20 (bounded by PI1 and PI2), 2018-10-29 (bounded by PI3 and PI4) and from 2018-11-14 (PI5) through to 2018-11-23 (PI6). A detailed look at the nature of these inversions as PSP crossed the HCS is given in [206]. Positive spikes on 2018-10-23 and 2018-11-13 are attributed to small coronal mass ejections (CMEs) as discussed in [128, 91, 144, 56, 135].

V_{SW} is shown in panel (B) and colorized by the magnetic polarity for ease of comparison with the B_r time series. We observe a mostly slow wind (<500 km s^{-1}) which is generally uncorrelated with the magnetic polarity inversions, except for PI5 which is coincident with a sudden transition to a moderately fast wind stream peaking at about 600km s^{-1}.

Panel (C) of figure 4.1 demonstrates the spatial distribution of magnetic polarities observed during PSP's Encounter 1. We plot the spacecraft trajectory (projected on to the solar equatorial plane) in Carrington coordinates (i.e. corotating with the Sun's equator) and color it according the polarity of B_r. In this co-rotating frame, PSP starts in the upper left quadrant and tracks clockwise (i.e. retrograde). As it's radial distance from the sun decreases, it's angular velocity catches up to that of the Sun, eventually reaching co-rotation prior to perihelion, it briefly rotates faster than the Sun before transitioning back to sub-corotational speeds as it climbs to higher altitudes. This results in the small loop centered near the 2018-11-5 date label. It should also be noted that this changing angular speed means the rate of change of longitude of PSP varied dramatically; two out of the six week interval shown were spent between the longitudes of the co-rotation loop. The extent and location of the positive polarity inversions in the time series are identified as the red regions of the trajectory. Clearly the PI1-PI2 and PI3-PI4 intervals occurred over a small range of solar longitudes (< 10 degrees), while the interval between PI5 and PI6 was protracted over a much larger region, spanning about 90 degrees of solar longitude.

Parker spiral stream structure and comparison to 1AU Measurements

In the previous section, we have shown the in situ data of B_r and V_{SW} measurements and it's orbital context. The orbital context allows us to directly assign solar wind parameters along a narrow path through a complex 3D medium. In this section we seek to extrapolate these measurements to infer a solar wind stream structure to connect this data out to 1AU and compare it to Wind/MFI observations of the magnetic field polarity.

To accomplish this, we use the Parker spiral [154] approximation in which we assume each point along the PSP trajectory is threaded by a Parker spiral field line with a curvature determined by the in situ solar wind speed, giving the spiral the following 2D parameterization of longitude and radius (ϕ, r):

$$\phi(r) = \phi_0 - \frac{\Omega_\odot}{V_{SW}}(r - r_0) \tag{4.1}$$

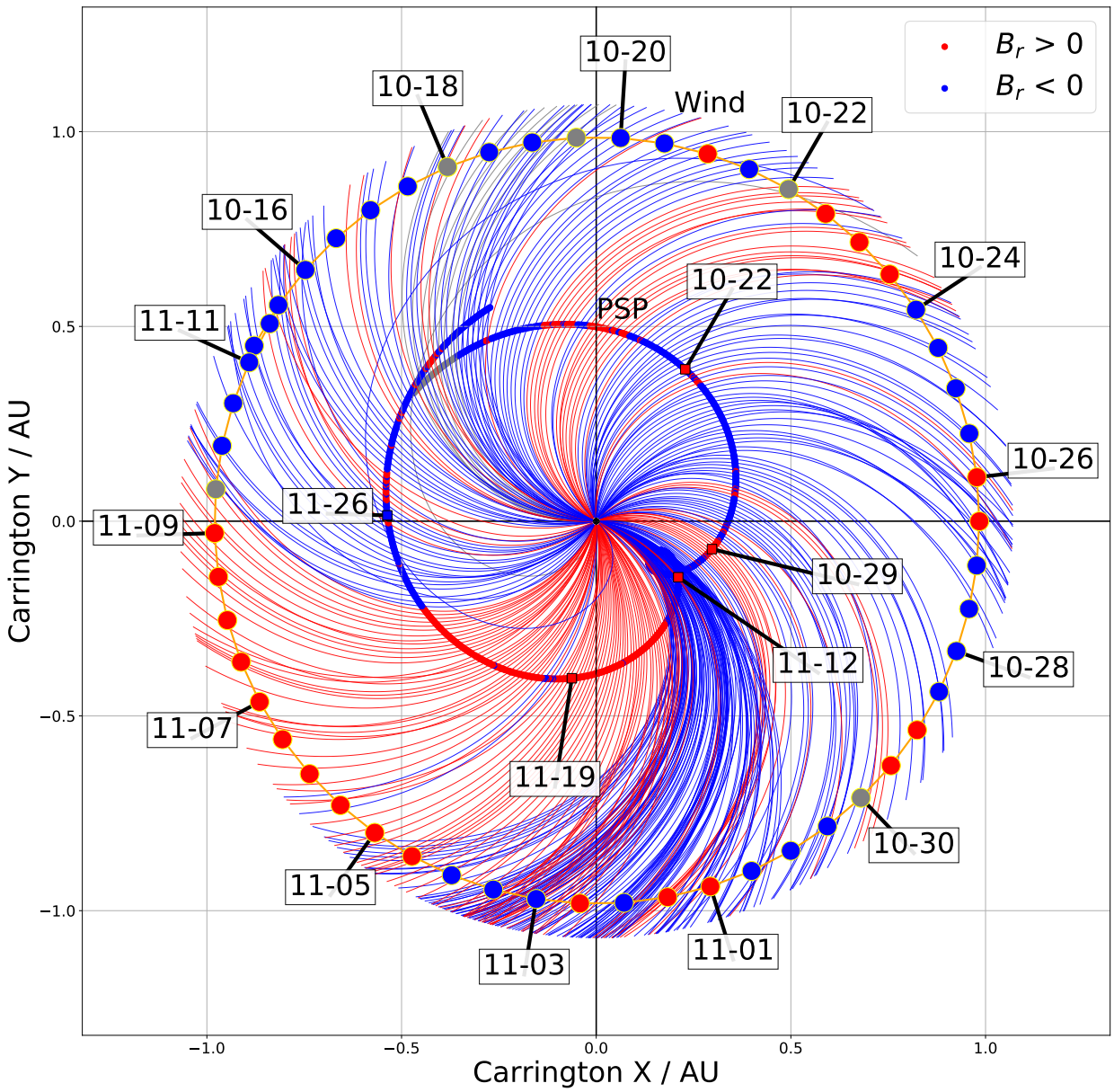

Figure 4.2: **Magnetic polarity sector structure implied by PSP extrapolated to 1AU.** Parker spiral field lines are initialized by the SWEAP V_{SW} measurements and colored by the FIELDS B_r polarity. These are propagated out to 1 AU. Measurements of the magnetic polarity by Wind/MFI are shown at a 12 hourly cadence. For each time, positive polarity is designated if the field is $> 7/12$ positive for ± 6 hours of **this time** and similar for negative, otherwise the polarity is designated mixed and colored grey. As in figure 4.1 (C), the coordinates corotate with the Sun.

where ϕ_0, r_0 are the longitude and radial distance of PSP at the time of the V_{SW} measurement. $\Omega_\odot$ is the solar rotation rate which we calculate from the equatorial rotation period of 24.47 days, assuming the latitudinal offset of PSP (< 5 degrees) is small enough to not consider differential rotation. This equation shows the qualitative dependence of the spiral field lines of solar wind speed: faster V_{SW} gives straighter field lines (smaller $d\phi/dr$), slower wind speed produces more curved field lines (larger $d\phi/dr$).

Each spiral field line is colored by the PSP measured polarity. The result is plotted in figure 4.2, again in Carrington coordinates. The date-labeled PSP trajectory is shown in the context of the stream structure out to 1AU where we plot the trajectory of the Wind spacecraft, located at the Earth L1 point, for a similar date range. At a 12 hour cadence, we plot the polarity of the radial magnetic field measured by the Wind/MFI instrument. Guided by a similar convention from [69], to assign this 12 hour interval a single polarity, we take all measurements at a minute cadence from $\pm$ 6 hours of the measurement time and assign a positive polarity (red) if more than 7/12 of all data values are positive, and negative polarity (blue) if more than 7/12 of all data values are negative. If neither of these criteria are satisfied, the field is designated "mixed" for that interval and colored grey.

The choice of generating field lines at a constant time interval means that as the relative angular velocity of the spacecraft gets smaller, the field lines appear to bunch together more. We emphasize this is a pure sampling effect and does not indicate anything physical about the field. It is further compounded by the corotation loop which means several field lines are generated at the same Carrington longitude.

It is important to note that PSP and Wind sampled the same solar longitudes at different times due to the differing orbits. In displaying the picture in figure 2, we are assuming the structure shown is essentially fixed in time as the spacecraft travel through it making measurements. Even so we see the dominant features in the PSP data bear out at 1AU using this simple picture. The PI1-PI2 interval connects via the spiral to positive polarity at 1AU. The PI3-PI4 interval merges into slowing wind which also mixes the negative polarity at perihelion with the onset of the positive polarity and fast wind during PI5. Although, as noted above, this region of the plot is made more complicated by the perihelion loop, the boundaries where field lines overlap further out than PSP represent likely locations where the Parker Spiral assumption breaks down and field lines would bend into compressions or rarefactions. The more complex picture of interacting streams corresponds to a greater mix of positive and negative polarity measured as Wind sampled this region. The continuous period of positive polarity between PI5 and PI6 at PSP is also seen by Wind, with the Parker spiral very accurately predicting the transition from positive back to negative (PI6) by Wind on 2018-11-10, well in advance of PSP traversing the same structure on 2018-11-23.

This good correspondence between PSP and 1AU measurements suggests the polarity inversions observed at PSP are relatively stable large scale features which must have an origin in open flux emerging from the solar corona. In addition, the implementation of the Parker spiral model lays the groundwork for the dicussion in the next section on connecting PSP measurements inwards to the corona where they can be compared to modeling results. As mentioned above, we also note that the stream structure implies magnetic pile-ups (and

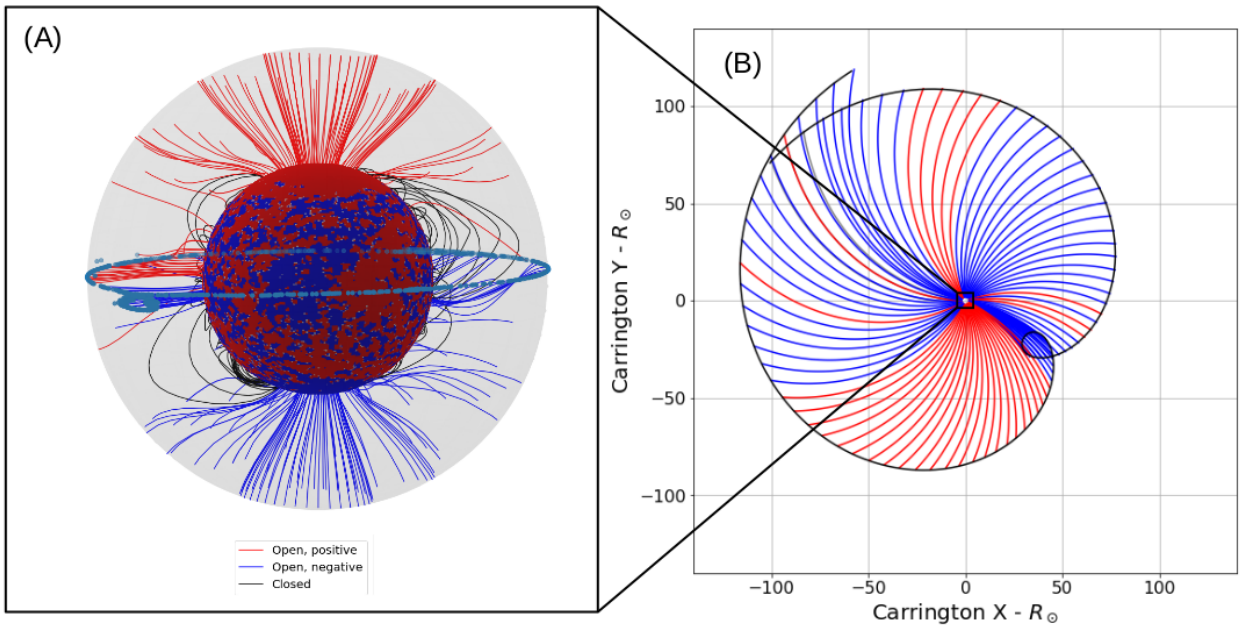

Figure 4.3: **Schematic of process to connect PSP Measurements to PFSS Modelling.** Panel (A) : PFSS model output from *pfsspy*. The synoptic magnetogram input is shown as the photospheric (inner) boundary. The model domain is bounded at at the exterior by the source surface (grey surface). Field lines initialized by a uniform grid at the photosphere are shown. Panel (B) : The outer boundary of the model is connected to the orbital position of PSP via an ideal Parker spiral magnetic field line. With some choice of solar wind speed, this maps the PSP trajectory to a locus of latitudes and longitudes at the source surface. This is illustrated by the near equatorial blue data points on the source surface in Panel (A).

therefore divergence from the Parker spiral picture) further out than PSP, suggesting the locations of stream interaction regions (SIRs) which are studied in [3, 39]. However, tracing the field lines inwards, the streams should interact and distort each other much less.

4.4 Modeling Method

Having introduced the PSP data from E1, it's spatial context and salient features, we now introduce our PFSS modeling procedure and method of producing resulting time series predictions at PSP. This procedure is schematically illustrated in Figure 4.3, and derives from [202].

PFSS Implementation

The PFSS model is run in python using the open source *pfsspy* package [235, 199]. This code is available online and is very flexible, fast and easy to use. As input, it takes synoptic maps of the radial magnetic field at the photosphere and a value for the source surface height parameter R_{SS}. From these data it produces a full 3D magnetic field within the modeled volume, as well as a utility to trace individual magnetic field lines through the model solution. This input/output mapping is illustrated in Figure 4.3 (A) which shows selected 3D field lines produced by *pfsspy*, the extent of the model and the photospheric map which seeds the model. The grey surface illustrates the spherical source surface at which the field is constrained to be radial. As shown by the coloring of the field lines, they may either be open (red or blue depending on polarity) or closed (black). Open field lines are those which by definition intersect the source surface. Where they connect to the inner boundary of the model they indicate the probable locations of coronal holes (see Section 4.5). During solar minimum, most open field lines emerge from large polar coronal holes.

For the input magnetogram, there are a number of possible sources of data. In this work we initally considered the Global Oscillation Network Group [GONG; 63] zero corrected data product [37], and the Heliospheric Magnetic Imager [HMI; 188] vector magnetogram data product [70]. GONG is measured from a network of ground based observatories and is operationally certified as input to a number of space weather prediction models. HMI, an instrument on board the Solar Dynamics Observatory [SDO; 156], is higher resolution and does not suffer atmospheric effects. Both of these have the limitation that they rely purely on observations and so cannot account for evolution on the far side of the Sun until that part of the Sun rotates into view. With this in mind, we have also used the Air Force Data Assimilative Photospheric Flux Transport (ADAPT) modeled magnetogram [9] evaluated with GONG input, and the DeRosa/LMSAL modeled magnetogram [189] (based on HMI) to compare results. ADAPT and LMSAL make use of surface flux transport models into which new observations are assimilated. This procedure therefore models the far side evolution, implying a more accurate global picture of the photosphere. In practice, on discriminating between PFSS outputs from different magnetogram inputs using PSP data, we find little impact on our conclusions. We find GONG maps produce smooth predictions combining maps from one day to the next (section 4.5), and require no pre-processing. While this smoothness may be a product of low resolution and atmospheric effects, it results in good clarity in displaying the features discussed in section 4.5 without changing the conclusions. ADAPT maps resulted in very similar predictions but with some small fluctuation in the flux strength prediction from one day to the next which can be interpreted as model uncertainty. HMI included some missing days in the magnetogram record and does not include reconstruction of unobserved polar regions. The DeRosa/LMSAL model reconstructs the polar region and produces very similar predictions to the other models at lower source surface heights. For source surfaces much higher than $2.0 R_\odot$ some deviation from the observations and other models takes place such as predicting constant positive field prior to October 29 (see Appendix A). This adds to the evidence we build in the results below that taking lower

source surface heights in general is necessary for the best agreement between PFSS modeling and the observations.

In addition, in certain parts of this work, we use a model from a single date to represent the entire encounter (figures 4.6C, 4.7, 4.8A). The extra model evolution of ADAPT or the DeRosa model actually makes this presentation difficult since times earlier than the model evaluation have changed significantly and no longer agree with what PSP measured at that time. For GONG, longitudes earlier in time are frozen after they go out of view and due to fortuitous orbital alignment the "older" parts of the model agree better with corresponding PSP measurements. For this reason, and in absence of any strong effects on conclusions, PFSS model results shown in this paper use GONG magnetograms unless otherwise stated. Further discussion of this choice, and comparisons of timeseries predictions using different magnetograms are included in Appendix C.1.

Ballistic Propagation Model

PFSS only models the coronal magnetic field out to the source surface at a couple of solar radii. PSP on the other hand made in situ measurements at radii down to a minimum of $35.7R_{\odot}$ during it's first encounter. To connect the model domain outwards to PSP's orbit we use ballistic propagation. Proposed by [146], this technique assumes an arbitrary point in the heliosphere can be connected inwards to the corona by an ideal Parker spiral field line. The curvature of the spiral is driven by the solar wind speed measured out in the heliosphere. This model implicitly assumes that this measured wind speed (and therefore spiral curvature) remains constant all the way down into the corona. While this is not an accurate picture of the real solar wind, the dominant correction to this (acceleration of the solar wind) is counterbalanced by the effect of corotation meaning that the real footpoint of the field line is in fact close to where the ballistic propagation assumption puts it. [146] conclude the error in longitude of this method is within 10 degrees. The implications of this error are discussed in section 4.5.

Much like in section 4.3, we assign a series of Parker spiral field lines to the orbit of PSP but this time propagate them *inwards* to derive a longitude and latitude on the source surface to which each position along the PSP trajectory is connected to. The spiral field lines initialized from the PSP orbit are show in figure 4.2(B) and the resulting locus of coordinates on the source surface are indicated by the near equatorial blue scatter points in panel (A). At each of these points on the source surface B_r is obtained from the model and then multiplied by the value r_{SS}^2/r_{PSP}^2 at that time to project this model field out to PSP. Finally, since mean total unsigned flux between magnetograms generally do not agree with each other, rather than assume one particular magnetogram is correctly normalized, we scale our results by a constant factor so that their peak magnitude is equal to the peak magnitude measured by PSP at perihelion (figure 4.1A). As shown in figure 4.6 and discussed in section 4.6, this factor is a function of source surface height and ranges from O(10) to order unity over the range of source surface heights considered in this work.

4.5 Results

We now present the results of comparison of the above modeling to the PSP data.

Time series prediction and comparison

In figure 4.4, we overlay time series predictions using GONG magnetograms and a source surface height $R_{SS} = 2.0R_\odot$ (the choice of this value is discussed in section 4.5). The model results are plotted as lines while the B_r data are plotted unchanged from figure 4.1(A) as a scatterplot colored by polarity. We compare a number of modeling variations across the four panels:

- In each panel a number of modeling realizations are plotted as faint colored lines. Each realization is generated using a GONG magnetogram from a different date spaced apart by 3 days over the encounter. We overplot a "time-integrated" model as a thick solid black line where these individual realizations are combined together: for each faint line only the data from ± 1.5 days from the date of the relevant magnetogram are used and stitched together sequentially. In terms of scaling, the models are stitched together first and then multiplied by a constant factor to match the peak measured B_r. For panels A and B this value is 6.90 while for panels C and D it is 6.73.
- From left to right (A,C vs B,D) we multiply the prediction and data by r_{PSP}^2 to compare the models and data without the $1/r^2$ scaling which dominates the overall shape of the time series in the raw data.
- We demonstrate the impact of using the measured solar wind velocity (bottom panels, C and D) when generating Parker spirals to connect PSP to the source surface vs just assuming a constant slow solar wind speed of 360 km s^{-1} (top panels, A and B).

We observe an overall good agreement with a generally negative polarity field, dominantly varying with $1/r^2$ as predicted by the Parker spiral model, and with a significant excursion into positive polarity bounded by PI5 and PI6. However, we note here that PI1, PI2, PI3 and PI4 are lacking in these predictions. This matter is discussed further in section 4.5 where we recover these polarity inversions through tuning of the source surface height parameter.

Examining the ensemble of models over different observations we see some scatter about the data, and in particular an unobserved "bump" in the field around 2018-11-4. This small disagreement with the data is mitigated by the time-integrated model which in all cases traces closer to the real data and ignores this unobserved bump. From this, we infer that the time evolution of the input magnetograms is important on the timescale over which the PSP observations took place but treating it as a time series of steady state models mitigates the lack of dynamics in PFSS modeling.

Comparing the models with and without the $1/r^2$ scaling, we observe the negative interval around perihelion infers a near constant (flat) magnetic field at the source surface. This is

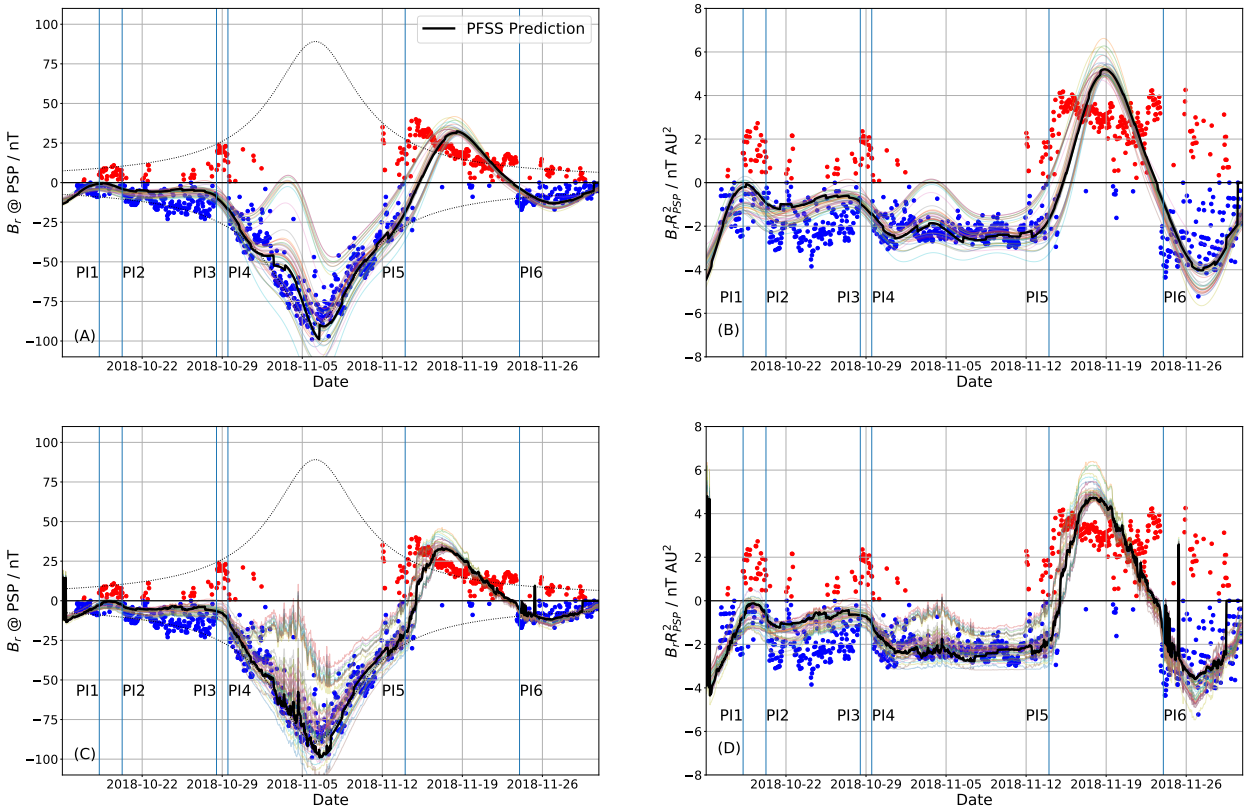

Figure 4.4: **Comparison of PFSS Predictions of B_r with observations.**. The left hand column (A,C) shows predictions and measurements in situ at PSP, while the right hand column (B,D) scales out the $1/r^2$ dependence to compare predictions near the source surface. The top row (A,B) shows predictions made assuming a constant wind speed of 360km s^{-1}, while the bottom (C,D) row shows the results of using the SWEAP V_{SW} measurements to connect the source surface to PSP. The faint colored lines in each plot indicate an ensemble of predictions made by using updating magnetograms at a cadence of 3 days. The solid black line indicates a synthesis of these predictions by combining segments from each prediction ± 1.5 days from the date of that photospheric map. Models all use GONG data and a source surface height of $R_{ss} = 2.0 R_\odot$

consistent with the fact that this time interval corresponds to times when PSP was corotating or moving very slowly compared to the solar surface and so was likely crossing flux tubes very slowly and observing a very slow change in source region (see section 4.5).

We also observe that using solar wind speed measurements to propagate field lines causes subtle improvement to model. For example, the timing of maximum field strength agrees better with data, the relative amplitude of the peak compared to the trough improves and the near perihelion field profile flattens in panel D vs B. The timing and steepness of the PI5 polarity inversion also improves.

Meanwhile, PI6 demonstrates a limitation of PFSS: The prediction is for a smooth, protracted transition through $Br = 0$ whereas the data shows a sharp transition. MHD modeling [169] has shown that further latitudinal evolution beyond the source surface sharpens the location of polarity inversions by homogenizing the radial field in latitude, which better matches Ulysses observations [194, 193]. This could explain this discrepancy.

Additionally, even after time integration and correction for varying solar wind speed, the general negative field predicted prior to PI3 is approximately a factor of two weaker than measurements suggest at the source surface (Panel D). This indicates the same A/r^2 scaling (with a constant A) of the PFSS-derived field magnitude is not globally applicable to the whole time series, particularly as PSP gets closer to the polarity inversion line (PIL, see section 4.5) where PFSS predicts a drop off in field strength. The sharpening effect of non-radial expansion outside the source surface is a likely explanation for this discrepancy too as it predicts the field strength remains constant closer to the PIl than PFSS suggests.

Impact of variation of source surface height parameter

In this section, the impact on the results of varying the source surface height are investigated. While this is a numerical modeling parameter, it does have physical consequences on the predictions of the model affecting the total open flux, the apparent size of coronal holes and the complexity of the polarity inversion line which seeds the heliospheric current sheet in other models such as WSA [11].

Coronal Hole Distribution

In figure 4.5 we begin our discussion of the source surface height parameter by comparing the footpoints of open field lines to synoptic maps of extreme ultraviolet (EUV) emission from the solar corona. This data is assembled from data observed during Carrington Rotation 2210 by STEREO/EUVI [234] observing at 193Å and SDO/AIA [102] observing at 193Å, these emissions are produced by Fe XII, a highly ionized state of Iron which is excited around 1,000,000 K. The brightness of these maps indicates the density of plasma at the 1,000,000 K isotherm which is approximately a surface of constant height in the lower corona. Dark regions identify coronal holes which are the probable locations of open field lines which allow plasma to escape outwards into the heliosphere resulting in an underdense region.

By comparing the locations of footpoints of open field lines implied by the PFSS model, we can evaluate how accurately the model reproduces the observed coronal hole distribution. We use model results using the GONG 2018-11-6 map (centered on perihelion) and vary the source surface from 2.5 $R_\odot$ down to 1.5 $R_\odot$. The open footpoints are generated by initializing field lines from a uniform grid at the source surface where the field lines are all open by construction. We then use the *pfsspy* field line tracing utility to propagate each line down into the model and find it's point of intersection with the lower boundary of the model.

From comparing dark regions with the modeled footpoint locations we see a generally sensible solar minimum model result: the majority of open field lines map to the north and south polar coronal holes, with some equatorward extensions picked out along with individual isolated mid-latitude and equatorial coronal holes.

However, we observe for the canonical $2.5R_\odot$ that these isolated coronal holes are very underexpanded in the PFSS model, with particular emphasis on the small negative equatorial coronal hole around 340 degrees longitude and the more extended positive polarity one just below 300 degrees longitude. Lowering the source surface height to $2.0R_\odot$ we find a more reasonable filling of these two features. Going further and examining a source surface height of $1.5R_\odot$, we start to overexpand the mid-latitude and equatorial coronal holes and produce some footpoints without obvious coronal hole correspondence.

It should be noted a precise match between dark EUV images and the footpoints of open field lines is not expected since the EUV coronal hole boundary is somewhat wavelength dependent. Nevertheless, it appears 2.0 $R_\odot$ is a reasonable height for a globally consistent PFSS model with regard to observed coronal hole locations. This inference is consistent with the parameter chosen for the predictive modeling work for PSP E1 by [178] to make PFSS results agree with MHD modeling as well as possible without overexpanding coronal holes. [100] also found that the canonical 2.5 $R_\odot$ source surface height resulted in underexpanded coronal holes for a similarly quiet solar minimum carrington rotation. More recently, [145] has made the same observation for PFSS extractions of GONG maps from 2006 to 2018. Further evidence for this lower source surface height is presented in appendix C.2 where we compute a cost function as a function of source surface height and show the "optimum" source surface height is significantly lower than $2.5R_\odot$ for both GONG and ADAPT evaluations. We use these findings to justify our use of this parameter value in our comparison in figure 4.4, and to inform our further investigation of variation of this parameter.

Impact on Timeseries Predictions

We next examine the results of varying the source surface height parameter on the time-integrated best fits from section 4.5. The results are summarised in Figure 4.6. Panel (A) shows time series predictions for source surface heights ranging from $2.5R_\odot$ down to $1.3R_\odot$. The B_r values are shown on a symmetric log scale to emphasize the polarity inversion features. The scaling factors applied to match the model peak field with the measured peak field are indicated in the legend. These range from 14.0 at the canonical $R_{SS} = 2.5R_\odot$ down to order unity for $R_{SS} = 1.3R_\odot$. Panels (B-D) are shown to contextualize the time

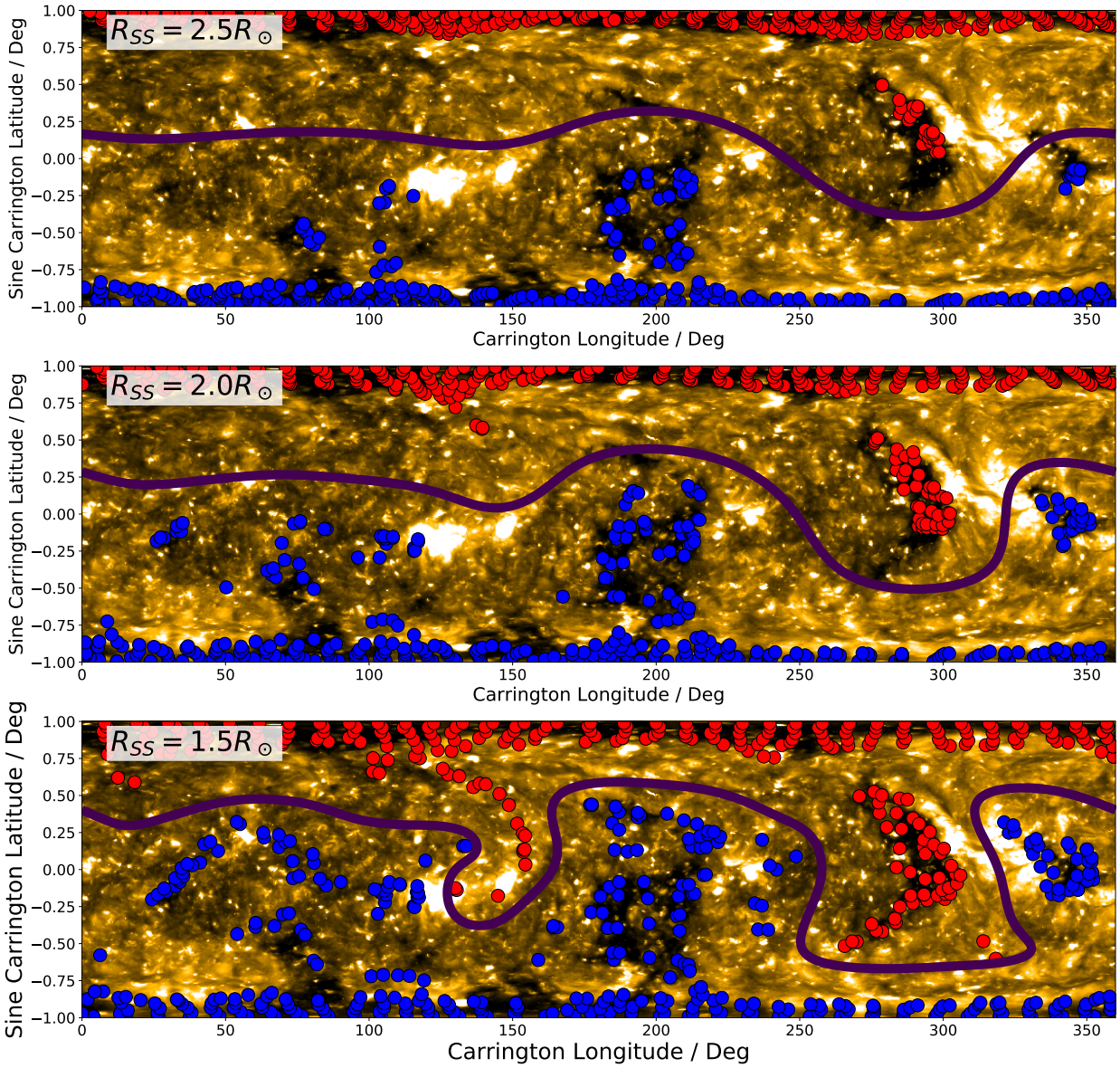

Figure 4.5: **Distribution of PFSS predicted open field line footpoints as a function of source surface height.** For the values of source surface height $2.5R_\odot$, $2.0R_\odot$, $1.5R_\odot$, field lines are initialized on a uniform grid at the source surface and mapped down to the photosphere. By definition, field lines initialized at the source surface are open and so this mapping shows the PFSS prediction of the source regions of open magnetic flux. For context, these mappings are overlayed on a synoptic map of the 193Å emission synthesized from STEREO/EUVI and SDO/AIA. At this wavelength, dark regions imply low density plasma regions in the lower solar corona, indicating the presence of coronal holes where open magnetic field lines allow plasma to evacuate into interplanetary space. The dark line overplotted is the PFSS neutral line at the source surface and can be seen to warp more at lower source surface heights.

series. In each of these, a colormap of magnetic field strength at the source surface is plotted along with the polarity inversion line (contour of $B_r = 0$) in black. On top of this, the PSP trajectory ballistically propagated down to the source surface is shown and colored by *measured* polarity. Where the measured color matches the color of the source surface below it, the model and data are in agreement. Panels B and C show model results evaluated from GONG magnetograms on 2018-10-20 and 2018-10-29 respectively, both for the extremely low source surface height $1.3R_\odot$ and zoom in to a specific part of the Sun to highlight specific PIL topology associated with the PI1-PI2 and PI3-PI4 intervals. Panel D meanwhile offers a more global view with the model at $2.0R_\odot$ showing the entire encounter. PSP began the encounter at approximately 180 degrees longitude and tracks in the direction of decreasing longitude in time, approximately reaching the position it started at at the end of the time interval considered.

Examining each measured polarity inversion in turn we observe that the timing of PI5 is accurately predicted by all models regardless of the source surface height. PI6 is well predicted for $R_{SS} \geq 2.0R_\odot$, but for lower R_{SS} it is predicted to occur too early. This is discussed further with figure 4.7.

Conversely, PI1, PI2, PI3 and PI4 are entirely missed in predictions using $R_{SS} \geq 2.0R_\odot$. Only at the very lowest source surface heights do these features convincingly appear in the prediction.

Panel D shows the overall distibution of magnetic field at the source surface for $2.0R_\odot$. An overall flat PIL generally skewed north of the equator explains why the near equatorial PSP mainly connected to negative polarity. A major southward warp of the PIL between 250 and 330 degrees longitude explains PSP's major excursion into positive polarity between PI5 and PI6 which is generally consistent with the shape of the HCS inferred by [206]. However the amplitude of the warps we infer and hence distance from the current sheet are larger than expected at the radius of PSP. This is expected since modeling beyond the source surface (either WSA's Schatten Current Sheet or flow dynamics in MHD) has the effect of flattening the PFSS-derived PIL as it evolves into the HCS [see fig 2. 206]. However, in spite of the discrepancy in distance to the current sheet, the timing of crossings and overall shape of the predicted magnetic timeseries is largely unaffected and remains consistent with other models.

Panels B and C show that when the source surface is lowered to $1.3R_\odot$ thin tenuous southward extrusions of the PIL develop at the correct longitudes at which PSP observed PI1-PI2 and PI3-PI4 intervals. However, to achieve this we find that the model must be generated using magnetograms from very close in time to when PSP was at that location. This suggests these features evolved quickly.

In the case of the PI1-PI2 interval, and the PI2 transition in particular, the predictions at the source surface can be traced to a distinct photospheric feature: A simple dipolar active region lies directly below the longitude where PSP observed positive polarity. The implied connection is discussed further with figure 4.8(B).

These model results and correspondence to data are compared in an alternative format in figure 4.7. Here, confining all data to the solar equatorial plane, we plot the PSP trajectory

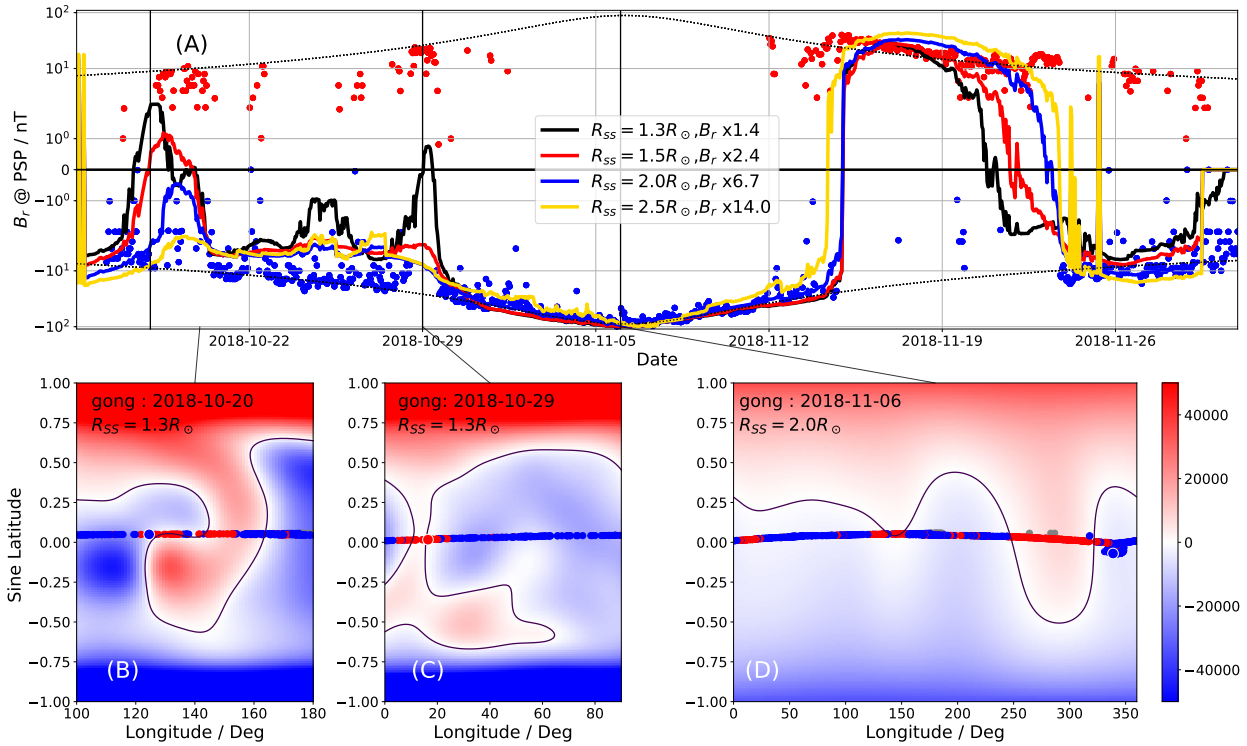

Figure 4.6: **PFSS Results as a function of Source Surface Height**. Panel (A) : comparisons of model predictions for different source surface heights. Predictions use time evolving magnetograms and SWEAP measurements. The scaling factors required to get the peak field strengths of the predictions and data to match for each source surface height are indicated in the legend. $1.3R_\odot$ and $2.0R_\odot$ models are as shown in [18] figure 1(b). Panels (B)-(D) show the magnetic field strength at the source surface predicted by PFSS projected onto longitude vs. sine(latitude). A black contour indicates the polarity inversion line. Overlayed on this are the source surface footpoints of PSP colored by the measured polarity. Panels (B) and (C) show zoom-ins on PIL structure consistent with small scale positive polarity inversions measured on 2018-10-18 and 2018-10-29 respectively for a source surface height of $1.3R_\odot$. Panel (D) shows the map for a $R_{SS} = 2.0R_\odot$ model over the whole Sun. PSP starts at approximately 180 degrees longitude and tracks from right to left as time passes. The lines between panels indicate the time on the timeseries when the model shown was evaluated.

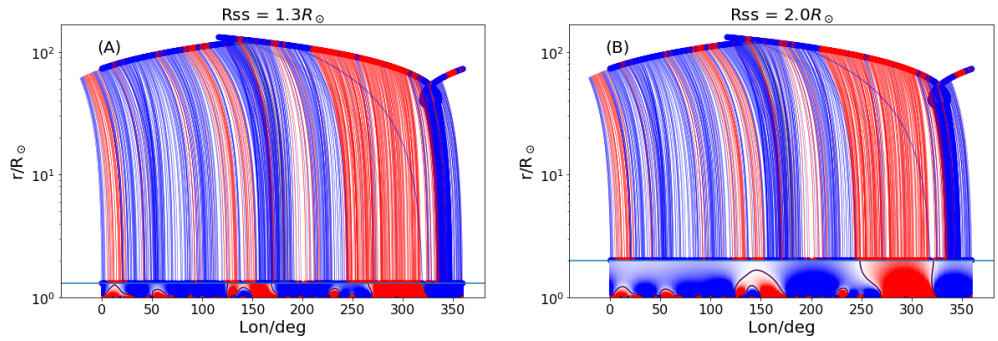

Figure 4.7: **Illustration of impact of Lowering SS Height on Model**. A comparison of the PFSS model and connection to PSP is shown in a plot of log(r) vs radius. Projecting everything into the ecliptic plane, we plot the PSP trajectory colored by measured polarity, then plot the parker spiral field lines down to the source surface, also colored by measurements. Below the source surface we plot a color map of an equatorial cut through the model colored by B_r, with black lines indicating contours of $B_r = 0$. Panel (A) shows the results at $R_{SS} = 1.3R_\odot$ while Panel (B) shows the results at $R_{SS} = 2.0R_\odot$. Comparison between model and observations are made at the source surface.

colored by measured polarity as log(radius) vs longitude. For each point along the trajectory we trace the Parker spiral used to connect it to the source surface and color this by data too. Below the source surface we plot a colormap of an equatorial cut through a PFSS model evaluated using GONG data from 2018-11-6 (perihelion). The comparison between model and observations is made at the source surface by comparing the model color just below and the observation color just above. By plotting log(radius) we are able to display both the interplanetary scale of the Parker spiral field lines and the coronal scale PFSS model. In panel (A) we plot the low source surface height model ($R_{SS} = 1.3R_\odot$) , and Panel (B) shows the high source surface model ($R_{SS} = 2.0R_\odot$).

Examining the evolution of the equatorial cut with radius, it can clearly be seen how higher order structures initialized at the photosphere smooth out and becomes simpler with increasing altitude. A general picture in the equatorial cut shown here is an overall negative polarity with small perturbations of positive polarity, most notably at 10, 55, 150 and 300 degrees longitude. Examining the high source surface case, panel (B), we see how only the 300 degrees longitude feature intersects the source surface and the others close over and revert back to negative. The 300 degrees longitude feature also exhibits expansion in it's longitudinal extent with altitude. On comparison to the observations, we notice this evolution is a vital element to explaining polarity inversion timings observed by PSP.

In comparison, panel (A) shows how the low source surface height is required for the "low-lying" strucures at 10 and 150 degrees longitude to be opened to interplanetary space. We also see how this source surface is likely the lowest possible since taking it further down would

open up structures at 55 and 240 degrees longitude, which have no observational support. However, while the lower height model recovers these small structure better, it intersects the 300 degree feature before it has expanded sufficiently, and so produces a prediction of positive to negative polarity inversion much earlier than was observed (figure 4.6A). These competing model features make the limitations of a single height source surface apparent: with this constraint our ability to globally match all observed features is hindered.

Figure 4.7 is also useful in making a qualitative assessment of the uncertainty associated with ballistic propagation. According to [146], this method has an estimated uncertainty in projected longitude of ± 10 degrees. Figure 4.7 allows visualization of the extent to which a shift of 10 degrees could shift projected footpoints relative to the observed structure in the PFSS model. For example, the westward expansion of the 300 degrees feature from 1.3 to 2.0 $R_\odot$ is approximately 20 degrees and so a 10 degree shift of the observed transition from positive to negative polarity could not explain the discrepancy in the two source surface height models. The blue sector from 330-360 degrees longitude indicates the extent of the source surface region which maps down to the coronal hole we infer PSP was connected to at perihelion (section 4.5). This is similarly larger in extent that the uncertainty and so we can state this connection is robust within uncertainty. With the smaller scale positive polarity features which are of order 10 degrees in extent a 10 degrees shift could just drive the footpoints of measured positive polarity out of consistency however it would not be sufficient to drive them to connect to any of the other positive polarity regions so the connectivity we infer remain the most likely sources of those measurements. Overall, we argue that 10 degrees can affect the details of the agreement of model and data but not our overall conclusions. In addition, with PSP orbiting much closer to the corona than the 1AU, this may result in a lower longitude error as the magnitude of the longitude correction is smaller. The excellent matching of observations and modeling to much less than 10 degrees may be evidence of this.

Implied Field Line Mappings

Having built confidence in the modeling approach by observing good time series predictions, as well as identifying it's response to variation in input parameters, we now explore the implications of the model results for the sources of the solar wind measured by PSP during it's first encounter.

Similar to how open field footpoints were generated for figure 4.5, we use the PSP trajectory projected down to the source surface to initialize a series of fieldlines which we propagate down into the model corona using the *pfsspy* field tracing routine. The results of this tracing with $R_{SS} = 2.0 R_\odot$ are summarised in figure 4.8A where we overplot the fieldlines colored by their polarity in the model on top of the same EUV data from figure 4.5. We also show the PSP trajectory projected on to the source surface and colored by *measured* polarity as in figure 4.6 (B,C,D).

In figure 4.8(B,C), we examine the field line traces of two subregions of the Sun of particular interest. Panel (B) shows results around the active region which appears associated

with the PI1-PI2 interval. The modeling results shown here are using the DeRosa/LMSAL model evaluated on 2018-10-20 with a source surface height of $1.4R_\odot$, the highest value of R_{SS} for which the model and measurements agree [see 153]. The faint contours of $|B|^2$ illustrate the topology of the active region, while the bold contour depicts the PIL at $1.1R_\odot$, indicating the polarity structure at the base of the corona. Crosses mark the positions on the source surface PSP connects to and track from right to left in time. The circles indicate the field footpoints these map to. It can clearly be seen that in this time interval the footpoints jump from the positive to negative region of active region and that the PFSS-inferred neutral line is guided along the neutral line of this active region. It is difficult to argue PFSS accurately captures the magnetic topology around such non-potential structures, but it is compelling that the longitude of this region matches with the projected longitude of PSP at the same time it measured PI2 implying at the very least an association of the observed feature with the measurements. This fine tuning of the crossing timing and more modeling with the DeRosa/LMSAL model is expanded on in more detail in [153] in which the authors explore optimizing source surface height for various polarity inversion case studies, suggest a resulting fitted non-spherical source surface height profile, and study the propagation and loss of Alfvènicity of slow wind streams en route to 1AU.

Panel (C) zooms in on the region of the Sun where PSP was located during the two periods of corotating either side of perihelion. The results here are shown for $R_{SS} = 2.0R_\odot$ but the qualitative conclusions here are largely independent of this choice. The major implication here is that for the entire "loop" part of the trajectory PSP was connected very stably to the small equatorial coronal hole at around 340 degrees longitude. This suggests PSP was connected to a region of the Sun of less than 10 degrees angular extent for over two weeks, over which time it's radial distance varied significantly. Therefore data from this interval can be interpreted as a time series of evolving solar wind from a single source convolved with changing sampling radius. Panel (C) also shows striking agreement between the location of the PIL at approximately 320 degrees longitude and the point at which PSP measurements indicated a polarity inversion from negative to positive.

Other general observations from figure 4.8A indicates that PSP connected to another (but this time positive) equatorial coronal shortly after perihelion, but with much more rapid footpoint motion tracking northwards over time. Comparison to SWEAP measurements suggests this configuration is responsible for the longest interval of fast wind observed in encounter 1 (figure 4.1B). After crossing back from positive to negative polarity on November 23, it continued to be connected to mid latitudes via a very large negative coronal hole.

4.6 Discussion

Overall, despite it's simplicity, our PFSS + ballistic propagation scheme produces compelling predictions of the B_r timeseries PSP measured during it's first encounter. The large scale features were well reproduced including the flat source surface field convolved with $1/r^2$ variation, the predominantly negative polarity and the timing of significant excursions into

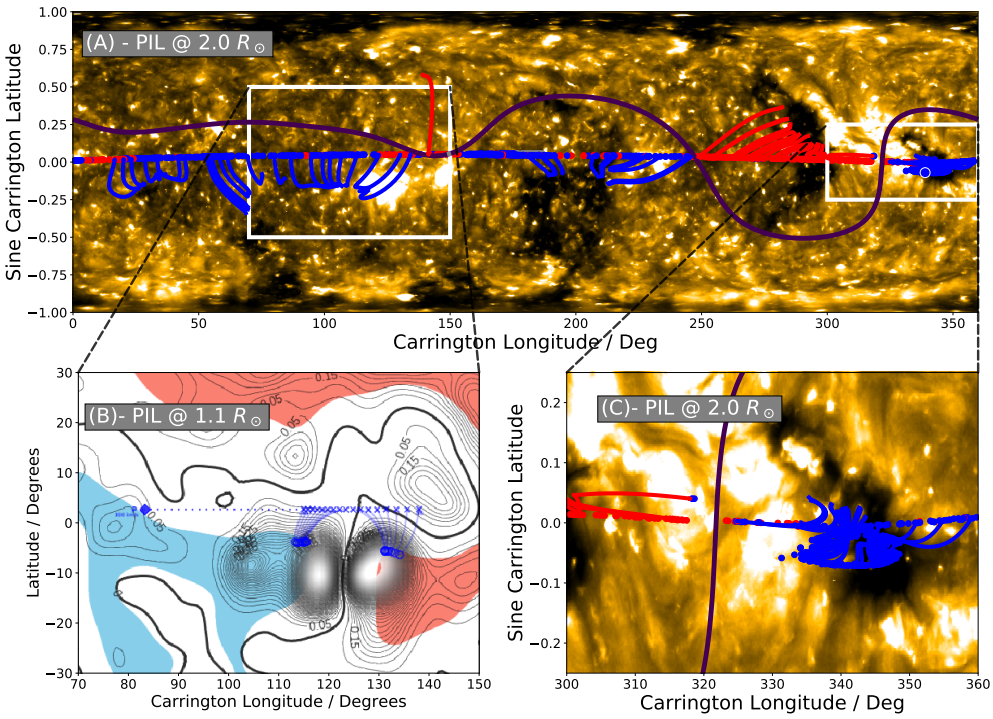

Figure 4.8: PFSS Predictions of photospheric connectivity of PSP. PFSS field line traces are initialized at the source surface footpoints of PSP and propagated down through the corona to the solar surface. These are contextualized with the same 193Å map from figure 5, and the polarity inversion line at the source surface from the model. Panel (A) shows a synoptic view of the whole encounter with the model evaluated at $R_{SS} = 2.0R_\odot$. Panel (B) shows a zoom in to the 2018-10-20 polarity inversion with the model evaluated at $R_{SS} = 1.4R_\odot$ using the DeRosa/LMSAL surface flux transport model. Contours of B^2 are shown and the polarity inversion line evaluated at $1.1R_\odot$ is plotted in bold. Coronal hole regions are shown as red and blue shading. The blue diamond at 85 degrees longitude indicates the carrington longitude of PSP, the crosses indicate the footpoints of PSP at the source surface. The circles indicate magnetic footpoints at 1.1 $R_\odot$ and the crosses and circles are connected by field line extrapolations. Panel (C) shows a zoom in of the connectivity around perihelion with $R_{SS} = 2.0R_\odot$. The field line mappings indicate connectivity to an equatorial negative-polarity coronal hole preceding a polarity inversion. Field lines shown in panels (A) and (C) are from same model evaluation depicted in [18] figure 1(c,d).

positive polarity. The model results are likely distorted by unmodeled chromospheric currents at the interior to the model, as well as field re-organization beyond the source surface, however empirically it appears these distortions were not great enough to destroy this overall good agreement. The applicability of PFSS is likely enhanced by the extremely low activity on the Sun at the time of observations which would result in fewer strong current systems. The impact of latitudinal reorganization between the source surface and $10R_{\odot}$ [169] is likely mitigated by the near equatorial sampling of the spacecraft. PSP's orbital inclination is ~ 4 degrees relative to the solar rotation axis which is even less than the Earth-ecliptic inclination of ~ 7.25 degrees. Even so, we do see PI6 is predicted to be a smoother transition than observations suggest and this sharpening can be explained by modeling beyond the source surface.

We also found the time evolution of the input photospheric maps was important to take into account, resulting in more robust and accurate time series predictions compared to those generated with a single magnetogram. The slow angular velocity of PSP compared to the surface of the Sun around perihelion likely plays a role in this finding, meaning since PSP tracked very slowly around the Sun in the corotating frame, the photospheric magnetic field changed significantly in this time interval. Since PFSS is a time independent model it is not possible to include dynamics, however we have shown that this limitation can be mitigated by treating the model as a snapshot of assumed static coronal structure sampled by the spacecraft for a small timestep, and chaining together these snapshots to approximate dynamical evolution.

Next, we discussed the impact of varying the source surface height parameter and found that on lowering it, new polarity inversion features emerged in the prediction which were consistent with observations. However, while this improved the predictions at some heliographic locations it worsened it at others, suggesting there is no clear "best" source surface height (see also Appendix C.2). This highlights the limitation of having a spherically symmetric source surface boundary condition. This qualitative finding is unsurprising given the lack of apparent spherical symmetry in observations of the outer corona, and development of PFSS since it's inception have sought to generalize beyond a spherical boundary [e.g. 106]. Comparisons to MHD modeling have suggested a boundary of near radial field which is far from spherical [e.g. 173]. This latter result however generally showed the dominant perturbation to sphericity was a latitudinal effect at solar minimum with the source surface elongated at high latitudes into a prolate spheroid shape. Given PSP's close to equatorial orbit and limited connectivity to high latitudes, producing model results which agree with observations is unlikely to contain information about the solar magnetic field at high latitudes. Instead, our results here are suggestive of variation in the height with *longitude* and perhaps with localized perturbations to the source surface below the canonical radius over specific magnetic structures as explored in [153].

The successful prediction of new observed features at low R_{SS} implies small, short lived magnetically open structures which persist out to interplanetary space are normally smoothed out by PFSS modeling but can be recaptured by investigating lower source surface heights. Figure 4.2 suggests such small scale features may even be measurable at 1AU. One

of these features appeared associated with a dipolar active region with a pronounced neutral line. Active regions are typically highly non-potential and dynamic, requiring MHD or non-linear force free modeling approaches. [173] found PFSS modeling (with the canonical $R_{SS} = 2.5R_\odot$) lacking in modeling fields in the vicinity of such a feature. Nevertheless PSP observed a polarity inversion from positive to negative at exactly the time low source surface height PFSS modeling suggests connectivity would have switched from the positive to negative lobes of the active region (Figure 4.8B). This implies in spite of the non-potential details, PFSS can be useful in associating such structures with observations in the inner heliosphere. The possibility of open field lines connecting to active regions has been discussed before for example in [205].

A brief discussion of the scaling factor as a function of R_{SS} shown in figure 4.6 is also warranted. We note that for $R_{SS} \geq 2.0$ a $1/r^2$ scaling from the source surface out into the heliosphere produces under-predicts the in situ field strength by an order of magnitude. This was first observed early in the history of PFSS by [105]. A simple interpretation is that non-radial evolution beyond the source surface is important in connecting the source surface far out to the heliosphere. At the source surface, PFSS predicts stronger field at the poles than the equator and it is known from Ulysses observations [194, 193] that this relaxes to a latitudinally independent state further out. The simplest configuration for this to happen is for the polar field to decrease faster than $1/r^2$ and for the equatorial field to drop more slowly than $1/r^2$ which is consistent with an underprediction of the field at low solar latitudes. It is possible that this underprediction could be mitigated with a Schatten Current Sheet model [187] as used in the WSA model, and this will be the subject of future work. However, from the results plotted in figure 4.4, the overall shape of the B_r time series is consistent to within this scaling factor from which we conclude this "extra" field strength is only weakly dependent on solar longitude, with some worsening agreement at higher PSP radii (early and late in the encounter). That the scaling factor drops to order unity with decreasing source surface height demonstrates how the radial field inside the PFSS model domain drops faster than $1/r^2$ since the dominant component is a dipolar $1/r^3$ field. Flux which opens up to the solar wind very low down in the corona likely escapes purely radially, which may explain why $1/r^2$ predicts the correct magnitude at PSP for these cases.

Lastly, in addition to the active region connectivity discussed above, we presented a synoptic view of the connectivity implied by PFSS during the whole encounter. The relatively low $2.0R_\odot$ source surface height suggests predominantly equatorial and mid-latitude connectivity as opposed to deep within polar coronal holes. This is consistent with PSP's predominantly slow wind observations (Figure 4.1B). However we note here that raising the source surface height to it's canonical value can change the connectivity very early in the encounter to the southern (negative) polar coronal hole. Given the time interval examined is dominated by the perihelion loop, our inference of a "best" source surface height is likely skewed towards the corotation interval and so statements of connectivity earlier or later in the encounter at $2.0R_\odot$ may be weakened. For example, [170] see polar connectivity at intervals prior to October 29 with MHD modeling results, while [206] examine an ensemble of different model and establish PSP was very close to the HCS at this time and thus may be

observing streamer belt plasma.

Of particular interest is the connectivity in the 2 week interval surround perihelion (figure 4.8C) which shows throughout the corotational period PSP was magnetically connected to an isolated, negative polarity equatorial coronal hole. This was also predicted prior to the encounter by [178] and now appears well corroborated by [84, 170, 206]. The coronal hole is approximately 10 degrees in longitudinal extent at the 193Å isosurface which implies a linear distance scale of order 100 Mm. Therefore without assuming detailed knowledge of the PFSS-derived footpoints we can state the source region for the sampled solar wind from this 2 week period (2018-10-30 to 2018-11-14) was confined to this 100 Mm size region, and thus variation in in situ data from this time can be interpreted as measurements of dynamics of the solar wind emitted by an approximately fixed source on the Sun [see e.g. 18]. This connectivity will also lead to interesting discussion on sources of the slow solar wind which is very much an active area of research [e.g. 226].

In summary, we have presented a first attempt at global coronal and inner heliospheric modeling to contextualize observations made by PSP in it's historic first solar encounter. Our potential field based modeling scheme is extremely simplistic and it will be vital to make detailed further comparison with concurrent or future global modeling work e.g. MHD [84, 170] or other PFSS models [153, 206],. Nevertheless we report various pieces of evidence that suggest the limitations of our modeling have been mitigated sufficiently to claim real and useful contextual information of PSP's magnetic connectivity. In particular, we find PSP spent the 14 days surrounding perihelion connected to a small negative equatorial coronal hole and may have also sampled open flux tubes associated with an active region around 2018-10-20 prior to perihelion.

The data discussed in this work comes from the first of many planned encounters for PSP. At the time of writing, encounters 2 and 3, which both sample down to the same perihelion distance of 35.7 $R_{\odot}$, have taken place. Following encounter 3, PSP will perform a gravity assist with Venus and begin to probe deeper into the solar atmosphere eventually reaching below $10R_{\odot}$. Repeating the analysis of this work on these future encounters will be interesting and will, for example, allow us to control for the impacts of solar activity on modeling results.

Chapter 5

Tracking a beam of electrons from the low solar corona into interplanetary space with the Low Frequency Array, Parker Solar Probe and 1 au spacecraft.

In this chapter, we present the submitted article, Badman et al. 2022b [16] (arxiv) which presents a study tracking a Type III radio burst from its injection at a soruce active region in the corona, through its propagation in the inner heliosphere and examines its diagnostics at 1 au where the electron beam causing the radio bursts is measured in situ by the STEREO AHEAD spacecraft. Although this study partially serves as a case study in the diagnostics and behaviour of type III bursts themselves it is also strongly tied into the large scale structure of the solar corona and heliosphere. One aspect of this is that type III bursts are caused by electron beams propagating along open field lines. For these electrons, the lorentz force keeps the beam tightly focus along a given field line and thus it in principle represents a passive tracer through heliospheric magnetic structure. This applies both low in the corona where the position of the burst in this case is shown to be coincident with open field lines and a coronal hole adjacent to the source region, and in the inner heliosphere where the location it follows ties it to a certain Parker spiral field line which aligns with STEREO A. As shown in this paper, the beam eventually arrives at STEREO A, validating this crude picture, however the in situ magnetic structure at STEREO A is also complex and divergent from this simplest picture, suggesting a perturbation with implications for the source connectivity. This study and methods therein also shows how type III bursts can provide diagnostic information about the density structure in the corona and heliosphere. Specifically, source size, source travel and escape time, and their impact on the time delay of arrival method presented in this work indicate the possibility of extracting density diagnostics convolved with the magnetic field information.

The full citation for this work as submitted is Samuel T. Badman et al. "Tracking a beam of electrons from the low solar corona into interplanetary space with the Low Frequency Array, Parker Solar Probe and 1 au spacecraft". In: *arXiv e-prints*, arXiv:2204.08497 (Apr. 2022), arXiv:2204.08497. arXiv: `2204.08497 [astro-ph.SR]`. The full author list is as follows: Samuel T. Badman, Eoin P. Carley, L. Alberto Cañizares, Nina Dresing, Lan K. Jian, David Lario, Peter T. Gallagher, Juan Carlos Martìnez Oliveros, Marc Pulupa and Stuart D. Bale.

5.1 Abstract

Type III radio bursts are the result of plasma emission from mildly relativistic electron beams propagating from the low solar corona into the heliosphere where they can eventually be detected *in situ* if they align with the location of a heliospheric spacecraft. Here we observe a type III radio burst from 0.1-16 MHz using the Parker Solar Probe (PSP) FIELDS Radio Frequency Spectrometer (RFS), and from 20 - 80 MHz using the Low Frequency Array (LOFAR). This event was not associated with any detectable flare activity but was part of an ongoing type III and noise storm that occurred during PSP encounter 2. A deprojection of the LOFAR radio sources into 3D space shows that the type III radio burst sources were located on open magnetic field from 1.6-3 $R_\odot$ and originated from a near-equatorial active region around longitude E48^o. Combining PSP/RFS observations with WIND/WAVES and STEREO/WAVES, we reconstruct the type III radio source trajectory in the heliosphere interior to PSP's position, assuming ecliptic confinement. An energetic electron enhancement is subsequently detected *in situ* at the STEREO-A spacecraft at compatible times although the onset and duration suggests the individual burst contributes a subset of the enhancement. This work shows relatively small-scale flux emergence in the corona can cause the injection of electron beams from the low corona into the heliosphere, without needing a strong solar flare. The complementary nature of combined ground and space-based radio observations, especially in the era of PSP, is also clearly highlighted by this study.

5.2 Introduction

Type III radio bursts are the characteristic signature of beams of energetic electrons injected by transient processes in the solar corona onto interplanetary magnetic field (IMF) lines first classified from observations of solar impulsive emission by [233]. As the electron beams propagate away from the Sun, they produce Langmuir waves (L) which mode convert [via one of several possible processes, e.g. 29, 30, 129] to radio emission at approximately the local electron plasma frequency (f_{pe}) or its second harmonic. As the electron plasma frequency is proportional to the square root of the electron plasma density (n_e) which decreases with the distance from the Sun, type III bursts are readily identified in radio spectrograms as transient signals dropping in frequency with time on a characteristic timescale of minutes

to hours [233]. This frequency ranges from as high as $\mathcal{O}(1$ GHz) very near the solar surface [although typically type III bursts are observed to start at 10s-100s of MHZ in the low corona, 168], and can extend down to $\mathcal{O}(10$ kHz) at $\sim$1 au. Above 10-15 MHz, type IIIs are readily observed and imaged by ground based observatories out to radial distances of a few solar radii. At lower frequencies, the burst passes below the typical cut-off frequency of the Earth's ionosphere and therefore can only be detected by space-based radio antennas. Most interplanetary type III bursts (where the electron beam escapes onto open field lines) are below this cutoff and can only be measured from space where imaging is not currently possible. The definition of "interplanetary" is not exactly defined but a frequency of 1 MHz at $7R_{\odot}$ is reasonable [168].

Further, this radio emission is widely beamed [e.g. 99, 22] and very luminous, meaning emission from the same event can be detected not just by Earth-based observatories, but also by widely separated spacecraft in the inner heliosphere. Additionally, the electron beam itself can survive out beyond 1 au and provide additional *in situ* information of the burst such as near-relativistic electron intensity enhancements [e.g. 48] or direct detection of Langmuir waves [e.g. 57]. For further context, [168] present a relatively recent review on type III burst properties and current theoretical understanding of the phenomena.

Type III radio bursts therefore produce a wide variety of diagnostic information about themselves and the ambient properties of the heliosphere such as the radial evolution of the solar wind plasma density and magnetic topology of the IMF lines [108]. However, much of this information requires obtaining knowledge about the burst's trajectory through the interplanetary space. For example, the electron beam trajectory traces open field lines starting low in the corona all the way out into interplanetary space. They therefore can be a passive tracer of both open coronal magnetic field (important for solar wind acceleration studies) and over larger scales in the heliosphere where the magnetic field forms the channels along which space weather events are guided. Additionally, since the emission frequency is directly related to the local plasma frequency and therefore plasma density, an accurate trace of the burst provides a trace through the density structure of the heliosphere allowing testing or development of density models [the latter of which was done by 98]. Further, since emission of type III radio emission occurs near the local plasma frequency, electromagnetic dispersion of the emitted waves is important. This means that propagation of the radio waves is affected by density variations, both through large scale gradients [e.g. 209, 210] and by small scale inhomogeneities [e.g. 107, 167]. For example, if radio emission is formed in a localized pocket of reduced plasma density surrounded by overdense regions, the radiation would not propagate through the overdense regions and so it would not be detected by widely separated spacecraft. Smaller scale density fluctuations also lead to random walks of photons before they escape to free stream. Measurements of apparent source size and source height allow these fluctuations to be quantified both in coronal contexts [89] and in the heliosphere [95, 140].

In this work we combine multiple observational signatures of a single type III radio burst observed by three well-separated spacecraft as well as ground-based telescopes during the outbound phase of the second solar encounter of NASA's Parker Solar Probe [PSP; 52]

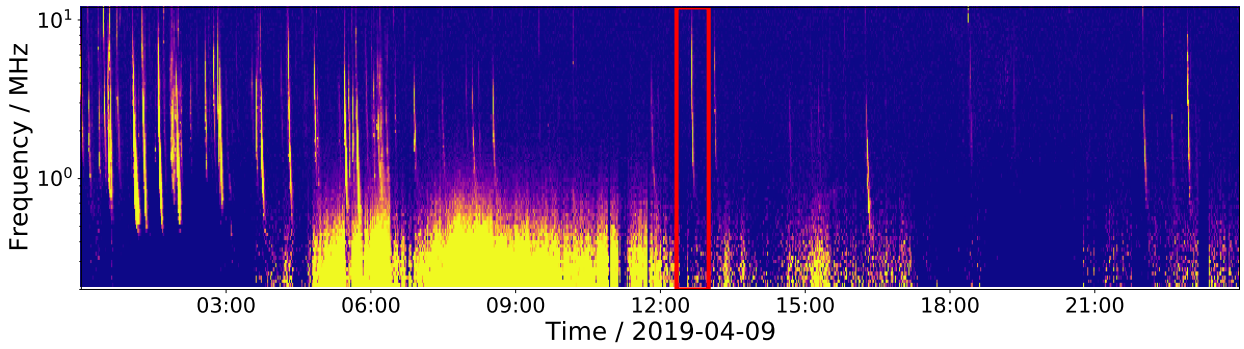

Figure 5.1: PSP/RFS radio spectrogram for 2019 April 9th. Each vertical stripe is a Type III burst. The ∼12:40 UT burst studied in this paper is indicated by the red box annotating the figure. The broadband signatures at lower frequencies are due to variations in the in situ electron plasma parameters [136, 114]

on 2019 April 9. We combine these observations in an effort to track the injection and escape from the corona of the electrons responsible for the type III burst, the interplanetary trajectory of those electrons, and their *in situ* signature at ∼1 au. In section 5.3 we introduce the various data sources and observations used in the project. The relative positions of these observing spacecraft and instruments are depicted in figure5.4. In section 5.4 we discuss the different methods used to probe the type III's behaviour on its journey out from the sun and the resulting information discovered about its journey from the corona to 1 au. In particular, we focus on ground based radio imaging of the burst in the outer corona (section 5.4), time-of-flight analysis between different heliospheric spacecraft to probe the burst's trajectory in the inner heliosphere (section 5.4), and finally study *in situ* signatures of the electron beam arrival at the Solar Terrestrial Relations Observatory A [STEREO A; 79] at 1 au (section 5.4). Lastly, in section 5.5 we discuss the results, interpretation and future outlook of our results and future opportunities for collaborative studies between ground and space-based radio observatories and other supporting instrumentation.

5.3 Observations and Data Sources

While PSP launched in an extremely quiet solar minimum, its second solar encounter in late March and April 2019 occurred during a wealth of solar radio activity with hundreds of individual type III bursts detected over this interval [165]. During this time, at least two active regions (ARs) were potentially contributing to this activity [AR 12738; 95, 34] and [AR 12737; 60]. In this work, we focus on a particular, well isolated Type III burst observed on 2019 April 9. The radio context for this day as observed by the FIELDS Radio Frequency Spectrometer [FIELDS/RFS; 19, 164] on board PSP is shown in Figure 5.1 with

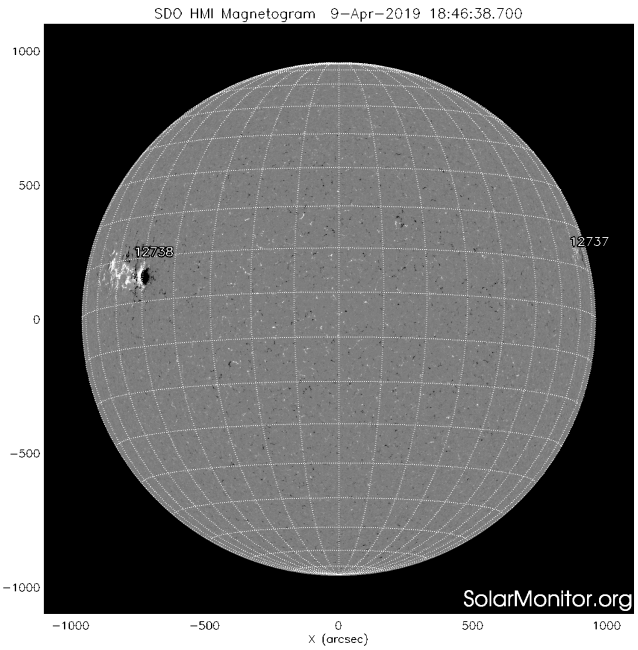

Figure 5.2: HMI magnetogram showing AR 12738 located near the east limb of the sun (48^{o}E). During PSP encounter 2, this AR was associated with a long-duration type III storm and noise storm [165, 95, 34]

the individual burst of interest indicated by a red box around 12:40 UT. While the burst is one of many on this day and not the most intense, it is chosen for this study since it is well isolated (a single electron beam) and clearly observed by multiple spacecraft and ground based instrumentation.

On 2019 April 9 the NOAA AR 12738 was an α-classified active region (unipolar sunspots only) located east of the central meridian and near the solar equator as viewed from Earth (N06^{o}E48^o at $\sim$18:00 UT and high magnetic flux density plage extending at least 10^o further eastwards, see Figure 5.2). At this time AR 12737 was near the west limb and decaying rapidly, consisting only of a magnetic plage at this time. The soft X-ray 1-8 Å flux measured by the GOES X-ray sensor [XRS, 35] showed very small levels of activity, with only B-class flares observable within the time range of our event of interest. The radio and X-ray observations are depicted in Figure 5.3 with panels (a-d) respectively showing radio spectrograms observed by Wind/WAVES [23], STEREO A/WAVES [S/WAVES, 24], PSP/FIELDS/RFS and the Low Frequency Array [LOFAR, 216]. The bottom panel zooms out to a longer time interval and shows GOES X-ray fluxes which are largely featureless both at the time of the burst and in the preceding and following hours. At 12:45 UT a type III radio burst was observed in the dynamic spectra from LOFAR at 20-90 MHz, and from STEREO-A/WAVES and WIND/WAVES from 0.4-14 MHz. The same type III was observed by the PSP/FIELDS/RFS instrument 6 minutes earlier, due to its closer proximity

to the sun during the event (timeshift applied in the plot, Figure 5.3c). The relative positions and nominal magnetic connectivity of the different spacecraft relative to the reference longitude of the source active region is indicated in Figure 5.4. Comparing the radio and X-ray data, this radio burst was not associated with any significant flaring activity. Specifically, no impulsive enhancements above B-class (which was also the background flux level) were observed by GOES at the time of the burst. The burst was therefore likely related to an ongoing noise storm and type III storm associated with AR 12738.

LOFAR observations of the type III from 20-80 MHZ measure the burst's radiation as it emerges in the lower corona, allowing it to be tracked out to $\sim$3 $R_\odot$ (section 5.4). The observations of the same type III radio burst by PSP, STEREO-A and WIND provide the opportunity to localise the position of this radio burst further out into the inner heliosphere. *In-situ* observations of energetic electrons by the STEREO A Solar Electron and Proton Telescope [SEPT; 139] and lower energy electrons by the STEREO-A Suprathermal Electron instrument [STE; 109] suggest the burst electrons from this type III burst can be tracked from its origin, low in the corona at AR 12738, far into the heliosphere all the way to STEREO-A (see Figure 5.4). An energetic electron enhancement of solar origin was indeed detected at STEREO A at compatible times, although as discussed in section 5.5, we do not conclusively isolate the individual contribution of this burst from the overall population produced by the ongoing type III storm.

5.4 Methods and Results

In this section we present the analysis methods used to track the type III burst from the corona to 1 au and the resulting localizations and observational evidence of the trajectory and its context.

Imaging and deprojection of LOFAR radio sources

During PSP encounter 2 the 36 core + remote stations of the LOFAR-provided interferometric observations of the sun, generating imaging spectroscopy observations in the range of 20-80 MHz (the remainder of the international array was also used to perform beam-formed observations of interplanetary scintillation during this observing period). A dynamic spectrum of the type III radio burst observed by LOFAR is shown in Figure 5.3(d). LOFAR interferometric data was calibrated (from simultaneous observations of Tau A) and processed using the Default Preprocessing Pipeline [DPPP; 215] followed by an implementation of w-stacking clean [WSClean; 147] to produce images with a cadence of 1.67 seconds. Images at seven frequencies from $\sim$20-80 MHz are displayed in Figure 5.5a, showing radio sources overplotted on an AIA 171 Å image and a potential field source surface (PFSS) magnetic field extrapolation using pfsspy [200] and data from the Global Oscillation Network Group project [GONG; 63]. The time of the GONG magnetogram used for the extrapolation was 13:04 UT, on April 9th 2019, with a source surface radius of 2.5 $R_\odot$. The type III radio

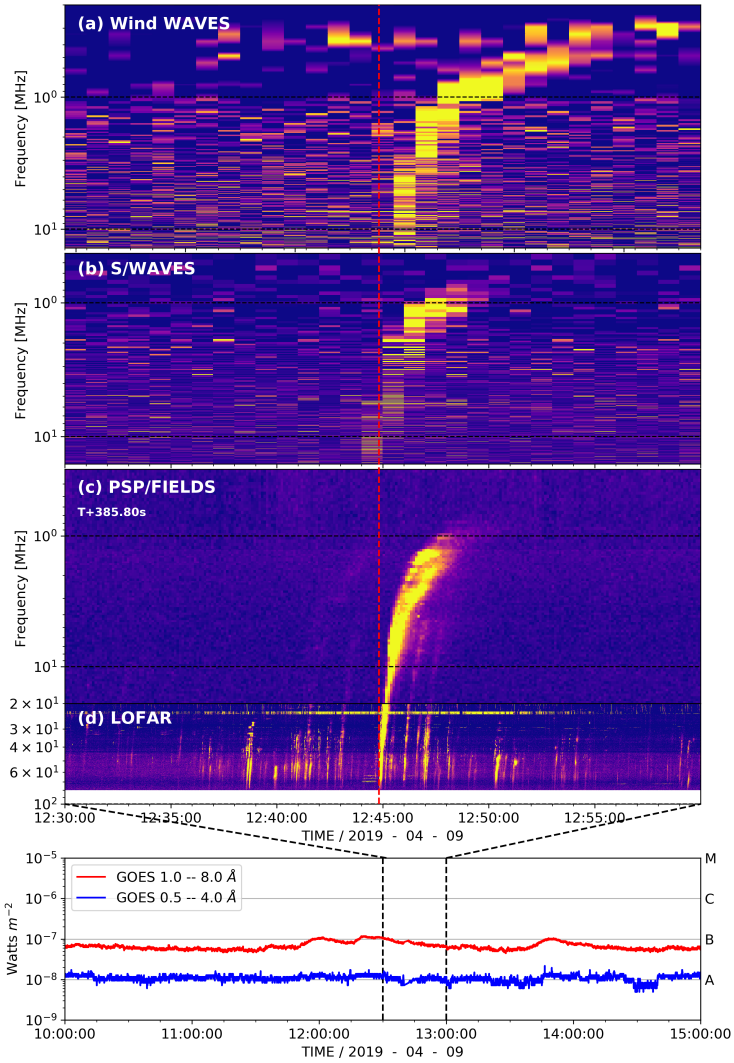

Figure 5.3: A type III radio burst observed with (a) WIND/WAVES, (b) STEREO-A/WAVES (S/WAVES), (c) PSP/FIELDS and (d) LOFAR. The radio burst is observed at LOFAR, S/WAVES and WIND/WAVES at ∼12:45 UT as they are all located at a distance of ∼1 au from the Sun, while it was observed 6 minutes earlier by PSP due to its closer proximity to the sun at $\sim 50R_{\odot}$. Using a PSP-Earth light travel time, PSP's dynamic spectra has been shifted by +385.80s to match the one of LOFAR. An additional zoom out panel shows GOES X-ray flux for several hours either side of the burst in energy channels 0.5-4.0 $\mathring{A}$ (blue) and 1.0-8.0 $\mathring{A}$ (red).

sources clearly emanate from AR 12738 along the negative open field to the south of the

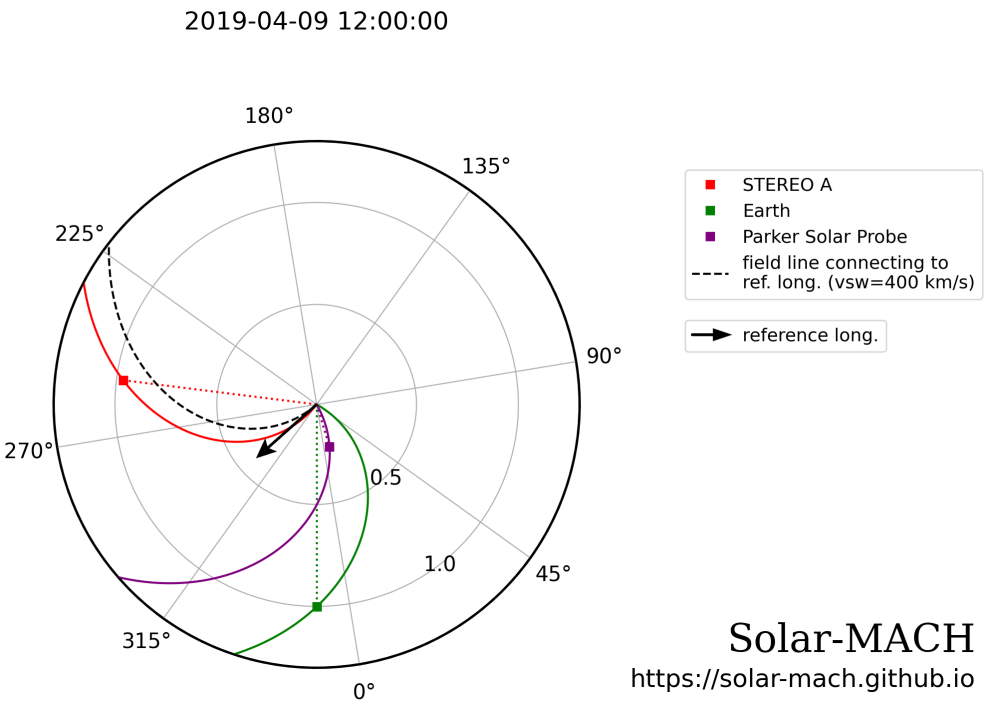

Figure 5.4: Instantaneous ecliptic positions of the spacecraft constellation used in this work at 12:00 UT on 2019/04/09, expressed in Stonyhurst coordinates (Sun-Earth line at 0^o longitude). Each spacecraft is connected back to the Sun by a 400 km/s reference Parker spiral. A black arrow and black dashed Parker spiral indicates the longitude and nominal trajectory of emission from AR 12738. Note the "Earth" location is a proxy for the locations of the Wind/WAVES, GOES-15/XRS and LOFAR instruments. Figure generated using `https://solar-mach.github.io`

active region.

In order to determine the location of the type III radio burst sources with respect to the parent active region, a basic deprojection using the Newkirk density model [143] was performed. We assume the type III emission is from harmonic emission in an atmosphere described by a coronal density model where the sources are located at a height of r_{model}. Their distance from the plane of sky (POS) is then $z = \sqrt{r_{model}^2 - r_{pos}^2}$, where r_{pos} is the height of the radio sources on the POS. The results of this deprojection are illustrated in Figure 5.5b. Although it is a rudimentary deprojection, it places the type III radio burst sources where we would expect them, in an open field region (from a PFSS model) accessible to an active region. The same procedure was performed using the 3.5×Saito density model [182], which is appropriate for active region radial density profiles [123, 122, 76], and the results were the same i.e., the radio sources were deprojected to be within the open magnetic field

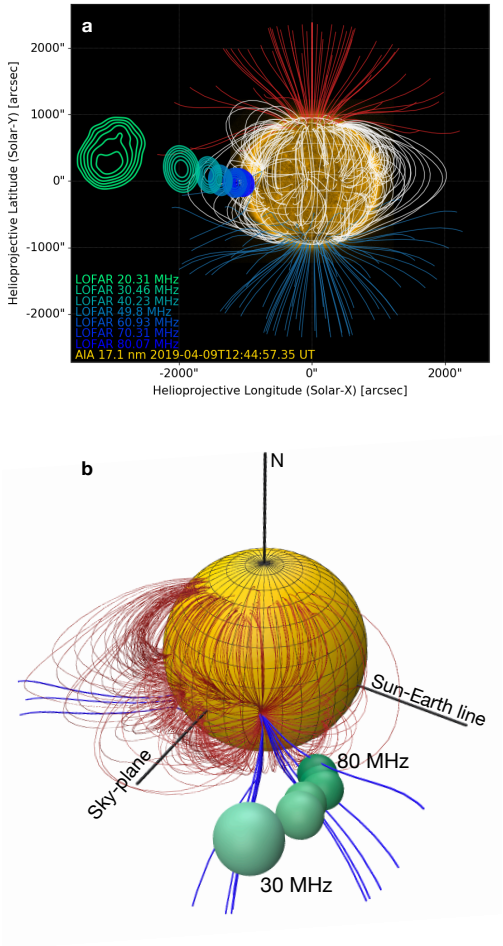

Figure 5.5: (a) Type III radio burst sources observed by LOFAR from 20-80 MHz overlaid on a PFSS magnetic field extrapolation using GONG. The type III sources emanate from the active region near the east limb and are situated close to the negative open magnetic field rooted in the active region. (b) A deprojection of the radio sources using a Newkirk density model [143], assuming emission at the second harmonic of the local plasma frequency. This places the radio sources on the open field lines $\sim 40°$ which are cospatial with AR12738

. This agrees well with the trajectory of the radio sources in Figure 5.6.

from AR12738. We also note that the non-radial propagation of the type III sources across the field lines in Figure 5.5 may not be physical. This is due to the various uncertainties in source positions on the sky-plane and in the deprojection method which of course neglects all non-radial density inhomogeneities.

The angle from the sky-plane of the type III burst roughly matches where the interplanetary type III is located from PSP-SWAVES-WAVES time-of-flight analysis (section 5.4, below). A few caveats are noted however: (i) the deprojection uses an arbitrary, and spherically symmetric, density model (one of many possibilities), so gives only a rough indication of the source positions, (ii) the radio sources are also large at these frequencies, the sizes of the green spheres in the 3D plot are 1-sigma from a Gaussian fit to the sources in the LOFAR images.

Time-of-flight using PSP, STEREO and Wind

As noted above, this burst was also observed at frequencies below $\sim$14 MHz in the three space-based radio instruments S/WAVES, Wind/WAVES and PSP/FIELDS (see Figure 5.3). These radio waves do not penetrate the Earth's ionosphere so are not visible to ground based instrumentation with interferometric imaging capabilities, and such capabilities are not yet available in space. Instead, to continue tracking the bursts we need to employ analysis methods on the more coarsely timestamped dynamic spectra produced by our current space based assets.

In this work, we make use of the fact that the burst is travelling over interplanetary distances and thus the length scales of the trajectory and variation in light travel time to the different observers are on the order of light minutes. Further, all the above instruments produce dynamic spectrum with a cadence of $\lesssim$1 minute (60s for Wind/WAVES, $\sim$38s for S/WAVES and $\sim$7s for PSP), and on the date of this case study were all located multiple light minutes apart. Therefore, the difference in light travel time from the burst to the different spacecraft is measurable. With the assumption of straight line propagation from a unique source position to each spacecraft, the difference in time of arrival at a given frequency between different spacecraft can be used to make a simple geometric reconstruction of the most likely source position (see [2] and Appendix D). With this method and a constellation of three well-separated instruments, the position may only be confined uniquely in 2D and so we make the assumption that the source is approximately located in the ecliptic plane. This assumption is supported for this specific burst by (1) the near-equatorial parent active region, (2) the associated coronal open field lines and (3) the imaging results of LOFAR for this burst (Figure 5.5) which place the burst around $\sim 4^o$ of the ecliptic plane.

The result of such a reconstruction as a function of frequency for the burst studied in this paper is depicted in Figure 5.6. The implementation procedure is detailed in appendix D. The top panel of Figure 5.6 provides an overview of the whole inner heliosphere, depicting the spacecraft constellation triangle consisting of PSP, Wind and STEREO-A, as well as the burst reconstruction coloured from light to dark as it drops in frequency and moves out from the sun. The solid markers indicate the positions corresponding to the central value of the

measured time delays, while the diffuse cloud indicates the uncertainty in position obtained by varying the measured time delay within the time resolution of the instruments (see the appendix for more details). Two dotted lines indicate Parker spirals initiated at 30^oE and 60^oE relative to the central meridian with solar wind speed of 400 km s^{-1}, informed by *in situ* measurements at STEREO-A at this time.

The bottom panel of Figure 5.6 zooms in on the reconstructed type III trajectory and uncertainty region. Red dots close to the origin indicate the source positions as reconstructed by LOFAR (Section 5.4) and plotted in the ecliptic plane.

It is worth noting the time delay generated trajectory implies the burst has been tracked out to 40 $R_\odot$. However, the lowest frequency observed at PSP is only 800 kHz for which typical density models [e.g. 98] would suggest the outer radius at which emitted radiation reaches PSP is only $\sim$10 $R_\odot$ (20 $R_\odot$) for fundamental (harmonic) radiation.

We note figure 5.3 shows clearly that the burst continues to propagate beyond the maximal triangulated distance, since radio emission is observed in Wind and STEREO-A at frequencies below the lowest frequencies observed by PSP. This suggests the beam reaches regions where the local plasma frequency is below the in situ plasma frequency at PSP, so radio emission cannot propagate inwards towards PSP. Thus, although we are unable to track the burst further with TDOA, it is plausible that electron beams along these mapped field lines can make it out to reach STEREO-A at 1 au.

In-situ analysis

As mentioned in the previous section, figure 5.6 shows that the magnetic connection along nearby Parker spiral field lines would allow the potential *in situ* detection by STEREO-A of the electrons produced during the solar eruption origin of the type III emission, although the exact nominal 400 km/s connection of STEREO A would be westward of the AR (see Figure 5.4).

We have analyzed energetic electrons measurements from the SEPT and the Solar Wind Electron Analyzer [SWEA; 185] instruments on board STEREO-A to determine whether such electrons were detected. We further contextualize the *in situ* environment around the spacecraft at this time with magnetic field measurements from STEREO-A/IMPACT/MAG [1], thermal plasma measurements from SWEA and composition data with STEREO-A/PLASTIC [54].

SEPT consists of two dual double-ended particle telescopes which measure electrons in the energy range of 40–400 keV. The four apertures of SEPT were termed Sun, Anti-Sun, North, and South owing to their looking directions along the nominal Parker spiral direction in the ecliptic plane (Sun and Anti-Sun) and perpendicular to the ecliptic plane (North and South). In the original configuration of the STEREO-A spacecraft, the longitudes of the central axis of the Sun and Anti-Sun apertures in the spacecraft-centered Radial-Tangential-Normal (RTN) coordinate system were $\phi_{Sun}\sim135^\circ$ and $\phi_{Asun}\sim-45^\circ$, respectively, designed to align with the nominal Parker Spiral azimuthal angle at 1 au. However, after the STEREO-A superior conjunction with Earth in early 2015, the spacecraft changed orientation resulting

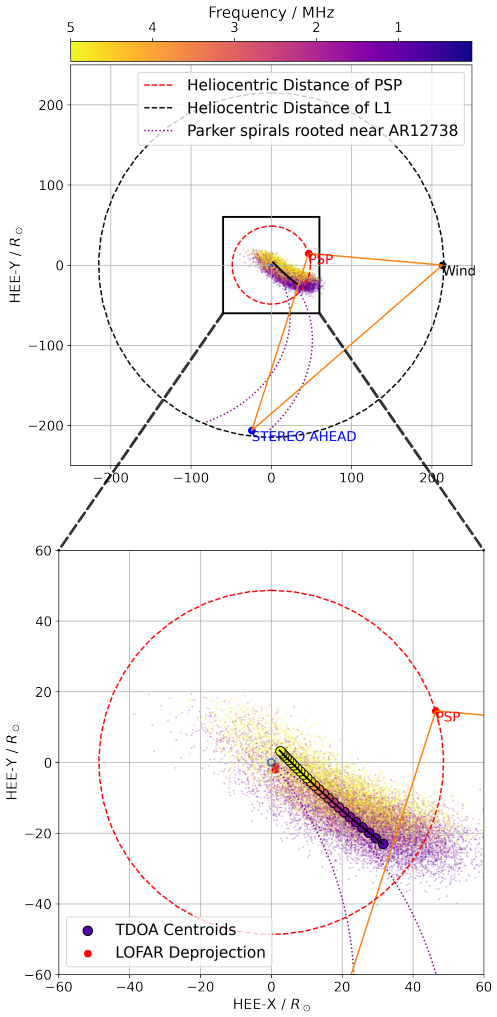

Figure 5.6: TDOA localization in the ecliptic plane of a type III radio burst trajectory in the inner heliosphere as measured by PSP, WIND and STEREO-A. The solid markers in the bottom panel represent the central value, while the diffuse cloud shows the position uncertainty due to the impact of the instrument time resolution on the time-of-flight measurement, both colored by measured frequency. The LOFAR deprojections are visible for comparison in the zoomed in bottom panel. The coordinate frame is Heliocentric-Earth-Ecliptic (HEE).

in the Sun and Anti-Sun apertures still pointing in the ecliptic plane but now *perpendicular* to the nominal Parker spiral direction, with $\phi_{Sun}\sim-135°$ and $\phi_{Asun}\sim45°$, respectively.

On 2019 April 9, a small electron intensity enhancement at energy channels below ~100 keV was observed by STEREO-A/SEPT close to the emission time of the Type III burst studied in the previous section. Figure 5.7 summarizes the *in situ* context at the location

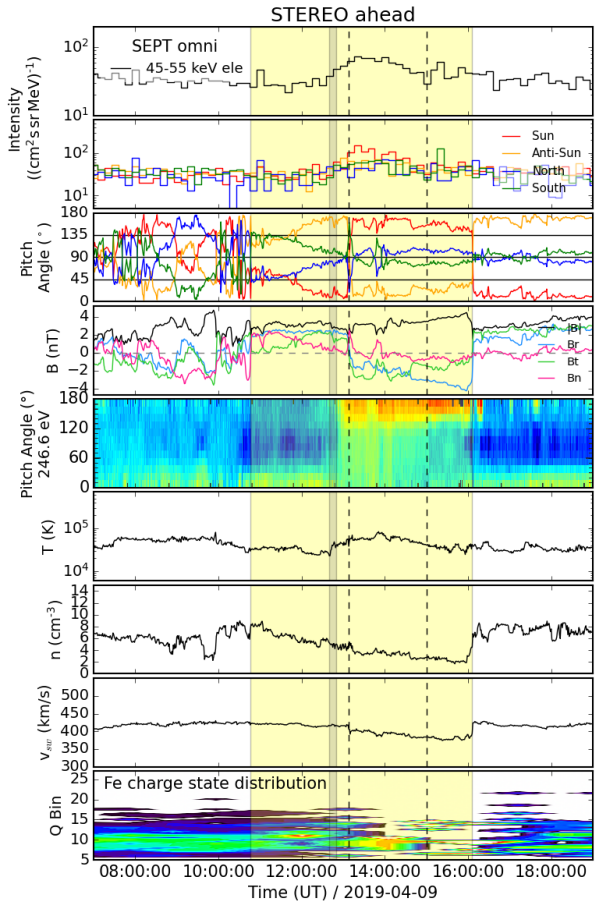

Figure 5.7: *In situ* observations by STEREO-A on 2019 April 9. From top to bottom: Omni-directional 45-55 keV electron intensities, sectored intensities measured by the four telescopes of the STEREO/SEPT instrument (both using 10-minute averaging, respectively). Pitch angles scanned by the central axes of these four-telescopes. Magnitude and components of the magnetic field vector in the spacecraft-centered RTN coordinate system. Pitch angle distribution of suprathermal electrons at 246.6 eV (color for the logarithm of phase space density). Solar wind proton temperature, density, and speed. Distribution of iron charge states Q_{Fe} as measured by STEREO-A/PLASTIC [54]. The yellow shaded period indicates a period with peculiar field direction studied in detail. Grey shaded bar marks the onset of the SEP event identified between 12:40 and 12:50 UT. First dashed line marks the sector boundary crossing at 13:08 UT. Second dashed line at 15:00 UT marks when electron flux return to background level.

of STEREO-A at the relevant times. In the top panel, we see timeseries of 45-55 keV electron omni-directional intensities, and in the second panel those of the sectored intensities

measured by the different apertures of SEPT. This energy channel was chosen as it most clearly demonstrates the event onset, peak and decay. The onset of the electron event is most clearly seen in the omni-directional intensities (top panel). We identify the onset to be between 12:40 UT and 12:50 UT, marked by the grey shaded range which reflects the coarse time resolution of the SEPT instrument. The current sheet crossing (sector boundary) indicated by the magnetic field orientation changing to $\phi \sim -135°$ occurred at ∼13:08 UT (first) dashed line) when electron intensities were still increasing. Electron intensities reached a maximum at about ∼13:30 UT principly in the 'Sun' aperture (red trace), and slowly decreased to pre-event intensities at about ∼15:00 UT (second dashed line).

The third panel of Figure 5.7 shows the angle between the instantaneous magnetic field direction (RTN components shown in the fourth panel of the figure) and the central axis of each one of the SEPT apertures. These panels show that throughout all this period, the magnetic field lay close to the ecliptic and perpendicular to the nominal Parker spiral field direction, which makes the post-superior-conjunction orientation of the Sun and Anti-Sun apertures of SEPT ideal for the detection of these electrons (as indicated by the orange and red trace's close alignments with 0° and 180° in the pitch-angle panel). Prior to the current sheet, the ecliptic component of the field was oriented at 45^o in the RTN coordinate system, and then flipped 180^o to point at -135^o. The entire stream containing this "perpendicular-to-Parker" interval is captured by the yellow box superimposed on the different panels. The current sheet crossing happens approximately halfway through this interval. There is a gradual rotation of the field into this initial configuration from the start of the yellow shaded interval, finally reaching "perpendicular" at very close to the electron event onset as seen from the SEPT pitch angle panel (3rd from top).

The fifth panel down presents the pitch angle distribution of suprathermal electrons at 246.6 eV as measured by SWEA. Prior to the current sheet crossing, the electron pitch angle distribution (defined relative to the local field orientation) is anisotropic and peaked at 0^o indicating it is parallel to the field lines. After the current sheet crossing, the distribution is peaked at ∼180° i.e. antiparallel to the field lines. Given the field orientation has flipped 180^o, this indicates the dominant direction of the suprathermals remains consistent and at all times is flowing into the direction of the SEPT "Sun" aperture. After the current sheet and coincident with the peak in 45-55 keV electrons, the suprathermal electrons do become more isotropic (but still clearly single-peaked); this pitch angle spread decays away on the same timescale as the energetic electron population decreases to background levels. We note the pitch angle distributions of the 246.6 eV electrons are consistent with the arrival direction of the energetic electrons (flowing into the SEPT "Sun" aperture).

Plasma temperature, density radial flow speed are shown respectively in the next three panels of Figure 5.7. There are no sharp changes in these quantities during the energetic electron enhancement. A small but steady rarefaction in solar wind speed occurs across the enhancement. The last panel shows the iron charge state distribution (Q_{Fe}) measured by PLASTIC. During the electron enhancement the distribution was enhanced and concentrated around values of 9-15, and contrasts with ambient solar wind prior to and following the event.

The event timing is important to remark on for relating it to the radio emission discussed

in the previous section. A 45 keV (55 keV) electron would take about ∼25 (∼ 23 minutes) to travel a distance of 1.2 au along a nominal Parker spiral for a spacecraft located at 1 au from the Sun. For an observer located at 0.967 au like STEREO-A, a 45 keV (55 keV) electron would take about ∼20 (∼ 19 minutes) to travel the radial distance from the Sun to the spacecraft. The actual path followed by these electrons before reaching STEREO-A when embedded in this structure, as well as how this structure modified the STEREO-A magnetic connection with the Sun, are uncertain. This means mapping arrival time of the event at STEREO-A back to a specific emission from the Sun is difficult. However, since the nominal Parker spiral represents the simplest possible field configuration, the arrival times quoted above are likely to represent a lower bound on expected time delays.

The first radio waves associated with the type III radio burst were detected by LOFAR at 12:45 UT implying a release time in the low corona of ∼12:37 UT. This appears too late therefore to explain the initial onset time of the energetic electrons observed in situ by STEREO-A/SEPT at ∼12:40-12.50 UT. Moreover, the timescale of the whole enhancement tracked by SEPT is of order 1-2 hours, significantly longer than the timescale of any given burst. However, the anisotropic electron enhancement which continued during the current sheet passage at 13:08 UT and the subsequent electron intensity peak at ∼13:30 UT are compatible with electrons injected during the type III radio burst analyzed in Section 5.4. This timing issue is discussed further in the following section.

5.5 Discussion

In this work we have presented a multi-instrument analysis where we tracked a single well-isolated, near-ecliptic-propagating type III radio burst. Specifically, we followed its injection onto open field lines by a source active region, its propagation through the corona and out into interplanetary space and lastly, its possible association with *in situ* measurements from the STEREO-A spacecraft near 1 au. In the following subsections, we discuss the implications and our interpretation for each part of the analysis.

Emergence from the Corona

Using radio imaging with the Low Frequency Array from $20-80$ MHz and a simple deprojection analysis assuming a Newkirk coronal electron density model [143], the burst was placed in 3D space at coronal altitudes at longitudes clearly associated with AR 12738 located at N06^{o}E48^o in helioprojective coordinates on April 9, 2019 (Figure 5.2). This was consistent with the association of the overall type III activity with this AR on these dates made by [165, 95, 34]. The imaging showed the burst increasing in altitude with decreasing frequency and the deprojection placed it in a region of open magnetic field lines in the vicinity of the relevant active region (figure 5.5). The deprojection analysis was found to be unchanged with the use of the 3.5xSaito density model [182], however the limitation of a spherically symmetric density profile leaves an unquantified error in the plane of sky distance.

GOES/XRS measurements of x-ray radiation over this time indicated that there was no significant flaring component associated with the injection of the burst (figure 5.3). This suggested non-flaring processes such as flux emergence and small-scale reconnection are responsible for the studied type III. This case study therefore represents an example of non-flare-associated interplanetary type III burst.

Additionally, many faint injections in LOFAR preceding and following this burst are not observed at interplanetary frequencies and some are measured only by PSP between 1-10 MHz (see panel c) and not by Wind or STEREO A. This suggests that more bursts are being injected onto interplanetary field lines than are visible in radio at 1 au during this time interval, and again without flare signatures. As discussed below, timing analysis of the *in situ* data at STEREO-A shows energetic electrons arrived earlier than can be explained by the tracked burst timing; earlier injections which are not bright in radio are a possible resolution to this.

Interplanetary Propagation

Having established the burst to be injected onto open field lines and therefore expected to reach interplanetary space, we investigated the source propagation out to several 10s of solar radii using a novel time delay technique termed Time Delay of Arrival (TDOA; see appendix D) leveraging the multi-light minute separation between the different heliospheric spacecraft with radio spectrograph instrumentation (PSP, Wind and STEREO-A at the time of the studied event). The method assumed that the burst was located in the ecliptic plane along with the observing spacecraft, and that the radio waves free streamed from source to observer. These sources of uncertainty are discussed further in appendix D where we conclude the former is well justified for this burst, while the second is harder to quantify.

This analysis yielded a trajectory for the burst at frequencies from 10 MHz down to 800 kHz (figure 5.6) at which point the radio frequency became evanescent along paths to PSP (this means the burst propagated beyond the heliocentric distance of PSP). The burst was still observed at lower frequencies by the 1 au spacecraft which shows that it continued propagating futher out into space, and is therefore plausible it would survive out to STEREO-A.

The derived trajectory showed the burst to be increasing in distance from the Sun with decreasing frequency, and to be directed along a longitude consistent with the active region and coronal trajectory found by LOFAR, as well as Parker spiral field lines connecting to the vicinity of STEREO A. As part of making these conclusions we utilize error regions computed by accounting for the limited time resolution of the individual instruments radio data products, most significantly that of Wind/WAVES at 60s (see appendix D). This error region is large and extended in the radial direction (see bottom panel, figure D.3) which leads to the error regions of adjacent frequency channels significantly overlapping. However both the centroid and radial extrema of the error region do shift outwards with decreasing frequency (the latter is not distinguished in figure 5.6 as the error regions are shown on a continuous color scale). The azimuthal extent of the error region is smaller but still significant

and is similar in scale to the apparent longitudinal offset between the TDOA centroids and the deprojected longitudes from the LOFAR imaging results. However, the small misalignment is also possibly contributed to by innacuracies in the LOFAR deprojection analysis.

The heliocentric distances computed from the TDOA analysis were significantly larger than expected from typical interplanetary density models. A potential explanation for this is propagation effects such as scattering by density fluctuations at the emission location (i.e. a breakdown of the above assumption of free streaming). This mechanism has been shown to make coronal radio sources appear to be lensed out to higher altitudes [89]. [94] and [95] have shown that density fluctuations also scatter type III radio emission at interplanetary frequencies and in particular play a key a role in shaping the exponential tail of type III flux-time profiles (see e.g. figure D.1). To further investigate this lensing interpretation, the TDOA method presented here should be applied to a large statistical sample of ecliptic-propagating type III bursts in future work.

We conclude that our application of this method shows it provides real and useful information about the propagation of type III bursts on interplanetary distances, provided the strong assumption of ecliptic propagation is justified and the observing spacecraft are multiple light minutes apart. Specifically, it allows association of the burst with an approximate source region, interplanetary propagation direction, and an estimate of its radial motion. Large uncertainties from instrument resolution appear to be a dominant error source. Nevertheless, the method is appealing since the construction does not make any assumption about density models or fundamental vs. harmonic emission, although the assumption of free streaming propagation needs further investigation and quantification.

Signature at 1 au

Lastly, motivated by the consistent longitude between the active region, LOFAR imaging, interplanetary triangulation, and Parker spiral field lines which mapped to the location of STEREO-A, we examined in detail the signatures of energetic electrons at that spacecraft to determine if the electron beam was detected at 1 au (figure 5.7). An energetic electron event was indeed observed at STEREO-A at compatible times, although its true onset (12:40-12.50 UT) was too early to be explained by the specific burst studied here (emitted at approximately 12:37 UT). The duration of the electron enhancement (peaking at 13:30 UT) is compatible with the electrons that generated the studied type III radio burst arriving at STEREO-A during the rising phase of the energetic electron event and suggests they contribute to the peak of this electron event.

Further, detailed *in situ* analysis of the solar wind stream that swept past STEREO A at this time demonstrated clear evidence that the energetic electrons measured were solar in origin and were not associated with any *in situ* electron energization processes. Specifically, evidence for solar origin included that 1) the energetic electron flux peaked highest in the sunward detector implying it was flowing from the sunward direction, 2) the electron pitch angle was singularly peaked at all times indicating open magnetic field lines, and 3) the iron charge state variation indicated a distinct solar source for the duration of electron

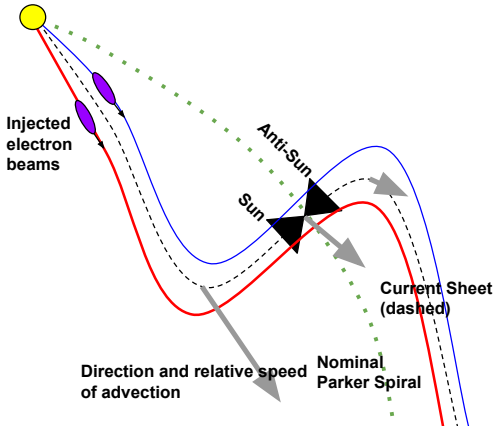

Figure 5.8: Proposed schematic of stream structure at STEREO A during the time interval studied (yellow shading in figure 5.7). STEREO A/SEPT FOVs indicated by the 2 black triangles. Red and blue kinked field lines of opposing polarities. Nominal Parker spiral indicated by green dotted curve . Purple ellipses with arrows indicate electron beams injected onto these field lines. Grey solid arrows indicate the proposed flow velocity across the kink and the overall advection direction of the structure.

enhancement [104]. Evidence that the electrons were not energized in situ included the lack of shock signatures in the solar wind parameters, and the lack of flux ropes, stream interaction regions or CME observations prior to or following the studied event.

Although there is good evidence that the electron enhancement was solar in origin, the magnetic configuration of the stream was unusual. Specifically, the measured magnetic field lines at the event time were perpendicular to the nominal Parker spiral direction and also included a current sheet crossing where the field direction flipped 180 degrees. This orientation was rotated into gradually and reached the "perpendicular" direction at the time the electron burst began.

In figure 5.8 we present a schematic representation of such a stream configuration which could explain the *in situ* signatures: Here, we propose a strong kink in an otherwise nominal set of Parker spiral field lines containing a current sheet to explain both the field orientation and the in situ evidence for an open field line connecting back to the sun. The orientation of the STEREO-A SEPT Sun and Anti-Sun apertures are also illustrated as black triangles, along with the direction of electron beam motion which shows how the instrument orientation is fortuitous for making the observations in this picture. As time passes, this kink would advect out radially anti-sunwards and over STEREO A, causing a current sheet crossing to be measured. The longitudinal mapping of the field line would be affected by the presence of such a kink, with the size of the shift determined by the transverse scale of the kink. With the kink oriented in the sense shown here, the extra shift relative to the nominal Parker spiral is in fact Eastwards, which is the right direction to account for the slight misalignment

indicated in Figure 5.4. Such a kink can be supported by a velocity shear [192]. For the schematic shown in figure 5.8, the velocity shear is oriented as indicated by the size of the large gray arrows at the inflection points of the curve. This leads to the expectation that STEREO A would measure a gradual decrease in solar wind velocity with time as the kink washes over it which is consistent with the in situ data (figure 5.7).

The timing analysis mentioned in section 5.4 implies the actual electron beam studied in this work would arrive during the rise in electron flux and potentially contributes to the overall peak at 13.30 UT. We note that although the nominal arrival time along a Parker spiral would be around 12.57 UT for a 12.37 UT emission, the perpendicular field configuration combined with the evidence that the field line is open and connects to the sun implies a longer travel time since all field line geometries consistent with these two observations have a longer path length than the nominal spiral.

Taken all together, we interpret these observations as showing that the studied burst contributes a subset of the population of energetic electrons measured by STEREO-A, but that the overall population forming the enhancement (top panel, figure 5.7) was comprised of multiple type III ejections of varying radio brightness which were happening near continuously on this and preceding days [figure 5.3d and 34]. In this picture, STEREO A only measures this population when a favorable stream configuration which connects back to the source active region advects over the spacecraft (for example, the configuration proposed in figure5.8). Thus the onset of the electron enhancement would not relate to a specific injection time, but rather the time when the "perp-to-parker" field configuration was reached and connected STEREO-A to the source active region.

It is interesting to note the energetic electron enhancement shows a smooth enhancement and takes place over a timescale of hours. There are no sudden enhancements in flux which would allow the contributions of individual beams to be identified as they arrived. This provides further evidence that the observations indicate the result of multiple injections smoothed together, which could occur via processes such as perpendicular diffusion [204]. This situation contrasts to previous studies where clear linkage was observed. For example, impulsive ($\mathcal{O}$(10 min)) electron enhancements have been observed from similar periodicity type IIIs [e.g., 86]. In other cases [93] and [58] identified near-relativistic electron events for which the estimated release time of the electrons was delayed with respect to the onset of the type III radio bursts, but still found the electron event could be associated with a specific burst after accounting for this delay. Such combinations of delayed emission could also contribute to the merging of arrival times of many electron beams.

Summary and outlook

In closing, we have studied and tracked a non-flare related interplanetary type III burst from its active region source, its injection onto open coronal field lines, its propagation along interplanetary field lines and shown evidence that it contributes to an energetic electron enhancement measured by STEREO-A at compatible times. Contextual in situ data taken by STEREO-A showed that the local magnetic field was oriented perpendicular to the Parker

spiral which suggests an off-nominal connectivity. We suggested an interpretation (figure 5.8) to explain this observation of kinked interplanetary field lines tracking back to the source active region.

A motivating goal for developing the interplanetary TDOA method was to use type III bursts as passive tracers of magnetic field lines in an application similar to [108], and to do so in a density-model independent way. Such tracing could then be applied to differentiate more complex magnetic models than the simple Parker spiral [e.g. 207], and could it principle operate as a cross-check on field line interpretations such as in figure 5.8. As yet, this goal has not been achieved as evidenced by the much larger than expected heliocentric distance of the source positions. Further work is needed to investigate the uncertainties, most notably the unquantified divergence from radio free streaming.

To bring this story together we needed to make use of complementary observations including solar magnetograms, GOES X-ray observations, LOFAR ground based radio imaging observations, interplanetary radio dynamic spectra from widely separated interplanetary spacecraft and lastly, the powerful suite of *in situ* instruments on board STEREO A. This demonstrates the power of using the heliospheric systems observatory (HSO) for connecting the inner heliosphere and solar corona and demonstrates a useful future combination of techniques for tracking type III burst both for studying their intrinsic properties, as well as the convolved information they carry about the medium they propagate through. It is important to reiterate that near ecliptic propagation of the burst was a strong assumption for the interplanetary portion of this work, and needs to be evidenced to re-apply the 3-spacecraft TDOA method to future events. However since the launch of Solar Orbiter in 2020 [SO; 138], there is a 4th source of interplanetary radio observations, leading to the possibility of extending this part of the analysis to full 3D localization Combined techniques as shown in this paper will therefore continue to become more capable and powerful as our instrumentation of the heliosphere continues to become more complete.

Chapter 6

Conclusion

In this thesis we have presented four studies which leverage the breadth of our heliospheric systems observatory, most notably with the recent addition of Parker Solar Probe (PSP), to derive new measurements of the inner heliosphere and corona and to constrain and evaluate coronal models in new ways.

6.1 New quantitative ways of evaluating coronal models

Chapter 2 presented Badman et al. 2022a [13] in which we focused on the latter endeavour. We developed three independent metric scores to quantify coronal model performance in their magnetic field representation. These metrics measured quality of representation of coronal holes, quality of representation of the streamer belt topology, using an analysis method developed in [161], and lastly how accurately the models can predict in situ magnetic polarity as measured at multiple positions in the inner heliosphere. These metrics were defined in such a way that inter-model comparison was possible by focusing on magnetic structure and specifying a format for models to produce data constituing "observables". The metrics usefulness was verified with inter-model comparison which showed that the differing physics present in each model improved specific metric scores in way that make sense. We also performed an extensive evaluation of Potential Field Source Surface (PFSS) models, of interest due to their ubiquity (both in this thesis as well as the broader literature around coronal modeling). We showed that PFSS models are useful due to their reasonable metric scores, but clearly show innacuracies which can be addressed with more sophisticated modeling. Further, we identified that metric scores had different qualitative trends with respect to the key PFSS source surface parameter (the source surface height). This had the implication that a global optimum PFSS model is poorly defined since an optimum could be obtained for one observable at the detriment to another. We therefore provide a note of caution to the field of global coronal modeling that multiple observables should be simultaneously considered when optimizing or judging the quality of models. Directions for future work

identified included a number of specific studies our metrics could be applied to (variation across solar cycle, dependence on magnetogram resolution) as well as the development of the metric framework as an open source software package to make it more usable by the community.

6.2 Testing the "open flux" problem in the near sun solar wind.

Next, in chapter 3, we followed the theme of model-data comparison, but focused on a specific comparison point which has previously been shown to be highly discrepant independent of the model used [110]. We presented Badman et al. (2021) [15] which examined the heliospheric magnetic flux measure by PSP as a function of radial distance from the Sun and compared it to the modeled amount of flux predicted to be open by PFSS models. As observed previously [110], carrying out this comparison with flux measurements at 1 au showed more magnetic flux in the heliosphere than can be explained with coronal models (not just PFSS). We extended this finding down to $16R_{\odot}$, finding the discrepancy still exists. Further, our conclusions was made more robust compared to processing 1 au data both due to the much improved signal to noise ratio coming from the larger field strength near the Sun, as well as significant efforts we made to be statistically rigorous in deriving our measurements - most importantly by casting the field measurements into spherical coordinates which is much more natural basis to describe the mostly Alfvenic (constant B magnitude) fluctuations in the near Sun solar wind [18]. This result clearly demonstrates that the so-called "open flux" problem is empirically present and not an *in situ* measurement artefact, which leads to the implication that the resolution must come from advances in coronal modeling. Two potential resolutions were suggested which included 1) possible unobserved strong flux concentrations in the solar poles which are not accounted for in magnetograms or 2) significant contributions to the total open flux in the heliosphere from non-coronal hole locations through dynamic processes such as interchange reconnection [e.g. 50], which we propose as future directions for advances in coronal modeling.

This study also served as an exposition of direct measurements of the heliospheric magnetic field. This showed the strikingly good applicability of the simplest Parker spiral model [154] to the large scale heliospheric magnetic field (equations 1.9-1.11), when fluctuations are properly accounted for. Figures 3.2 and 3.5 showed that the radial magnetic field very accurately follows the conservation of magnetic flux ($1/R^2$ variation) over a wide range of averaging timescales, down to at least $16R_{\odot}$. Secondly, figure 3.5 also showed very good correspondence with the Parker spiral clock angle over the same range of distances. While plenty of scatter exists in both cases, the most probable field values followed the large scale trends.

6.3 Reproducing in situ measurements and establishing magnetic connectivity

Next, in chapter 4 we presented Badman et al. (2020) [14] which investigated the very first perihelion pass of PSP and used one of the modeling techniques tested and evaluated in previous chapters (PFSS corona and ballistic inner heliosphere) to reproduce the magnetic field data measured *in situ* within ±2 weeks of closest approach. The overall structure was reproduced very well despite the simplicity of the models, again tying in to the surprising applicability of the crudest models to in situ properties from a region of space never visited before. Specifically, the large scale $1/R^2$ variation (inner heliosphere model prediction) of the radial magnetic field was reproduced along with all of its major current sheet crossings (PFSS coronal configuration prediction). (This early success was in fact the motivation for using this crossing timing as an evaluation metric in chapter 2.) As shown in that chapter (again 2), PFSS models are far from perfect, however a clear advantage they have over more sophisticated models is that they are computationally inexpensive to run. This was shown to be a useful and relevant aspect for applications to PSP data as it allowed time dependence to be introduced into our modeling through runnning the model repeatedly with time-evolving boundary conditions. This was observed to improve the overall prediction quality.

After doing the exercise of reproducing in situ data from PSP and finding the best set of PFSS modeling parameters to do so, we next used these models to investigate solar wind source regions, tracing magnetic field lines from PSP inwards to the photosphere. This led to important contextual information for the PSP first light data, including pointing to an unusual source (a small equatorial coronal hole) for the first perihelion from which PSP made the first striking observations of near-Sun ubiquitous magentic switchbacks [18, 81, 45, 72] (and many more). This finding also resulted in the inference that although PSP observed slow solar wind, it was clearly associated with a coronal hole and highly alfvenic [199, 18], a key data point in tackling questions about the fast and slow solar wind bifurcation.

6.4 Tracking a type III radio burst from an active region to 1 au

Lastly, in chapter 5 which presented Badman et al. (2022b, in review) [16], we diverged slightly from the previous chapters in which direct *in situ* measurements in the inner heliosphere were used to investigate the coronal and heliospheric magnetic structure. Instead, in this chapter we investigated a possible pathway to *remotely* observing this same magnetic structure. Towards this, we combined numerous observations and measurements to track the propagation through space of a type III radio burst: a phenomenon in which an electron beam is injected onto interplanetary field lines by a solar transient event. Unlike larger eruptive events such as CMEs where the coronal and heliospheric structure is strongly perturbed, the electron beams which result in type III emission act as passive tracers. Confined

to magnetic field lines they propagate outwards along this structure. Therefore tracking these beams has the potential to yield direct measurements of magnetic topology and moreover to do so over a large spatial distance (from the corona to 1 au) in a relatively short time since the electron beams can cover the distance to 1 au in as short as 20 minutes compared to $\sim$4 days for the advection of a typical solar wind parcel.

Our tracking results produced a coherent and consistent picture with emergence in the low corona as imaged by ground based radio telescopes, radially outwards propagation from 5-40$R\odot$ in the inner heliosphere determined by time delay measurements between several single point spacecraft radio observations, and lastly a confirmation of arrival of the electron beam at 1 au. While the fidelity of the tracking is not fine enough yet to make stronger statements than that "the coronal field lines were open and the consistent with a bundle of HMF Parker spiral field lines tracked in the inner heliosphere and reaching the vicinity of STEREO A", the concept and combination of techniques was proven to be useful and avenues for future development were identified.

6.5 Overarching conclusions and directions for future work

Aside from the distinct individual results, taken together these investigations show:

1. **The power of combining complementary observatories and using independent information and constraints** to investigate a system that is usually difficult to generalize from single point measurements: In chapter 2 we saw how using different, *independent* remote observations and in situ measurements to constrain different physical aspects of the corona led to a more complete and quantitative way to compare and tune coronal models. In chapter 3 we used the unique orbital trajectory of Parker Solar Probe with respect to distance from the Sun to make more powerful inferences with in situ data than can be done from a single point in space. Chapter 4 figure4.4 showed a simple but powerful way to estimate heliospheric structure with simple Parker spiral field lines compared at multiple radii with the use of PSP and 1 au spacecraft. Lastly, multi-observer measurements were central to chapter 5 where the goal was to make near simultaneous measurements throughout the corona and inner heliosphere and making full use of the various remote observational and in situ instrumentation throughout the inner solar system was a necessary condition to achieving this.

2. **The advantage of taking measurements from new vantage points in interplanetary space and with new instrumentation**: This was most clearly shown in 3 where the unprecedented radial variation in PSP's orbit was a key ingredient in showing the persistence of the open flux problem near the Sun, and in 4, the longitudinal behaviour (changing angular velocity with respect to the sun), was a key aspect of finding a coherent solar wind source for PSP for nearly 2 weeks as the spacecraft

hovered over the same location of the sun for an extended period of time. Additionally, in 5, one particular limitation for the time delay method was found to be instrument time resolution, and the observations by PSP of the same radio burst as observed by STEREO and Wind but at much higher time resolution showed the advantage and extra detail that can be captured by more modern instrumentation and more powerful on board computers.

3. **The surprisingly strong applicability of the simplest models to contemporary spacecraft measurements.** The models we have predominantly used in this work (PFSS for the corona and the Parker spiral for the inner heliosphere) are both over 60 years old, highly simplistic and limited in the amount of physics they contain, and as shown in chapter 2 readily improved upon at the cost of increased computational time. However, for the purpose of the investigations studied in this thesis (the magnetic structure of the corona and inner heliosphere), these simplest models have proved to be of great use. As remarked above, the Parker spiral model for the heliospheric magnetic field matches the large scale background field measured by PSP is its orbits to date (chapter 3). Further, the PFSS method of predicting the heliospheric current sheet proves to be highly predictive of when PSP will measure current sheet crossings in space (including in all later orbits not reported in this thesis). Chapter 2 also quantified how PFSS provides good representations of coronal hole locations in the lower corona, and the streamer belt topology, although in both cases also showed that improvement can be achieved with other models. Lastly, despite being manifestly time-independent and not containing any free energy in the magnetic field, PFSS even proved useful in the context of solar eruptive events where an open field region was determined to lie cospatially with a source active region and offered a consistent explanation of how and where the type III burst studied in that chaper could escape the corona.

4. Finally, these investigations showed that **there remains significant gaps in our understanding and offered directions for future improvement of our knowledge of the coronal and heliospheric magnetic fields**. The clearest example of this was in our finding of the persistence of the "open flux" problem close to the sun, showing that the amount of magnetic flux open in coronal field models remains smaller than that seen in interplanetary space. This points to gaps in our coronal model physics (one that is not even addressed by MHD physics). As discussed above, resolutions may be found in modeling approaches (e.g. time dependence), or perhaps in future observations (e.g. of the Sun's polar regions). In chapter 5, while our methodology was shown to be useful and complementary it still resulted in very coarse localization. Two clear directions for improvement were identified. Firstly, we need to examine the underlying assumptions of the methods, notably the assumption of a spherically symmetric coronal density profile for deprojecting the radio plane of sky images, and the assumption of no scattering or refraction in the radio propagation path from source

to receiver in interplanetary space. More sophisticated modeling of these aspects have the potential of making our sources more accurate, and could simultaneously allow density structures of the corona and heliosphere to be probed along with the magnetic field. The other direction for improvement was instrumentation-wise : a strong limitation on the heliospheric localization shown in this chapter was that we had to assume the radio burst was located in the equatorial plane which is not always true. More multi-spacecraft collaboration is now possible wiht the launch of Solar Orbiter (SO), allowiong 4 point measurements of the same radio burst (e.g. [140]). Adding this to our construction will allow the source localization to be performed in 3D rather than 2D, meaning all type IIIs can be studied and 3D heliospheric structure also. Chapter 2 didn't provide many surprises about how well different coronal models perform but it did show the importance of inspecting multiple aspects of coronal models in evaluating their quality, suggesting this should be standard practice. Towards facilitating this we therefore concluded that implementing the framework discussed there as an open source tool was a high priority next step.

In closing, this thesis has discussed numerous studies in the era of Parker Solar Probe which investigate and improve our knowledge and understanding of the heliospheric and coronal magnetic fields. PSP directly cuts through new, never before reached regions of the heliosphere providing new and direct measurements of these structure. Even though it has not yet dived deep into what can be reasonably called coronal plasma, PSP's close approach has with the assistance of models allowed significant headway in making new constraints on this medium. In the next few years, PSP will reach with $10R_{\odot}$ and joined by new out-of-ecliptic remote (and in situ) observations for Solar Orbiter, these techniques and studies will be extended and more widely applied. Ultimately, these results will be traceable to direct improvement in our understanding in the Sun-earth connection and our ability to predict ahead of time what effect the Sun will have on its local environment.

Bibliography

[1] M. H. Acuña et al. "The STEREO/IMPACT Magnetic Field Experiment". In: *SSR* 136.1-4 (Apr. 2008), pp. 203–226. DOI: 10.1007/s11214-007-9259-2.

[2] Benjamin Thomas Alcock. "Solar electron and radio propagation in the turbulent solar corona". PhD thesis. University of Glasgow, UK, Jan. 2018.

[3] R. C. Allen et al. "Solar Wind Streams and Stream Interaction Regions Observed by the Parker Solar Probe with Corresponding Observations at 1 au". In: *ApJS* 246.2, 36 (Feb. 2020), p. 36. DOI: 10.3847/1538-4365/ab578f.

[4] M. D. Altschuler and G. Newkirk. "Magnetic Fields and the Structure of the Solar Corona. I: Methods of Calculating Coronal Fields". In: *Solar Physics* 9 (Sept. 1969), pp. 131–149. DOI: 10.1007/BF00145734.

[5] W. M. Arden, A. A. Norton, and X. Sun. "A "breathing" source surface for cycles 23 and 24". In: *Journal of Geophysical Research (Space Physics)* 119.3 (Mar. 2014), pp. 1476–1485. DOI: 10.1002/2013JA019464.

[6] C. N. Arge and V. J. Pizzo. "Improvement in the prediction of solar wind conditions using near-real time solar magnetic field updates". In: *Journal of Geophysical Research: Space Physics* 105.A5 (2000), pp. 10465–10479. DOI: 10.1029/1999JA000262. eprint: https://agupubs.onlinelibrary.wiley.com/doi/pdf/10.1029/1999JA000262. URL: https://agupubs.onlinelibrary.wiley.com/doi/abs/10.1029/1999JA000262.

[7] C. N. Arge et al. "Improving Data Drivers for Coronal and Solar Wind Models". In: *J. Phys.* Ed. by N. V. Pogorelov, E. Audit, and G. P. Zank. Vol. CS-444. Oct. 2011, Astron. Soc. Pacific, San Francisco, 99.

[8] C. N. Arge et al. "Modeling the corona and solar wind using ADAPT maps that include far-side observations". In: *Solar Wind 13*. Ed. by G. P. Zank et al. Vol. CS-1539. June 2013, Am. Inst. Phys., Melville, 11–14. DOI: 10.1063/1.4810977.

[9] C. Nick Arge et al. "Air Force Data Assimilative Photospheric Flux Transport (ADAPT) Model". In: *AIP Conference Proceedings* 1216.1 (2010), pp. 343–346. DOI: 10.1063/1.3395870. eprint: https://aip.scitation.org/doi/pdf/10.1063/1.3395870. URL: https://aip.scitation.org/doi/abs/10.1063/1.3395870.

[10] C.N. Arge et al. "Stream structure and coronal sources of the solar wind during the May 12th, 1997 CME". In: *Journal of Atmospheric and Solar-Terrestrial Physics* 66.15 (2004). Towards an Integrated Model of the Space Weather System, pp. 1295–1309. ISSN: 1364-6826. DOI: https://doi.org/10.1016/j.jastp.2004.03.018. URL: http://www.sciencedirect.com/science/article/pii/S1364682604001403.

[11] Charles N. Arge et al. "Improved Method for Specifying Solar Wind Speed Near the Sun". In: *AIP Conference Proceedings* 679.1 (2003), pp. 190–193. DOI: 10.1063/1.1618574. eprint: https://aip.scitation.org/doi/pdf/10.1063/1.1618574. URL: https://aip.scitation.org/doi/abs/10.1063/1.1618574.

[12] S. T. Badman et al. *Observational Dataset for "Constraining Global Coronal Models with Multiple Independent Observables", Badman et al. (2022)*. Zenodo, Mar. 2022. DOI: 10.5281/zenodo.6342187. URL: https://doi.org/10.5281/zenodo.6342187.

[13] Samuel T. Badman et al. "Constraining Global Coronal Models with Multiple Independent Observables". In: *The Astrophysical Journal* 932.2, 135 (June 2022), p. 135. DOI: 10.3847/1538-4357/ac6610. arXiv: 2201.11818 [astro-ph.SR].

[14] Samuel T. Badman et al. "Magnetic Connectivity of the Ecliptic Plane within 0.5 au: Potential Field Source Surface Modeling of the First Parker Solar Probe Encounter". In: *Astrophysical Journal Supplement* 246.2, 23 (Feb. 2020), p. 23. DOI: 10.3847/1538-4365/ab4da7. arXiv: 1912.02244 [astro-ph.SR].

[15] Samuel T. Badman et al. "Measurement of the open magnetic flux in the inner heliosphere down to 0.13 AU". In: *A&A* 650, A18 (June 2021), A18. DOI: 10.1051/0004-6361/202039407. arXiv: 2009.06844 [astro-ph.SR].

[16] Samuel T. Badman et al. "Tracking a beam of electrons from the low solar corona into interplanetary space with the Low Frequency Array, Parker Solar Probe and 1 au spacecraft". In: *arXiv e-prints*, arXiv:2204.08497 (Apr. 2022), arXiv:2204.08497. arXiv: 2204.08497 [astro-ph.SR].

[17] S. D. Bale et al. "A Solar Source of Alfvénic Magnetic Field Switchbacks: In Situ Remnants of Magnetic Funnels on Supergranulation Scales". In: *The Astrophysical Journal* 923.2, 174 (Dec. 2021), p. 174. DOI: 10.3847/1538-4357/ac2d8c. arXiv: 2109.01069 [astro-ph.SR].

[18] S. D. Bale et al. "Highly structured slow solar wind emerging from an equatorial coronal hole". In: *Nature* 576.7786 (Dec. 2019), pp. 237–242. DOI: 10.1038/s41586-019-1818-7.

[19] S. D. Bale et al. "The FIELDS Instrument Suite for Solar Probe Plus. Measuring the Coronal Plasma and Magnetic Field, Plasma Waves and Turbulence, and Radio Signatures of Solar Transients". In: *SSR* 204 (Dec. 2016), pp. 49–82. DOI: 10.1007/s11214-016-0244-5.

[20] L. Biermann. "Kometenschweife und solare Korpuskularstrahlung". In: *Zeitschrift für Astrophysik* 29 (Jan. 1951), p. 274.

[21] Benjamin Boe, Shadia Habbal, and Miloslav Druckmuller. "Coronal Magnetic Field Topology From Total Solar Eclipse Observations". In: *arXiv e-prints*, arXiv:2004.08970 (Apr. 2020), arXiv:2004.08970. arXiv: 2004.08970 [astro-ph.SR].

[22] X. Bonnin, S. Hoang, and M. Maksimovic. "The directivity of solar type III bursts at hectometer and kilometer wavelengths: Wind-Ulysses observations". In: *Astronomy & Astrophysics* 489.1 (Oct. 2008), pp. 419–427. DOI: 10.1051/0004-6361:200809777.

[23] J. -L. Bougeret et al. "Waves: The Radio and Plasma Wave Investigation on the Wind Spacecraft". In: *SSR* 71.1-4 (Feb. 1995), pp. 231–263. DOI: 10.1007/BF00751331.

[24] J. L. Bougeret et al. "S/WAVES: The Radio and Plasma Wave Investigation on the STEREO Mission". In: *SSR* 136.1-4 (Apr. 2008), pp. 487–528. DOI: 10.1007/s11214-007-9298-8.

[25] T. A. Bowen et al. "A Merged Search-Coil and Fluxgate Magnetometer Data Product for Parker Solar Probe FIELDS". In: *Journal of Geophysical Research (Space Physics)* 125.5, e27813 (May 2020), e27813. DOI: 10.1029/2020JA027813. arXiv: 2001.04587 [astro-ph.IM].

[26] David H. Brooks, Ignacio Ugarte-Urra, and Harry P. Warren. "Full-Sun observations for identifying the source of the slow solar wind". In: *Nature Communications* 6, 5947 (Jan. 2015), p. 5947. DOI: 10.1038/ncomms6947. arXiv: 1605.09514 [astro-ph.SR].

[27] G. E. Brueckner et al. "The Large Angle Spectroscopic Coronagraph (LASCO)". In: *Solar Physics* 162.1-2 (Dec. 1995), pp. 357–402. DOI: 10.1007/BF00733434.

[28] D. A. Bryant et al. "New Evidence for Long-Lived Solar Streams in Interplanetary Space". In: *Physical Review Letters* 11.4 (Aug. 1963), pp. 144–146. DOI: 10.1103/PhysRevLett.11.144.

[29] Iver H. Cairns. "Fundamental plasma emission involving ion sound waves". In: *Journal of Plasma Physics* 38.2 (Oct. 1987), pp. 169–178. DOI: 10.1017/S0022377800012496.

[30] Iver H. Cairns. "Second harmonic plasma emission involving ion sound waves". In: *JPP* 38.2 (Oct. 1987), pp. 179–198. DOI: 10.1017/S0022377800012502.

[31] R. M. Caplan, C. Downs, and J. A. Linker. "Synchronic Coronal Hole Mapping Using Multi-instrument EUV Images: Data Preparation and Detection Method". In: *Astrophysical Journal* 823.1, 53 (May 2016), p. 53. DOI: 10.3847/0004-637X/823/1/53. arXiv: 1510.04718 [astro-ph.SR].

[32] Ronald M. Caplan et al. "Variations in Finite-difference Potential Fields". In: *Astrophysical Journal* 915.1, 44 (July 2021), p. 44. DOI: 10.3847/1538-4357/abfd2f. arXiv: 2102.05618 [astro-ph.SR].

[33] A. W. Case et al. "The Solar Probe Cup on the Parker Solar Probe". In: *The Astrophysical Journals* 246.2, 43 (Feb. 2020), p. 43. DOI: 10.3847/1538-4365/ab5a7b. arXiv: 1912.02581 [astro-ph.IM].

[34] Cynthia Cattell et al. "Periodicities in an active region correlated with Type III radio bursts observed by Parker Solar Probe". In: *Astronomy & Astrophysics* 650, A6 (June 2021), A6. DOI: 10.1051/0004-6361/202039510. arXiv: 2009.10899 [astro-ph.SR].

[35] Phillip C. Chamberlin et al. "Next generation x-ray sensor (XRS) for the NOAA GOES-R satellite series". In: *Solar Physics and Space Weather Instrumentation III*. Ed. by Silvano Fineschi and Judy A. Fennelly. Vol. 7438. Society of Photo-Optical Instrumentation Engineers (SPIE) Conference Series. Aug. 2009, p. 743802. DOI: 10.1117/12.826807.

[36] Rohit Chhiber et al. "Contextual Predictions for the Parker Solar Probe. I. Critical Surfaces and Regions". In: *The Astrophysical Journal Supplement* 241.1, 11 (Mar. 2019), p. 11. DOI: 10.3847/1538-4365/ab0652. arXiv: 1806.00570 [astro-ph.SR].

[37] R. Clark et al. "GONG Magnetogram Zero-Point Correction Status". In: *AAS/Solar Physics Division Meeting #34*. Vol. 35. Bulletin of the American Astronomical Society. May 2003, p. 822.

[38] E. W. Cliver, I. G. Richardson, and A. G. Ling. "Solar Drivers of 11-yr and Long-Term Cosmic Ray Modulation". In: *SSR* 176.1-4 (June 2013), pp. 3–19. DOI: 10.1007/s11214-011-9746-3.

[39] C. M. S. Cohen et al. "Energetic Particle Increases Associated with Stream Interaction Regions". In: *ApJS* 246.2, 20 (Feb. 2020), p. 20. DOI: 10.3847/1538-4365/ab4c38. arXiv: 1912.08244 [physics.space-ph].

[40] Steven R. Cranmer and Amy R. Winebarger. "The Properties of the Solar Corona and Its Connection to the Solar Wind". In: *Ann. Rev. Astro. & Astron.* 57 (Aug. 2019), pp. 157–187. DOI: 10.1146/annurev-astro-091918-104416. arXiv: 1811.00461 [astro-ph.SR].

[41] Judith de Patoul, Claire Foullon, and Pete Riley. "3D Electron Density Distributions in the Solar Corona during Solar Minima: Assessment for More Realistic Solar Wind Modeling". In: *Astrophysical Journal* 814.1, 68 (Nov. 2015), p. 68. DOI: 10.1088/0004-637X/814/1/68. arXiv: 1512.04135 [astro-ph.SR].

[42] C. E. Deforest and C. C. Kankelborg. "Fluxon modeling of low-beta plasmas". In: *Journal of Atmospheric and Solar-Terrestrial Physics* 69.1-2 (Feb. 2007), pp. 116–128. DOI: 10.1016/j.jastp.2006.06.011. arXiv: astro-ph/0609508 [astro-ph].

[43] V. Domingo, B. Fleck, and A. I. Poland. "The SOHO Mission: an Overview". In: *Solar Physics* 162.1-2 (Dec. 1995), pp. 1–37. DOI: 10.1007/BF00733425.

[44] Miloslav Druckmuller. "August 1, 2008, Total Solar Eclipse". In: *Sky & Telescope* 116.6 (Dec. 2008), p. 102.

[45] Thierry Dudok de Wit et al. "Switchbacks in the Near-Sun Magnetic Field: Long Memory and Impact on the Turbulence Cascade". In: *The Astrophysical Journal Supplement Series* 246.2 (Feb. 2020), p. 39. DOI: 10.3847/1538-4365/ab5853. URL: https://doi.org/10.3847%2F1538-4365%2Fab5853.

[46] G. Erdős and A. Balogh. "MAGNETIC FLUX DENSITY IN THE HELIOSPHERE THROUGH SEVERAL SOLAR CYCLES". In: *The Astrophysical Journal* 781.1 (Jan. 2014), p. 50. DOI: 10.1088/0004-637x/781/1/50. URL: https://doi.org/10.1088%2F0004-637x%2F781%2F1%2F50.

[47] G. Erdős and A. Balogh. "Magnetic Flux Density Measured in Fast and Slow Solar Wind Streams". In: *Astrophysical Journal* 753.2, 130 (July 2012), p. 130. DOI: 10.1088/0004-637X/753/2/130.

[48] R. E. Ergun et al. "Wind Spacecraft Observations of Solar Impulsive Electron Events Associated with Solar Type III Radio Bursts". In: *Astrophysical Journal* 503.1 (Aug. 1998), pp. 435–445. DOI: 10.1086/305954.

[49] Xueshang Feng. *Magnetohydrodynamic Modeling of the Solar Corona and Heliosphere*. 2020. DOI: 10.1007/978-981-13-9081-4.

[50] L. A. Fisk and J. C. Kasper. "Global Circulation of the Open Magnetic Flux of the Sun". In: *The Astrophysical Journal* 894.1 (Apr. 2020), p. L4. DOI: 10.3847/2041-8213/ab8acd. URL: https://doi.org/10.3847%2F2041-8213%2Fab8acd.

[51] L. A. Fisk, N. A. Schwadron, and T. H. Zurbuchen. "On the Slow Solar Wind". In: *SSR* 86 (July 1998), pp. 51–60. DOI: 10.1023/A:1005015527146.

[52] N. J. Fox et al. "The Solar Probe Plus Mission: Humanity's First Visit to Our Star". In: *SSR* 204 (Dec. 2016), pp. 7–48. DOI: 10.1007/s11214-015-0211-6.

[53] S. L. Freeland and B. N. Handy. "Data Analysis with the SolarSoft System". In: *Solar Physics* 182.2 (Oct. 1998), pp. 497–500. DOI: 10.1023/A:1005038224881.

[54] A. B. Galvin et al. "The Plasma and Suprathermal Ion Composition (PLASTIC) Investigation on the STEREO Observatories". In: *SSR* 136.1-4 (Apr. 2008), pp. 437–486. DOI: 10.1007/s11214-007-9296-x.

[55] Tadhg M. Garton, Peter T. Gallagher, and Sophie A. Murray. "Automated coronal hole identification via multi-thermal intensity segmentation". In: *Journal of Space Weather and Space Climate* 8, A02 (Jan. 2018), A02. DOI: 10.1051/swsc/2017039. arXiv: 1711.11476 [astro-ph.SR].

[56] J. Giacalone et al. "Solar Energetic Particles Produced by a Slow Coronal Mass Ejection at ∼0.25 au". In: *ApJS* 246.2, 29 (Feb. 2020), p. 29. DOI: 10.3847/1538-4365/ab5221.

[57] D. A. Gurnett and R. R. Anderson. "Electron Plasma Oscillations Associated with Type III Radio Bursts". In: *Science* 194.4270 (Dec. 1976), pp. 1159–1162. DOI: 10.1126/science.194.4270.1159.

[58] Dennis K. Haggerty and Edmond C. Roelof. "Impulsive Near-relativistic Solar Electron Events: Delayed Injection with Respect to Solar Electromagnetic Emission". In: *Astrophysical Journal* 579.2 (Nov. 2002), pp. 841–853. DOI: 10.1086/342870.

[59] Shirley F. Hansen, C. Sawyer, and Richard T. Hansen. "K corona and magnetic sector boundaries". In: *Geophysical Review Letters* 1.1 (Jan. 1974), pp. 13–15. DOI: 10.1029/GL001i001p00013.

[60] L. Harra et al. "The active region source of a type III radio storm observed by Parker Solar Probe during encounter 2". In: *Astronomy & Astrophysics* 650, A7 (June 2021), A7. DOI: 10.1051/0004-6361/202039514. arXiv: 2102.04964 [astro-ph.SR].

[61] Charles R. Harris et al. "Array programming with NumPy". In: *Nature* 585.7825 (Sept. 2020), pp. 357–362. DOI: 10.1038/s41586-020-2649-2. URL: https://doi.org/10.1038/s41586-020-2649-2.

[62] Ronald Harten and Kenn Clark. "The Design Features of the GGS Wind and Polar Spacecraft". In: *SSR* 71.1-4 (Feb. 1995), pp. 23–40. DOI: 10.1007/BF00751324.

[63] J. W. Harvey et al. "The Global Oscillation Network Group (GONG) Project". In: *Science* 272.5266 (1996), pp. 1284–1286. ISSN: 0036-8075. DOI: 10.1126/science.272.5266.1284. eprint: https://science.sciencemag.org/content/272/5266/1284.full.pdf. URL: https://science.sciencemag.org/content/272/5266/1284.

[64] Karen L. Harvey and Frank Recely. "Polar Coronal Holes During Cycles 22 and 23". In: *Solar Physics* 211.1 (Dec. 2002), pp. 31–52. DOI: 10.1023/A:1022469023581.

[65] David H. Hathaway. "The Solar Cycle". In: *Living Reviews in Solar Physics* 12.1, 4 (Sept. 2015), p. 4. DOI: 10.1007/lrsp-2015-4. arXiv: 1502.07020 [astro-ph.SR].

[66] K. S. Hickmann et al. "Data Assimilation in the ADAPT Photospheric Flux Transport Model". In: *Solar Physics* 290 (Apr. 2015), pp. 1105–1118. DOI: 10.1007/s11207-015-0666-3. arXiv: 1410.6185 [math-ph].

[67] Frank Hill. "The Global Oscillation Network Group Facility—An Example of Research to Operations in Space Weather". In: *Space Weather* 16.10 (Oct. 2018), pp. 1488–1497. DOI: 10.1029/2018SW002001.

[68] J. T. Hoeksema. "Structure and evolution of the large scale solar and heliospheric magnetic fields". PhD thesis. Stanford Univ., CA., 1984.

[69] J. Todd Hoeksema, John M. Wilcox, and Philip H. Scherrer. "The structure of the heliospheric current sheet: 1978–1982". In: *Journal of Geophysical Research: Space Physics* 88.A12 (1983), pp. 9910–9918. DOI: 10.1029/JA088iA12p09910. eprint: https://agupubs.onlinelibrary.wiley.com/doi/pdf/10.1029/JA088iA12p09910.

[70] J. Todd Hoeksema et al. "The Helioseismic and Magnetic Imager (HMI) Vector Magnetic Field Pipeline: Overview and Performance". In: *Solar Physics* 289.9 (Sept. 2014), pp. 3483–3530. DOI: 10.1007/s11207-014-0516-8. arXiv: 1404.1881 [astro-ph.SR].

[71] T. S. Horbury et al. "The Solar Orbiter magnetometer". In: *Astronomy & Astrophysics* 642, A9 (Oct. 2020), A9. DOI: 10.1051/0004-6361/201937257.

[72] Timothy S. Horbury et al. "Sharp Alfvénic Impulses in the Near-Sun Solar Wind". In: *The Astrophysical Journal Supplement Series* 246.2 (Feb. 2020), p. 45. DOI: 10.3847/1538-4365/ab5b15. URL: https://doi.org/10.3847%2F1538-4365%2Fab5b15.

[73] R. A. Howard and M. J. Koomen. "Observation of Sectored Structure in the Outer Solar Corona: Correlation with Interplanetary Magnetic Field". In: *Solar Physics* 37.2 (Aug. 1974), pp. 469–475. DOI: 10.1007/BF00152504.

[74] R. A. Howard et al. "Sun Earth Connection Coronal and Heliospheric Investigation (SECCHI)". In: *Space Sciences Review* 136.1-4 (Apr. 2008), pp. 67–115. DOI: 10.1007/s11214-008-9341-4.

[75] Opal Issan and Pete Riley. "Theoretical Refinements to the Heliospheric Upwind eXtrapolation Technique and Application to in-situ Measurements". In: *Frontiers in Astronomy and Space Sciences* 8, 245 (Jan. 2022), p. 245. DOI: 10.3389/fspas.2021.795323.

[76] I. C. Jebaraj et al. "Using radio triangulation to understand the origin of two subsequent type II radio bursts". In: *Astronomy & Astrophysics* 639, A56 (July 2020), A56. DOI: 10.1051/0004-6361/201937273. arXiv: 2006.04586 [astro-ph.SR].

[77] Bibhuti Kumar Jha et al. "Measurements of Solar Differential Rotation Using the Century Long Kodaikanal Sunspot Data". In: *Solar Physics* 296.1, 25 (Jan. 2021), p. 25. DOI: 10.1007/s11207-021-01767-8. arXiv: 2101.01941 [astro-ph.SR].

[78] M. L. Kaiser. "STEREO: an overview". In: *35th COSPAR Scientific Assembly*. Vol. 35. Jan. 2004, p. 458.

[79] M. L. Kaiser. "The STEREO mission: an overview". In: *Advances in Space Research* 36 (2005), pp. 1483–1488. DOI: 10.1016/j.asr.2004.12.066.

[80] M. L. Kaiser et al. "The STEREO Mission: An Introduction". In: *SSR* 136.1-4 (Apr. 2008), pp. 5–16. DOI: 10.1007/s11214-007-9277-0.

[81] J. C. Kasper et al. "Alfvénic velocity spikes and rotational flows in the near-Sun solar wind". In: *Nature* 576.7786 (Dec. 2019), pp. 228–231. DOI: 10.1038/s41586-019-1813-z.

[82] J. C. Kasper et al. "Parker Solar Probe Enters the Magnetically Dominated Solar Corona". In: *Physical Review Letters* 127.25, 255101 (Dec. 2021), p. 255101. DOI: 10.1103/PhysRevLett.127.255101.

[83] J. C. Kasper et al. "Solar Wind Electrons Alphas and Protons (SWEAP) Investigation: Design of the Solar Wind and Coronal Plasma Instrument Suite for Solar Probe Plus". In: *SSR* 204 (Dec. 2016), pp. 131–186. DOI: 10.1007/s11214-015-0206-3.

[84] T. K. Kim et al. "Predicting the Solar Wind at the Parker Solar Probe Using an Empirically Driven MHD Model". In: *ApJS* 246.2, 40 (Feb. 2020), p. 40. DOI: 10.3847/1538-4365/ab58c9. arXiv: 1912.02397 [physics.space-ph].

[85] J. H. King and N. E. Papitashvili. "Solar wind spatial scales in and comparisons of hourly Wind and ACE plasma and magnetic field data". In: *Journal of Geophysical Research (Space Physics)* 110.A2, A02104 (Feb. 2005), A02104. DOI: 10.1029/2004JA010649.

[86] A. Klassen, R. Gómez-Herrero, and B. Heber. "Electron Spikes, Type III Radio Bursts and EUV Jets on 22 February 2010". In: *Solar Physics* 273.2 (Nov. 2011), pp. 413–419. DOI: 10.1007/s11207-011-9735-4.

[87] Jens Kleimann et al. "The Structure of the Large-Scale Heliosphere as Seen by Current Models". In: *Space Sciences Reviews* 218.4, 36 (June 2022), p. 36. DOI: 10.1007/s11214-022-00902-6.

[88] James A. Klimchuk. "On Solving the Coronal Heating Problem". In: *Solar Physics* 234.1 (Mar. 2006), pp. 41–77. DOI: 10.1007/s11207-006-0055-z. arXiv: astro-ph/0511841 [astro-ph].

[89] Eduard P. Kontar et al. "Anisotropic Radio-wave Scattering and the Interpretation of Solar Radio Emission Observations". In: *apj* 884.2, 122 (Oct. 2019), p. 122. DOI: 10.3847/1538-4357/ab40bb. arXiv: 1909.00340 [astro-ph.SR].

[90] Jason E. Kooi et al. "Modern Faraday Rotation Studies to Probe the Solar Wind". In: *Frontiers in Astronomy and Space Sciences* 9, 841866 (Apr. 2022), p. 841866. DOI: 10.3389/fspas.2022.841866.

[91] Kelly E. Korreck et al. "Source and Propagation of a Streamer Blowout Coronal Mass Ejection Observed by the Parker Solar Probe". In: *ApJS* 246.2, 69 (Feb. 2020), p. 69. DOI: 10.3847/1538-4365/ab6ff9.

[92] Larisza D. Krista and Peter T. Gallagher. "Automated Coronal Hole Detection Using Local Intensity Thresholding Techniques". In: *Solar Physics* 256.1-2 (May 2009), pp. 87–100. DOI: 10.1007/s11207-009-9357-2. arXiv: 0905.1814 [astro-ph.SR].

[93] Säm Krucker et al. "On the Origin of Impulsive Electron Events Observed at 1 AU". In: *Astrophysical Journal* 519.2 (July 1999), pp. 864–875. DOI: 10.1086/307415.

[94] V. Krupar et al. "Interplanetary Type III Bursts and Electron Density Fluctuations in the Solar Wind". In: *ApJ* 857, 82 (Apr. 2018), p. 82. DOI: 10.3847/1538-4357/aab60f.

[95] Vratislav Krupar et al. "Density Fluctuations in the Solar Wind Based on Type III Radio Bursts Observed by Parker Solar Probe". In: *The Astrophysical Journal Supplement Series* 246.2 (Feb. 2020), p. 57. DOI: 10.3847/1538-4365/ab65bd. URL: https://doi.org/10.3847%2F1538-4365%2Fab65bd.

[96] M. Kruse, V. Heidrich-Meisner, and R. F. Wimmer-Schweingruber. "Evaluation of a potential field source surface model with elliptical source surfaces via ballistic back mapping of in situ spacecraft data". In: *Astronomy & Astrophysics* 645, A83 (Jan. 2021), A83. DOI: 10.1051/0004-6361/202039120.

[97] M. Kruse et al. "An elliptic expansion of the potential field source surface model". In: *Astronomy & Astrophysics* 638, A109 (June 2020), A109. DOI: 10.1051/0004-6361/202037734. arXiv: 2005.12843 [astro-ph.SR].

[98] Yolande Leblanc, George A. Dulk, and Jean-Louis Bougeret. "Tracing the Electron Density from the Corona to 1au". In: *Solar Physics* 183.1 (Nov. 1998), pp. 165–180. DOI: 10.1023/A:1005049730506.

[99] A. Lecacheux et al. "Characteristics of type III bursts in the solar wind from simultaneous observations on board ISEE-3 and Voyager". In: *Astronomy & Astrophysics* 217.1-2 (June 1989), pp. 237–250.

[100] C. O. Lee et al. "Coronal Field Opens at Lower Height During the Solar Cycles 22 and 23 Minimum Periods: IMF Comparison Suggests the Source Surface Should Be Lowered". In: *Solar Physics* 269 (Apr. 2011), pp. 367–388. DOI: 10.1007/s11207-010-9699-9.

[101] E. Leer, T. E. Holzer, and T. Fla. "Acceleration of the solar wind." In: *Space Sciences Review* 33.1-2 (Mar. 1982), pp. 161–200. DOI: 10.1007/BF00213253.

[102] James R. Lemen et al. "The Atmospheric Imaging Assembly (AIA) on the Solar Dynamics Observatory (SDO)". In: *Solar Physics* 275.1 (Jan. 2012), pp. 17–40. ISSN: 1573-093X. DOI: 10.1007/s11207-011-9776-8. URL: https://doi.org/10.1007/s11207-011-9776-8.

[103] R. P. Lepping et al. "The WIND magnetic field investigation". In: *Space Science Reviews* 71.1 (Feb. 1995), pp. 207–229. ISSN: 1572-9672. DOI: 10.1007/BF00751330. URL: https://doi.org/10.1007/BF00751330.

[104] S. T. Lepri and T. H. Zurbuchen. "Iron charge state distributions as an indicator of hot ICMEs: Possible sources and temporal and spatial variations during solar maximum". In: *Journal of Geophysical Research (Space Physics)* 109.A1, A01112 (Jan. 2004), A01112. DOI: 10.1029/2003JA009954.

[105] R. H. Levine et al. "Open magnetic structures on the sun." In: *Astrophysical Journal* 215 (July 1977), pp. 636–651. DOI: 10.1086/155398.

[106] Randolph H. Levine, Michael Schulz, and E. N. Frazier. "Simulation of the magnetic structure of the inner heliosphere by means of a non-spherical source surface". In: *Solar Physics* 77.1 (Apr. 1982), pp. 363–392. ISSN: 1573-093X. DOI: 10.1007/BF00156118. URL: https://doi.org/10.1007/BF00156118.

[107] B. Li, Iver H. Cairns, and P. A. Robinson. "Frequency Fine Structures of Type III Bursts Due to Localized Medium-Scale Density Structures Along Paths of Type III Beams". In: *Solar Physics* 279.1 (July 2012), pp. 173–196. DOI: 10.1007/s11207-012-0001-1.

[108] B. Li et al. "Mapping magnetic field lines between the Sun and Earth". In: *Journal of Geophysical Research (Space Physics)* 121.2 (Feb. 2016), pp. 925–948. DOI: 10.1002/2015JA021853.

[109] R. P. Lin et al. "The STEREO IMPACT Suprathermal Electron (STE) Instrument". In: *SSR* 136.1-4 (Apr. 2008), pp. 241–255. DOI: 10.1007/s11214-008-9330-7.

[110] J. A. Linker et al. "The Open Flux Problem". In: *The Astrophysical Journal* 848.1 (Oct. 2017), p. 70. DOI: 10.3847/1538-4357/aa8a70. URL: https://doi.org/10.3847%2F1538-4357%2Faa8a70.

[111] Roberto Lionello, Jon A. Linker, and Zoran Mikić. "Including the Transition Region in Models of the Large-Scale Solar Corona". In: *Astrophysical Journal* 546.1 (Jan. 2001), pp. 542–551. DOI: 10.1086/318254.

[112] Roberto Lionello, Jon A. Linker, and Zoran Mikić. "MULTISPECTRAL EMISSION OF THE SUN DURING THE FIRST WHOLE SUN MONTH: MAGNETOHYDRODYNAMIC SIMULATIONS". In: *The Astrophysical Journal* 690.1 (Dec. 2008), pp. 902–912. DOI: 10.1088/0004-637x/690/1/902. URL: https://doi.org/10.1088%2F0004-637x%2F690%2F1%2F902.

[113] Roberto Lionello, Jon A. Linker, and Zoran Mikić. "Multispectral Emission of the Sun During the First Whole Sun Month: Magnetohydrodynamic Simulations". In: *Astrophysical Journal* 690.1 (Jan. 2009), pp. 902–912. DOI: 10.1088/0004-637X/690/1/902.

[114] M. Liu et al. "Solar wind energy flux observations in the inner heliosphere: first results from Parker Solar Probe". In: *Astronomy & Astrophysics* 650, A14 (June 2021), A14. DOI: 10.1051/0004-6361/202039615. arXiv: 2101.03121 [astro-ph.SR].

[115] M. Lockwood and M. Owens. "The Accuracy of Using the Ulysses Result of the Spatial Invariance of the Radial Heliospheric Field to Compute the Open Solar Flux". In: *Astrophysical Journal* 701.2 (Aug. 2009), pp. 964–973. DOI: 10.1088/0004-637X/701/2/964.

[116] M. Lockwood, M. Owens, and A. P. Rouillard. "Excess open solar magnetic flux from satellite data: 1. Analysis of the third perihelion Ulysses pass". In: *Journal of Geophysical Research (Space Physics)* 114.A11, A11103 (Nov. 2009), A11103. DOI: 10.1029/2009JA014449.

[117] M. Lockwood, M. Owens, and A. P. Rouillard. "Excess open solar magnetic flux from satellite data: 2. A survey of kinematic effects". In: *Journal of Geophysical Research (Space Physics)* 114.A11, A11104 (Nov. 2009), A11104. DOI: 10.1029/2009JA014450.

[118] J. Luhmann, D. Curtis, and Impact Team. "IMPACT: Science Goals and Firsts with STEREO". In: *35th COSPAR Scientific Assembly*. Vol. 35. Jan. 2004, p. 2065.

[119] J. G. Luhmann et al. "STEREO IMPACT Investigation Goals, Measurements, and Data Products Overview". In: *SSR* 136.1-4 (Apr. 2008), pp. 117–184. DOI: 10.1007/s11214-007-9170-x.

[120] Allan R Macneil et al. "The evolution of inverted magnetic fields through the inner heliosphere". In: *Monthly Notices of the Royal Astronomical Society* 494.3 (Apr. 2020), pp. 3642–3655. ISSN: 0035-8711. DOI: 10.1093/mnras/staa951. eprint: https://academic.oup.com/mnras/article-pdf/494/3/3642/33144993/staa951.pdf. URL: https://doi.org/10.1093/mnras/staa951.

[121] Allan R. Macneil et al. "A statistical evaluation of ballistic backmapping for the slow solar wind: The interplay of solar wind acceleration and corotation". In: *Monthly Notices of the Royal Astronomical Society* (Oct. 2021). DOI: 10.1093/mnras/stab2965.

[122] J. Magdalenić et al. "Flare-generated Type II Burst without Associated Coronal Mass Ejection". In: *ApJ* 746.2, 152 (Feb. 2012), p. 152. DOI: 10.1088/0004-637X/746/2/152.

[123] J. Magdalenić et al. "Origin of Coronal Shock Waves Associated with Slow Coronal Mass Ejections". In: *ApJ* 718.1 (July 2010), pp. 266–278. DOI: 10.1088/0004-637X/718/1/266.

[124] O. V. Malanushenko and H. P. Jones. "Differentiating Coronal Holes from the Quiet Sun by He 1083 nm Imaging Spectroscopy". In: *Solar Physics* 226.1 (Jan. 2005), pp. 3–16. DOI: 10.1007/s11207-005-4972-z.

[125] David M. Malaspina et al. "The Digital Fields Board for the FIELDS instrument suite on the Solar Probe Plus mission: Analog and digital signal processing". In: *Journal of Geophysical Research (Space Physics)* 121.6 (June 2016), pp. 5088–5096. DOI: 10.1002/2016JA022344.

[126] R. G. Marsden, K-P. Wenzel, and E. J. Smith. "The Ulysses Mission". In: *The Sun and the Heliosphere in Three Dimensions*. Ed. by R. G. Marsden. Dordrecht: Springer Netherlands, 1986, pp. 477–490. ISBN: 978-94-009-4612-5.

[127] D. J. McComas et al. "Integrated Science Investigation of the Sun (ISIS): Design of the Energetic Particle Investigation". In: *SSR* 204 (Dec. 2016), pp. 187–256. DOI: 10.1007/s11214-014-0059-1.

[128] D. J. McComas et al. "Probing the energetic particle environment near the Sun". In: *Nature* 576 (Dec. 2019), pp. 223–227. DOI: 10.1038/s41586-019-1811-1.

[129] D. B. Melrose. "Coherent emission mechanisms in astrophysical plasmas". In: *Reviews of Modern Plasma Physics* 1.1, 5 (Dec. 2017), p. 5. DOI: 10.1007/s41614-017-0007-0. arXiv: 1707.02009 [physics.plasm-ph].

[130] A. Mignone et al. "PLUTO: A Numerical Code for Computational Astrophysics". In: *Astrophysical Journal Supplement* 170.1 (May 2007), pp. 228–242. DOI: 10.1086/513316. arXiv: astro-ph/0701854 [astro-ph].

[131] Zoran Mikic and Jon A. Linker. "Disruption of Coronal Magnetic Field Arcades". In: *Astrophysical Journal* 430 (Aug. 1994), p. 898. DOI: 10.1086/174460.

[132] Zoran Mikić and Jon A. Linker. "The large-scale structure of the solar corona and inner heliosphere". In: *Proceedings of the eigth International solar wind Conference: Solar wind eight*. Ed. by D. Winterhalter et al. Vol. 382. American Institute of Physics Conference Series. July 1996, pp. 104–107. DOI: 10.1063/1.51370.

[133] Zoran Mikić et al. "Magnetohydrodynamic modeling of the global solar corona". In: *Physics of Plasmas* 6.5 (May 1999), pp. 2217–2224. DOI: 10.1063/1.873474.

[134] Zoran Mikić et al. "Predicting the corona for the 21 August 2017 total solar eclipse". In: *Nature Astronomy* (2018), p. 1.

[135] D. G. Mitchell et al. "CME-associated Energetic Ions at 0.23 au: Consideration of the Auroral Pressure Cooker Mechanism Operating in the Low Corona as a Possible Energization Process". In: *ApJS* 246.2, 59 (Feb. 2020), p. 59. DOI: 10.3847/1538-4365/ab63cc. arXiv: 1912.08891 [physics.space-ph].

[136] Michel Moncuquet et al. "First In Situ Measurements of Electron Density and Temperature from Quasi-thermal Noise Spectroscopy with Parker Solar Probe/FIELDS". In: *Astrophysical Journal Supplement* 246.2, 44 (Feb. 2020), p. 44. DOI: 10.3847/1538-4365/ab5a84. arXiv: 1912.02518 [astro-ph.SR].

[137] Huw Morgan and Anthony C. Cook. "The Width, Density, and Outflow of Solar Coronal Streamers". In: *Astrophysical Journal* 893.1, 57 (Apr. 2020), p. 57. DOI: 10.3847/1538-4357/ab7e32. arXiv: 2003.04809 [astro-ph.SR].

[138] D. Müller et al. "The Solar Orbiter mission. Science overview". In: *Astronomy & Astrophysics* 642, A1 (Oct. 2020), A1. DOI: 10.1051/0004-6361/202038467. arXiv: 2009.00861 [astro-ph.SR].

[139] R. Müller-Mellin et al. "The Solar Electron and Proton Telescope for the STEREO Mission". In: *SSR* 136.1-4 (Apr. 2008), pp. 363–389. DOI: 10.1007/s11214-007-9204-4.

[140] S. Musset et al. "Simulations of radio-wave anisotropic scattering to interpret type III radio burst data from Solar Orbiter, Parker Solar Probe, STEREO, and Wind". In: *Astronomy & Astrophysics* 656, A34 (Dec. 2021), A34. DOI: 10.1051/0004-6361/202140998. arXiv: 2109.13713 [astro-ph.SR].

[141] M. Neugebauer. "The quiet solar wind". In: *Journal of Geophysical Research* 81.25 (Sept. 1976), p. 4664. DOI: 10.1029/JA081i025p04664.

[142] Marcia Neugebauer and Conway W. Snyder. "Solar Plasma Experiment". In: *Science* 138.3545 (Dec. 1962), pp. 1095–1097. DOI: 10.1126/science.138.3545.1095-a.

[143] Jr. Newkirk Gordon. "The Solar Corona in Active Regions and the Thermal Origin of the Slowly Varying Component of Solar Radio Radiation." In: *Astrophysical Journal* 133 (May 1961), p. 983. DOI: 10.1086/147104.

[144] Teresa Nieves-Chinchilla et al. "Analysis of the Internal Structure of the Streamer Blowout Observed by the Parker Solar Probe During the First Solar Encounter". In: ().

[145] L. Nikolić. "On Solutions of the PFSS Model With GONG Synoptic Maps for 2006–2018". In: *Space Weather* 0.0 (2019). DOI: 10.1029/2019SW002205. eprint: https://agupubs.onlinelibrary.wiley.com/doi/pdf/10.1029/2019SW002205. URL: https://agupubs.onlinelibrary.wiley.com/doi/abs/10.1029/2019SW002205.

[146] J. T. Nolte and E. C. Roelof. "Large-Scale Structure of the Interplanetary Medium, I: High Coronal Source Longitude of the Quiet-Time Solar Wind". In: *Solar Physics* 33 (Nov. 1973), pp. 241–257. DOI: 10.1007/BF00152395.

[147] A. R. Offringa et al. "WSCLEAN: an implementation of a fast, generic wide-field imager for radio astronomy". In: *Monthly Notices of the Royal Astronomical Society* 444.1 (Oct. 2014), pp. 606–619. DOI: 10.1093/mnras/stu1368. arXiv: 1407.1943 [astro-ph.IM].

[148] M. J. Owens and N. U. Crooker. "Coronal mass ejections and magnetic flux buildup in the heliosphere". In: *Journal of Geophysical Research (Space Physics)* 111.A10, A10104 (Oct. 2006), A10104. DOI: 10.1029/2006JA011641.

[149] M. J. Owens et al. "Estimating total heliospheric magnetic flux from single-point in situ measurements". In: *Journal of Geophysical Research: Space Physics* 113.A12 (2008). DOI: 10.1029/2008JA013677. URL: https://agupubs.onlinelibrary.wiley.com/doi/abs/10.1029/2008JA013677.

[150] M. J. Owens et al. "Sunward Strahl: A Method to Unambiguously Determine Open Solar Flux from In Situ Spacecraft Measurements Using Suprathermal Electron Data". In: *Journal of Geophysical Research: Space Physics* 122.11 (2017), pp. 10, 980–10, 989. DOI: 10.1002/2017JA024631. eprint: https://agupubs.onlinelibrary.wiley.com/doi/pdf/10.1002/2017JA024631. URL: https://agupubs.onlinelibrary.wiley.com/doi/abs/10.1002/2017JA024631.

[151] Mathew Owens et al. "A Computationally Efficient, Time-Dependent Model of the Solar Wind for Use as a Surrogate to Three-Dimensional Numerical Magnetohydrodynamic Simulations". In: *Solar Physics* 295.3, 43 (Mar. 2020), p. 43. DOI: 10.1007/s11207-020-01605-3.

[152] Mathew J. Owens and Robert J. Forsyth. "The Heliospheric Magnetic Field". In: *Living Reviews in Solar Physics* 10.1, 5 (Nov. 2013), p. 5. DOI: 10.12942/lrsp-2013-5.

[153] Olga Panasenco et al. "Exploring Solar Wind Origins and Connecting Plasma Flows from the Parker Solar Probe to 1 au: Nonspherical Source Surface and Alfvénic Fluctuations". In: *The Astrophysical Journal Supplement Series* 246.2 (Feb. 2020), p. 54. DOI: 10.3847/1538-4365/ab61f4. URL: https://doi.org/10.3847%2F1538-4365%2Fab61f4.

[154] E. N. Parker. "Dynamics of the Interplanetary Gas and Magnetic Fields." In: *The Astrophysical Journal* 128 (Nov. 1958), p. 664. DOI: 10.1086/146579.

[155] Barbara Perri et al. "COCONUT, a novel fast-converging MHD model for solar corona simulations: I. Benchmarking and optimization of polytropic solutions". In: *arXiv e-prints*, arXiv:2205.03341 (May 2022), arXiv:2205.03341. arXiv: 2205.03341 [astro-ph.SR].

[156] W. D. Pesnell, B. J. Thompson, and P. C. Chamberlin. "The Solar Dynamics Observatory (SDO)". In: *Solar Physics* 275 (Jan. 2012), pp. 3–15. DOI: 10.1007/s11207-011-9841-3.

[157] Rui F. Pinto and Alexis P. Rouillard. "A Multiple Flux-tube Solar Wind Model". In: *Astrophysical Journal* 838.2, 89 (Apr. 2017), p. 89. DOI: 10.3847/1538-4357/aa6398. arXiv: 1611.08744 [astro-ph.SR].

[158] Vic Pizzo et al. "Wang-Sheeley-Arge-Enlil Cone Model Transitions to Operations". In: *Space Weather* 9.3, 03004 (Mar. 2011), p. 03004. DOI: 10.1029/2011SW000663.

[159] N. V. Pogorelov et al. "Modeling Heliospheric Phenomena with the Multi-Scale Fluid-Kinetic Simulation Suite". In: *Numerical Modeling of Space Plasma Flows, Astronum-2009*. Ed. by Nikolai V. Pogorelov, Edouard Audit, and Gary P. Zank. Vol. 429. Astronomical Society of the Pacific Conference Series. Sept. 2010, p. 266.

[160] N. V. Pogorelov et al. "Modeling Solar Wind Flow with the Multi-Scale Fluid-Kinetic Simulation Suite". In: *Numerical Modeling of Space Plasma Flows (ASTRONUM2012)*. Ed. by N. V. Pogorelov, E. Audit, and G. P. Zank. Vol. 474. Astronomical Society of the Pacific Conference Series. Apr. 2013, p. 165.

[161] Nicolas Poirier et al. "Exploiting white-light observations to improve estimates of magnetic connectivity". In: *Frontiers in Astronomy and Space Sciences* 8, 84 (May 2021), p. 84. DOI: 10.3389/fspas.2021.684734.

[162] Jens Pomoell and S. Poedts. "EUHFORIA: European heliospheric forecasting information asset". In: *Journal of Space Weather and Space Climate* 8, A35 (June 2018), A35. DOI: 10.1051/swsc/2018020.

[163] H. Porsche. "HELIOS mission: Mission objectives, mission verification, selected results". In: *Solar System and its Exploration*. Ed. by W. R. Burke. Vol. 164. ESA Special Publication. Nov. 1981, pp. 43–50.

[164] M. Pulupa et al. "The Solar Probe Plus Radio Frequency Spectrometer: Measurement requirements, analog design, and digital signal processing". In: *Journal of Geophysical Research: Space Physics* 122.3 (2017), pp. 2836–2854. DOI: 10.1002/2016JA023345.

[165] Marc Pulupa et al. "Statistics and Polarization of Type III Radio Bursts Observed in the Inner Heliosphere". In: *Astrophysical Journal Supplement* 246.2, 49 (Feb. 2020), p. 49. DOI: 10.3847/1538-4365/ab5dc0. arXiv: 1912.03371 [astro-ph.SR].

[166] S. Régnier. "Magnetic Field Extrapolations into the Corona: Success and Future Improvements". In: *Solar Physics* 288.2 (Dec. 2013), pp. 481–505. DOI: 10.1007/s11207-013-0367-8. arXiv: 1307.3844 [astro-ph.SR].

[167] Hamish A. S. Reid and Eduard P. Kontar. "Fine structure of type III solar radio bursts from Langmuir wave motion in turbulent plasma". In: *Nature Astronomy* 5 (May 2021), pp. 796–804. DOI: 10.1038/s41550-021-01370-8. arXiv: 2103.08424 [astro-ph.SR].

[168] Hamish Andrew Sinclair Reid and Heather Ratcliffe. "A review of solar type III radio bursts". In: *Research in Astronomy and Astrophysics* 14.7 (July 2014), pp. 773–804. DOI: 10.1088/1674-4527/14/7/003. arXiv: 1404.6117 [astro-ph.SR].

[169] Victor Réville and Allan Sacha Brun. "Global Solar Magnetic Field Organization in the Outer Corona: Influence on the Solar Wind Speed and Mass Flux Over the Cycle". In: *The Astrophysical Journal* 850.1 (Nov. 2017), p. 45. DOI: 10.3847/1538-4357/aa9218. URL: https://doi.org/10.3847%2F1538-4357%2Faa9218.

[170] Victor Réville et al. "The Role of Alfvén Wave Dynamics on the Large-scale Properties of the Solar Wind: Comparing an MHD Simulation with Parker Solar Probe E1 Data". In: *The Astrophysical Journal Supplement Series* 246.2 (Feb. 2020), p. 24. DOI: 10.3847/1538-4365/ab4fef. URL: https://doi.org/10.3847%2F1538-4365%2Fab4fef.

[171] Oliver E. K. Rice and Anthony R. Yeates. "Global Coronal Equilibria with Solar Wind Outflow". In: *arXiv e-prints*, arXiv:2110.01319 (Oct. 2021), arXiv:2110.01319. arXiv: 2110.01319 [astro-ph.SR].

[172] J. D. Richardson et al. "Observations of the Outer Heliosphere, Heliosheath, and Interstellar Medium". In: *Space Sciences Review* 218.4, 35 (June 2022), p. 35. DOI: 10.1007/s11214-022-00899-y.

[173] P. Riley et al. "A Comparison between Global Solar Magnetohydrodynamic and Potential Field Source Surface Model Results". In: *The Astrophysical Journal* 653 (Dec. 2006), pp. 1510–1516. DOI: 10.1086/508565.

[174] P. Riley et al. "A Multi-Observatory Inter-Comparison of Line-of-Sight Synoptic Solar Magnetograms". In: *Solar Physics* 289.3 (Mar. 2014), pp. 769–792. DOI: 10.1007/s11207-013-0353-1.

[175] Pete Riley. "An Alternative Interpretation of the Relationship between the Inferred Open Solar Flux and the Interplanetary Magnetic Field". In: *Astrophysical Journall* 667.1 (Sept. 2007), pp. L97–L100. DOI: 10.1086/522001.

[176] Pete Riley and Opal Issan. "Using a Heliospheric Upwinding eXtrapolation (HUX) Technique to Magnetically Connect Different Regions of the Heliosphere". In: *Frontiers in Physics* 9, 268 (May 2021), p. 268. DOI: 10.3389/fphy.2021.679497.

[177] Pete Riley, J. A. Linker, and Z. Mikić. "An empirically-driven global MHD model of the solar corona and inner heliosphere". In: *Journal of Geophysical Research* 106.A8 (Aug. 2001), pp. 15889–15902. DOI: 10.1029/2000JA000121.

[178] Pete Riley et al. "Predicting the Structure of the Solar Corona and Inner Heliosphere during Parker Solar Probe's First Perihelion Pass". In: *The Astrophysical Journal* 874.2 (Mar. 2019), p. L15. DOI: 10.3847/2041-8213/ab0ec3. URL: https://doi.org/10.3847%2F2041-8213%2Fab0ec3.

[179] Pete Riley et al. "Predicting the Structure of the Solar Corona and Inner Heliosphere during Parker Solar Probe's First Perihelion Pass". In: *The Astrophysical Journal* 874.2 (Mar. 2019), p. L15. DOI: 10.3847/2041-8213/ab0ec3. URL: https://doi.org/10.3847%5C%2F2041-8213%5C%2Fab0ec3.

[180] Pete Riley et al. "Using Parker Solar Probe observations during the first four perihelia to constrain global magnetohydrodynamic models". In: *Astronomy & Astrophysics* 650 (2021), A19.

[181] Alexis P. Rouillard et al. "Relating Streamer Flows to Density and Magnetic Structures at the Parker Solar Probe". In: *Astrophysical Journal Supplement* 246.2, 37 (Feb. 2020), p. 37. DOI: 10.3847/1538-4365/ab579a. arXiv: 2001.01993 [astro-ph.SR].

[182] K. Saito, A. I. Poland, and R. H. Munro. "A study of the background corona near solar minimum." In: *Solar Physics* 55.1 (Nov. 1977), pp. 121–134. DOI: 10.1007/BF00150879.

[183] Takashi Sakurai. "Calculation of force-free magnetic field with non-constant α". In: *Solar Physics* 69.2 (Feb. 1981), pp. 343–359. DOI: 10.1007/BF00149999.

[184] C. Sasso et al. "Comparing extrapolations of the coronal magnetic field structure at 2.5 $R_\odot$ with multi-viewpoint coronagraphic observations". In: *Astronomy & Astrophysics* 627, A9 (July 2019), A9. DOI: 10.1051/0004-6361/201834125. arXiv: 1905.09005 [astro-ph.SR].

[185] J. -A. Sauvaud et al. "The IMPACT Solar Wind Electron Analyzer (SWEA)". In: *SSR* 136.1-4 (Apr. 2008), pp. 227–239. DOI: 10.1007/s11214-007-9174-6.

[186] K. H. Schatten, J. M. Wilcox, and N. F. Ness. "A model of interplanetary and coronal magnetic fields". In: *Solar Physics* 6 (Mar. 1969), pp. 442–455. DOI: 10.1007/BF00146478.

[187] Kenneth H. Schatten. "Current Sheet Magnetic Model for the Solar Corona". In: *Solar Wind. Edited by Charles P. Sonett, Paul J. Coleman, and John M. Wilcox. Washington, Scientific and Technical Information Office, National Aeronautics and Space Administration., p.44*. Ed. by Charles P. Sonett, Paul Jerome Coleman, and John Marsh Wilcox. Vol. 308. 1972, p. 44.

[188] P. H. Scherrer et al. "The Helioseismic and Magnetic Imager (HMI) Investigation for the Solar Dynamics Observatory (SDO)". In: *Solar Physics* 275.1 (Jan. 2012), pp. 207–227. ISSN: 1573-093X. DOI: 10.1007/s11207-011-9834-2. URL: https://doi.org/10.1007/s11207-011-9834-2.

[189] C. J. Schrijver and M. L. De Rosa. "Photospheric and heliospheric magnetic fields". In: *Solar Physics* 212 (Jan. 2003), pp. 165–200. DOI: 10.1023/A:1022908504100.

[190] Hagen Schulte in den Bäumen, Iver H. Cairns, and P. A. Robinson. "Nonzero azimuthal magnetic fields at the solar source surface: Extraction, model, and implications". In: *Journal of Geophysical Research (Space Physics)* 117.A10, A10104 (Oct. 2012), A10104. DOI: 10.1029/2012JA017705.

[191] M. Schulz, E. N. Frazier, and Jr. Boucher D. J. "Coronal magnetic-field model with non-spherical source surface." In: *Solar Physics* 60.1 (Nov. 1978), pp. 83–104. DOI: 10.1007/BF00152334.

[192] N. A. Schwadron and D. J. McComas. "Switchbacks Explained: Super-Parker Fields - The Other Side of the Sub-Parker Spiral". In: *Astrophysical Journal* 909.1, 95 (Mar. 2021), p. 95. DOI: 10.3847/1538-4357/abd4e6. arXiv: 2102.03696 [astro-ph.SR].

[193] E. J. Smith. "Solar cycle evolution of the heliospheric magnetic field: The Ulysses legacy". In: *Journal of Atmospheric and Solar-Terrestrial Physics* 73 (Feb. 2011), pp. 277–289. DOI: 10.1016/j.jastp.2010.03.019.

[194] E. J. Smith and A. Balogh. "Ulysses observations of the radial magnetic field". In: *Geophysical Review Letters* 22 (1995), pp. 3317–3320. DOI: 10.1029/95GL02826.

[195] Edward J. Smith et al. "Open Magnetic Flux: Variation with Latitude and Solar Cycle". In: *AIP Conference Proceedings* 679.1 (2003), pp. 67–70. DOI: 10.1063/1.1618543. eprint: https://aip.scitation.org/doi/pdf/10.1063/1.1618543. URL: https://aip.scitation.org/doi/abs/10.1063/1.1618543.

[196] Igor V. Sokolov et al. "Magnetohydrodynamic Waves and Coronal Heating: Unifying Empirical and MHD Turbulence Models". In: *Astrophysical Journal* 764.1, 23 (Feb. 2013), p. 23. DOI: 10.1088/0004-637X/764/1/23. arXiv: 1208.3141 [astro-ph.SR].

[197] S. K. Solanki et al. "The Polarimetric and Helioseismic Imager on Solar Orbiter". In: *Astronomy & Astrophysics* 642, A11 (Oct. 2020), A11. DOI: 10.1051/0004-6361/201935325. arXiv: 1903.11061 [astro-ph.IM].

[198] Lyman Spitzer and Richard Härm. "Transport Phenomena in a Completely Ionized Gas". In: *Physical Review* 89.5 (Mar. 1953), pp. 977–981. DOI: 10.1103/PhysRev.89.977.

[199] D. Stansby. *Dstansby/Pfsspy: Pfsspy 0.1.2 Zenodo*. 2019–. DOI: 10.5281/zenodo.2566462. URL: https://github.com/dstansby/pfsspy.

[200] David Stansby, Anthony Yeates, and Samuel Badman. "pfsspy: A Python package for potential field source surface modelling". In: *The Journal of Open Source Software* 5.54, 2732 (Oct. 2020), p. 2732. DOI: 10.21105/joss.02732.

[201] David Stansby, Anthony Yeates, and Samuel T. Badman. "pfsspy: A Python package for potential field source surface modelling". In: *Journal of Open Source Software* 5.54 (2020), p. 2732. DOI: 10.21105/joss.02732. URL: https://doi.org/10.21105/joss.02732.

[202] David Stansby et al. "Predicting Large-scale Coronal Structure for Parker Solar Probe Using Open Source Software". In: *Research Notes of the AAS* 3.3 (Mar. 2019), p. 57. DOI: 10.3847/2515-5172/ab13b7. URL: https://doi.org/10.3847%2F2515-5172%2Fab13b7.

[203] E. C. Stone et al. "The Advanced Composition Explorer". In: *Space Sciences Review* 86 (July 1998), pp. 1–22. DOI: 10.1023/A:1005082526237.

[204] R. Du Toit Strauss, Nina Dresing, and N. Eugene Engelbrecht. "Perpendicular Diffusion of Solar Energetic Particles: Model Results and Implications for Electrons". In: *Astrophysical Journal* 837.1, 43 (Mar. 2017), p. 43. DOI: 10.3847/1538-4357/aa5df5. arXiv: 1804.03693 [astro-ph.SR].

[205] Z. Svestka et al. "Open magnetic fields in active regions." In: *Solar Physics* 55.2 (Dec. 1977), pp. 359–369. DOI: 10.1007/BF00152579.

[206] Adam Szabo et al. "The Heliospheric Current Sheet in the Inner Heliosphere Observed by the Parker Solar Probe". In: *The Astrophysical Journal Supplement Series* 246.2 (Feb. 2020), p. 47. DOI: 10.3847/1538-4365/ab5dac. URL: https://doi.org/10.3847%2F1538-4365%2Fab5dac.

[207] S. Tasnim et al. "Mapping Magnetic Field Lines for an Accelerating Solar Wind". In: *Solar Physics* 294.11, 155 (Nov. 2019), p. 155. DOI: 10.1007/s11207-019-1541-4. arXiv: 1907.08683 [physics.space-ph].

[208] Manuela Temmer. "Space weather: the solar perspective". In: *Living Reviews in Solar Physics* 18.1, 4 (Dec. 2021), p. 4. DOI: 10.1007/s41116-021-00030-3. arXiv: 2104.04261 [astro-ph.SR].

[209] G. Thejappa and R. J. MacDowall. "Localization of a Type III Radio Burst Observed by the STEREO Spacecraft". In: *The Astrophysical Journal* 720.2 (2010), p. 1395. URL: http://stacks.iop.org/0004-637X/720/i=2/a=1395.

[210] G. Thejappa, R. J. MacDowall, and N. Gopalswamy. "Effects of Refraction on Angles and Times of Arrival of Solar Radio Bursts". In: *The Astrophysical Journal* 734.1 (2011), p. 16. URL: http://stacks.iop.org/0004-637X/734/i=1/a=16.

[211] GáBor Tóth et al. "Space Weather Modeling Framework: A new tool for the space science community". In: *Journal of Geophysical Research (Space Physics)* 110.A12, A12226 (Dec. 2005), A12226. DOI: 10.1029/2005JA011126.

[212] B. van der Holst et al. "A Data-driven, Two-temperature Solar Wind Model with Alfvén Waves". In: *The Astrophysical Journal* 725.1 (Dec. 2010), pp. 1373–1383. DOI: 10.1088/0004-637X/725/1/1373.

[213] B. van der Holst et al. "Alfvén Wave Solar Model (AWSoM): Coronal Heating". In: *Astrophysical Journal* 782.2, 81 (Feb. 2014), p. 81. DOI: 10.1088/0004-637X/782/2/81. arXiv: 1311.4093 [astro-ph.SR].

[214] B. van der Holst et al. "Predictions for the First Parker Solar Probe Encounter". In: *The Astrophysical Journal Letters* 872.2, L18 (Feb. 2019), p. L18. DOI: 10.3847/2041-8213/ab04a5. arXiv: 1902.03921 [physics.space-ph].

[215] Ger van Diepen, Tammo Jan Dijkema, and André Offringa. *DPPP: Default Pre-Processing Pipeline*. Astrophysics Source Code Library, record ascl:1804.003. Apr. 2018. ascl: 1804.003.

[216] M. P. van Haarlem et al. "LOFAR: The LOw-Frequency ARray". In: *Astronomy & Astrophysics* 556, A2 (Aug. 2013), A2. DOI: 10.1051/0004-6361/201220873. arXiv: 1305.3550 [astro-ph.IM].

[217] Nicholeen M. Viall and Joseph E. Borovsky. "Nine Outstanding Questions of Solar Wind Physics". In: *Journal of Geophysical Research (Space Physics)* 125.7, e26005 (July 2020), e26005. DOI: 10.1029/2018JA026005.

[218] A. Vourlidas et al. "The Wide-Field Imager for Solar Probe Plus (WISPR)". In: *SSR* 204 (Dec. 2016), pp. 83–130. DOI: 10.1007/s11214-014-0114-y.

[219] A. Wagner et al. "Validation scheme for solar coronal models – constraints from multi-perspective observations in EUV and white-light". In: *arXiv e-prints*, arXiv:2110.01893 (Oct. 2021), arXiv:2110.01893. arXiv: 2110.01893 [astro-ph.SR].

[220] S. Wallace et al. "Estimating Total Open Heliospheric Magnetic Flux". In: *Solar Physics* 294.2, 19 (Feb. 2019), p. 19. DOI: 10.1007/s11207-019-1402-1. arXiv: 1903.12613 [astro-ph.SR].

[221] Y. -M. Wang, Jr. Sheeley N. R., and J. Lean. "Understanding the evolution of the Sun's open magnetic flux". In: *Geophysical Review Letters* 27.5 (Mar. 2000), pp. 621–624. DOI: 10.1029/1999GL010759.

[222] Y. -M. Wang, Jr. Sheeley N. R., and N. B. Rich. "Coronal Pseudostreamers". In: *Astrophysical Journal* 658.2 (Apr. 2007), pp. 1340–1348. DOI: 10.1086/511416.

[223] Y. -M. Wang and N. R. Sheeley Jr. "On potential field models of the solar corona". In: *The Astrophysical Journal* 392 (June 1992), pp. 310–319. DOI: 10.1086/171430.

[224] Y. -M. Wang, R. K. Ulrich, and J. W. Harvey. "Magnetograph Saturation and the Open Flux Problem". In: *Astrophysical Journal* 926.2, 113 (Feb. 2022), p. 113. DOI: 10.3847/1538-4357/ac4491. arXiv: 2112.09969 [astro-ph.SR].

[225] Y. -M. Wang et al. "Origin of Streamer Material in the Outer Corona". In: *Astrophysical Journall* 498.2 (May 1998), pp. L165–L168. DOI: 10.1086/311321.

[226] Y.-M. Wang and Y.-K. Ko. "Observations of Slow Solar Wind from Equatorial Coronal Holes". In: *The Astrophysical Journal* 880.2 (Aug. 2019), p. 146. DOI: 10.3847/1538-4357/ab2add. URL: https://doi.org/10.3847%2F1538-4357%2Fab2add.

[227] Y.-M. Wang and N. R. Sheeley Jr. "Solar wind speed and coronal flux-tube expansion". In: *Astrophysical Journal* 355 (June 1990), pp. 726–732. DOI: 10.1086/168805.

[228] Harry P. Warren and David H. Brooks. "The Temperature and Density Structure of the Solar Corona. I. Observations of the Quiet Sun with the EUV Imaging Spectrometer on Hinode". In: *Astrophysical Journal* 700.1 (July 2009), pp. 762–773. DOI: 10.1088/0004-637X/700/1/762. arXiv: 0901.1621 [astro-ph.SR].

[229] K. P. Wenzel et al. "The ULYSSES Mission". In: *Astronomy and Astrophysics Supplement* 92 (Jan. 1992), p. 207.

[230] Phyllis L. Whittlesey et al. "The Solar Probe ANalyzers—Electrons on the Parker Solar Probe". In: *The Astrophysical Journals* 246.2, 74 (Feb. 2020), p. 74. DOI: 10.3847/1538-4365/ab7370. arXiv: 2002.04080 [astro-ph.IM].

[231] Thomas Wiegelmann, Gordon J. D. Petrie, and Pete Riley. "Coronal Magnetic Field Models". In: *Space Science Reviews* 210.1 (Sept. 2017), pp. 249–274. ISSN: 1572-9672. DOI: 10.1007/s11214-015-0178-3. URL: https://doi.org/10.1007/s11214-015-0178-3.

[232] Thomas Wiegelmann and Takashi Sakurai. "Solar force-free magnetic fields". In: *Living Reviews in Solar Physics* 18.1, 1 (Dec. 2021), p. 1. DOI: 10.1007/s41116-020-00027-4. arXiv: 1208.4693 [astro-ph.SR].

[233] J. P. Wild and L. L. McCready. "Observations of the Spectrum of High-Intensity Solar Radiation at Metre Wavelengths. I. The Apparatus and Spectral Types of Solar Burst Observed". In: *Australian Journal of Scientific Research A Physical Sciences* 3 (Sept. 1950), p. 387. DOI: 10.1071/CH9500387.

[234] Jean-Pierre Wuelser et al. *EUVI: the STEREO-SECCHI extreme ultraviolet imager*. 2004. DOI: 10.1117/12.506877. URL: https://doi.org/10.1117/12.506877.

[235] A. Yeates. *Antyeates1983/Pfss: First Release of Pfss Code Zenodo*. 2018–. DOI: 10.5281/zenodo.1472183. URL: https://github.com/antyeates1983/pfss.

Appendix A

Appendix for Chapter 2 : Full Model-Observation Comparisons

This appendix section contains summary plots of the observation-model comparisons for all metrics considered in chapter 2. The plots are also available as animations as a function of time in the online version of the published version of this chapter [13].

A.1 Metric 1 : Coronal Hole - Open Field Comparison

Here, in figures A.1-A.3 we show schematics of the binary classification from EZSEG and the coronal model open field maps detailed in section 2.5. The panels are organized to differentiate the models and (for PFSS models), the source surface height. Each panel has the precision and recall shown as a text inset. As a reminder, the quantity quoted in the main text (section 3.4), the 'F-score', is the harmonic mean of these two quantities. These figures are animated over each 60 day interval in the online version of this manuscript. The still images shown here are the first frame of the movie from October-01-2018, March-01-2019 and August-01-2019 for encounters 1-3 respectively.

A.2 Metric 2 : Neutral Line - Streamer Belt Comparison

Following the format of section A.1, we next show schematically the comparison between the modeled and measured streamer belt topology. Again we show a multi-panel figure for each encounter (figures A.4-A.6) with panels organized by model and source surface height. Each panel follows the same format as the bottom panel of figure 2.3: the background image, black contour and dashed centroid curve show the white light (WL) carrington map and extracted streamer belt (SMB line), while the red curve shows the model HCS and the blue lines show

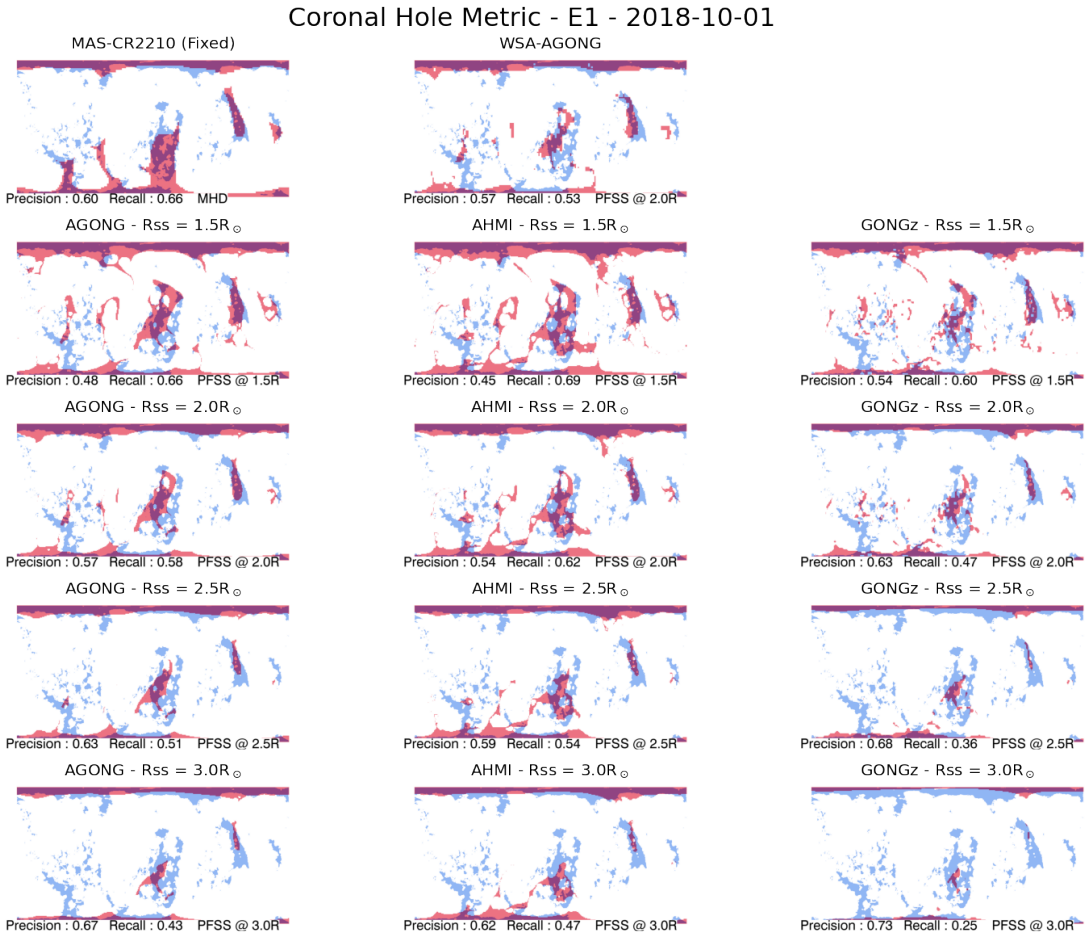

Figure A.1: Metric 1 (Coronal Hole) model-observation comparison for the first PSP encounter. The panels depict the binary classification scheme used to define our coronal hole metric, as detailed in section 2.5 and illustrated in the bottom panel of figure 2.1. Blue shading indicates the coronal hole area determined by applying the EZSEG algorithm to EUV synoptic maps, red shading indicates the open field area determined from the particular coronal model run. Where the model and observations agree, the pixels are shaded purple. The titles of each panel indicate the model and model parameters. The top row shows MAS and WSA results, while the bottom four rows show PFSS results with the columns differentiating the model and the rows differentiating the source surface height. Inset text in each panel records the associated precision and recall scores. In the online material, this figure is animated as a function of time for the encounter from October-1-2018 to November-30-2018 at a daily cadence. Although the background EUV map is fixed, the model coronal hole distributions evolve except for the MAS MHD results (top-left panel) which are based on a single magnetogram for this encounter.

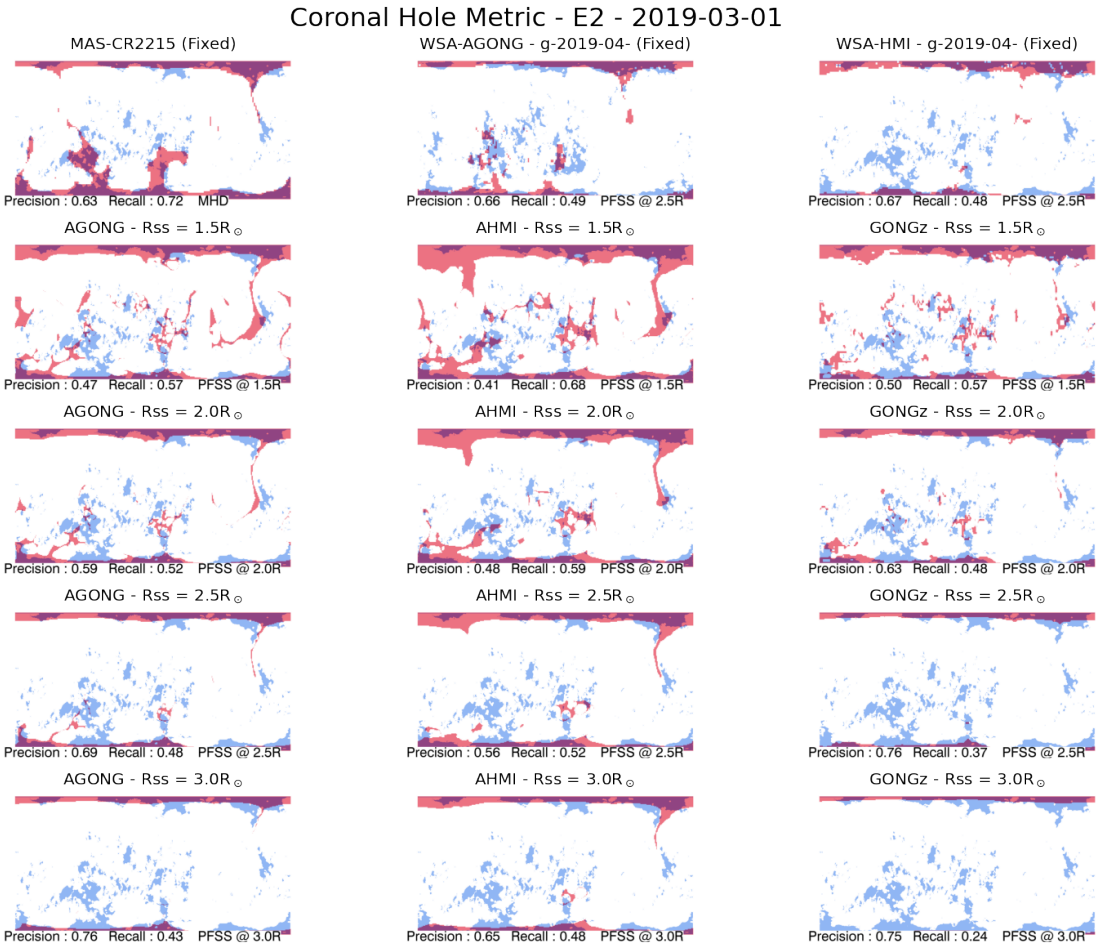

Figure A.2: Metric 1 (Coronal Hole) model-observation comparison for the second PSP encounter. The panels are organized as in figure A.1. The online animation shows daily evolution from 2019-03-01 to 2019-04-30 except for the MAS and WSA models (top row) which are based on a single magnetogram for this encounter.

the distances between the curves which contribute to the metric score, as detailed in section 2.5 and [161]. In the online version of this manuscript, these figures are movies for each encounters over the 60 day intervals (in which both elements evolve with time for the 60 day interval around perihelion, except where noted in the figure captions). The static versions of these figures show the first frame of each movie from dates October-01-2018, March-01-2019 and August-01-2019 for encounters 1-3 respectively.

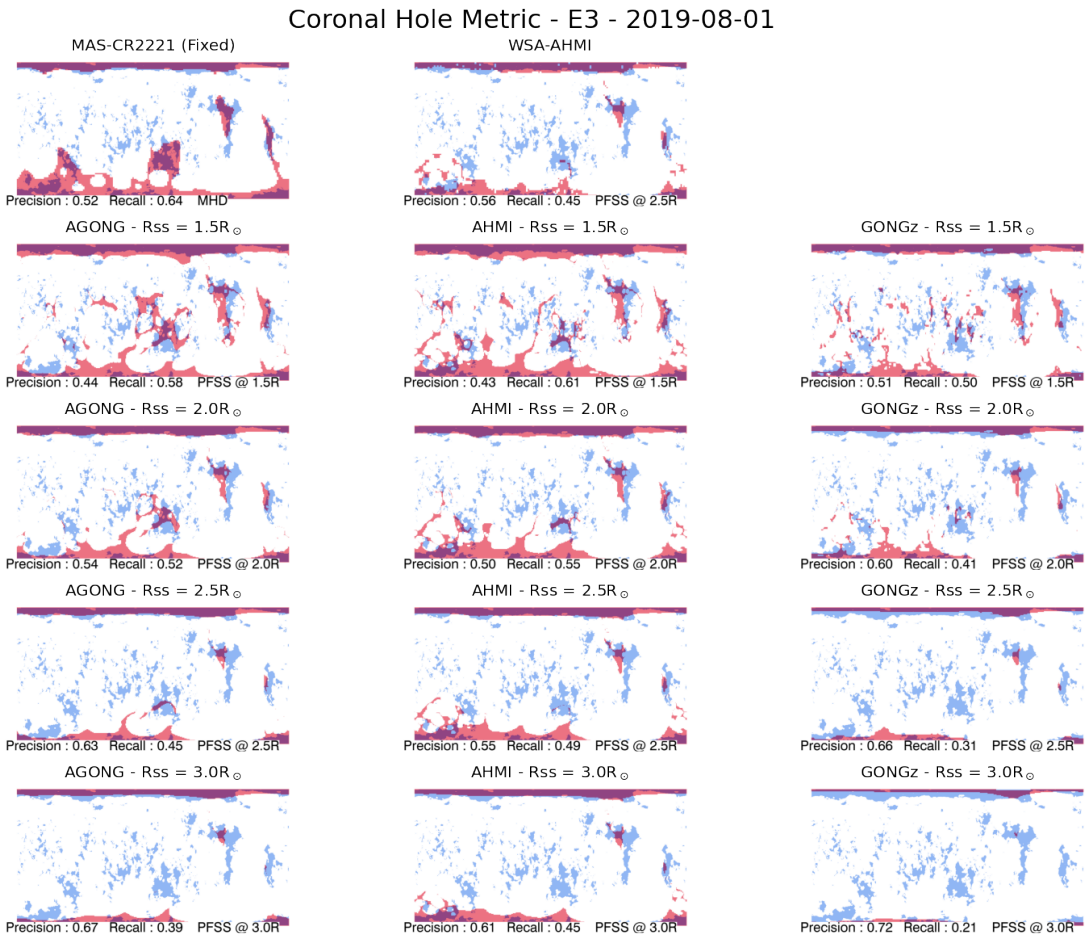

Figure A.3: Metric 1 (Coronal Hole) model-observation comparison for the third PSP encounter. The panels are organized as in figure A.1. The online animation shows daily evolution from 2019-08-01 to 2019-09-30 except for the MAS model (top-left panel) which are based on a single magnetogram for this encounter.

A.3 Metric 3 : *In situ* polarity - HCS Comparison

Finally, in figures A.7-A.9 we summarize model-observation comparisons for the third metric studied (*in situ* polarity). These figures are corollaries to figure 2.7 which already displayed in a compact way all model/data comparisons for this metric as function of time. Here we plot the measured data in the format of the middle panel of the illustrative figure 2.3, showing the measured polarity timeseries data plotted as the spacecraft trajectory ballistically mapped across the model outer boundary. This is to allow the reader to see visually how the change in the model's HCS topology affects agreement with the *in situ* data.

As in sections A.1 and A.2, here we have an individual multi-panel plot for each encounter

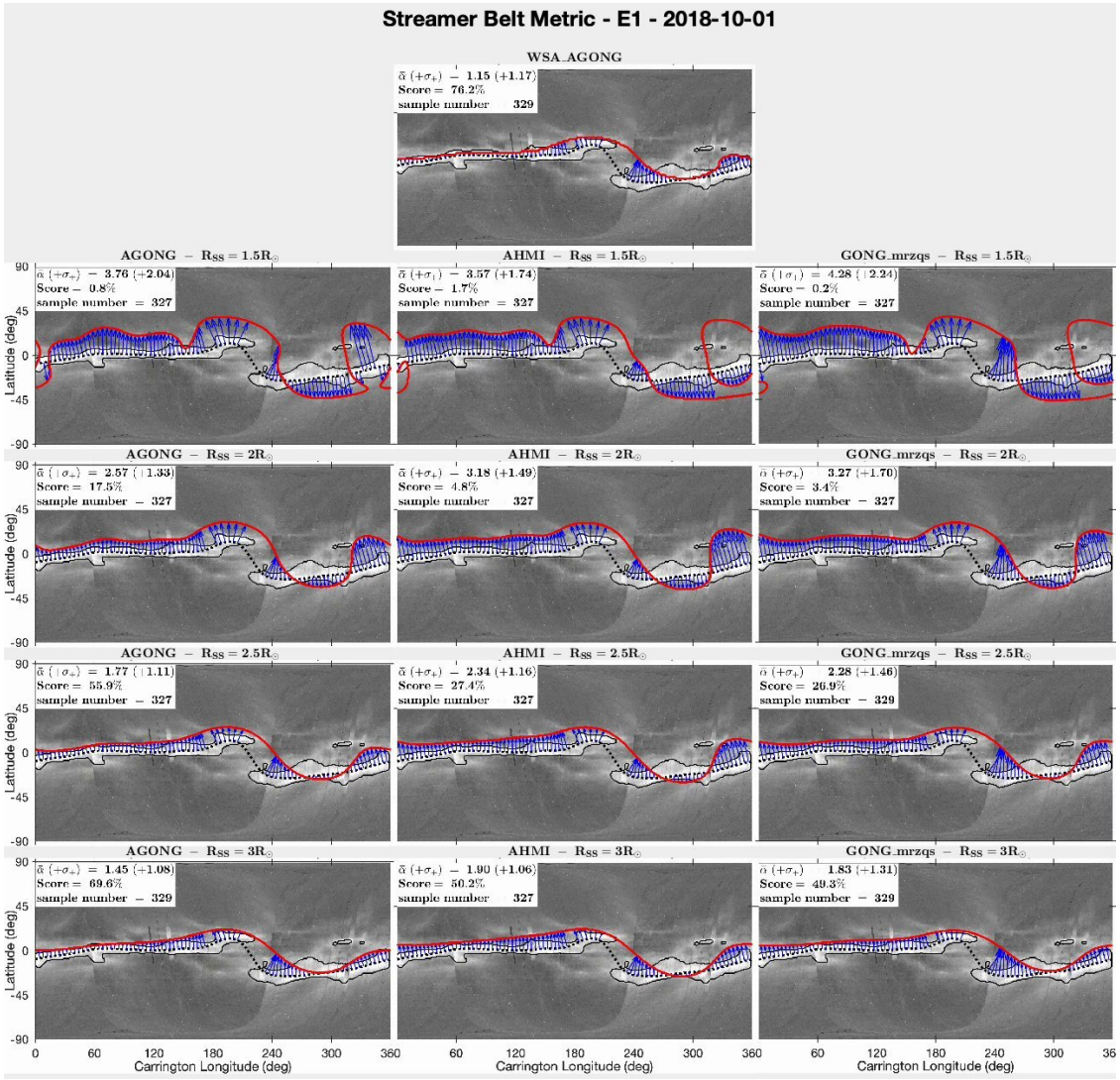

Figure A.4: Metric 2 (Streamer belt) model-observation comparison for the first PSP encounter. The panels show the comparison between the extracted streamer belt line and the model HCS, as detailed in section 2.5 and illustrated in the bottom panel of figure 2.2. The streamer belt score as well as the intermediate $\bar{\alpha}$ and σ_+ quantities are given in the top-left corner of each panel. In the online version of this manuscript, this figure is animated at a daily cadence from October-01-2018 to November-30-2018, showing how the model neutral lines and background Carrington white light (WL) maps evolve as a function of time (except the MAS model, top left panel, for which only the WL map evolves in this encounter).

for all model and model input parameters studied in this work. In the online versionof this manuscript, these figures are animated over the relevant 60 day interval for each encounter,

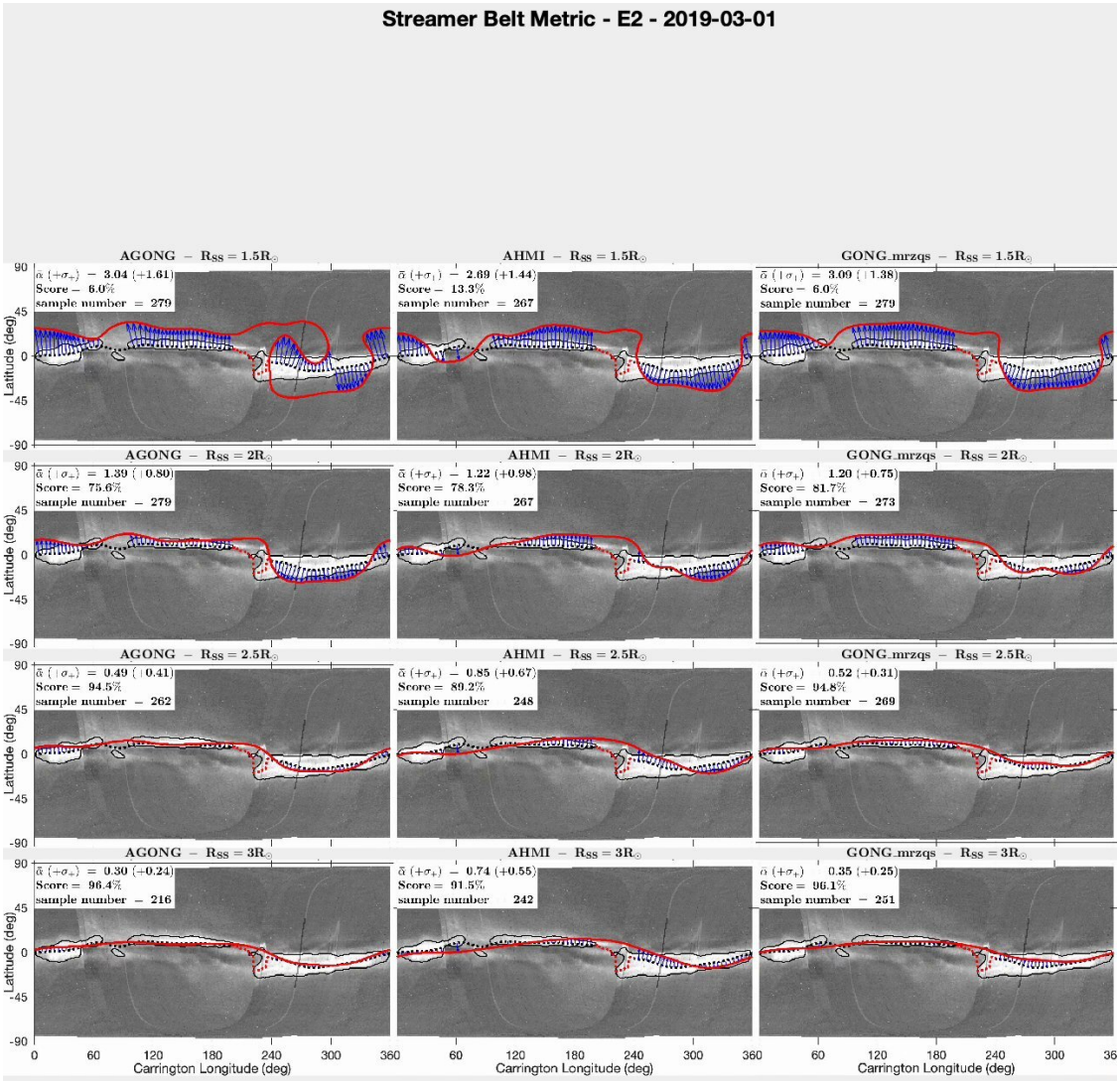

Figure A.5: Metric 2 (Streamer belt) model-observation comparison for the second PSP encounter. The panels are organized as in figure A.4. In the online version of this manuscript, this figure is animated at a daily cadence from March-01-2019 to April-30-2019, except for the MAS and WSA models, (top row), for which only the WL map evolves.

showing the movement of the HCS as the models evolve (except where noted in the figure captions) as the spacecraft whose *in situ* data we use move in the heliographic frame. The still images shown here are the first frame of theese movies, snapshotting October-01-2018, March-01-2019 and August-01-2019 for encounters 1-3 respectively.

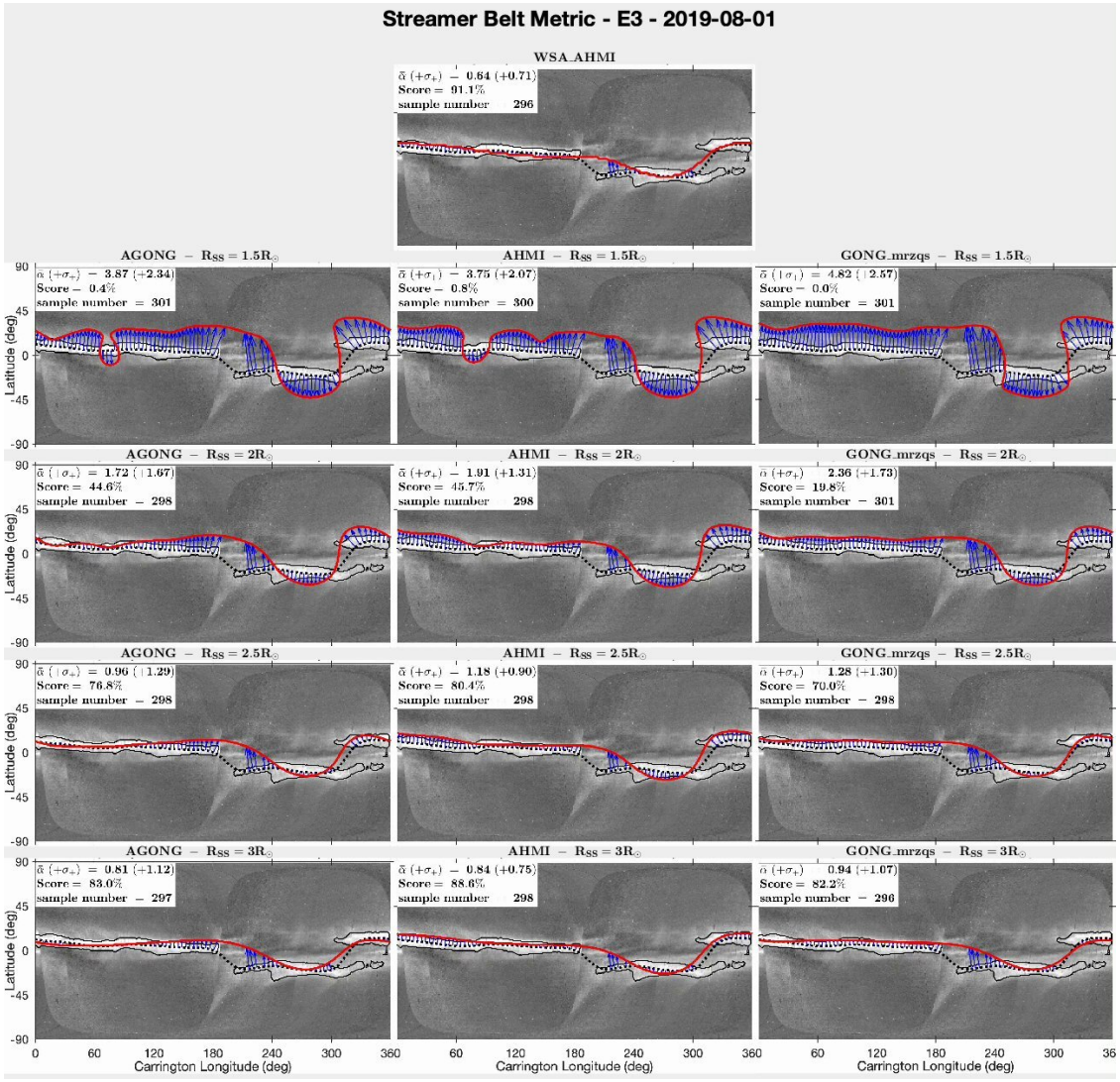

Figure A.6: Metric 2 (Streamer belt) model-observation comparison for the third PSP perihelion. The panels are organized as in figure A.4. In the online version of this manuscript, this figure is animated at a daily cadence from August-01-2019 to September-30-2019, except for the MAS models (top-right panel) for which only the WL map evolves.

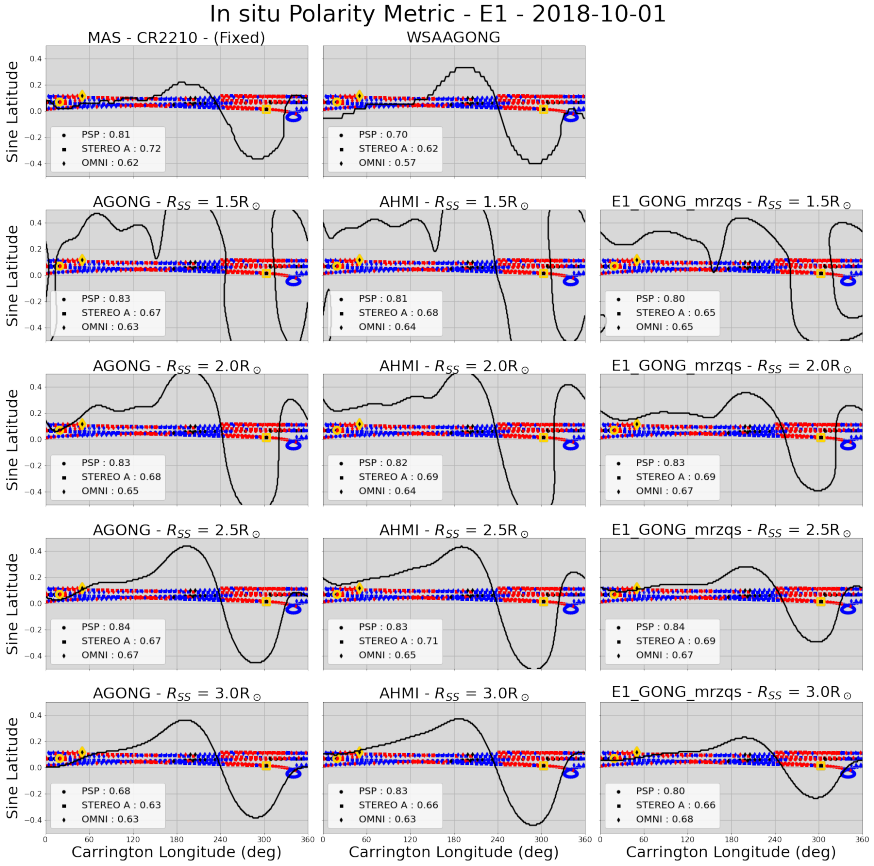

Figure A.7: *In situ* polarity model-observation comparison for models for the first PSP encounter. The panels schematically show the extent to which the *in situ* measured polarity (blue/red markers) corresponds to the modeled heliospheric current sheet (black contour), as detailed in section 2.5 and illustrated in the middle panel of figure 2.3. Model-data agreement occurs where the *in situ* data is taken northwards of a HCS contour *and* is red (positive polarity) or where the data is taken southwards of the HCS contour *and* is blue (negative polarity). The panel titles indicate the model parameters. The top row shows MAS and WSA results, while the bottom four rows show PFSS results with the columns differentiating the model and the rows differentiating the source surface height. In the online edition, this figure is animated for the 60 day interval hith each frame advancing in time one day at a time from October-01-2018 to November-30-2018. As time evolves, the model HCSs evolve for each model (except for the MAS model, top left panel which only has a single model run for E1). Simultaneously, the spacecraft (yellow symbols) move in the solar corotating reference frame. The static version of the figure is the first frame for the video, showing the metrics for the date October-01-2018.

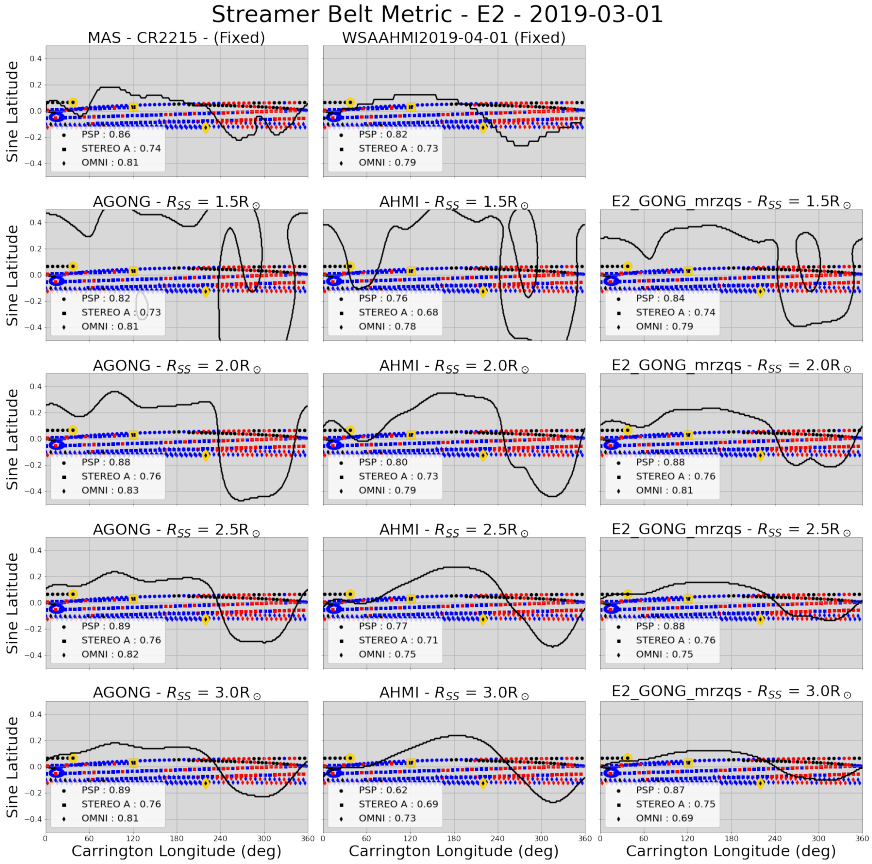

Figure A.8: *In situ* polarity model-observation comparison for models for the second PSP encounter. The panels are organized as in figure A.7. In the online edition of this manuscript, this figure is animated for the 60 day interval for encounter 2 from March-01-2019 to April-30-2019 showing relative motion of the model HCS and spacecraft positions (projected to the source surface). Here the model HCS from MAS and WSA (top row) are frozen in time.. The static version of the figure is the first frame for the video, showing the metrics for the date March-01-2019.

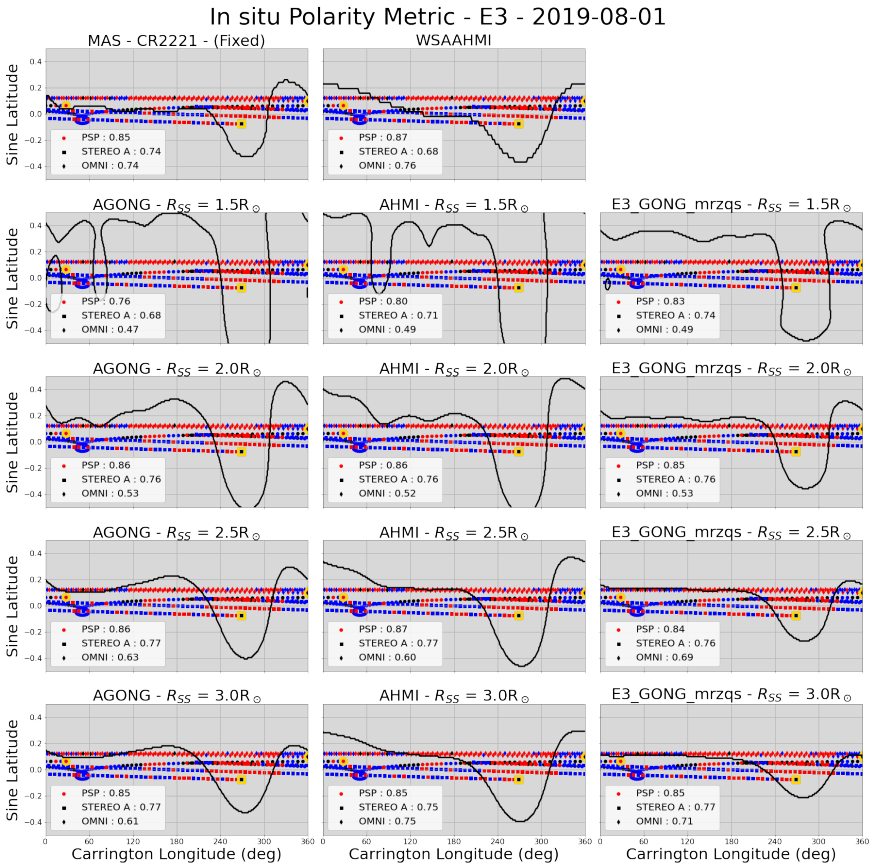

Figure A.9: *In situ* polarity model-observation comparison for models for the third PSP encounter. The panels are organized as in figure A.7. In the online edition of this manuscript, this figure is animated for the 60 day interval for encounter 3 from August-01-2019 to September-30-2019, showing relative motion of the model HCS and spacecraft positions (projected to the source surface). Here the model HCS from MAS (top-left panel) is frozen in time. The static version of the figure is the first frame for the video, showing the metrics for the date August-01-2019.

Appendix B

Appendix for Chapter 3

This section presents the appendices for Chapter 3.

B.1 Justification of removing normal fluctuations

In this paper, we treated the fluctuations as 2D (R-T plane) and assumed we can replace B_R and B_T with a parameterization using the field magnitude and R-T clock angle. This is justified because the normal component generally fluctuates normally about the R-T plane, and these fluctuations are predominantly rotational (magnitude conserving). In addition, normal and tangential fluctuations are typically uncorrelated, and thus suppressing them in the vector magnitude-preserving method chosen here does not effect the distribution of vectors in the R-T plane. Figure B.1 shows the effect on the 2D distribution of making this substitution, with the top row of panels showing the 2D distribution of the raw $B_R R^2$ and $B_T R^2$ measurements for PSP, STEREO A, and Wind, respectively. We note PSP data at all radii is here binned together. The bottom row shows the same distribution but with the normal component corrected for in the vector magnitude.

We see the effect at PSP is negligible, indicating the population of normal fluctuations is sub-dominant to fluctuations in the R-T plane. The effect at 1AU is quite striking. We see that just by taking the raw B_R and B_T values in a 2D distribution, a large population of data points exist near the origin. These data are actually just a projection of the normal component onto the R-T plane. Therefore, this population is nonphysical: from the 2D distribution, we would conclude there is a large population of near-zero field magnitude, whereas, in fact, from the bottom row of Figure B.1, we see by making this normal correction, this population vanishes and we get a more accurate measure of the RT distribution, especially the magnitude. Thus, we conclude it is a robust and useful transformation to correct the R-T components of the field by the normal component and use this data throughout the paper.

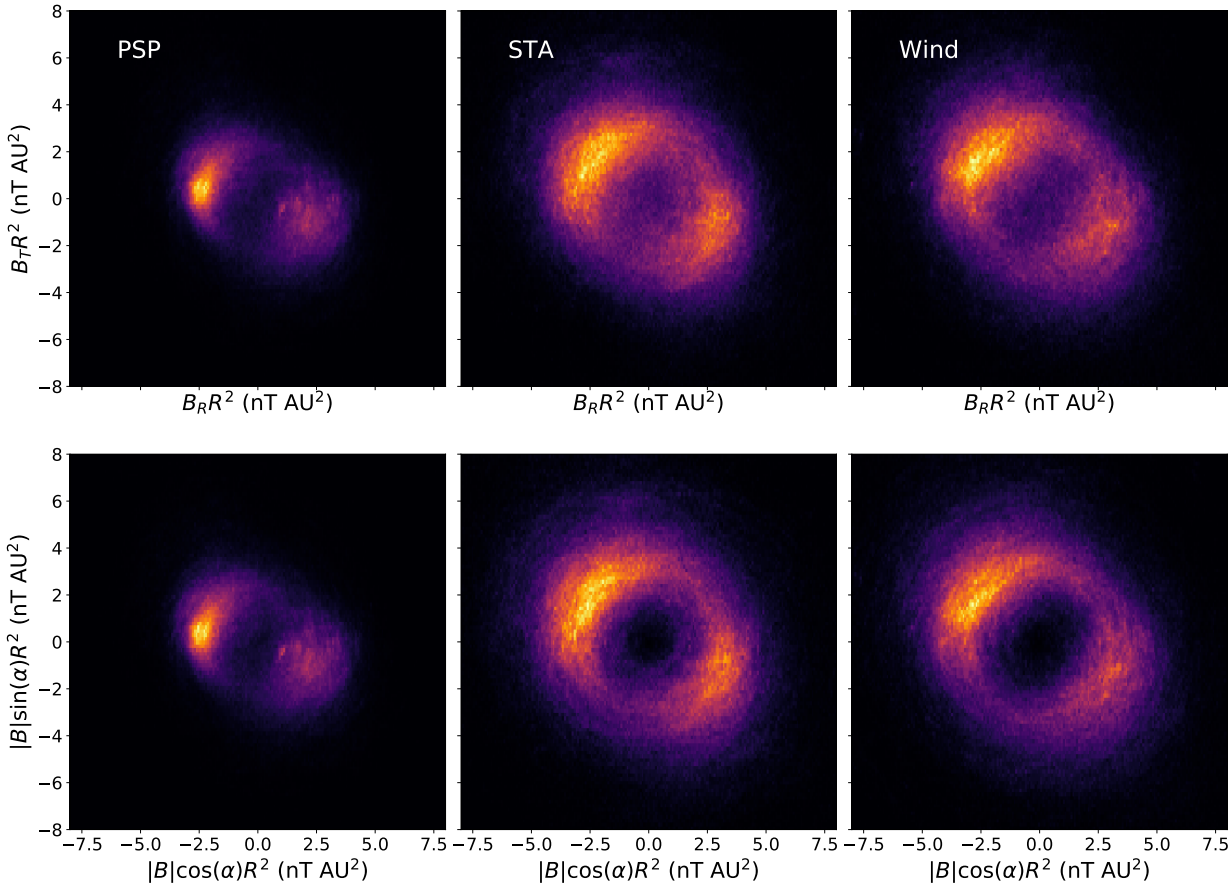

Figure B.1: Justification of the treatment of the normal field component. Each panel shows a 2D distribution of field values across the full data set (see Figure 3.1). The top row shows the distribution of 1 min average values of B_TR^2 versus B_RR^2. The bottom row shows on the same axes and colour scale, the distribution formed by rotating the normal component into the R-T plane via the substitution $B_R = |B|\cos(\alpha)$, $B_T = |B|\sin(\alpha)$. The three columns show PSP, STA, and Wind data, respectively.

B.2 Synthetic versus real distributions

In Appendix B.2, we compute estimates of B_RR^2 for data binned by radius (meaning from multiple orbits) and compared them to estimates from derived synthetic data. In Figures B.2 and B.3, we display the corresponding 2D distributions and 1D distributions in magnitude and clock angle for radial bins from 0.1 to 1.0 AU. We note that these bins are slightly wider than what we describe in Section 3.3, for the sake of brevity. These plots show how the large scale variation and growth of fluctuations and Parker spiral background is captured

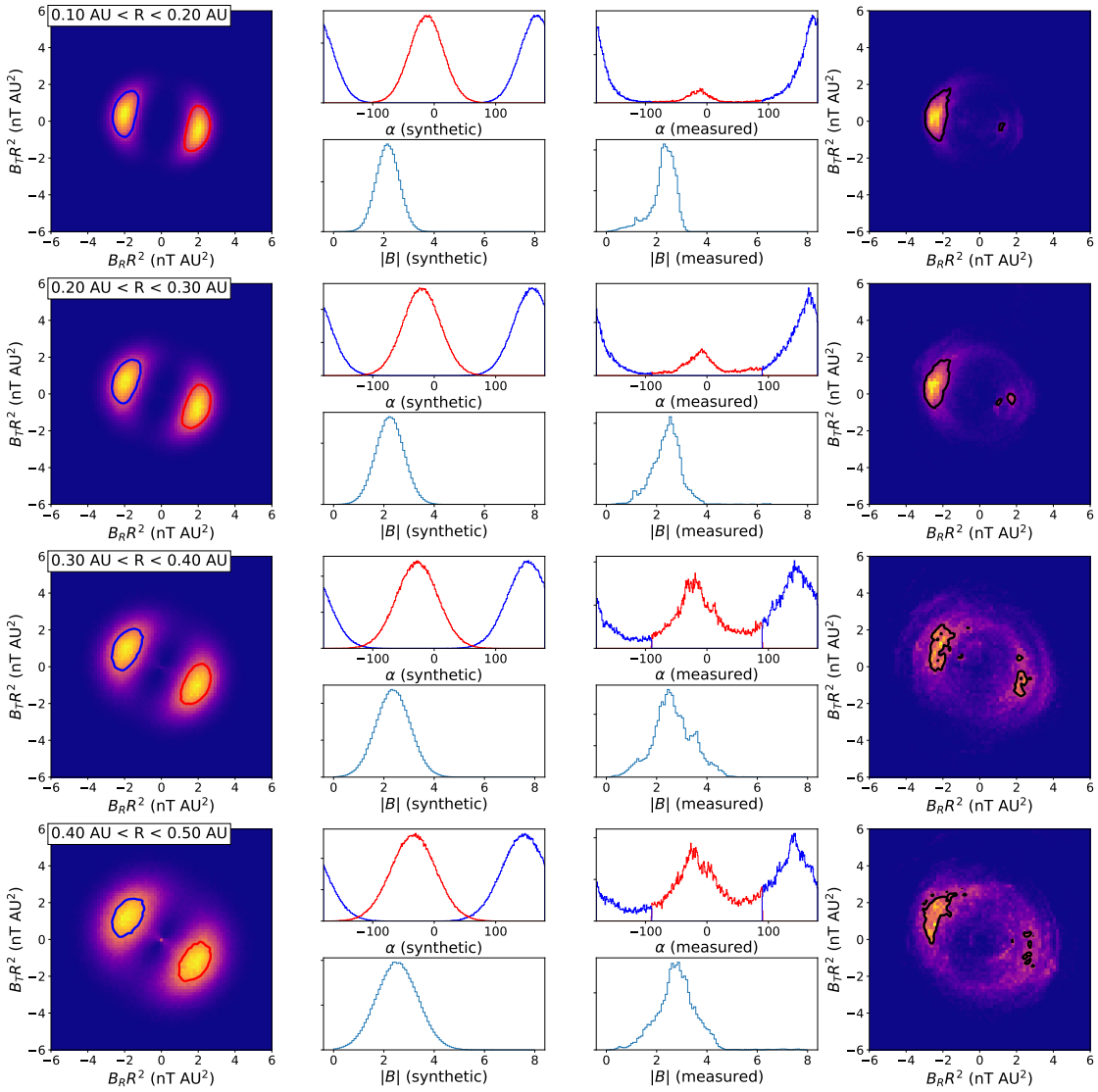

Figure B.2: Synthetic and measured flux distributions as a function of radius (0.1AU-0.5AU). The left-hand column shows the 2D synthetic distributions of $B_T R^2$ versus $B_R R^2$, the rightmost column shows the corresponding measured distribution. For both 2D histograms, a contour shows the 90th percentile of the data. The middle columns consist of corresponding 1D distributions of clock angle (top panel for each radial bin) and field vector magnitude (x R^2) (bottom panel for each radial bin). For the clock angle, red (blue) curves represent anti-sunward (sunward) sector populations.

by the synthetic data and the generic 2D shape compares well to the raw data. We also see that the 1D distributions we use to approximate the magnitude and the clock angle do

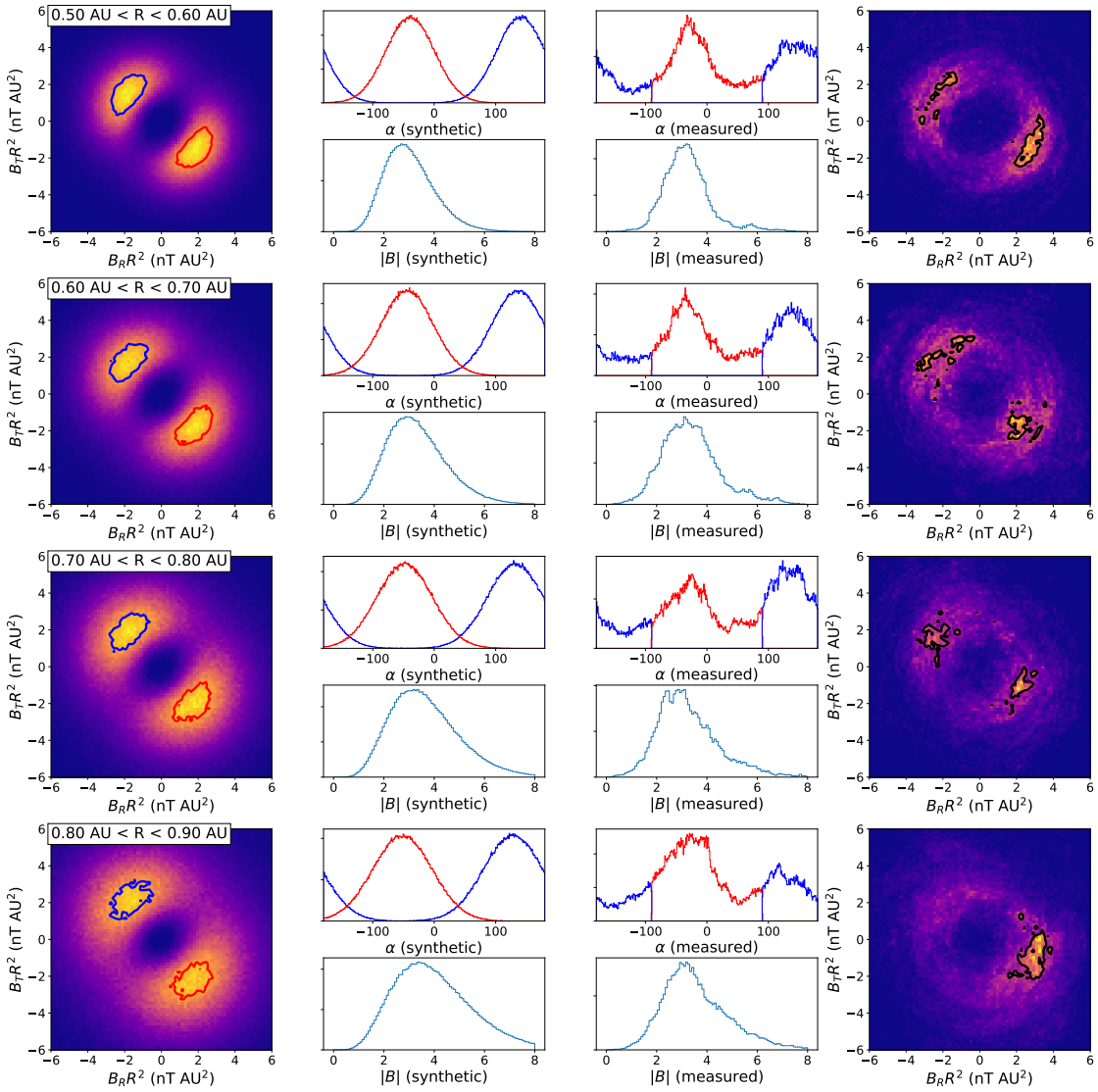

Figure B.3: Continuation of Figure B.2 : Synthetic and Measured Flux distributions as a function of radius (0.1AU-0.5AU).

have limitations. In particular, the real distributions are spikier and in some cases appear to show different streams merged together, while the synthetic data assumes one smooth population. The distributions of clock angle are generally formed more like a triangular-shaped distribution compared to the approximated Gaussian distributions. We also see a systematic skew in the the magnitude with higher radii. For cases where the skew is large enough that a normal distribution with the same standard deviation would predict negative values of —B—, we allow the synthetic distribution to have non-zero skew. As noted in the

main text, in these cases we continue to interpret the distribution peak (rather than the mean) as the 'central value' about which fluctuations occur.

B.3 Pre-averaging and vector representations

As discussed in Section 3.3, pre-averaging raw spacecraft data to a lower cadence can have an impact on the data distributions in a non-trivial way. For vector data, the coordinate representation can have an impact on the effect of pre-averaging. In Figure B.4, we demonstrate this with the STEREO A 1 min averaged base data product which was introduced in Figure 3.1. From top to bottom, the panels show one-minute, one-hour, and one-day averages of the vector magnetic field. The left-hand column shows the data parameterised in Cartesian coordinates (R and T), while the right-hand column shows the data parameterised in polar coordinates by the vector magnitude and clock angle (α in the main text). The top panels show exactly the same data ($B_R = |B| \cos\alpha$, $B_T = |B| \sin\alpha$. While in Cartesian distribution it fills out an annular region of parameter space, in polar coordinates, the region is more like two Gaussian ellipses. In particular, the major and minor axes of these ellipses are aligned with the axes in this case, suggesting fluctuations in —B— and α have low correlation - their fluctuations are independent. The further panels are generated by producing averages from the above 1 min averaged data, meaning that for the polar coordinate plots, the time series $|B|(t)$ and $\alpha(t)$ are the quantities that are averaged. For both cases, the resolution of the histograms worsens with larger averaging due to the lower statistics.

In both columns, a consistent contour of $|B|R^2 = 3\text{nT AU}^2$ is shown as a black curve. This is a circle in Cartesian and a vertical line in polar coordinates. For the Cartesian coordinates, as mentioned in the main text, the distribution is strongly distorted, especially noticeable in the one day averages. While the raw data is quite tightly confined to an annulus but spread quite widely around that annulus, averaging reduces the spread around the annulus but importantly also causes the data to migrate towards the origin, effectively reducing the field magnitude of the distribution. While the averaging out of the angular fluctuations is arguably a useful effect, the magnitude effect is an artificial distortion.

In polar coordinates, on the other hand, the only perceptible change of the distribution is the worsening resolution. Since the data are quite well distributed around a mean and the distribution is aligned with the $|B|$ and α axes, when successive averages of samples from this distribution are taken, the resulting means are essentially in the same distribution. As mentioned above, an equivalent inference is that the fluctuations in $|B|$ and α are independent or uncorrelated. The 3nT AU^2 contour cuts the distribution at approximately the same place. Thus, using this polar representation of the vector is useful since it produces vector time series whose distribution is much less affected by time averaging as compared to the Cartesian representation.

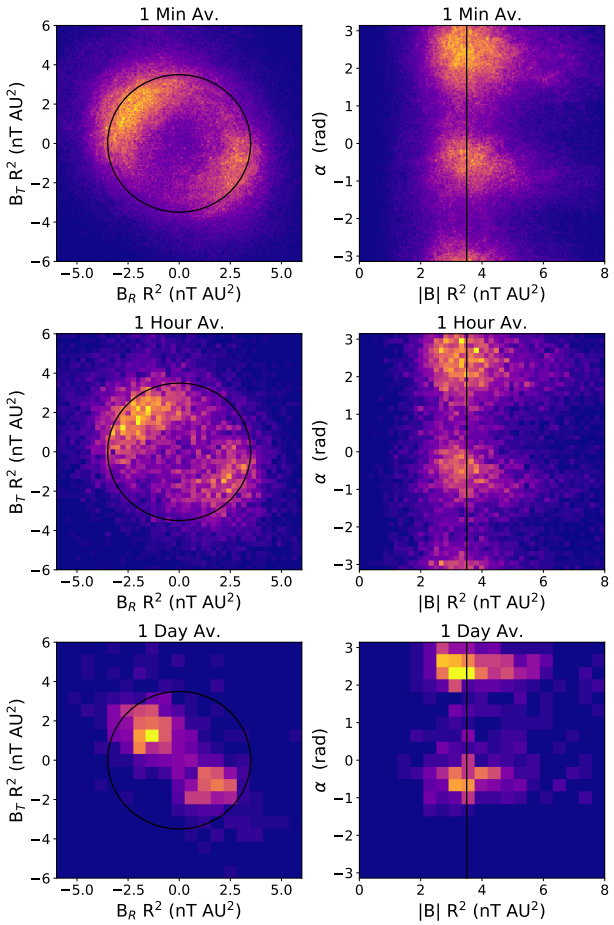

Figure B.4: Demonstration of the effect of pre-averaging HMF vector data on 2D data distributions under Cartesian and spherical representations. Each panel shows a 2D histogram of data from STEREO A for the time interval considered in this work. From top to bottom, successively more aggressive pre-averaging is applied to the data set with panels showing one minute, one hour, and one day averages. The left hand panel shows the Cartesian components $B_R R^2$ versus $B_T R^2$, while the right hand column shows the spherical representation (clock angle versus magnitude). The histogram resolution is decreased with successive averages as the number of data points reduces. A black circle in the left hand column and vertical line in the right hand column shows a curve of $|B|R^2 = 3\text{nT AU}^2$ as a guide and point of comparison between the different averages and shows the averaging transformation is more magnitude preserving when applied to the polar representation as compared to the Cartesian representation.

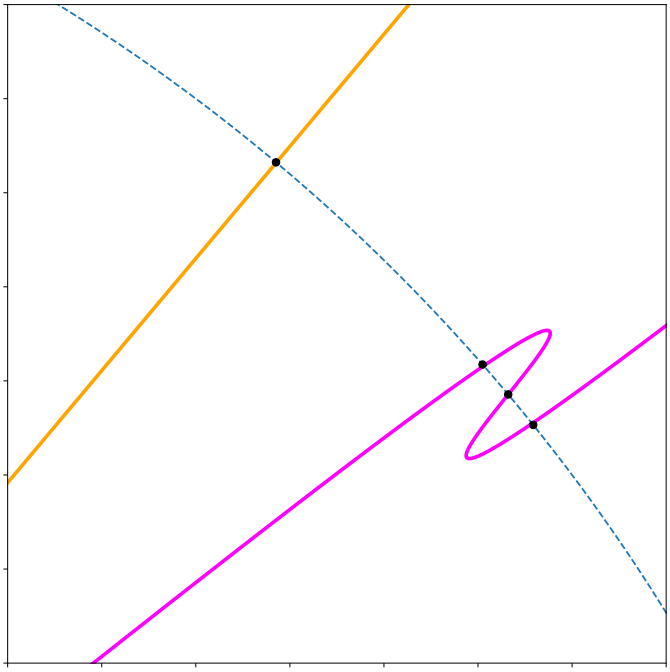

Figure B.5: Schematic of of a local field inversion and it's impact on the flux. A standard, non-inverted field-line (orange) and a field line which folds back on itself (magenta). The inverted field line intersects the spherical surface (dotted line) three times and therefore has a three times greater contribution to the flux at this radius compared to it's contribution in escaping the corona.

B.4 Schematic of a local field-line inversion

In Section 3.4, we discussed the possible contribution of excess flux due to local topological inversions of the magnetic field, as per [150]. Here we illustrate schematically the statement that 'inverted field lines contribute three times the flux as non-inverted field lines'. In this schematic, we show a surface of constant radius (dotted black line) and a non-inverted (orange), and inverted (magenta) field line. Black scatter points indicate where these curves intersect with the radial surface. As we can see, the inverted field line intersects the surface three times, compared to the orange curves single intersection. Thus, when we conserve flux by tracing field lines from the corona out to this radius, the orange field line will contribute

the same flux at the corona and this outer radius, but the inverted line will contribute three times as much. This means when contributions are all summed up at the two different radii, there will be a larger flux and, therefore, a larger value for $B_R R^2$ at the outer radius.

Appendix C

Appendix for Chapter 4

This section presents the appendices for Chapter 4.

C.1 Choice of Magnetogram Source

As mentioned in section 4.4, although we show throughout this paper results using GONG zero point corrected magnetograms we did consider a range of other possible sources. Here we show that our results are largely independent of the choice but that GONG produces the most compelling predictions.

In figure C.1 we compare the GONG results from the main text figure 4.4 with those obtained by an identical procedure on different magnetogram outputs. On the top row, are results from GONG and HMI which are both purely observational data products. Below are results from ADAPT and the DeRosa/LMSAL models which are surface flux transport models which assimilate the GONG and HMI data respectively. On visual comparison, we see GONG and ADAPT results are very similar as expected. HMI is largely consistent but with a too small a peak amplitude predicted, and has some spurious data from some of the magnetograms considered. The DeRosa/LMSAL-based result shows significant departure from the data: The period before 2018-10-29 is predicted to connect to the positive side of the heliospheric current sheet (HCS), the 2018-11-4 bump which is smoothed out by time integration (section 4.5; main text) in the other models is still prevalent and the peak positive amplitude is significantly overestimated. The variation between these models demonstrates that because PSP traversed generally very close to the HCS during Encounter 1, the predictions are quite sensitive and a small change in the modeled PIL can produce a sudden reversal in polarity measured at PSP. We err towards the GONG based data due to this empirical observation.

In terms of the difference between GONG and ADAPT, the main noticeable change is that on time integration, the ADAPT prediction becomes "choppier", subsequent 3 day intervals don't smoothly meet each other. This is likely due to the extra physical modeling in ADAPT meaning flux variations are captured at higher time resolution than with pure GONG data.

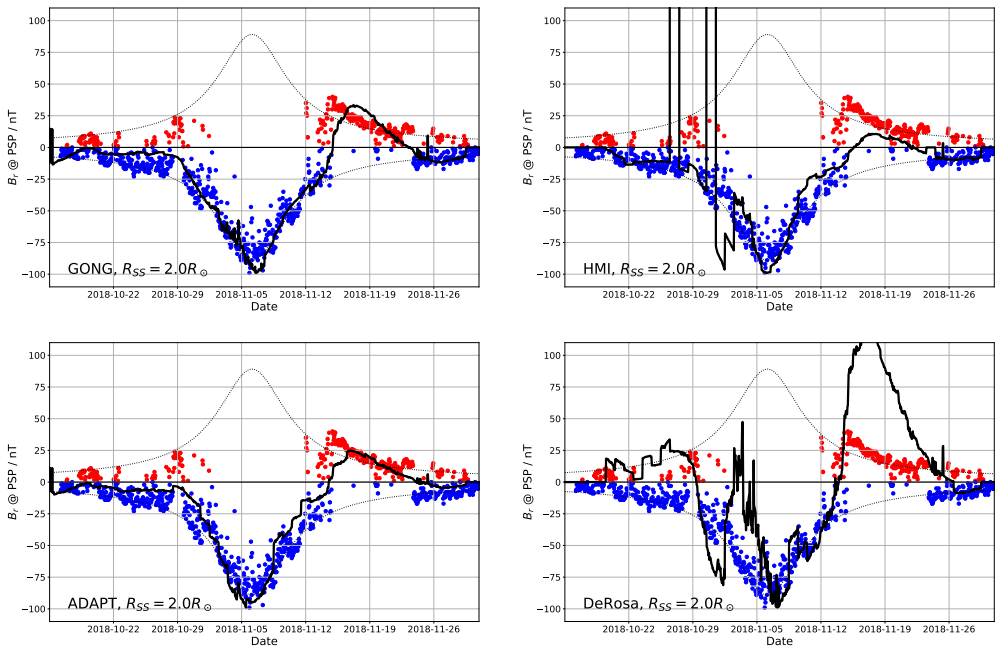

Figure C.1: **Comparison of timeseries predictions using different magnetograms**. The "best" GONG timeseries prediction from figure 4.4 (main text) is shown here in comparison to the same procedure applied to magnetograms from HMI, ADAPT and the DeRosa/LMSAL model. GONG produces the smoothest prediction on time integration but the general picture of negative polarity, $1/r^2$ variation and the times of polarity inversions are not strongly perturbed by choice of magnetogram.

Nevertheless the major conclusions from section 4.5 are unchanged from use of either of these magnetograms. Since these fluctuations don't immediately appear to correspond to data we infer although they may be physical, they are likely smoothed out exterior to the source surface via processes not considered by PFSS. Beyond this, the choice of GONG vs. ADAPT does not affect the outcome of this paper and hence we make the choice of the smoother predictions and proceed with our analysis using this.

For further comparison and to offer some insight into possible sources of discrepancy above, in figure C.2 we compare the same choices of magnetograms with a source surface height of $1.3R_\odot$ which, as discussed in section 4.5, produces predictions of new small scale polarity inversions prior to perihelion.

In this case we observe excellent consistency between all models including the DeRosa/LMSAL model. Since at this source surface height the polarity and field strength at the source surface is much more related to the field strength radially below, this is suggestive that high latitude field is the dominant cause of disparity in figure C.1 above, for example differences in how the unobserved polar regions are modeled. Nevertheless, we again note conclusions based

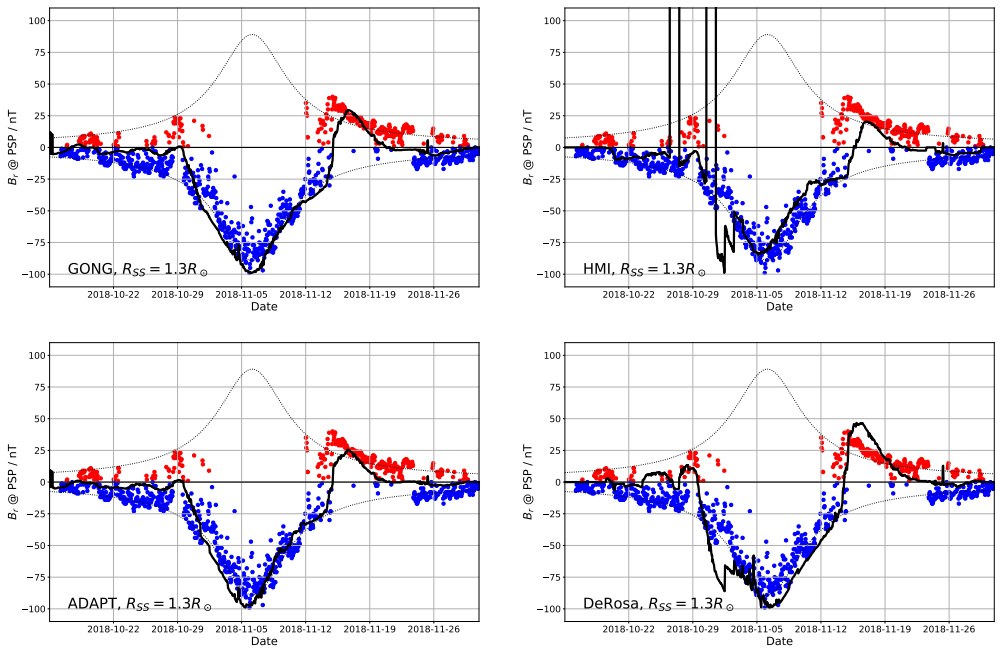

Figure C.2: **Comparison of timeseries predictions using different magnetograms at low source surface height**. Compared to $2.0R_\odot$, here all the models are very consistent with each other including LMSAL/DeRosa

on the GONG prediction are unchanged with different magnetogram sources and therefore work with this data in the main text.

C.2 Cost Function for Comparing Source Surface Heights

Further supporting evidence for our general use source surface heights below the canonical value of $2.5R_\odot$ is shown in figure C.3. Here, we compute a least squares cost function evaluating the relative similarity between time integrated models (see section 4.5).

This cost function is given by :

$$L(M, O) = \sqrt{\sum_{i=0}^{N} (M_i - O_i)^2} \tag{C.1}$$

where the model, M and observations, O are N dimensional vectors. Since both the model and observations are expressed in nT this is also the unit of the cost function. In figure C.3

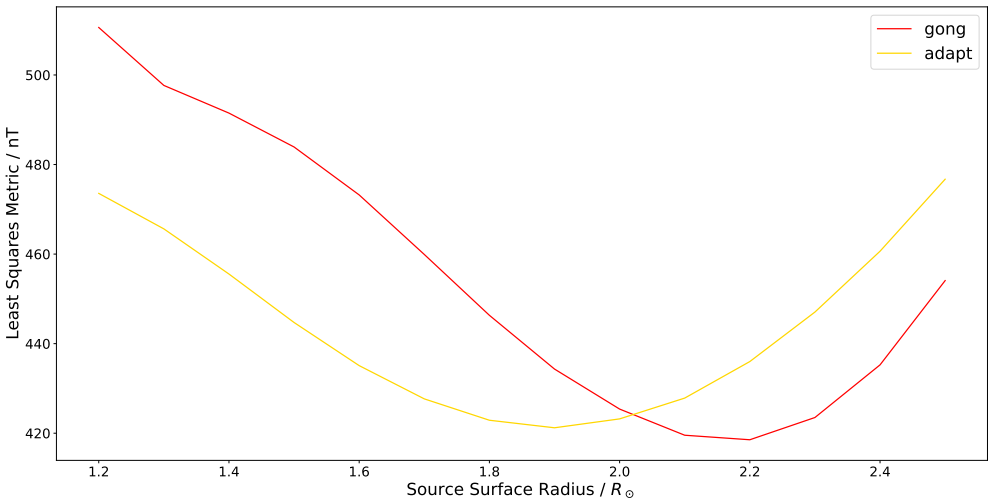

Figure C.3: **Least squares metric computed between time integrated model results and PSP data as a function of source surface height**. Results for GONG and ADAPT are shown and exhibit a distinct minimum below the canonical $2.5R_\odot$ for both cases.

we show the least squares result as a function of source surface height using the GONG (red) and ADAPT (gold) input magnetograms.

Both models show a distinct minimum (best fit) at a significantly lower source surface height that $2.5R_\odot$. The ADAPT "best" height is approximately $1.9R_\odot$ while for GONG it is approximately $2.2R_\odot$. However, these minima are both very broad and have overlapping full width half maxima. In addition, as discussed in the main text the concept of a single source surface height to fit all longitudes and for a 6 week long interval is likely not a good approximation. We settle on a value of $2.0R_\odot$ to discuss a global picture in the main text, but note here a range of $\pm 0.2R_\odot$ will have very little affect on the overall goodness of fit.

Appendix D

Appendix for Chapter 5

This final section presents the appendix for chapter 5.

D.1 Time Delay of Arrival (TDOA) Technique

In this work, we utilized the time delay of arrival [TDOA; 2] technique to derive the trajectory of the type III source region at heliospheric distance scales (i.e. large fractions of an au). In this appendix we explain the methodology used to derive these distance estimates.

At the top level, we take radio spectrogram data from three individual spacecraft (for

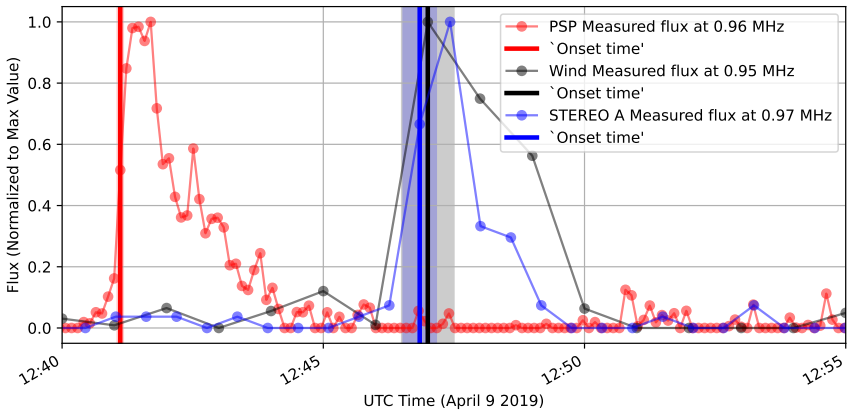

Figure D.1: Example radio flux vs time profile and onset extraction example. Each profile is normalized by its maximum value so they can be shown on the same axes. Profile is from the closest frequency channel to 0.96 MHz in each spacecraft receiver. Red, blue and black profiles respectively show PSP/FIELDS/RFS, S/WAVES and Wind/WAVES observations. Data points are shown explicitly to demonstrate differing instrument resolution.

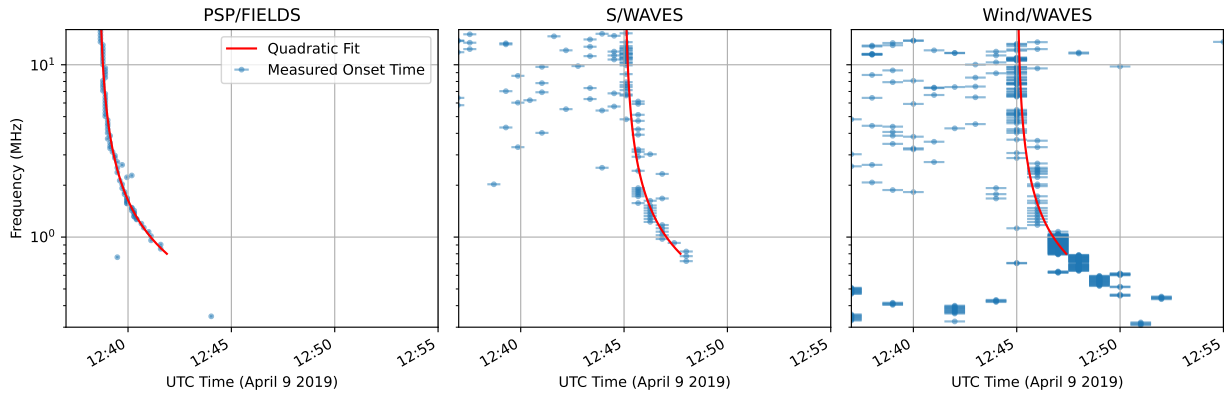

Figure D.2: Onset time feature extraction (blue) and quadratic fitting (red) to the type III burst studied in this work as observed by PSP, STEREO A and Wind. Error bars show the instrument time resolution. Fitting is only done over the frequency range clearly observed in all three spacecraft.

the event studied in this work, Parker Solar Probe/FIELDS/RFS, STEREO-A/WAVES and Wind/WAVES, figure 5.3a-c) which are mutually separated by large enough distances (light travel time longer than several minutes and therefore longer than each instrument's time resolution). For each spacecraft we measure the "onset time" of the burst in each frequency channel. We define this as the first time stamp at which the radio flux reaches half its maximum value in that channel (an example flux-time profile for similar frequencies in the three spacecraft receivers is shown in figure D.1). By measuring the onset rather than, for example the time of peak flux, we minimize the effects of refraction and scattering effects by measuring the radio waves which have taken the shortest path length from source to receiver, although as seen in D.1 the burst rise time can be a similar timescale to the instrument resolution of Wind.

Extracting these features from the spectrograms produces a frequency (f) vs. time (t) profile for each spacecraft describing the "time of arrival" of the radio burst at each frequency. The frequency values of these profiles are set by the different channels measured by each instrument. To derive relative time delays between pairs of spacecraft we need to cast this data to a common grid of frequencies. To accomplish this, we fit a smooth curve to each frequency time profile. we fit a second order polynomial function to the set of values ($1/f$, t), where we use the reciprocal of the frequency (wavenumber) since this results in a curve well approximated by a quadratic. We then resample each (f, t) profile at a common set of frequencies to derive time of arrivals which can be directly differenced between spacecraft. This fitting process and output is shown in figure D.2 which shows that in addition to allowing frequency interpretation, (1) the fitted curve follows the onset data very closely (within the instrument time resolution in most cases), (2) allows rejection

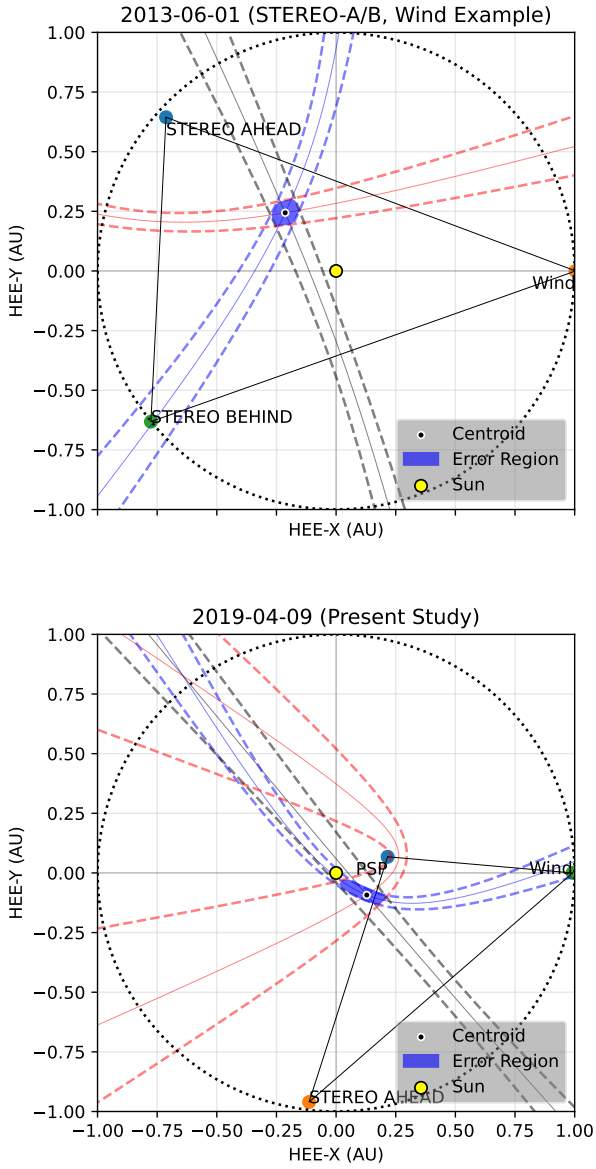

Figure D.3: Schematic of the time delay of arrival localization method and associated error region. The top panel shows a synthetic example using the positions of STEREO A/B and Wind in 2013 to clearly show how the hyberbola intersection defines the error region. The right hand panel shows the specific geometry for the event in this study using the measured time delays at 1.04MHz. Each panel shows in the HEE frame: the spacecraft geometry, the hyperbola generated from each pair of time delays, the resulting source centroid and error region. Annotations on the plot also include the position of the Sun and a dotted circle indicates 1 au where all three spacecraft in this constellation are approximately located.

of outliers in the onset detection especially at higher frequencies where the background is noisier, and (3) smoothly interpolates the Wind/WAVES (and to a lesser extent S/WAVES) data which has an extremely coarse time resolution.

Following the feature extraction step, for each pair of spacecraft, we find the *difference* in time of arrival as a function of frequency. At a given frequency, we can combine this derived time delay with a baseline defined by the vector separation of the relevant spacecraft to produce a single 2D hyperbola in the ecliptic plane along which the radio emission at that wavelength originates subject to the following two assumptions:

1. Free streaming radio emission from source to receiver. We note that by extracting the burst onset we have attempted to minimize this error source, but it otherwise largely remains unquantified.

2. Near-ecliptic propagation of the burst. By "near-ecliptic", the precise approximation we are making is as follows: We are assuming that the source trajectory and the three spacecraft where the measurements are made are mutually coplanar. There will therefore be small but non-zero errors coming from the differing heliographic latitudes of STEREO A and PSP, and any angular displacement between the true burst propagation direction and the ecliptic plane. Although a full estimate is non-trivial, the magnitude of these errors can be estimated by finding the perpendicular light travel time between each location and the ecliptic plane. For the studied time interval, we find the following values for the constellation of receivers : PSP=5.42s, Wind/L1=0.01s, STEREO A=-1.00s. For the burst, we estimate the off-ecliptic latitude from figure 5.5 as $\lesssim 4^o$. At the maximum radius of around $50R_\odot$ we obtain a light travel time of 8s. In summation, we find the error is sub-dominant to the instrument resolution.

Obtaining such a hyperbola for two pairs of spacecraft (three spacecraft total) is sufficient to constrain the source position to a single point. Algorithmically, it results in two points, one sunward of the baseline and one anti-sunward, but we can rule out the anti-sunward source due to (1) the monotonically decreasing solar wind electron plasma density which prevents radio emission travelling inwards in the heliosphere, (2) simply that there are no credible alternatives to the canonical picture that type III bursts originate at the Sun. Thus for each frequency we produce a 2D source position in the ecliptic plane.

Further, we can estimate a conservative error region by utilizing the instrument resolution for each spectrogram measurement. For PSP/RFS, S/WAVES and Wind/Waves these are err= 7s, 38.05s and 60s respectively. We therefore allow that each onset time is accurate to $\pm err/2$. These errors are then summed pairwise to give an error in relative time of arrival between each pair. As noted above our fitted quadratic curves to the burst profile track the measured burst onset to within these error bars for the majority of frequency channels. The propagation of this error to the source position effectively blurs the hyperbolae to give finite thickness. Intersecting these blurred profiles with three independent spacecraft measurements results in a hexagonal source region whose aspect ratio depends on relative

spacecraft position (note that while the centroid is uniquely determined by two time delay measurements from three spacecraft, the error region is further constrained by including all permutations (three time delay measurements) from the three spacecraft. This hexagon can be found either by forming a minimum area convex hull from the analytic intersections of the edges of the blurred hyperbolae as illustrated in figure D.3, or more simply as done in the main text in figure 5.6 by randomly sampling time delay measurements within the stated error bounds and populating the source positions in the ecliptic plane.

This source analysis method and error region formation process, similar to that presented by [2], is summed up here in figure D.3. We show both an example configuration with STEREO-A, STEREO-B and Wind in 2013 to clearly illustrate how the hyperbolae intersect to create the hexagonal error region as well as the configuration for the presently studied event where the hyperbola intersection is stretched and narrowed due to the orbital geometry.